

Pulsar searching and timing with the Parkes telescope

Dissertation

zur

Erlangung des Doktorgrades (*Dr. rer. nat.*)

der

Rheinischen Friedrich–Wilhelms–Universität, Bonn

vorgelegt von

Cherry Wing Yan NG

aus

Hong Kong, China

Bonn 2014

Angefertigt mit Genehmigung der Mathematisch-Naturwissenschaftlichen Fakultät
der Rheinischen Friedrich-Wilhelms-Universität Bonn

1. Referent: Prof. Dr. Michael Kramer [Supervisor]
2. Referent: Prof. Dr. Norbert Langer [2nd referee]

Tag der Promotion: 19 - 11 - 2014
Erscheinungsjahr: 2014

Diese Dissertation ist auf dem Hochschulschriftenserver der ULB Bonn unter
http://hss.ulb.uni-bonn.de/diss_online elektronisch publiziert

Abstract

by Cherry Wing Yan Ng

for the degree of

Doctor rerum naturalium

Pulsars are highly magnetised, rapidly rotating neutron stars that radiate a beam of coherent radio emission from their magnetic poles. An introduction to the pulsar phenomenology is presented in Chapter 1 of this thesis. The extreme conditions found in and around such compact objects make pulsars fantastic natural laboratories, as their strong gravitational fields provide exclusive insights to a rich variety of fundamental physics and astronomy.

The discovery of pulsars is therefore a gateway to new science. An overview of the standard pulsar searching technique is described in Chapter 2, as well as a discussion on notable pulsar searching efforts undertaken thus far with various telescopes. The High Time Resolution Universe (HTRU) Pulsar Survey conducted with the 64-m Parkes radio telescope in Australia forms the bulk of this PhD. In particular, the author has led the search effort of the HTRU low-latitude Galactic plane project part which is introduced in Chapter 3. We discuss the computational challenges arising from the processing of the petabyte-sized survey data. Two new radio interference mitigation techniques are introduced, as well as a partially-coherent segmented acceleration search algorithm which aims to increase our chances of discovering highly-relativistic short-orbit binary systems, covering a parameter space including the potential pulsar-black hole binaries. We show that under a linear acceleration approximation, a ratio of ≈ 0.1 of data length over orbital period results in the highest effectiveness for this search algorithm.

Chapter 4 presents the initial results from the HTRU low-latitude Galactic plane survey. From the 37 per cent of data processed thus far, we have re-detected 348 previously known pulsars and discovered a further 47 pulsars. Two of which are fast-spinning pulsars with periods less than 30 ms. PSR J1101–6424 is a millisecond pulsar (MSP) with a heavy white dwarf companion while its short spin period of 5 ms indicates contradictory full-recycling. PSR J1757–27 is likely to be an isolated pulsar with an unexpectedly long spin period of 17 ms. In addition, PSR J1847–0427 is likely to be an aligned rotator, and PSR J1759–24 exhibits transient emission property. We compare this newly-discovered pulsar population to that previously known, and we suggest that our current pulsar detection yield is as expected from population synthesis.

The discovery of pulsars is just a first step and, in fact, the most interesting

science can usually only be revealed when a follow-up timing campaign is carried out. Chapter 5 focuses on the timing of 16 MSPs discovered by the HTRU. We reveal new observational parameters such as five proper motion measurements and significant temporal dispersion measure variations in PSR J1017–7156. We discuss the case of PSR J1801–3210, which shows no significant period derivative (\dot{P}) after four years of timing data. Our best-fit solution shows a \dot{P} of the order of 10^{-23} , an extremely small number compared to that of a typical MSP. However, it is likely that the pulsar lies beyond the Galactic Centre, and an unremarkable intrinsic \dot{P} is reduced to close to zero by the Galactic potential acceleration. Furthermore, we highlight the potential to employ PSR J1801–3210 in the strong equivalence principle test due to its wide and circular orbit. In a broader comparison with the known MSP population, we suggest a correlation between higher mass functions and the presence of eclipses in ‘very low-mass binary pulsars’, implying that eclipses are observed in systems with high orbital inclinations. We also suggest that the distribution of the total mass of binary systems is inversely-related to the Galactic height distribution. We report on the first detection of PSRs J1543–5149 and J1811–2404 as gamma-ray pulsars.

Further discussion and conclusions arise from the pulsar searching and timing efforts conducted with the HTRU survey can be found in Chapter 6. Finally, this thesis is closed with a consideration of future work. We examine the prospects of continuing data processing and follow-up timing of discoveries from the HTRU Galactic plane survey. We also suggest potential improvements in the search algorithms aiming at increasing pulsar detectability.

Contents

1	Pulsar Phenomenology	5
1.1	Neutron stars	5
1.2	The lighthouse model	7
1.3	Propagation effects	9
1.3.1	Pulse dispersion	9
1.3.2	Interstellar scattering	11
1.4	Pulsar diversity	11
1.4.1	Binary systems	13
1.4.2	Magnetars	15
1.5	Pulsar timing	16
1.6	Pulsars as physical tools	19
1.7	Thesis outline	22
2	Pulsar Searching	23
2.1	Instrumentation and algorithms	23
2.1.1	Data acquisition	23
2.1.2	The standard periodicity search	25
2.1.2.1	RFI removal	25
2.1.2.2	De-dispersion	26
2.1.2.3	The discrete Fourier transform	28
2.1.2.4	Spectral whitening	29
2.1.2.5	Harmonic summing	30
2.1.2.6	False-alarm probability	31
2.1.3	Binary pulsar searches	32
2.1.3.1	Time domain resampling	32
2.1.3.2	Other techniques	34
2.1.4	Candidate selection and optimisation	36
2.2	An overview of pulsar surveys	37
2.2.1	Previous generations	37
2.2.2	Contemporary pulsar surveys	39
2.2.3	Next generations of pulsar surveys	42
3	The HTRU Pulsar Survey	45
3.1	Introduction to the HTRU Pulsar Survey	45
3.1.1	Observing system	48
3.1.2	Survey sensitivity	50
3.2	Discovery highlights	53
3.2.1	‘Planet-pulsar’ binaries	53
3.2.2	Magnetar PSR J1622–4950	54
3.2.3	Fast Radio Bursts	55

3.3	The low-latitude Galactic plane survey	57
3.3.1	RFI mitigation	60
3.3.1.1	Time domain	60
3.3.1.2	Fourier domain	61
3.3.2	Acceleration search	63
3.3.2.1	The ratio of data length over orbital period, r_{orb}	63
3.3.2.2	Acceleration ranges	66
3.3.2.3	Partially-coherent segmentation	68
3.3.3	Candidate confirmation and gridding strategy	71
4	The low-latitude Galactic plane survey discoveries	73
4.1	Re-detections of known pulsars	73
4.2	New pulsars	78
4.3	Individual pulsars of interest	84
4.3.1	PSR J1101–6424, a Case A Roche lobe overflow cousin of PSR J1614–2230	84
4.3.2	PSR J1759–24, an intermittent pulsar?	85
4.3.3	PSR J1757–27, likely to be a fast-spinning isolated pulsar?	87
4.3.4	PSR J1847–0427, a pulsar with an extremely wide pulse	87
4.4	Comparing with known pulsar population	88
4.4.1	Luminosity	88
4.4.2	Characteristic ages	89
4.4.3	Spin-down power and Fermi association	94
4.5	A comparison with the estimated survey yield	94
5	Discovery of four millisecond pulsars and updated timing solutions of a further 12	97
5.1	Observations and analysis	98
5.2	Discovery of four millisecond pulsars	100
5.2.1	On the nature of the binary companions	100
5.2.2	Polarisation Profiles	101
5.3	Updated timing of 12 HTRU millisecond pulsars	107
5.3.1	Dispersion measure variations	107
5.3.2	Proper motion and transverse velocities	108
5.3.3	Observed and inferred intrinsic period derivatives	109
5.3.3.1	PSR J1017–7156	110
5.3.3.2	PSR J1801–3210	112
5.3.4	Binary companions and mass functions	116
5.3.5	Galactic height distribution	118
5.3.6	Orbital eccentricity	121
5.3.7	Change in projected semi-major axis, \dot{x}	123
5.3.8	Orbital period variation, \dot{P}_{orb}	124
5.3.9	Variation in the longitude of periastron, $\dot{\omega}$	125
5.3.10	Gamma-ray pulsation searches	125

6	Conclusion and future work	129
6.1	Conclusion	129
6.1.1	The HTRU Galactic plane survey	129
6.1.2	Timing 16 MSPs from the medium latitude survey	132
6.2	Future work	133
6.2.1	Continued processing	133
6.2.2	Follow-up on discoveries from the Galactic plane survey	134
6.2.3	Further improvements in the search algorithms	134
6.3	Closing remarks	135
	Bibliography	137
	Appendix A HTRU Galactic plane survey known pulsar re-detections	149

List of Figures

1.1	An illustration of the pulsar lighthouse ‘toy model’.	7
1.2	DM of all pulsars in the direction towards the Galactic centre.	10
1.3	Period-period derivative ($P - \dot{P}$) diagram of all published pulsars.	12
1.4	Two different binary evolutionary tracks leading to MSP-WDs and DNSs.	14
1.5	Illustration of the effects of incomplete timing models.	17
1.6	Definition of the Keplerian orbital parameters for a binary pulsar.	18
2.1	A block diagram of a receiver system and a pulsar ‘searching backend’.	24
2.2	Schematic flowchart of a standard pipeline based on a periodicity search.	25
2.3	The effect of dispersion smearing as seen in a frequency versus phase plot.	27
2.4	The degradation of S/N versus DM offset.	28
2.5	The red noise component as seen in a Fourier spectrum.	29
2.6	Illustration of the Fourier spectrum harmonic summing technique.	30
2.7	PDFs of the Fourier power and amplitude spectra.	32
2.8	Spectral smearing caused by the uncorrected orbital acceleration.	33
2.9	The characteristic modulation in Fourier spectrum due to orbital motion.	35
2.10	Two candidate plots as generated by the search pipeline.	36
2.11	Sky coverage of Parkes blind pulsar surveys conducted in the 1990’s.	38
2.12	Sky coverage of all contemporary pulsar surveys.	40
3.1	The HTRU split into three regions of the sky.	46
3.2	A schematic diagram of the Parkes telescope.	48
3.3	Contours of constant pulse broadening time scale in ms.	50
3.4	The minimum detectable flux density for the HTRU survey.	51
3.5	All HTRU discoveries as of 15 June 2014.	53
3.6	Various contributions to the observed band delay of the FRBs	56
3.7	Spatial distribution of the processed HTRU Galactic plane observations.	59
3.8	Histogram of the time samples removed per Galactic plane observation	61
3.9	Comparison of the effectiveness in various RFI mitigation techniques.	62
3.10	Orbital acceleration and S/N of the double pulsar at various orbital phases.	64
3.11	Detected S/N versus r_{orb} at selected orbital phases	65
3.12	Maximum orbital acceleration vs orbital period assuming circular orbits.	67
3.13	A schematic of the ‘partially-coherent segmented’ pipeline.	69
3.14	Relative processing time required for the parallel acceleration searches.	70
3.15	Gridding configuration used in the HTRU Galactic plane survey.	71
4.1	The S/Ns of pulsars re-detected in the HTRU Galactic plane survey.	76
4.2	Average pulse profile of the 47 newly-discovered pulsars.	81
4.3	Spin period vs minimum companion mass for all published binary pulsars.	85
4.4	Discovery plot of PSR J1759–24.	86

4.5	Luminosity vs distance of the 20 newly-discovered pulsars.	88
4.6	Placing 16 newly-discovered pulsars on a $P-\dot{P}$ diagram.	91
4.7	Characteristic age histograms for various period bins.	92
4.8	Histograms and CDFs of characteristic ages of known and newly discovered pulsars.	93
5.1	Polarisation profiles of four newly-discovered MSPs.	102
5.2	Temporal DM variations for PSR J1017–7156.	108
5.3	Placing the 16 MSPs on a $P-\dot{P}$ diagram.	111
5.4	Different M_3 and the respective orbital period and semi-major axis.	114
5.5	Various \dot{P} contributions for PSR J1801–3210.	115
5.6	Mass function vs orbital period for all binary pulsars.	117
5.7	Mass function vs absolute Galactic height from the Galactic plane.	119
5.8	Eccentricity vs. orbital period (P_{orb}).	122
5.9	ΔT_0 as a function of time for PSR J1731–1847.	125
5.10	Radio and gamma-ray light curves for four MSPs.	126

List of Tables

2.1	Specifications of pulsar surveys conducted with contemporary technology.	41
3.1	Specifications of the HTRU-North and HTRU-South surveys.	47
3.2	Specifications of the Parkes 20-cm multibeam receiver.	49
3.3	Minimum detectable flux for the HTRU Galactic plane survey.	52
3.4	Comparison between the two ‘Planet-pulsar’ binaries.	54
4.1	Previously-known binary pulsars re-detected thus far.	75
4.2	Previously known pulsars with an $S/N_{\text{exp}} > 9$ that have been missed.	77
4.3	The S/N , S_{1400} , L_{1400} , W_{50} and W_{10} of the 47 pulsar discoveries.	80
4.4	Parameters of 22 newly-discovered pulsars without timing solution.	82
4.5	TEMPO2 best-fitting parameters of the 25 newly-discovered pulsars.	83
4.6	Binary parameters for PSR J1101–6424.	84
5.1	Observing systems employed for the timing observations in Chapter 5	99
5.2	TEMPO2 best-fit parameters for the four newly-discovered MSPs.	103
5.3	TEMPO2 best-fit parameters using the ELL1 timing model.	104
5.4	TEMPO2 best-fit parameters using the ELL1 timing model.	105
5.5	TEMPO2 best-fit parameters using the DD and BTX timing model.	106
5.6	The derived \dot{P}_{shk} and \dot{P}_{gal} for 12 MSPs.	109
5.7	Statistical distribution of Galactic height for each binary pulsar group.	120
5.8	Gamma-Ray emission properties of four MSPs with Fermi associations.	127
A1	The 348 previously known pulsars re-detected.	149

Nomenclature

Frequently Used Symbols

a / a_{orb}	Orbital acceleration
\dot{a}	First derivative of orbital acceleration (jerk)
a_{p}	Semi-major axis
B	Bandwidth
B_{surf}	Characteristic dipole surface magnetic field strength
b	Galactic latitude
c	Speed of light
d	Distance
\dot{E}	Spin-down energy
e	Orbital eccentricity
f	Mass function
f_{c}	Central observing frequency
G	Gravitational constant or antenna gain
i	Orbital inclination
L	Luminosity
l	Galactic longitude
m_{c}	Companion mass
m_{p}	Pulsar mass
n_{chan}	Number of channels
n_{e}	Electron number density
n_{FFT}	Number of samples in FFT
n_{p}	Number of polarisations
n_{samp}	Number of samples
P	Spin period
\dot{P}	First derivative of spin period
P_{orb}	Orbital period
P_{thres}	False-alarm power threshold
r_{orb}	Ratio of data length over orbital period
S_{min}	Characteristic minimum detectable flux density
T_0	Epoch of periastron
T_{asc}	Epoch of ascending node passage
T_{rec}	Temperature of receiver
T_{sky}	Temperature of sky background
T_{sys}	Temperature of observing system ($T_{\text{rec}} + T_{\text{sky}}$)
t_{int}	Integration time
t_{samp}	Time sampling rate
V_{T}	Transverse velocity
W_{50}	Pulse width at 50 per cent of the highest peak

W_{eff}	Effective pulse width
W_{int}	Intrinsic pulse width
x	Projected semi-major axis
α	Right ascension (R.A.) or the angle between the magnetic rotational axis
β	Digitisation degradation factor
δ	Declination (Dec.) or pulsar duty cycle
μ	Proper motion
ν	Spin frequency
π	Parallax
ϕ	Orbital phase
Ω	Longitude of ascending node
ω	Longitude of periastron
τ_c	Characteristic age
τ_s/τ_{sc}	Scattering time scale

Numerical Constants

π	= 3.14156
1 rad	= 57.296°
e	= 2.7183

Physical Constants

Speed of light	$c = 2.9979 \times 10^8 \text{ m s}^{-1}$
Gravitational constant	$G = 6.670 \times 10^{-11} \text{ m}^3 \text{ kg}^{-1} \text{ s}^{-2}$

Astronomical Constants

Astronomical unit (1 AU)	= $1.496 \times 10^{11} \text{ m}$
Parsec (1 pc)	= $3.086 \times 10^{16} \text{ m}$
Julian light year (1 ly)	= $9.460730472 \times 10^{15} \text{ m}$
Julian year (1 yr)	= $3.15576 \times 10^7 \text{ s}$
Solar mass (1 M_{\odot})	= $1.989 \times 10^{30} \text{ kg}$
Earth mass	= $5.974 \times 10^{24} \text{ kg}$
Jupiter mass (1 M_J)	= $1.899 \times 10^{27} \text{ kg}$
T_{\odot}	= $4.925490947 \mu\text{s}$
Jansky (1 Jy)	= $10 \times 10^{26} \text{ W m}^{-2} \text{ Hz}^{-1}$

Frequently used acronyms

APSR	The ATNF Parkes Swinburne Recorder
BH	Black hole
BPSR	The Berkeley-Parkes-Swinburne Recorder
BW	Black widow pulsar

CASPSR	The CASPER Parkes Swinburne Recorder
CO-WD	Carbon-oxygen white dwarf
DFB	Digital Filter bank system
DM	Dispersion measure
DNS	Double neutron star
EoS	Equation of state
FFT	The <i>fast Fourier Transform</i>
FPGA	Field Programmable Gate Array
FRB	Fast Radio Transient Burst
FWHM	Full width at half-maximum
GC	Globular Cluster
GR	General relativity
GBT	The 100-m Robert C. Byrd Green Bank telescope
He-WD	Helium white dwarf
HTRU	The High Time Resolution Universe Pulsar Survey
ISM	Interstellar medium
IMXB	Intermediate mass X-ray binary pulsar
LAT	<i>Fermi</i> Large Area Telescope
LMXB	Low mass X-ray binaries
MS	Main sequence star
MSP	Millisecond pulsar
NS	Neutron star
ONeMg-WD	Oxygen-neon-magnesium white dwarf
P.A.	Position angle
PK	Post-Keplerian
PMPS	The Parkes multibeam pulsar survey
PSR	Pulsar
PSRCAT	The <i>ATNF Pulsar Catalogue</i>
PTA	Pulsar timing array
RFI	Radio frequency interference
RLO	Roche-lobe overflow
RM	Rotation measure
RMS	Root mean square
RRAT	Rotating RAdio Transients
SEP	The strong equivalence principle
SKA	The Square Kilometre Array
S/N_{thres}	False-alarm signal-to-noise threshold
SNR	Supernova remnant
SSB	The Solar system's barycentre
TOA	Time of arrival
UL binaries	Ultra-light binaries
VLMBP	Very low-mass binary pulsars
WD	White dwarf

Pulsar Phenomenology

The first pulsar discovery was made by chance in 1967, from the data charts of Anthony Hewish and his research student Jocelyn Bell (Hewish et al., 1968). The periodic signal was originally thought to come from a new population of pulsating radio sources hence the portmanteau ‘pulsar’. The discoveries of the Vela (Large et al., 1968) and the Crab pulsars (Staelin & Reifenstein, 1968), both with spin periods less than 100 ms, indicated that these objects must be very compact compared to normal stellar objects. In fact, only a star composed entirely of neutrons could potentially vibrate or rotate that fast. Neutron stars had already been predicted theoretically by Baade & Zwicky (1934) more than 30 years before these discoveries. The observed slow down in the periodicity of the Crab pulsar (Richards & Comella, 1969) further ruled out the possibility of radial pulsations or binary-motion induced period changes. Pre- and post-discovery work respectively by Pacini (1967) and Gold (1968); Hewish et al. (1968) established the identity of the sources of these pulsed emission to be rotating neutron stars. Then it was soon recognised that pulsars, with extremely high density and gravitational field impossible to be re-created on Earth, would become fantastic natural laboratories providing exclusive insights to a rich variety of fundamental physics and astronomy.

Contents

1.1 Neutron stars	5
1.2 The lighthouse model	7
1.3 Propagation effects	9
1.3.1 Pulse dispersion	9
1.3.2 Interstellar scattering	11
1.4 Pulsar diversity	11
1.4.1 Binary systems	13
1.4.2 Magnetars	15
1.5 Pulsar timing	16
1.6 Pulsars as physical tools	19
1.7 Thesis outline	22

1.1 Neutron stars

Once a main-sequence star consumes all its nuclear fuel and exhausts its sources of energy, the star undergoes gravitational collapse as its nuclear reaction can no longer

act against its own force of gravity. Depending on the mass of the progenitor star, there are three possible endpoints of stellar evolution. The least massive stars contract to form white dwarfs, while the most massive stars collapse to become black holes. The intermediate mass stars (between 8 and $25 M_{\odot}$) result in what is known as neutron stars.

Initially the gravitational collapse leads to the formation of a growing core within an expanding shell, and a total collapse is prevented by electron degeneracy pressure of the core. If the progenitor star is massive enough, the mass of the iron core eventually exceeds the Chandrasekhar limit of $1.4 M_{\odot}$. At this point, even the electron degeneracy pressure of the core is insufficient to balance the increasing gravitational self-attraction, leading to a second stage of rapid collapse much more violent than the first. A large amount of gravitational potential energy of the star is released within a few seconds, and such a catastrophic event is observed as a supernova explosion.

Most of the original mass of the progenitor star, which lies outside of the collapsing core, is lost during the supernova explosion, while the remaining core has a mass of the order of the Chandrasekhar limit and theoretical models based on current constraints predict a maximum neutron star mass of about $2.4\text{--}2.5 M_{\odot}$ (Steiner et al., 2013). The radius of the remaining core is predicted to be around 10 to 12 km (Lattimer & Prakash, 2001), which is only about 3 times larger than the Schwarzschild radius, showing that neutron stars are highly compact objects almost like black holes. Recall that a typical main-sequence progenitor star has a radius of the order of 10^6 km, therefore much larger in size with respect to the neutron star. Conservation of angular momentum during their formation thus leads to the rapid rotation of neutron stars, while conservation of magnetic flux means the magnetic field lines of the progenitor star are pulled close together during the gravitational collapse and intensifying the magnetic fields of neutron stars to $10^{10\text{--}12}$ G. The rotation and the dipolar magnetic field lead to the basis of pulsar phenomenon, as discussed below in Section 1.2.

A back-of-the-envelope calculation using the above mass and radius shows that a neutron star has an extremely high density exceeding 10^{17} kg m⁻³, which is similar to nuclear matter. At such a density, free electrons can interact with the nuclei and combine with protons to form neutrons. As the nuclei become more and more neutron-rich, they release free neutrons and eventually all, but a small percentage of the interior matter, exists in the form of a neutron superfluid. The first model of a neutron star comes from Oppenheimer & Volkoff (1939). They postulated that under such conditions the neutrons form a degenerate Fermi gas, with large neutron degeneracy pressure that prevents further collapse. In fact for such a degenerate star, the only important characteristics are its density and pressure. The relationship of density and pressure is described by the equation-of-state (EoS). The EoS of a neutron star is, however, uncertain as such highly compressed matter cannot be recreated and studied on Earth.

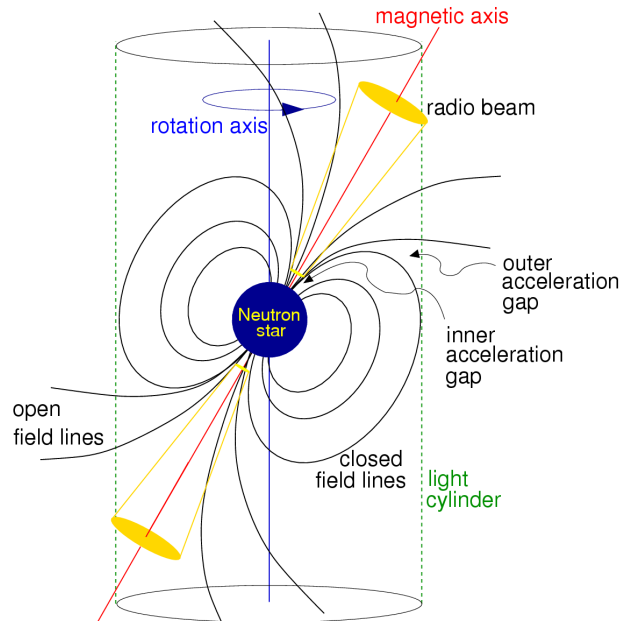


Figure 1.1: An illustration of the lighthouse ‘toy model’ as applied to the rotating neutron star and its magnetosphere. Image taken from [Lorimer & Kramer \(2005\)](#). Figure not to scale.

1.2 The lighthouse model

The most used analogy for the pulsar mechanism is the ‘lighthouse’ model as illustrated in Fig. 1.1. Instead of seeing a continuous light from a lamp, we receive a radiation that appears to be flashing. This lighthouse characteristic is a result of the misalignment between the rotation axis and the emission axis. As the neutron star spins around its rotation axis, charged particles are accelerated along the magnetic field lines which forms a conical beam of electromagnetic radiation. Should this emission beam cross our line of sight, it can be observed most readily in radio wavelengths. However, given that the rotation and the emission axes are misaligned, we will only catch the emission beam at some particular phases per rotation as it swings by our line of sight. Hence, the apparent pulsed emission naturally has the same periodicity as the spin period of the neutron star.

As predicted by the neutron star model ([Pacini, 1967](#); [Gold, 1968](#)), the spin period of a pulsar is observed to increase with time, i.e. $\dot{P} = dP/dt > 0$, as a result of the outgoing radiation carrying away the rotational kinetic energy of the pulsar. All radio pulsars are rotation-powered objects hence their respective spin period, P , and period derivative, \dot{P} , are fundamental to their identities. As we shall see in the following, we can derive a number of pulsar properties from these two parameters.

Given that the rotational energy is $E = 1/2I\Omega^2$, where I is the moment of inertia and for a canonical pulsar it is 10^{38} kg m^2 . The angular velocity of the pulsar is represented by $\Omega = 2\pi/P$, where P is the spin period. The maximum total output

power of a pulsar can then be identified with the spin-down luminosity, \dot{E} . We have the following equation from Lorimer & Kramer (2005),

$$\dot{E} = I\Omega\dot{\Omega} \simeq 3.95 \times 10^{31} \text{ erg s}^{-1} \left(\frac{\dot{P}}{10^{-15}} \right) \left(\frac{P}{\text{s}} \right)^{-3}. \quad (1.1)$$

Only a small portion of \dot{E} is converted to the radio emission that we will be studying in this PhD thesis, whereas most of the rotational energy loss is converted to magnetic dipole radiation, pulsar wind and high energy emission.

According to classical electrodynamics (see e.g., Jackson, 1962), a rotating magnetic dipole radiates an electromagnetic wave at its rotation frequency. Since we can assume that, this radiation power, \dot{E}_{dipole} , is the main consumer of the rotational kinetic energy, we can equate \dot{E}_{dipole} with \dot{E} , and the rotational frequency $\nu = 1/P$ then can be expressed as a simple power law as shown for example in Lorimer & Kramer (2005),

$$\dot{\nu} = -K\nu^n, \quad (1.2)$$

where K is a constant and n is known as the braking index which quantifies the ‘efficiency of spin-down braking’. For a pure magnetic dipole $n = 3$, whereas in reality other dissipation mechanisms may carry away some of the rotational kinetic energy hence the observed n ranges between 0.9 to 2.9 (see e.g., Espinoza et al., 2011b; Kaspi & Helfand, 2002).

Integrating Equation (1.2) in terms of pulse period we can derive the age of the pulsar. By assuming that the spin period at birth is much smaller than now (i.e. $P_0 \ll P$) and that the spin-down is entirely due to magnetic dipole radiation so $n = 3$, Lorimer & Kramer (2005) expressed the characteristic age of a pulsar as,

$$\tau_c \equiv \frac{P}{2\dot{P}} \simeq 15.8 \text{ Myr} \left(\frac{P}{\text{s}} \right) \left(\frac{\dot{P}}{10^{-15}} \right)^{-1}. \quad (1.3)$$

Although a useful indicator of pulsar age, τ_c should be considered with care. As already mention $n = 3$ is not always the case in reality, and when it comes to millisecond pulsars (MSPs) which have undergone a different evolutionary track, the pulsar is ‘spun-up’ through a process known as recycling (see Section 1.4.1) leading to a decrease in the spin period and thus often breaks the assumption of $P_0 \ll P$ (Tauris et al., 2012).

Again by assuming that the spin-down process is dominated by dipole braking, we can infer the strength of the pulsar surface magnetic field. Lorimer & Kramer (2005) showed that for a canonical neutron star the characteristic surface magnetic field can be expressed as,

$$B_{\text{surf}} = 3.2 \times 10^{19} \text{ G} \sqrt{P\dot{P}} \simeq 10^{12} \text{ G} \left(\frac{\dot{P}}{10^{-15}} \right)^{1/2} \left(\frac{P}{\text{s}} \right)^{1/2}. \quad (1.4)$$

This is a useful indication of the otherwise rarely measurable pulsar magnetic field. Again due to the assumptions included, B_{surf} should be considered only as an order of

magnitude estimate. Nonetheless, as can be seen in the expression of Equation (1.4) and as discussed in Section 1.1, pulsars have extremely high B -fields. In fact, outside the pulsar the magnetic field completely dominates all physical processes, even by far outweighing the effect of gravitation. This rotating B -field induces an external electric field E outside the pulsar (Goldreich & Julian, 1969; Deutsch, 1955). The E -field subsequently results in the extraction of plasma from the neutron star surface, and the plasma fills the surrounding dominated by the magnetic field which forms what known as the pulsar magnetosphere. This plasma experiences the same $E \times B$ force as the neutron star interior, hence it is forced to co-rotate rigidly with the pulsar. The co-rotating field lines can only be maintained out to a certain distance, r_{lc} , where the plasma reaches the speed of light, which marks an imaginary surface known as the light cylinder (Fig. 1.1), where $\Omega = c/r_{lc}$. The light cylinder divides the dipolar magnetic field lines into two types: the ‘closed field lines’ in which particles move along the lines and are confined within the light cylinder; and the ‘open field lines’ which are the only places where particles can flow out from the magnetosphere.

The open field lines are thus closely related to pulsar emission regions. Two likely emission regions have been identified in the literature, namely the polar cap region and the outer gap region. The polar gap region is where charged particles are pulled from the neutron star surface and are accelerated to relativistic energies. Here gamma-ray photons are produced by curvature emission (see e.g., Ruderman & Sutherland, 1975) or inverse Compton scattering (see e.g., Daugherty & Harding, 1986). It has been suggested that these gamma-ray photons can split and result in electron-positron pair creation (Erber, 1966). This new generation of particles may lead to secondary (or tertiary) pair cascade (Sturrock, 1971) and has been speculated to be the source of the beamed radio emission observed. The outer gap region is located near the last open field lines close to the light cylinder, and may be the explanation for high energy curvature and synchrotron emission of the pulsar as a result of pair production (Cheng et al., 1986; Romani, 1996).

1.3 Propagation effects

The pulsar emission has to travel through the interstellar medium (ISM) before reaching us. The turbulent and inhomogeneous nature of the ISM lead to several propagation effects. In addition to scintillation which is analogue to the ‘twinkling’ star appearance in the optical wavelength, dispersion and scattering are two phenomenon relevant to pulsar emission propagation, and are discussed in this section.

1.3.1 Pulse dispersion

If space was a vacuum the broadband emission of pulsar would all arrive simultaneously at the observer. Instead, the ISM is a cold, ionised plasma. Just like any electromagnetic waves, the group velocity (v_g) of a pulsar signal propagating through the ISM

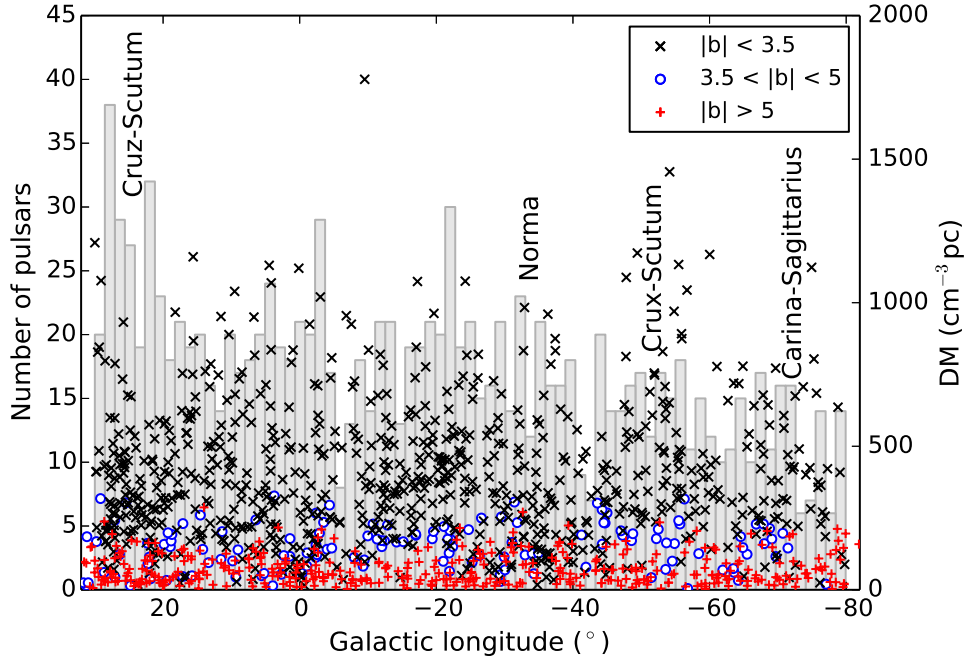


Figure 1.2: DM of all published pulsars in the general direction towards the Galactic centre, with Galactic longitude between $30^\circ \leq l \leq -80^\circ$. The known spiral arm structures coincide with the line of sights with the highest DMs.

can be expressed by

$$v_g = c \sqrt{1 - \left(\frac{f_{\text{plasma}}}{f_{\text{obs}}} \right)^2}, \quad (1.5)$$

where f_{plasma} is the plasma frequency. It is a function of the electron number density n_e along the line of sight and is typically taken to be $n_e \approx 0.03 \text{ cm}^{-3}$ (see .e.g., [Ables & Manchester, 1976](#)). The observing frequency is f_{obs} and from Equation (1.5), it can be seen that a higher frequency component would arrive earlier as compared to that of a lower frequency.

We can quantify the amount of time delay between two frequencies, f_1 and f_2 both in MHz, to be

$$\Delta t = D \times (f_1^{-2} - f_2^{-2}) \times \text{DM}, \quad (1.6)$$

where D is the dispersion constant and is approximately $4.15 \times 10^6 \text{ ms}$ ([Manchester & Taylor, 1972](#)). The dispersion measure, DM, sums the electron number density n_e along the line of sight l over a distance d , and is expressed as

$$\text{DM} = \int_0^d n_e dl \text{ cm}^{-3} \text{ pc}. \quad (1.7)$$

In theory dispersion affects every broadband emission and in particular the long wavelength electromagnetic spectrum. However, most astrophysical sources produce continuum emission hence dispersion becomes really only relevant for the time varying pulsar

emission. If dispersion is not well accounted for, the observed pulsed signal will be smeared over the bandwidth which reduces our detectability. Fig. 1.2 gives an idea of the DM distribution of pulsars towards the direction of the Galactic centre.

A useful implication of the dispersion delay is that, by observing Δt between two frequencies, we can calculate the corresponding DM by Equation (1.6). This, combined with some knowledge of the Galactic electron distribution (e.g., Cordes & Lazio, 2002), provides an estimate of the pulsar distance, d . The DM distribution of pulsars can also provide insight of the free electron distribution in our Galaxy. As shown in Fig. 1.2, the known spiral arm structures of our Galaxy coincide with the line of sights with the largest DM distribution.

1.3.2 Interstellar scattering

As the spatially coherent pulsar emission travels through the ISM, this turbulent plasma essentially acts as multiple scattering disks with different refractive indices, which bend and distort the pulsar signal. Photons passed through scattering disks of different radii will be phase shifted by the variable path lengths and will arrive at different times at the observer. The overall result is an undesirable broadening of the observed pulse profile. This scattered pulse profile has a characteristic one-sided ‘exponential tail’ (see Fig. 4.4 for an example), with the photons with the longest time delays accounting for the most extended part of the exponential tail.

This scattered pulse profile is often modelled as a convolution between the true undistorted pulse shape with a one-sided exponential with $1/e$ time constant, which is more commonly quantified as the scattering time scale τ_s . In other words, the pulse emission which left the pulsar at the same time now arrives at the observer over a time interval of τ_s . By empirically measuring τ_s of a number of pulsars, Bhat et al. (2004) showed that τ_s is strongly correlated with DM, therefore a high DM pulsar tends to be more affected by scattering and vice versa.

As predicted by the thin-screen model (Scheuer, 1968), the effect of interstellar scattering decreases with higher observing frequencies ν , such that $\tau_s \propto 1/\Delta\nu \propto \nu^{-4}$. Hence, although the random nature of scattering means that it cannot be corrected for like the case of dispersion, its effect can be minimised by going to higher observing frequency, as is illustrated by the example of Galactic centre search given in Section 2.2.2.

1.4 Pulsar diversity

As mentioned earlier, radio pulsars are rotation-powered objects and hence their respective spin periods and period derivatives (\dot{P}) are fundamental to their identities. A classical way to distinguish different pulsars is to populate them on a period-period derivative diagram (P - \dot{P} diagram) as in Fig. 1.3. The bulk of the known pulsar population falls into two distinct groups on a P - \dot{P} diagram. The group of pulsars at the bottom left corner of a P - \dot{P} diagram has rapid spin periods measured in milliseconds, together with small \dot{P} and low magnetic field strengths of 10^{8-9} G. Members of this population are often referred to as the millisecond pulsars or MSPs. Lee et al. (2012)

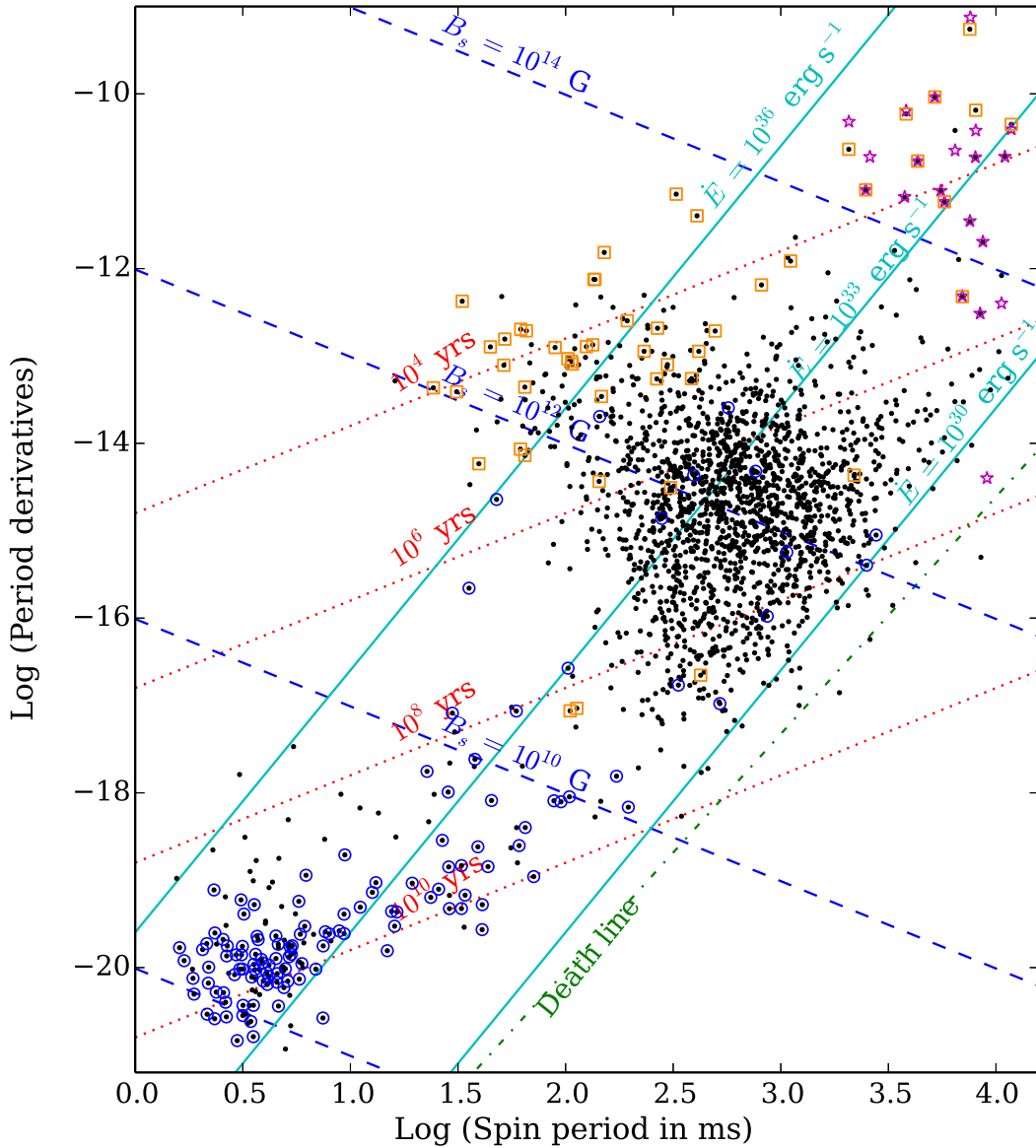


Figure 1.3: $P-\dot{P}$ diagram of known pulsars. Known pulsars as listed in the *ATNF Pulsar Catalogue*¹ (PSRCAT; Manchester et al., 2005) are plotted as black dots. In addition, pulsars in binary systems are plotted with blue circles, magnetars as listed in the *McGill Online Magnetar Catalog*² are plotted with magenta stars, and pulsars with known SNR associations are plotted with orange squares. Lines of constant surface magnetic field (B_{surf}), characteristic age (τ_c), and spin-down luminosity (\dot{E}) are drawn, as introduced in Section 1.2. The pulsar death line as presented in Chen & Ruderman (1993) is also shown.

¹ <http://www.atnf.csiro.au/people/pulsar/psrcat/>

² <http://www.physics.mcgill.ca/~pulsar/magnetar/main.html>

derived an empirical definition to classify MSP. For simplicity, we adopt a definition of $P \leq 30$ ms and $\dot{P} < 10^{-17}$ for MSP throughout this thesis. The second group of pulsars, also known as the normal or slow pulsars, typically have longer spin periods between 0.1 and a few seconds, higher \dot{P} of $\sim 10^{-15}$, and higher derived magnetic field strengths of 10^{11-13} G.

The P - \dot{P} diagram is an analogue to the Hertzsprung-Russell diagram which shows the stages of stellar evolution for ordinary stars. A possible starting point of the ‘evolutionary track’ for a normal pulsar would be birth with short spin period at the upper left-hand region of the P - \dot{P} diagram. As can be seen in Fig. 1.3, a large number of pulsars from this region have supernova remnant (SNR) associations, a direct evidence for their relatively young ages (see e.g., Camilo et al., 2002a,b, 2009). Pulsars then rapidly spin down into the ‘main pulsar island’ on a timescale of 10^{5-6} yr, their surface magnetic fields possibly getting weaker at the same time. After about 10^7 yr, pulsars reach what known as the ‘pulsar death line’ (see e.g., Chen & Ruderman, 1993). At this point, the electrostatic potentials across the pulsar polar cap regions become too weak to maintain the radio emission and pulsars cease to be detectable.

Note that for the rest of this thesis we have set aside the eight bright pulsars in the large and small Magellanic clouds (Crawford et al., 2001), as well as about 80 pulsars found within globular clusters (GCs, see a review from e.g., Freire, 2013). Pulsars found in GCs have more complicated evolutionary histories, due to the significant probability of multiple exchange interactions with other cluster stars. In this thesis we focus our discussion only on pulsars in the Galactic field.

1.4.1 Binary systems

The bimodal pulsar population of normal pulsars and MSPs can mainly be explained by the typical binarity found in MSPs. As can be appreciated from Fig. 1.3, more than 70 per cent of MSPs are in binary systems whereas less than 2 per cent are of the normal pulsars are found in binaries. In a binary system the evolution scenario begins with two main-sequence stars (see e.g., Bhattacharya & van den Heuvel, 1991) as illustrated in Fig. 1.4. The initially more massive star evolves first, undergoes a supernova explosion and gradually spins down afterwards, as it radiates its rotational energy similar to the case of a normal pulsar as mentioned earlier. At a later stage the secondary star comes to the end of its life and turns into a red giant. If the system is not disrupted and if the gravitational field of the first-formed pulsar is strong enough, it will attract matter from the red giant companion, gaining mass and angular momentum during the process (e.g., Alpar et al., 1982; Tauris & van den Heuvel, 2006). An accreting disk is formed and the system is visible as an X-ray binary. The pulsar is thus spun up to very short spin periods during this phase of mass transfer, a process known as ‘recycling’. At the same time the strength of its magnetic field is reduced, resulting in the typically small observed period derivative (e.g., Bhattacharya, 2002). Convincing evidence for this evolution scenario has been recently discovered from the ‘missing link’ pulsar PSR J1824–2452, which swings between being an X-ray binary and a radio MSP (Papitto et al., 2013).

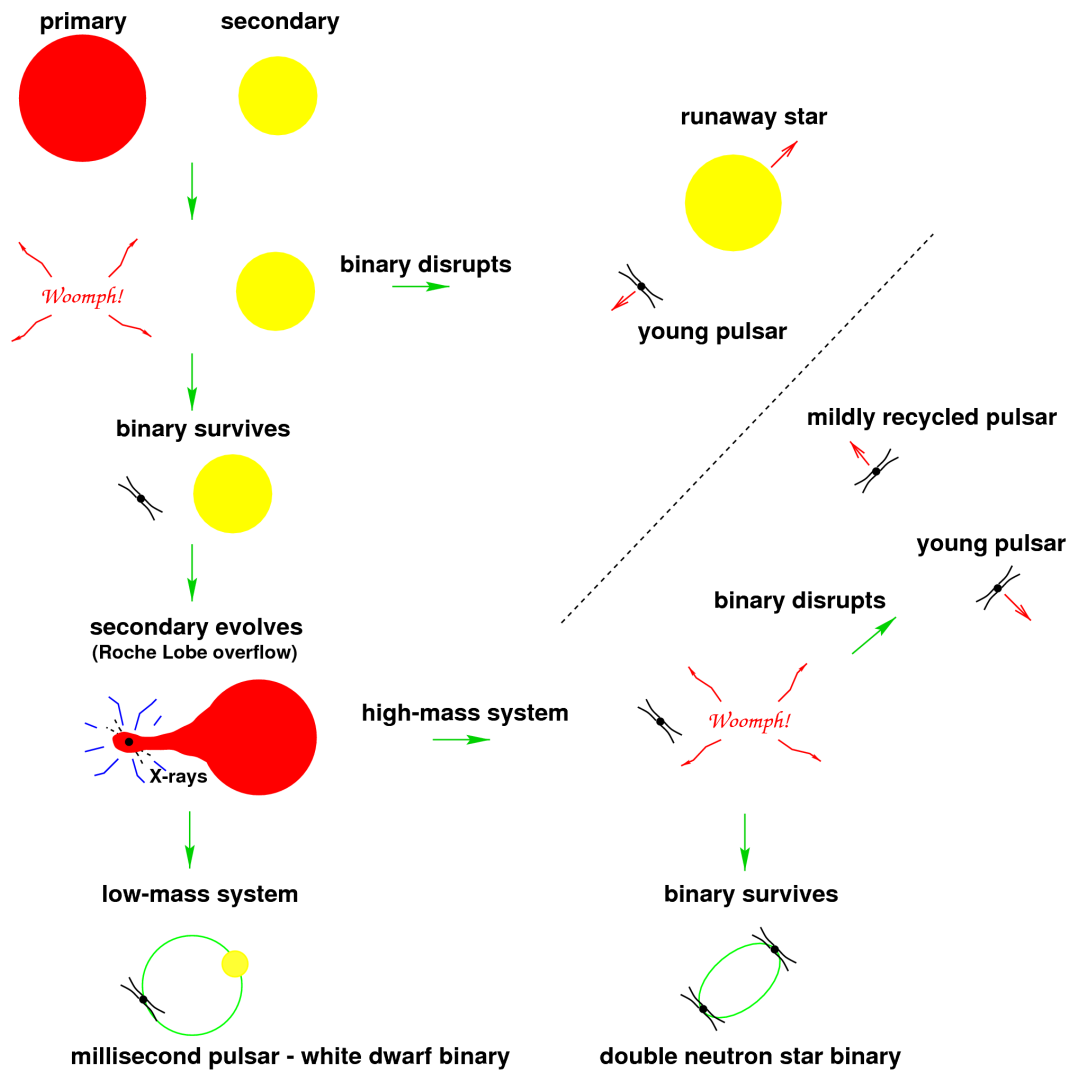


Figure 1.4: A cartoon taken from Lorimer (2008) illustrating the two different binary evolutionary tracks, leading to the formation of MSP-WD binaries (left) and DNS systems (right) respectively.

The final nature of the binary companion depends strongly on the initial mass of the secondary star. There are two major outcomes, namely double neutron star (DNS) binaries and MSP-white dwarf binaries. A DNS can form if the secondary star is sufficiently massive and undergoes a supernova explosion itself to form a younger, second neutron star. Until now, PSR J0737–3039 is the only double pulsar system known (Burgay et al., 2003; Lyne et al., 2004), for which the pulsed emission from both neutron stars are observed. In case the secondary star is not massive enough to undergo core collapse, the mass transfer phase can last much longer exceeding 10^9 yr (Tauris & Savonije, 1999), which explains the typically shorter spin periods and smaller eccentricities observed in these binaries. The companion star eventually shed its outer layer and results in a white dwarf. The companions of low-mass binary systems are predominantly Helium white dwarfs (He-WD) with companion mass $m_c \lesssim 0.5 M_\odot$. These systems have the fastest spin periods of the order of milliseconds and their orbits are essentially circular with eccentricities $10^{-7} \lesssim e \lesssim 0.01$. The companions of intermediate-mass binary systems are massive white dwarfs composed of carbon-oxygen (CO-WD) or of oxygen-neon-magnesium (ONeMg-WD) (see e.g., Lazarus et al., 2014). These systems tend to have slower spin periods of a few tens of milliseconds and slightly more eccentric orbits. Finally, six further pulsars are found in binaries with unevolved (main-sequence) companion stars.

1.4.2 Magnetars

The ‘magnetars’ are a small group of X-ray pulsars occupying the top right corner of a $P-\dot{P}$ diagram. They have long spin periods between 2 to 12 s and high spin-down rates implying a short lifetime. The most defining characteristic of magnetars is their extremely high effective dipole magnetic field. Assuming magnetic dipole radiators as described in Section 1.2 and using Equation (1.4), their inferred surface magnetic fields appear to be of the order of 10^{14-15} G, literally the strongest magnetic fields in the known Universe. Magnetars have strong X-ray emission of the order of 10^{35} erg s $^{-1}$, which is too high and too variable to be explained by the rate of loss of rotational energy as in the case for normal pulsars, while at the same time no evidence for companion has been found for any magnetar as in the case of accretion-powered X-ray binaries.

Magnetars were thought to be radio quiet objects for a few decades, and their high energy emission were attributed to the decay and instability of their strong magnetic fields stored in the interior of the neutron stars (Duncan & Thompson, 1992). In 2004 a transient magnetar was found to coincide with the discovery of radio pulsed emission from it (Camilo et al., 2006). Levin et al. (2010) reported the first magnetar discovered blindly from its radio emission (see also Section 3.2.2). The magnetar discovered near the Galactic centre is another recent example of multiwavelength emission associated with a magnetar outburst (Eatough et al., 2013c). These radio pulsed emission from magnetars appeared to be slightly different from that of a normal pulsar, with flatter radio spectra, higher variability, and connected to X-ray outbursts of the magnetar. Some high magnetic field radio pulsars turned out to be magnetars also seen in X-ray (Gavriil et al., 2008; Kumar & Safi-Harb, 2008), and other examples of ‘apparently

normal' radio pulsars with less high magnetar field have also been observed as X-ray magnetars (Rea et al., 2010). It does seem that although magnetars and radio pulsars are powered by different mechanisms, some similarities are shared among the two groups.

1.5 Pulsar timing

Most observational research work on pulsars involve a technique known as 'pulsar timing', a direct consequence of the rotational stability of pulsars. Pulsars have high rotational kinetic energy and relatively low spin-down energy loss rate. They can be considered as natural clocks emitting highly polarised, coherent signals with a stability that rivals atomic clocks. This makes them reliable and precise timing tools for a variety of astrophysical applications (see Section 1.6). MSPs have the highest rotational stability of all pulsars, which combined with their short spin periods, explain their particular importance in pulsar timing.

The key quantity of pulsar timing is the time stamps of pulses as they are observed at the telescope, also known as time of arrivals (TOAs). TOAs can be determined accurately by cross-correlating the pulse profiles with a noise-free analytical template, created by representing the pulse profile as a sum of Gaussian components (Foster et al., 1991; Kramer et al., 1994). As the pulses have a certain width, a TOA typically refers to some fiducial point on the profile (e.g. the peak of the main pulse). A useful property of pulsar emission is that the mean profile of a pulsar has a stable form at any particular observing frequency. That implies that the integrated pulse profile can be used to increase the signal-to-noise (S/N), hence reducing the uncertainties of the TOAs. Typically, at least a few hundred pulses are added to achieve a stable high S/N profile. For MSPs, tens of thousands of pulses can be easily collected in just a few minutes of observing time, co-added to form extremely stable profiles. Note that the TOAs have to be transformed to the rest frame at the Solar system's barycentre (SSB) typically using a planetary ephemeris such as the JPL DE421 (Folkner et al., 2009), and effects such as that due to the classical light-travel time between the telescope and the SSB (Römer delay), the time dilation due to the motion of the Earth combined with the gravitational redshift as a result of other bodies in the Solar system (Einstein delay) and the extra delays along the line of sight as the radio signals passing close by the curved space-time induced by the presence of the Sun (Shapiro delay) have to be taken into account.

A 'pulsar timing model' is developed to predict the rotational behaviour of the pulsar. The aim is to achieve a phase-coherent timing solution which is capable of accounting for every rotation of the pulsar within the desired epoch. The timing residual is defined by the difference between the predicted and the observed TOA. A least-squares fit analysis is typically carried out to minimise the timing residuals. When a phase-coherent timing solution is achieved, the post-fit residuals should show a Gaussian distribution around zero with a root mean square (RMS) that is comparable to the TOA uncertainties. If the timing model is incorrect or incomplete, systematic

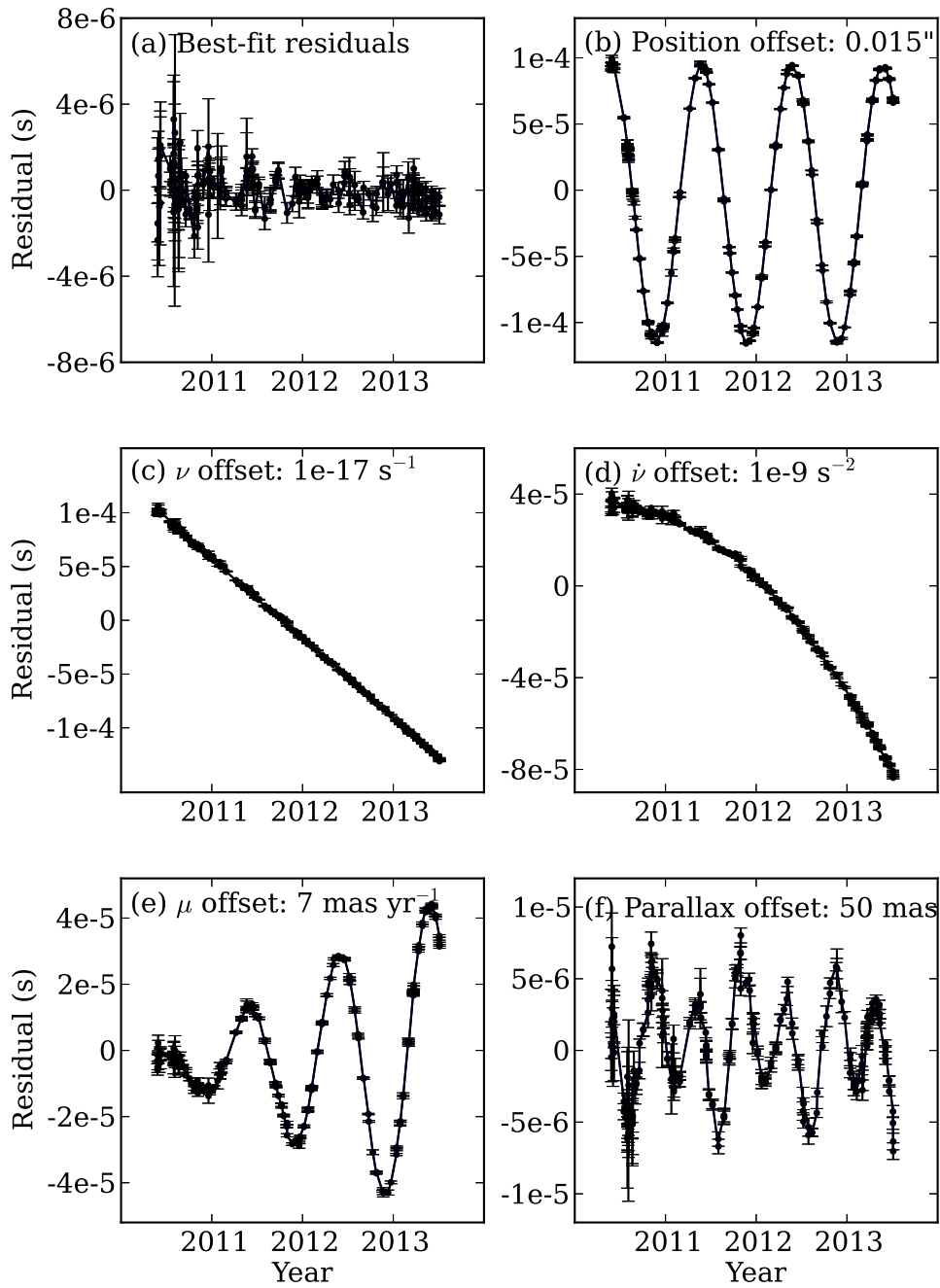


Figure 1.5: Timing residuals of MSP J1017–7156. In panel (a) a correct timing model is applied and the timing residuals are white with a small RMS. In panel (b) the pulsar position is offset and resulted in a yearly sinusoid in the timing residuals with a significantly larger RMS. In panel (c) the spin frequency is offset and resulted in a linear trend in the timing residuals. In panel (d) the frequency derivative is offset and resulted in a quadratic deviation in the residuals. In panel (e) the proper motion is offset and resulted in a yearly sinusoid in the residuals with a linearly increasing magnitude. In panel (f) the parallax is offset and resulted in a six-month sinusoid in the timing residuals.

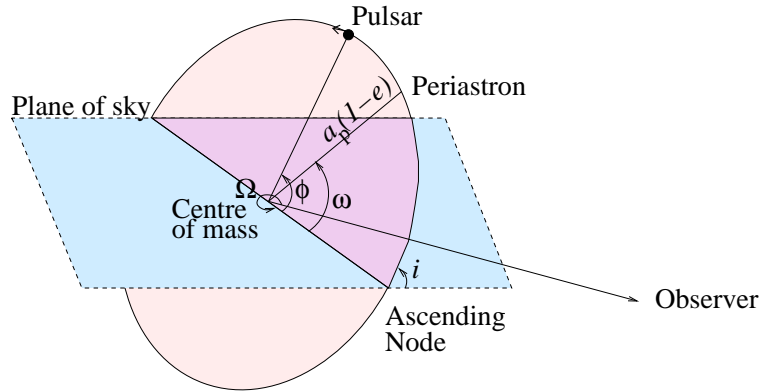


Figure 1.6: Definition of the Keplerian orbital parameters for a binary pulsar. The intersection between the orbital plane and the plane of the sky is known as the ascending node. The angle Ω gives the longitude of ascending node in the plane of the sky. The orbital phase of the pulsar, ϕ , is measured relative to the ascending node. The closest approach to the centre of mass of the binary system marks the periastron. The angle between the periastron and the ascending node is given by the longitude ω and a chosen epoch T_0 of its passage. The distance between the centre of mass and the periastron is given by $a_p(1 - e)$ where a_p is the semi-major axis of the pulsar orbit and e its eccentricity. Usually only the projection on the plane of the sky $a_p \sin i$, is measurable, where i is the orbital inclination defined as the angle between the orbital plane and the plane of the sky.

structures can be identified in the timing residuals as illustrated in Fig. 1.5.

Standard parameters included in the fitting of a pulsar timing model can be categorised into three groups: (1) astrometric parameters (i.e. position, proper motion, parallax); (2) spin parameters (i.e. rotation frequency, ν , and higher derivatives); (3) binary parameters, if any. The precision of the fitted parameters generally improves as a function of the length of the data span and the cadence of the timing observations, as well as with orbital coverage in the case of binary pulsars. The following is an overview of the main parameters typically considered in a pulsar timing model and the effects of their measured uncertainties.

Position: If the position of the pulsar is inaccurate a sinusoid with a one-year periodicity with constant amplitude is observed in the timing residuals (see Fig. 1.5b).

Period: If the spin period of the pulsar is modelled inaccurately, the predicted TOAs will deviate progressively more with time from the observed TOAs (see Fig. 1.5c). The timing residuals can be improved by the least-squares fitting of a straight line.

Period derivative: An inaccurate modelling of the period derivative, \dot{P} , results in a quadratic deviation in the timing residuals (see Fig. 1.5d). Typically, at least one year of timing data is required to break the degeneracy between \dot{P} and the apparent change in spin period as a result of inaccuracy in the pulsar position.

Dispersion measure: Any error in dispersion measure can be determined if multiple frequency observations are available. In such a case, different frequency data will

appear offsetting to each other, which can be rectified by a constant offset between arrival times for different frequencies.

Proper motion: If the pulsar is moving relative to the SSB with a total proper motion, μ , the transverse component of the velocity, V_T , leads to a sinusoid with a one-year periodicity in the timing residuals with a linearly-increasing magnitude (see Fig. 1.5e), which is more pronounced for a pulsar with large distance away from the observer (see Equation (5.2)).

Parallax: Parallax measurements can be used to determine distances of pulsars. Radio timing parallax is however only measurable for nearby pulsars, whereas for pulsars with larger distances parallax measurements can only be achieved via VLBI observations. Currently less than 3 per cent of all known pulsars have a published parallax with the majority of them located within ~ 2 kpc¹. An incorrect parallax measurement results in a sinusoid in the timing residuals with a six-month periodicity (see Fig. 1.5f).

Keplerian binary parameters: If the pulsar is in a binary system, the orbital motion of the pulsar around the common centre of mass of the binary system can be described using Kepler’s laws. Five ‘Keplerian parameters’ are required to refer the TOAs to the binary barycentre in the pulsar timing model: (1) orbital period, P_{orb} ; (2) projected semi-major orbital axis, $a_p \sin i$; (3) orbital eccentricity, e ; (4) longitude of periastron, ω ; and (5) the epoch of periastron passage, T_0 . These parameters are illustrated in Fig. 1.6.

Post-Keplerian binary parameters: For pulsars in tight binary systems with companions of white dwarfs, other neutron stars or potentially black holes, relativistic effects due to the strong gravitational field mean a purely Keplerian description of the orbit is not sufficient, and relativistic corrections are necessary. Five of such post-Keplerian (PK) parameters can be determined from pulsar timing (Backer & Hellings, 1986): (1) the angular movement of the semi-major axis of an elliptical orbit due to GR or tidal interaction leading to the advancement of periastron, $\dot{\omega}$; (2) the diminishing of the orbital energy through quadrupolar gravitational radiation, leading to an in-spiral of the stars and thus a decrease of orbital period, \dot{P}_{orb} ; (3) the gravitational redshift plus the transverse Doppler shifts in the orbit, γ ; (4) the ‘range’ of Shapiro time delay, r , due to the curvature of space-time in the presence of the companion; and (5) the ‘shape’ of the Shapiro delay, s .

1.6 Pulsars as physical tools

It has been 47 years since the discovery of the first radio pulsar. Today there are over 2000 pulsars known, and pulsar research still continues with great motivation within the community. Apart from the fact that open questions remain to be solved, most importantly pulsars offer a breadth of scientific applications in fundamental physics and astrophysics. The following is a selection of examples illustrating pulsars as physical tools, with references to relevant work in this thesis.

¹For a list of all pulsar parallaxes and the associated measurement technique employed see astro.cornell.edu/research/parallax/

- **Individual interesting systems:** Unique pulsar systems are constantly being discovered, challenging our theories of MSP formation and binary evolution. Notable examples include triple systems (Ransom et al., 2014), a highly-eccentric system (Champion et al., 2008) and the MSP J1719–1438 discovered by Bailes et al. (2011) with an ultra-low mass companion (see also Section 3.2.1). One of the holy grails in pulsar astronomy is the potential discovery of highly relativistic system such as pulsar-black hole binaries (Belczynski et al., 2002), which is of great interest as their strong gravitational fields would provide the best studies for black hole physics as well as tests for general relativity (GR; Kramer et al., 2004).
- **Probes of stellar astrophysics:** The observed orbital and stellar properties of binary pulsars are fossil records of their evolutionary tracks. Thus binary pulsars are key probes of stellar astrophysics and the many interactions at work. See various discussion in Chapter 5 for examples.
- **Galactic pulsar population:** A blind pulsar survey is the only way to significantly increase the known population of pulsars in an unbiased way. Our current picture of the Galactic pulsar distribution suffers from observational bias, with an apparent clustering of known pulsars near the Sun. Contemporary pulsar surveys with state-of-the-art technologies provide high frequency and time resolution, giving unprecedented sensitivity to distant pulsars and allowing us to probe the lowest luminosity end of the pulsar population (see Section 2.2.2). Surveys of this type allow us to remain sensitive to all varieties of pulsars, exploring the true boundaries of pulsar phase space. As part of this thesis a study of the Galactic plane pulsar properties has been carried out (Section 4.4), as well as an investigation of the Galactic height distribution of binary pulsars (Section 5.3.5). An accurate model of the Galactic pulsar parameters has many applications. For instance it helps to predict the merger rate of binary neutron stars, essential for a better understanding of the observable events of any gravitational wave detector (see e.g., Abbott et al., 2008). A study of the Galactic pulsar population also provides valuable knowledge for the planning of survey strategies with future telescopes such as MeerKAT and SKA.
- **Multi-wavelength counterparts:** Theoretical expectations and results from gamma-ray telescopes (e.g., Thompson, 2008; Abdo et al., 2013) indicate that pulsars with large spin-down power ($\dot{E} > 1 \times 10^{34} \text{ erg s}^{-1}$) are the most likely gamma-ray pulsar candidates. Successful identification of multiwavelength counterparts provides key insights to the relative geometry of the different emission regions, and allow us to study the population of gamma-ray emitting pulsars as a whole. Phase-folding the gamma-ray photons with a radio ephemeris is a very effective way to recover gamma-ray pulsations from high-energy data, for example from the Large Area Telescope (LAT) on the *Fermi Gamma-Ray Space Telescope* (e.g., Abdo et al., 2009; Espinoza et al., 2013). A similar discovery of two gamma-ray pulsars has also been made as part of this thesis (see Section 5.3.10).
- **Probing our Galaxy and the ISM:** Pulsars have a large velocity as inherited from their violent birth during the supernova explosion. Hence they can move away from their birth place within the Galactic plane. Pulsars are thus widely distributed

in the Galaxy and their emission travels to us from many directions. As the broadband emission of pulsars propagates through the ISM and get dispersed because of free-free absorption by thermal electrons, it acts as a probe of the Galactic free electron distribution, and can reflect changes even on short time-scale (see an example described in Section 5.3.1). In addition, pulsars can be considered as effective point sources to probe the scattering medium. The highly polarised emission of pulsars can be studied on a broad scale to map the large-scale structure of the Galactic magnetic field and to reveal any field line reversal (see e.g., [Noutsos et al., 2008](#)).

- **Plasma physics under extreme conditions:** Despite the good reputation of pulsars being stable clock-like rotators, as mentioned earlier, there exist timing irregularities most readily observed from long-period normal pulsars that are not well-understood. These small perturbations are quasi-random variations in the rotational behaviour of the pulsar and may be manifested as mode-changing, nulling, intermittency and pulse shape variability. A recent study has linked these observables to changes in the pulsar’s magnetosphere ([Lyne et al., 2010](#)), thus making the study of timing noise a powerful tool to probe the pulsar magnetosphere and to study plasma physics under extreme condition.
- **Matter at supra-density:** Binary pulsars can provide a unique laboratory for exploring the properties of cold matter at supra-nuclear density. Notable examples are the binary MSPs J1614–2230 and J0348+0432 which have the highest implied pulsar masses of 1.97 ± 0.04 and $2.01 \pm 0.04 M_{\odot}$ respectively ([Demorest et al., 2010](#); [Antoniadis et al., 2013](#)), effectively ruling out some of the neutron star equations-of-state. Coincidentally, one MSP discovered from the HTRU Galactic plane survey as part of this thesis, PSR J1101–6425, has binary parameters very similar to PSR J1614–2230 (see Section 4.3.1). Both of these two systems have heavy white dwarf companions but fast spin periods of a few ms that indicate contradictory full-recycling (see, e.g. [Tauris et al., 2011](#)). A potential detection of Shapiro delay in PSR J1101–6425 implies good prospects for measuring a pulsar with an extreme mass, and continued monitoring of such binary systems is thus of great interest. In addition, irregularities in pulsar behaviours can be considered as a tool for ‘neutron star seismology’. One example is the discrete changes of the pulsar rotation rate, also known as ‘Glitches’. They are thought to originate from the interior of a neutron star hence carrying the properties of matter at supra-nuclear density ([Baym et al., 1969](#)). Frequent glitches of the Vela pulsar has been used as an evidence for the superfluid nature of neutron star core (see e.g., [Anderson & Itoh, 1975](#); [Lyne, 1992](#)).
- **Gravitational physics in the strong-field regime:** The strong gravitational field in the vicinities of pulsars is an extreme condition not encountered on Earth. Pulsars can hence be used uniquely to conduct precise tests of GR and alternative theories in the strong field regime. DNS systems are particularly useful because they can be considered essentially as two point sources compared to the orbital separation, with no mass transfer nor tidal effect in a ‘clean’ orbit. PSR B1913+16 provided the first evidence of gravitational radiation predicted by GR, showing orbital shrinkage of 1 cm day^{-1} ([Taylor & Weisberg, 1989](#)). The double pulsar ([Burgay et al., 2003](#); [Lyne et al., 2004](#)) has been used to obtain five independent tests for GR predictions

and has shown that GR passes these yet most stringent tests with a measurement uncertainty of only 0.05 per cent (Kramer et al., 2006). Apart from DNS systems, the extreme difference in gravitational binding energy within a neutron star-white dwarf (NS-WD) pair is suitable for tests of the strong equivalence principle (SEP) (Damour & Schäfer, 1991; Stairs et al., 2005; Freire et al., 2012). A discussion on such an SEP test is presented as part of this thesis in Section 5.3.6. Finally, MSPs distributed across the sky can be employed through the concept of Pulsar Timing Arrays (PTAs) for the detection of low-frequency gravitational waves (Yardley et al., 2011; van Haasteren et al., 2011), a technique complementary to ground-based laser interferometers such as LIGO and space-based interferometers. The discovery of more MSPs and continued high-precision timing campaigns are fundamental to enable PTAs for GW detection (Jenet et al., 2005).

1.7 Thesis outline

This thesis demonstrates current efforts to discover new pulsars with the Parkes 64-m radio telescope, as well as an attempt to fulfil the motivations for pulsar studies through the application of pulsar timing as listed above.

In **Chapter 2** we discuss the standard algorithm for pulsar searching. We review the success of pulsar surveys conducted previously, and we compare the merits of various large-scale pulsar surveys.

In **Chapter 3** we introduce the High Time Resolution Universe (HTRU) Pulsar survey conducted with the Parkes telescope. Particularly emphasis is paid on the HTRU low-latitude Galactic plane pulsar survey, which forms the basis of the work related to this thesis. We present in detail the implementation of an innovative segmented acceleration search technique for the data processing of this survey, as well as improvements made in the RFI mitigation techniques.

In **Chapter 4** we report on the discovery of 47 pulsars from the HTRU low-latitude Galactic plane pulsar survey, which include a fully-recycled MSP J1101–6424 with an unusually heavy companion, a 17-ms fast-spinning isolated pulsar PSR J1757–27, an intermittent pulsar PSR J1759–24 and a pulsar with an extremely wide pulse PSR J1847–0427. As a whole, these newly discovered pulsars are compared to the published pulsar population and we discuss the implications arising for future pulsar surveys along the Galactic plane.

In **Chapter 5** we present the timing solutions of four newly-discovered MSPs from the HTRU medium-latitude pulsar survey, as well as the long-term timing of a further 12 MSPs. Notable highlights include the discovery of associated gamma-ray pulsations from two of the MSPs, and PSR J1801–3210 which shows no significant period derivative after four years of timing data.

In **Chapter 6** we conclude this thesis and propose future research plans.

Pulsar Searching

The discovery of pulsars is a gateway to new science. Pulsars are weak radio sources with observed flux densities between $5\mu\text{Jy}$ to just above 1Jy at 1.4GHz (Manchester et al., 2005). Fortunately, their periodicities provide an effective way to search for them. By coherently adding many hundreds or even thousands of pulses, a strong and detectable pulsar signal can be recovered. This chapter describes the instrumentation and algorithms typically employed for pulsar searching, as well as a discussion on notable pulsar searching efforts undertaken thus far with various telescopes.

Contents

2.1 Instrumentation and algorithms	23
2.1.1 Data acquisition	23
2.1.2 The standard periodicity search	25
2.1.3 Binary pulsar searches	32
2.1.4 Candidate selection and optimisation	36
2.2 An overview of pulsar surveys	37
2.2.1 Previous generations	37
2.2.2 Contemporary pulsar surveys	39
2.2.3 Next generations of pulsar surveys	42

2.1 Instrumentation and algorithms

2.1.1 Data acquisition

Because pulsars are so intrinsically weak, telescopes with large collecting areas and high instantaneous sensitivities are desirable for pulsar observations. Currently, several large single-dish telescopes around the world are capable of conducting pulsar observations. Notable examples are the 64-m Parkes radio telescope in Australia, the 100-m Effelsberg radio telescope in Germany, as well as the 100-m Robert C. Byrd Green Bank telescope (GBT) and the 300-m Arecibo radio telescope in the US. All these telescopes possess a paraboloid reflecting surface (the dish) that converts the incoming plane wave front into a spherical one, which can then be collected by a receiver system placed at the focal plane of the dish.

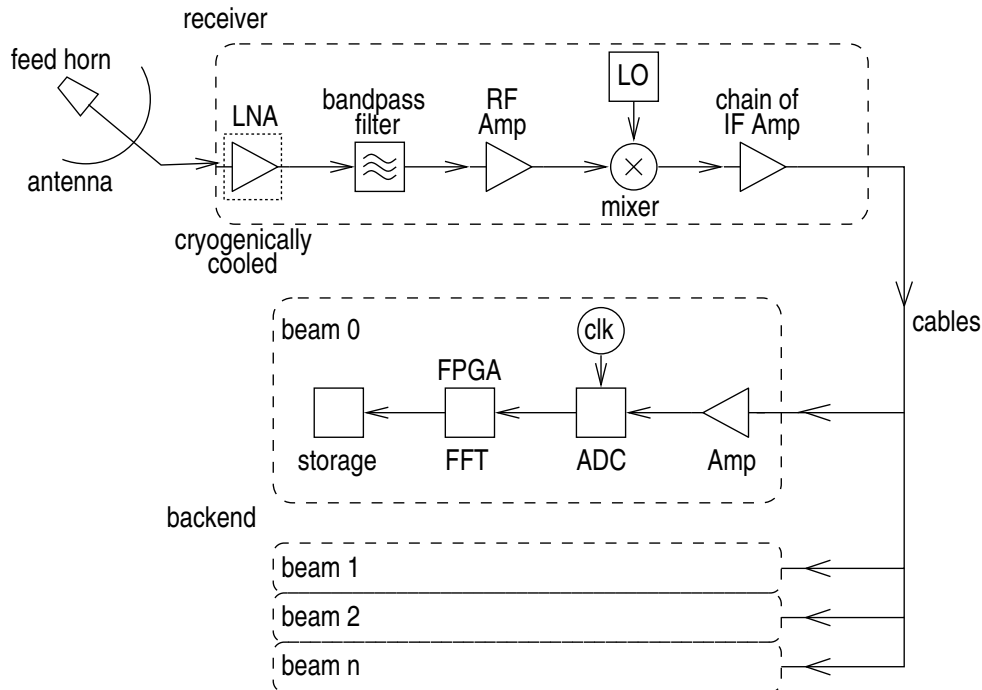


Figure 2.1: A simplified block diagram showing the basic components in a receiver system and a pulsar ‘searching backend’.

Fig. 2.1 shows the basic components involved in a typical receiver. A receiver system receives the signal at the incoming radio frequency (RF). Firstly, a feed horn placed in the focus of the telescope collects the radiation reflected from the primary or secondary mirror of the telescope into two orthogonal polarisations. Because the radio signals from astrophysical sources are extremely weak, they need to be amplified as early as possible in the system and by a significant amount in order to be detected. This is the reason why, unlike radio antennas for artificial signals (e.g. radio, TV and radar), an amplifier is the first component in a radio-astronomical receiver system, even before any filter is installed. However, the amplifier itself generates extra thermal noise. Hence a low-noise amplifier (LNA), cryogenically cooled to temperatures of the order of a few tens of Kelvin, is employed to minimise this extra noise. A bandpass filter then selects the desired frequency band of the RF. Next, a mixer fitted with a local oscillator (LO) down converts the RF to a lower intermediate frequency (IF), in order to reduce losses during signal transmission caused by attenuation which decreases with decreasing frequency. An additional advantage of the mixer is that, the amplified signals can be decoupled from the original ones to avoid feedback caused by such high amplifications. The IF is then further amplified by a chain of amplifiers, a set up necessary for achieving stable amplification, before being sent along cables to the dedicated backend.

The backend is where signals get digitised, processed and stored. In the specific case of a pulsar ‘searching backend’, the incoming IF undergoes an analogue-to-digital converter (ADC) which converts from raw voltages to n -bit numbers, while a hydro-

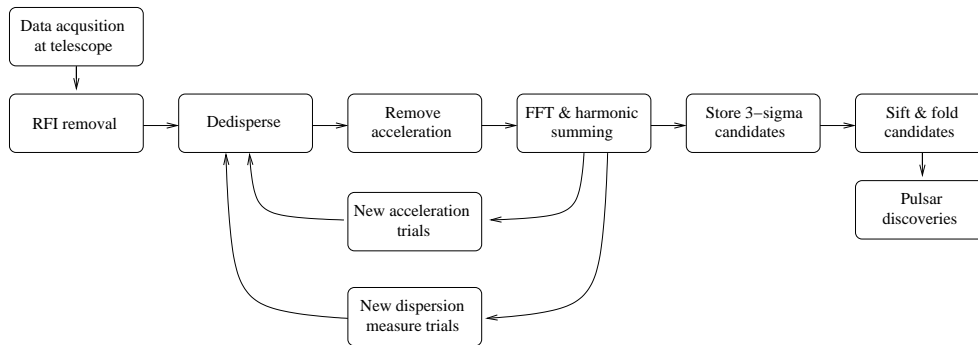


Figure 2.2: Schematic flowchart of a standard pipeline based on a periodicity search.

gen maser clock provides well-defined time stamps for the data. The dispersed and time varying nature of pulsar signals, as explained in Section 1.3.1, means that if the bandwidth of the IF is large, the pulses will be entirely smeared out over the bandpass. Hence we stream the now digitised data to Field Programmable Gate Array (FPGA) logic blocks, which performs polyphase filterbank *fast Fourier transforms* (FFT; Cooley & Tukey, 1965) on discrete data blocks to channelise the input IF into many individual narrow frequency channels. The spectra produced are detected and integrated to give sampling rates of several tens of microseconds. The resultant filterbank data format thus allows artificial time delays to be applied to the individual channels during a later data processing stage to de-disperse the signal (see Section 2.1.2.2). The final data to be stored typically have the two polarisations summed, as this information is not required for the purpose of pulsar searching.

2.1.2 The standard periodicity search

Fig. 2.2 shows a schematic flowchart of a generic pulsar searching pipeline based on a periodicity search. In this section we will outline the basic steps involved, with examples relevant to the HTRU low-latitude Galactic plane survey (see Section 3.3) given as applicable. Note that there are other pulsar search techniques in the literature, for instance, the ‘single pulse’ and the ‘fast folding’ algorithms. We do not discuss these alternative methods as they are not employed in this work.

2.1.2.1 RFI removal

Radio frequency interference (RFI) generated by terrestrial sources can hamper our ability to detect any astronomical pulsar signals. Strong RFI signals present in an observation can reduce the nominal sensitivity of our instruments by suppressing the dynamic range, and can also saturate the number of candidates produced from a search pipeline. Potential sources that are responsible for RFI are for instance lightning, as well as signals from nearby electrical devices of artificial nature, such as the AC frequency of the power lines, communication systems such as airport or military radar systems, mobile phones, and even computers and electronics at the observatory if not

properly shielded.

Therefore, the very first step in a pulsar searching pipeline, is to identify and excise these spurious RFI signals in the data. Two main approaches of RFI removal techniques exploit the fact that RFI is terrestrial hence usually non-dispersed (i.e., most prominent in the time series at $DM = 0 \text{ cm}^{-3} \text{ pc}$). By first creating a time series of the non-dispersed observation, time samples contaminated by impulsive RFI can be identified and replaced with noise. Secondly, spectral channels with excessive power due to the presence of narrow band interference can be removed.

Further improvements related to RFI mitigation techniques have been developed as part of this PhD thesis and are incorporated into the current HTRU low-latitude Galactic plane survey data processing pipeline. The details are presented in Section 3.3.1.

2.1.2.2 De-dispersion

The filter bank data format can be considered as a two-dimensional array of samples, $\mathcal{S}(f_l, t_j)$, at frequency f_l and time t_j . To correct for the dispersion delay as mentioned in Section 1.3.1, appropriate time delays can be added to each frequency channel so that the original pulse can be aligned properly (see an illustration of a dispersion correction in Fig. 2.3). Equation (1.6) can be re-written to

$$k(l) = \left(\frac{t_{\text{samp}}}{4.15 \times 10^3} \right)^{-1} \left(\frac{DM}{\text{cm}^{-3} \text{ pc}} \right) \left[\left(\frac{f_l}{\text{MHz}} \right)^{-2} - \left(\frac{f_1}{\text{MHz}} \right)^{-2} \right], \quad (2.1)$$

where $k(l)$ is the integer number of time samples to be shifted at any DM for frequency channel f_l with respect to the highest frequency channel f_1 and t_{samp} is the time sampling rate. The data can then be collapsed in frequency summing all the n_{chan} number of frequency channels, to create a *de-dispersed time series* (\mathcal{T}_j) at the specific DM,

$$\mathcal{T}_j = \sum_{l=1}^{n_{\text{chan}}} \mathcal{S}(f_l, t_{j+k(l)}). \quad (2.2)$$

As the DM of the pulsar to be discovered is an *a priori* unknown, a range of possible DMs has to be searched. Looking at the known pulsars distribution as plotted in Fig. 1.2, it can be seen that, for example, towards the direction of the ‘inner Galaxy’ with Galactic longitude $-80^\circ < l < 30^\circ$, pulsars along the Galactic plane (with Galactic latitude $|b| < -3.5^\circ$) has DMs over $1000 \text{ cm}^{-3} \text{ pc}$, whereas for higher latitudes the reasonable DM range to be searched can be smaller, with all currently known pulsars having $DM \leq 50 \text{ cm}^{-3} \text{ pc}$.

Another important consideration is the dispersion step size to search. Too fine a step size means computing power is wasted on searching DM trials that are essentially the same, whereas too coarse a step size means a pulsar with a true DM value that falls in between two DM trials might be significantly broadened and remains undetected. To quantify the loss of sensitivity versus the amount of offset in DM value, we can consider the effect of dispersion broadening for the case of a top-hat pulse with intrinsic pulse

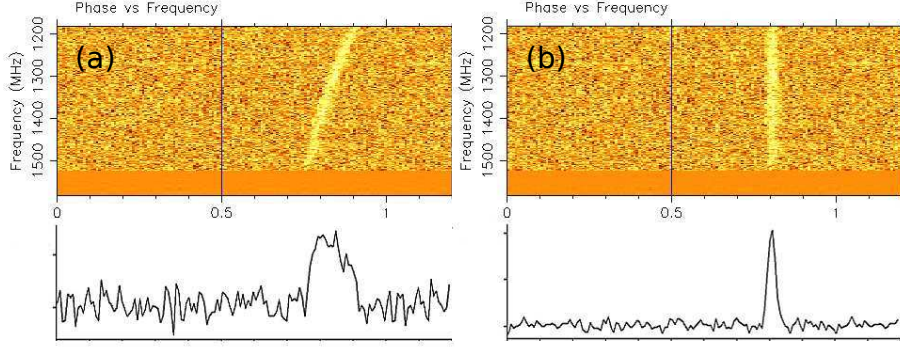


Figure 2.3: An HTRU survey observation which contains the known pulsar PSR B1841–04, with a DM of $123.16 \text{ cm}^{-3} \text{ pc}$. Panel (a) shows the frequency versus phase plot and the resulting pulse profile when this dispersion is not corrected for (i.e., at $\text{DM} = 0 \text{ cm}^{-3} \text{ pc}$). Panel (b) shows the same observation after the dispersion correction.

width, W_{int} . The effective pulse width, W_{eff} , is calculated by

$$W_{\text{eff}} = \sqrt{W_{\text{int}}^2 + \left(8.3 \times 10^6 \times \frac{\Delta\nu}{f_c^3} \times |\Delta\text{DM}|\right)^2 + t_{\text{samp}}^2}, \quad (2.3)$$

where $\Delta\nu$ is the frequency resolution in MHz, f_c is the central observing frequency in MHz, t_{samp} is the time sampling rate in ms and ΔDM is the amount of DM offset from the true value in the unit of $\text{cm}^{-3} \text{ pc}$. Note that this equation includes the assumption that $\Delta\nu \ll f_c$. The degradation in S/N as a result of pulse broadening can be estimated by

$$\text{S/N} \propto \sqrt{\frac{P - W_{\text{eff}}}{W_{\text{eff}}}}, \quad (2.4)$$

where P is the spin period of the pulsar. This relationship is illustrated in Fig. 2.4, where panel (a) compares between top-hat pulses with different spin periods and panel (b) compares between different duty cycles δ (in effect, different W_{int}). It is obvious that pulsars with spin periods less than a few hundred ms or with small duty cycles are most affected by an incorrect DM trial.

The ideal choice of DM step size which optimises pulsar detection, is letting the sampling time (t_{samp}) to define the maximum dispersion delay across the entire frequency bandwidth (Δf). As shown by Lorimer & Kramer (2005), the i th DM step can thus be expressed by

$$\text{DM}_i = 1.205 \times 10^{-7} \text{ cm}^{-3} \text{ pc} (i - 1) t_{\text{samp}} (f^3 / \Delta f). \quad (2.5)$$

Note that at $i = n_{\text{chan}} + 1$, we reach the so-called ‘diagonal DM’. It can be seen from Equation (2.5) that, the total dispersion delay to be applied across the whole bandwidth is now $n_{\text{chan}} \times t_{\text{samp}}$. And more importantly, the uncorrectable broadening across an

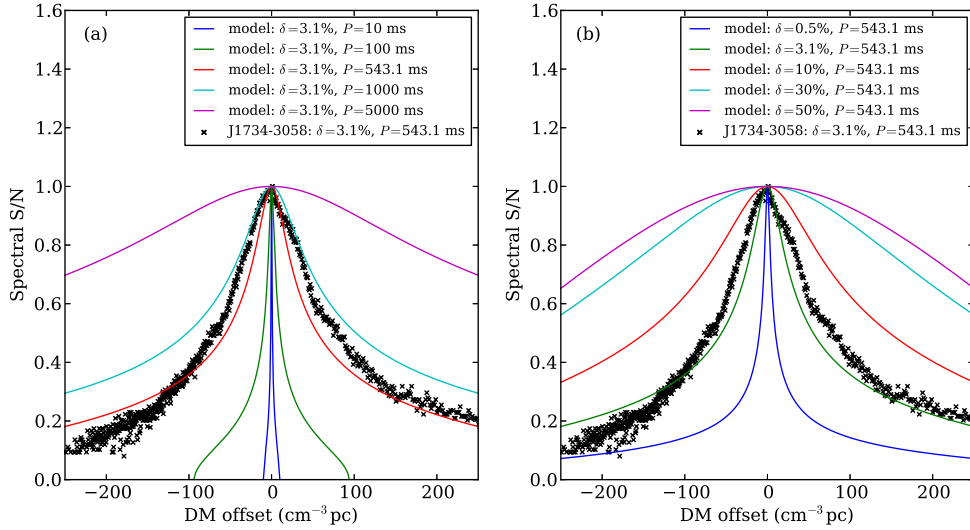


Figure 2.4: Plot illustrating the degradation of S/N versus DM offset. Panel (a) shows top-hat pulses with different spin period, whereas panel (b) shows different duty cycle δ . The spectral S/N of a newly-discovered pulsar, PSR J1734–3058 (see Section 4.2), as detected from the search pipeline of the HTRU Galactic plane survey is plotted as black cross as a comparison.

individual channel is thus t_{samp} . Subsequently, after the second diagonal DM is reached (i.e., $i = 2 \times (n_{\text{chan}} + 1)$), the broadening across an individual channel becomes $> 2t_{\text{samp}}$, which effectively re-defines the time resolution. This means that the data can now be down-sampled by a factor of two to save computing power.

2.1.2.3 The discrete Fourier transform

The most effective way to search for any periodic signal in an uniformly-sampled time series is by taking a Fourier transform and studying the Fourier (frequency) domain. As our time series is non-continuous and independently sampled data, the discrete Fourier transform (DFT) is used, where the k th Fourier component is defined by

$$\mathcal{F}_k = \sum_{j=1}^{N-1} \mathcal{T}_j \exp(-2\pi i j k / N). \quad (2.6)$$

In the above equation, N is the number of samples in the time series \mathcal{T}_j and $i = \sqrt{-1}$. According to Nyquist sampling theory, the frequency of the k th Fourier bin is given by $\nu_k = k / (N t_{\text{samp}}) = k / t_{\text{int}}$, where t_{int} is the integration time and $1 \leq k \leq N/2$. It is then apparent that, at $k = 1$, we have the width of a Fourier ‘bin’ $1/t_{\text{int}}$, which is also the slowest possible spin frequency of a periodic signal to be detected. At the other extreme where $k = N/2$, we have the Nyquist frequency $\nu_{\text{Nyq}} = 1/(2t_{\text{samp}})$, which is also the highest possible spin frequency of a periodic signal to be detected.

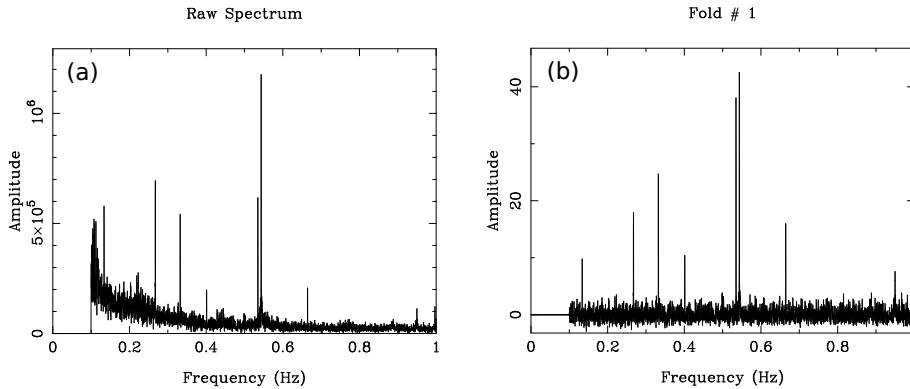


Figure 2.5: Fourier spectrum of a HTRU survey data taken at the Parkes telescope containing the known pulsar PSR B1839–04. This pulsar has long spin period of 1.8399 s which corresponds to a fundamental frequency at 0.5435 Hz. Panel (a) shows the raw spectrum where red noise is clearly visible and of comparable amplitude to the sub-harmonics of the 0.5435 Hz pulsar signals. Panel (b) shows the whitened spectrum using a running mean calculation.

Brute-force DFT using Equation (2.6) is however computationally expensive, particularly for long observations with a large N , as the number of computations goes as N^2 . An optimised algorithm known as the *fast Fourier Transform* (FFT; [Cooley & Tukey, 1965](#)) is typically used to reduce the number of operations to $N \ln(N)$. The other speed improvement is related to the fact that our time series \mathcal{T}_j contains only real numbers. Hence the Fourier components with $k > N/2$ are just the complex conjugates of those lower frequency components with $k < N/2$, in other words, $\mathcal{F}_{N-k} = (\mathcal{F}_k)^*$. It is then obvious that the DFT is symmetrical about the point $k = N/2$ corresponding to the Nyquist frequency. Finally, a Fourier power spectrum \mathcal{P}_j can be created, by summing the real and the imaginary parts, where $\mathcal{P}_j = \Re(\mathcal{F}_j)^2 + \Im(\mathcal{F}_j)^2$.

2.1.2.4 Spectral whitening

After implementing the FFT, the resulting Fourier power spectrum can then be inspected for prominent spikes that correspond to a periodic signal. An ideal observation with pure Gaussian noise would have a ‘white’ (i.e., with uniformly distributed power) Fourier spectrum. In reality, fluctuations and instabilities of the data acquisition hardware and/or the presence of strong, long-period RFI can contribute to excess power in the low-frequency end of the Fourier spectrum. This ‘red’ noise should be rectified to avoid skewing the significance level in the Fourier power spectrum and masking any long period pulsar signal that might be present in the lower end of the spectrum.

First, brute-force red-noise suppression is performed setting the lowest Fourier frequency region to be zero. In the case of the HTRU survey this range is chosen to be ≤ 0.1 Hz, and the result can be seen in Fig. 2.5. This procedure is justified because the first Fourier bin, the *DC bin*, contains no useful information except the offset of the mean of the transformed time series. In addition, due to the re-leveling of attenua-

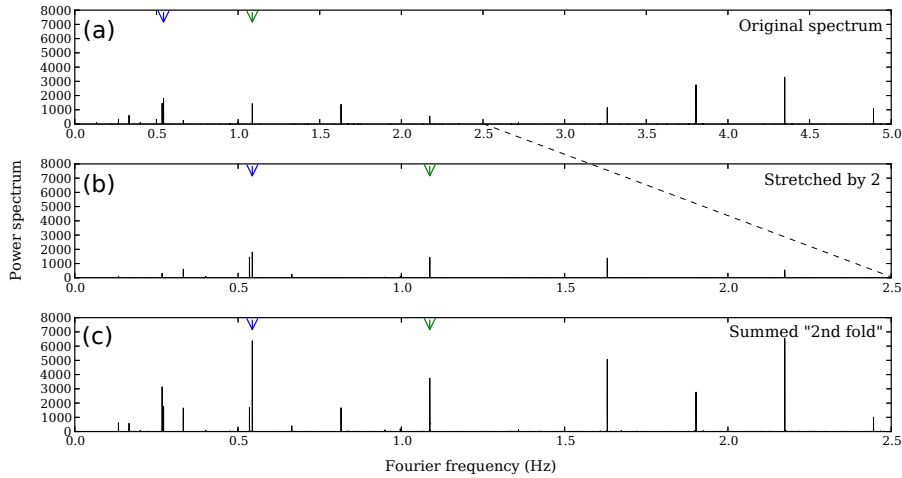


Figure 2.6: The power spectrum of the same observation as Fig. 2.5. The blue arrow shows the fundamental frequency of PSR B1839-04 at 0.5435 Hz, whereas the green arrow shows the corresponding second harmonic. Panel (a) is the original spectrum after whitening. Panel (b) illustrates how we stretch the original spectrum by a factor of two, before summing panels (a) and (b) to achieve the ‘second fold’ spectrum shown in panel (c).

tion in the HTRU backend every 10 s (see Section 3.1.1) in order to maximise dynamic range, we anyway have no ability to detect periodic signals with Fourier frequencies less than 0.1 Hz.

To whiten the remaining red noise component, an effective method is to subtract a running mean from the data and normalise it by the RMS of the original spectrum. Fig. 2.5 shows an HTRU survey observation before and after the running mean implementation. The red noise presents in panel (a) has been successfully removed and resulted in a ‘whitened’ spectrum in panel (b). The base line now has a mean of zero and a RMS of unity. At this point, the Fourier amplitude also represents the spectral S/N.

We note that care must be taken when selecting the window size of the running mean. A window that is too wide would be insensitive to follow the steep shape of the red noise, whereas a narrow window that is comparable with the number of Fourier bins occupied by a pulsar signal could accidentally prevent pulsar discovery. A potential improvement is to employ a ‘running window size’, with increasing window size at higher Fourier frequency, red-noise-free regions.

2.1.2.5 Harmonic summing

A periodic, sinusoidal signal would show up as a single spike in the Fourier spectrum. However, pulsars have a duty cycle that is usually only a few per cent. The Fourier power from such a narrow pulse is thus spread between a fundamental frequency and a number of related spectral harmonics. In principle, the smaller the duty cycle, the

larger the number of harmonics. Hence, in order to maximise our sensitivity to pulsar signals, we have to collect the power distributed in the harmonics.

A solution first devised by [Taylor & Huguenin \(1969\)](#), known as ‘incoherent harmonic summing’, is illustrated in Fig. 2.6 with a HTRU survey observation containing the known pulsar PSR B1839–04. In harmonic summing, the original power spectrum (panel (a)) is summed with a stretched version of itself, say by a factor of two (panel (b)), such that all second harmonics of each periodic signal are incoherently added to their corresponding fundamentals. The resultant spectrum, known as the ‘second fold’ spectrum, is shown in panel (c) of Fig. 2.6. In theory, the net gain in S/N is of the order of $\sqrt{2}$ when two spectra are summed together. This is because even though every incoherent summation adds up noise by a factor of $\sqrt{2}$, the signals of two harmonics would add directly. This procedure can be repeated by summing spectra of higher factors to recover even higher harmonics. As an example, the HTRU Galactic plane survey creates five spectra corresponding to the original, second, fourth, eighth and 16th harmonic fold. This should provide optimal summing for all pulsars with duty cycles > 2 per cent ([Ransom et al., 2002](#)).

2.1.2.6 False-alarm probability

Studying the statistical properties of the DFT can provide a way to decide which of those signals identified in the Fourier domain are actually statistically significant, hence worth investing more resources for a follow-up. In the ideal case where only Gaussian noise is present in the time series, the real and imaginary components of the Fourier spectrum will both have Gaussian probability density functions (PDFs). As we sum these two components, the powers follow a PDF of a χ^2 distribution with two degrees of freedom, i.e., an exponential PDF (see panel (a) of Fig. 2.7). Integrating this exponential PDF shows that, the probability for the power in any spectral bin to exceed a threshold P_{thres} is proportional to $\exp(-P_{\text{thres}})$. This defines the *false-alarm probability*, which quantifies the odds of a candidate signal that is actually due to noise but not of genuine significance. Note that in the case when m harmonic foldings have been performed, the PDF becomes a χ^2 distribution with $2m$ degrees of freedom.

The threshold power level, P_{thres} , can be estimated by setting the number of false-positive to be one,

$$P_{\text{thres}} = \ln(1/(2n_{\text{samp}})). \quad (2.7)$$

For the case of the HTRU Galactic plane survey, the number of samples in the time series takes the value of $n_{\text{samp}} = 2^{26}$, which gives a $P_{\text{thres}} \approx 19$. This threshold power level is marked by the red dashed line in panel (a) of Fig. 2.7.

[Lorimer & Kramer \(2005\)](#) show that by converting between power and signal-to-noise, a similar threshold level, S/N_{thres} , can be given by

$$S/N_{\text{thres}} = \frac{\sqrt{\ln[n_{\text{trials}}]} - \sqrt{\pi/4}}{\sqrt{1 - \pi/4}} \simeq \frac{\sqrt{\ln[n_{\text{trials}}]} - 0.88}{0.47}. \quad (2.8)$$

For the HTRU Galactic plane survey, we have 1069 DM trials, each producing a time series with 2^{26} samples to be Fourier transformed, and five harmonic sums are car-

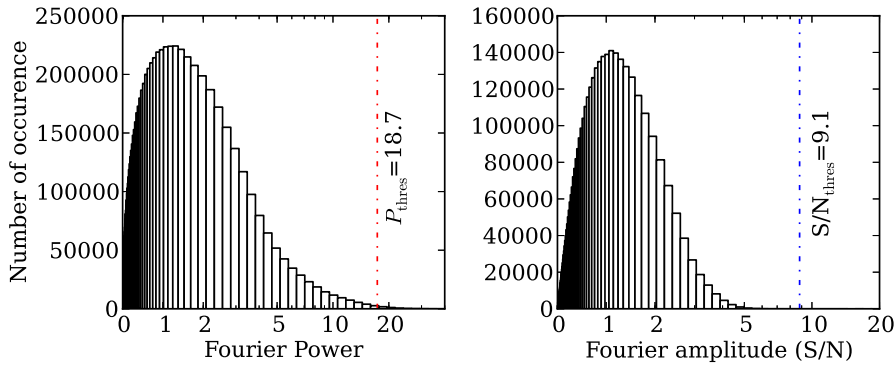


Figure 2.7: Panel (a) shows the PDF of the Fourier power spectrum of a time series created from a HTRU survey observation that contains no pulsar signal. Panel (b) shows the PDF of the amplitude spectrum of the same time series. The blue and red dashed lines represent the P_{thres} and S/N_{thres} as described in the main text.

ried out, each analysed independently. This gives an n_{trials} of 3.6×10^{11} , hence a $S/N_{\text{thres}} \simeq 9$. This threshold S/N level is marked by the blue dashed line in panel (b) of Fig. 2.7. In reality the S/N_{thres} could be even higher due to the presence of RFI or any instrumental effects which have contributed to non-Gaussian components in the noise distribution.

2.1.3 Binary pulsar searches

The ‘standard’ pulsar search algorithm, which makes use of Fourier transforms as described above, is very effective in identifying periodic signals. However, when it comes to the detection of pulsars in binary systems, the story becomes complicated. The high orbital acceleration attained by fast relativistic binaries results in a Doppler shift in the spin frequency of the pulsar as a function of the orbital phase. This is manifested as smearing in the spectral bins of the Fourier power spectrum, hence a reduction in the detectability of the periodicity search. Below we discuss some techniques developed to recover the loss of sensitivity due to its binary motion.

2.1.3.1 Time domain resampling

By quadratically stretching or compressing a time series by the amount dictated by a particular acceleration, the time series is re-binned into equal time steps in the rest frame of an inertial observer with respect to the pulsar in binary orbit. This resampled time series can then be Fourier transformed to coherently search for peaks in the power spectrum just like the standard periodicity search. The recipe for this time domain resampling can be found by a simple consideration of the Doppler formula, which relates the time interval in the reference frame of the orbiting pulsar, τ , to that of the observer, t . Ignoring higher order terms,

$$\tau(t) = \tau_0(1 + V_1(t)/c + \dots), \quad (2.9)$$

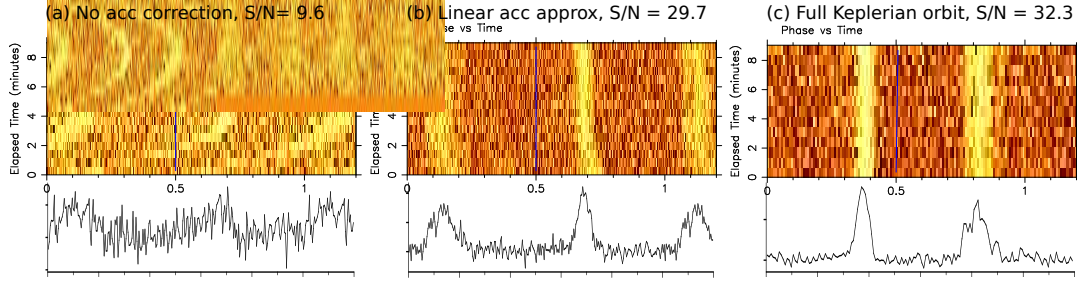


Figure 2.8: Phase vs time plots (top panels) and the corresponding pulse profiles (bottom panels) of an observation containing the double pulsar PSR J0737–3039A. Panel (a) shows severe spectral smearing caused by the uncorrected high orbital acceleration, resulting in a low S/N barely above the false-alarm threshold of $S/N_{\text{thres}} = 9$. Panel (b) shows the application of the time domain resampling technique where $a_1 = -159.82 \text{ m s}^{-2}$, resulting in a much improved S/N and pulse profile. Panel (c) has been created using an accurate ephemeris of the double pulsar which takes full account of the Keplerian orbit.

where τ_0 is a normalisation constant (see e.g., Camilo et al., 2000), $V_1(t)$ is the line-of-sight radial velocity of the orbiting pulsar and c is the speed of light. New time samples can be calculated by linear interpolation (Middleditch & Kristian, 1984) or by adding and removing samples as required by the desired phase drifts. We note that linear interpolation nonetheless lead to changes in the statistics of the data, and sensitivity for high-frequency signals might be compromised in portions of data where the time samples are effectively two-bin averaged.

Baring these caveats in mind, if given a precise form of $V_1(t)$ assuming a Keplerian model, this method of time domain resampling can in principle fully recover the sensitivity of a binary pulsar. However, this requires full account of the unknown binary orbits which is an almost impossible task, as theoretically one should trial all five Keplerian orbital parameters which would be extremely computationally expensive to search. A more computationally manageable approach is to approximate any unknown orbital motion as a simple line-of-sight linear acceleration, i.e., $V_1(t) = a_1 t$. Fig. 2.8 shows the application of this time domain resampling technique with a linear acceleration approximation. The improvement in the recovered S/N is apparent (comparing panel (a) and (b)), yet the compromise from a full Keplerian solution is only tiny (comparing panel (b) and (c)).

Just like the planning of de-dispersion as discussed in Section 2.1.2.2, an important consideration is the step size of the acceleration trials. The loss in sensitivity can be quantified by calculating the amount of spectral smearing. Re-writing Equation (2.9) in terms of the spin frequency, we have $\nu_{\text{app}}(t) = \nu_0(1 - V_1(t)/c)$, where ν_{app} and ν_0 are the apparent and intrinsic spin frequencies of the pulsar, respectively. Differentiating this with respect to time, we get the corresponding drift in frequency,

$$\dot{\nu}_{\text{app}} = a_1 \nu_0 / c. \quad (2.10)$$

Recall from Section 2.1.2.3 that a Fourier bin has the width $\Delta\nu = 1/T$ for an integration

of length T , Equation (2.10) can then be translated into the number of Fourier bins, N_{drift} , that the pulsed signal has drifted in,

$$N_{\text{drift}} = \frac{\dot{\nu}_{\text{app}} T}{\Delta\nu} = \frac{a_1 \nu_0 T^2}{c}. \quad (2.11)$$

In the best-case scenario, the acceleration step size Δa_1 should be chosen such that $\Delta N_{\text{drift}} \leq 1$. In other words, $\Delta a_1 \leq cP/T^2$, where P is the pulsar spin period.

Time domain resampling has been a frequent choice for previous pulsar surveys targeting binary pulsars. Notable examples are the 47 Tucanae observations by [Camilo et al. \(2000\)](#) and the Parkes multibeam pulsar survey (PMPS; [Manchester et al., 2001](#)) re-analysis carried out by [Eatough et al. \(2013b\)](#). This technique is the fundamental concept of the acceleration search implemented for the HTRU Galactic plane survey as part of this PhD work, and is detailed in Section 3.3.2.

2.1.3.2 Other techniques

The following is a brief comparison of other techniques available in the literature targeting the search for binary pulsars.

- **‘Stack/slide search’** works by chopping a time series into n_{seg} contiguous segments ([Wood et al., 1991](#)). Each of the segments is first independently Fourier-transformed. Provided that each segment is short and that the Fourier bin size is relatively wide, the period of a pulsar in binary can be considered unchanged within a segment. Hence a frequency shift (slide) can be applied to each of n_{seg} Fourier spectra to align the orbital-motion induced frequency variations across the segments, in analogue to applying time delays to ‘slide’ every frequency channels in de-dispersion (Section 2.1.2.2). The amount of slide between any two spectra caused by a constant line-of-sight acceleration a_1 is simply a slight variation of Equation (2.10), where now $\dot{\nu}_{\text{app}} = \nu_0 a_1 T / (n_{\text{seg}} c)$ Hz. These slided spectra can then be incoherently summed (stacked) together and search for significant peak corresponding to a periodic signal. This incoherent stack/slide search sacrifice phase information and is thus less sensitive than a fully coherent acceleration search as described for example in the previous section. [Faulkner et al. \(2004\)](#) report a roughly 20 per cent lost of sensitivity, depending on orbital phase. Nonetheless, this method can be relatively less computationally demanding, and has led [Faulkner et al. \(2004\)](#) to discover PSR J1756–2251, a pulsar in a 7.7-hr binary orbit.
- **‘Match filtering’** technique can be applied in the Fourier domain ([Ransom et al., 2002](#)). Instead of trying to correct for the spectral smearing as in the case of the time domain resampling technique, one can predict the amount of spectral smearing (in other words, N_{drift}) present in the zero acceleration time series. An analytically-predicted signal response function of width N_{drift} can be created as a match filter, which is cross-correlated with the Fourier amplitude spectrum. This effectively re-collects all the signal power smeared within the

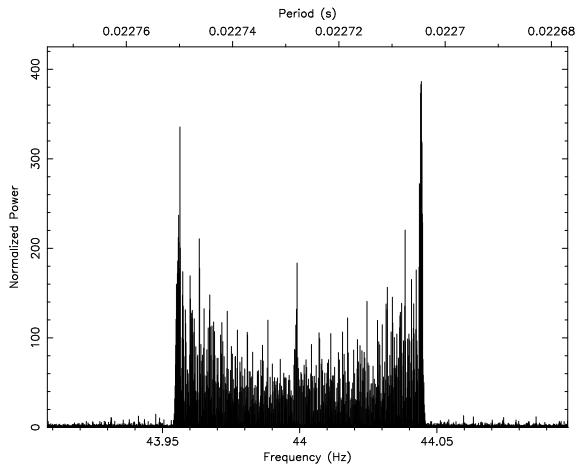


Figure 2.9: Fake data containing a double pulsar-like periodic signal, with a spin period ~ 22.7 ms and an orbital period of ~ 0.1 d. Five complete orbits are encompassed in this fake observation. The characteristic modulated pattern centring around 22.7 ms can be clearly seen.

neighbouring spectral bins. ‘Match filtering’ is in principle computationally efficient as only one FFT is needed per DM trial, while a range of N_{drift} values (corresponding to a range of linear acceleration) can be searched by applying a range of match filters. This technique was first used to discover the 0.070-d binary pulsar PSR J1807–2459 (Ransom et al., 2001).

- ‘Phase modulation’ technique as described in Jouteux et al. (2002); Ransom et al. (2003) is optimal for long observations that encompass at least one complete orbit of the binary pulsar to be discovered. The Doppler effect of the orbital motion will lead to spectral smearing as described earlier, which actually has a characteristic shape (see Fig. 2.9) in the Fourier spectrum as dictated by the orbital parameters. This pattern centres around the spin frequency of the pulsar, and has a set of sidebands on either side composed of a family of regularly spaced Bessel functions. Ransom et al. (2003) shows that the spacing of these individual sideband spikes is just the orbital period (P_{orb}); hence, by doing a second DFT around this region, we can retrieve both the spin and the orbital period of the binary pulsar. The greater the number of orbits observed, the more prominent is this modulated pattern. Hence this technique is particularly suited for detecting tight binary systems (say with P_{orb} of a few hours or shorter) in long observations typically employed for globular clusters (with T typically 2–10 hr). A caveat of this technique is that, although the phase modulation pattern is well-modeled for a circular orbit, it is non-trivial to take into account any orbital eccentricity. Having said that, pulsars known to be in extremely tight binaries with $P_{\text{orb}} < 1$ hr typically have insignificant eccentricity (see Fig. 5.8), which can be safely approximated by a circular orbit.

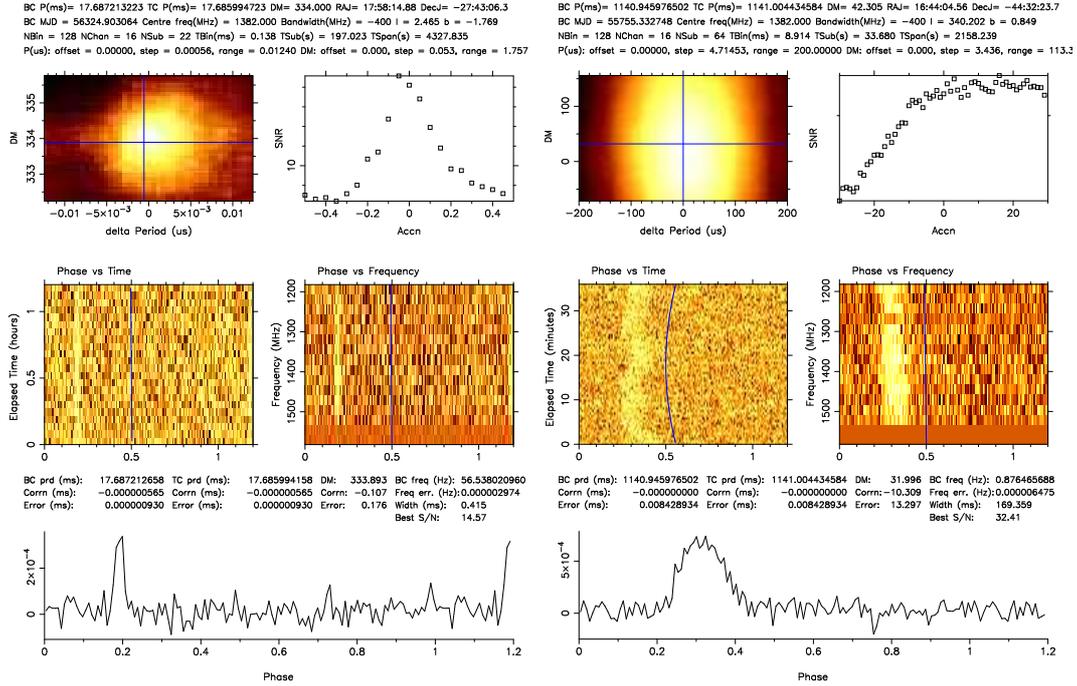


Figure 2.10: Two candidate plots as generated by the search pipeline used in the HTRU Galactic plane survey. The plot on the left shows genuine pulsar signal from PSR J1757–27, a newly-discovered MSP from this survey (see Section 4.2). The plot on the right contains a ‘pulsar-like’ RFI signal. The main difference is that the RFI signal has an optimal DM that is consistent with zero (top left panel). In addition, small ‘unnatural’ fluctuations are seen in the ‘phase vs time’ plot (middle left panel).

2.1.4 Candidate selection and optimisation

If a true pulsar signal is present in the observation, after the above mentioned search algorithm it is likely to be detected above S/N_{thres} at multiple DM trials, with the highest S/N corresponding to the true intrinsic DM value. Similarly, it could be detected at multiple acceleration trials with decreasing S/N around the true acceleration value. A strong pulsar could also be detected at its fundamental frequency as well as its related harmonics. It is thus useful to carry out ‘candidate sifting’ to identify duplicated candidates that belong to the same source. First, all detected spin frequencies that are integer multiples or common fractions (i.e., $\frac{a}{b}$ where a and b are both integers) of each other can be grouped, as they are likely harmonically related, provided that their S/Ns and DMs also fall within the predicted range of a pulsar (see e.g., a sample DM-SN curve in Fig. 2.4). Among this group, a nominal fundamental frequency can then be selected with the DM and acceleration values that provide the highest S/N.

At this stage, further RFI mitigation methods can also be incorporated. For example, any signal that does not follow the predicted DM-SN curve, as well as signal that shows an optimal value at a DM compatible with $DM = 0 \text{ cm}^{-3} \text{ pc}$ (i.e., of terrestrial nature) can be removed. Candidates with frequencies matching known RFI frequencies

can also be disregarded.

Subsequently, the condensed candidate list can then be subjected to a closer visual examination. Typically, raw data of the observation are phase-folded with the candidate parameters to create a diagnostic plot. At the same time, a finer search in the DM-period-acceleration space can be performed to fine-tune the parameters for the optimal S/N. Two examples of such diagnostic plots are shown in Fig. 2.10. In each of the two plots, the top left panel shows a color map of the period-DM plane, where the colour scale illustrates the decrease in S/N with increasing offsets from the nominal period and DM. The top right panel shows the detected S/N as a function of trial accelerations. The middle left panel shows 128 sub-integrations of the observation split in 16 sub-bands. A promising pulsar candidate should be clearly visible during the survey integration aligning at the same phase, provided orbital acceleration has been taken into account. The middle right panel shows 16 frequency sub-bands, and again a real pulsar should produce broadband emission with stable flux density over the observing frequency bandwidth. The blue cross hairs in these panels indicate the optimal parameters that provide the highest S/N. Finally, the bottom panel shows the time- and frequency-scrunched integrated pulse profile, created by folding the raw filterbank data with the optimised parameters. From this folded profile, the folded S/N can be defined as

$$S/N_{\text{fold}} = \frac{\sqrt{W_{\text{eq}}}}{\sigma_{\text{off}}} (\bar{S}_{\text{on}} - \bar{S}_{\text{off}}) , \quad (2.12)$$

where W_{eq} is the equivalent width of a top-hat pulsed signal with the same area and peak height as the integrated pulse profile. The off-pulse standard deviation is represented by σ_{off} . The mean flux densities at the on- and off-pulse phase are denoted by \bar{S}_{on} and \bar{S}_{off} respectively.

2.2 An overview of pulsar surveys

2.2.1 Previous generations

In the late 1980's, examples of pulsar surveys conducted at ~ 1.4 GHz (Clifton et al., 1992; Johnston et al., 1992b) showed that these relatively high-frequency searches were fruitful for discovering pulsars. However, high-frequency observations have the disadvantage of a smaller beam pattern (with area decreasing with the observing frequency to the power of -2) and hence were regarded inefficient for large-area surveys. The turning point arrived in 1994 when a 20-cm multibeam receiver (Staveley-Smith et al., 1996) was commissioned for the Parkes telescope, a receiver originally designed for a neutral hydrogen survey of the local universe (see Lyne, 2008, for a narration of this history). It was soon recognised that such a receiver could bring tremendous benefits to the pulsar community, with its wide bandwidth of 300 MHz and its multibeam design allowing 13 patches of sky to be observed simultaneously, increasing the survey speed by approximately the same factor. Four main blind surveys for radio pulsars were conducted in this light, namely the PMPS, the Swinburne intermediate latitude surveys (Edwards et al., 2001; Jacoby, 2004), the Parkes high latitude (PH) multi-

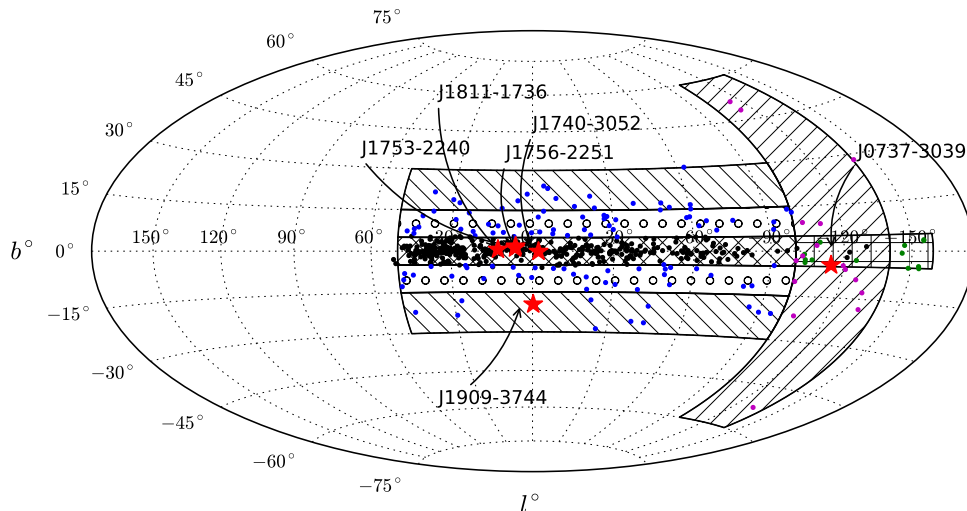


Figure 2.11: Sky coverage of the four main blind surveys for radio pulsars conducted in the 1990's. The Parkes multibeam pulsar survey is represented by cross hatch and its discoveries by black dots. The regions of the Swinburne intermediate latitude surveys are filled with circular hatch for SWIN1 or back diagonal hatching (\backslash) for SWIN2 and the discoveries by blue dots. The Parkes high latitude (PH) multibeam pulsar survey is represented by diagonal hatching ($/$) and its discoveries by magenta dots. The Perseus Arm (PA) multibeam survey is represented by 'plus' hatching ($+$) and its discoveries by green dots. Also plotted in red stars are the notable discoveries from these surveys mentioned in the main text.

beam pulsar survey (Burgay et al., 2006) and the Perseus Arm (PA) multibeam survey (Burgay et al., 2013a). Figure 2.11 illustrates the sky coverage of these four surveys as well as some of their discovery highlights.

The PMPS is arguably the most successful pulsar survey in history. It commenced in 1997 and was completed in 2003, covered a thin strip of survey region along the Galactic plane with $260^\circ < l < 50^\circ$ and $|b| < 5^\circ$. The PMPS comprised of 35-min long pointings with a time resolution of $250 \mu\text{s}$. These long pointings provided low minimum detectable flux density threshold and the high sensitivity has allowed the PMPS to discover over 830 pulsars, which is equivalent to ~ 35 per cent of all pulsars currently known (Manchester et al., 2005). Highlight discoveries of PMPS include a binary pulsar, PSR J1740–3052, with a massive non-degenerate companion (Stairs et al., 2001); three double neutron star (DNS) systems, PSRs J1753–2240 (Keith et al., 2009), J1756–2251 (Faulkner et al., 2005) and J1811–1736 (Lyne et al., 2000), out of the current known DNS population of about 10; the first Rotating Radio Transient sources (RRATs; McLaughlin et al., 2006); as well as hundreds of young and high-magnetic-field pulsars (Manchester et al., 2001; Morris et al., 2002; Kramer et al., 2003; Hobbs et al., 2004; Lorimer et al., 2006) which provided for the first time insights into the Galactic population of pulsars (Lorimer et al., 2006). In fact even more than a decade later, re-analyses of PMPS data are still generating new results. Notable examples are the discovery of 28 pulsars using new candidate sorting techniques (Keith et al.,

2009), the discovery of 16 pulsars as well as the use of a coherent acceleration search technique (Eatough et al., 2013b), and the discovery of 24 pulsars with the volunteer distributed computing project called Einstein@Home (Knispel et al., 2013).

The Swinburne surveys aimed to search for pulsars at intermediate Galactic latitudes, at which the smaller DM-broadening favours the detection of MSPs at larger distances. The Swinburne surveys covered the same Galactic longitude as the PMPS, but extended in Galactic latitude from the PMPS boundary of $\pm 5^\circ$ to $\pm 15^\circ$ in the first stage (SWIN1) and to $\pm 30^\circ$ in a second stage (SWIN2). The Swinburne surveys were relatively shallow surveys with integration time of 4.5 min per pointing, whereas the sampling time was improved to 125 μ s in order to increase sensitivity to MSPs. Indeed 15 per cent of the newly-discovered pulsars from the Swinburne surveys were MSPs which is a significantly high percentage, including PSR J1909–3744 (Jacoby et al., 2003) which is one of the most precisely-timed MSPs.

The PH survey covered a vertical strip of sky up to higher latitude near the Galactic anti-centre. It observed between Galactic longitudes $220^\circ < l < 260^\circ$ and Galactic latitude $\pm 60^\circ$. This survey has led to the outstanding discovery of the double pulsar system PSR J0737–3039 (Burgay et al., 2003; Lyne et al., 2004). It is the most relativistic binary pulsar with an orbital period of 2.4 hr, and its strong gravitational field has provided the best tests of GR and other theories of gravity. The double pulsar has been used to obtain five independent tests for GR predictions and has shown that GR passes these yet most stringent tests with a measurement uncertainty of only 0.05 per cent (Kramer et al., 2006).

The PA survey focused in the region of the Perseus Arm enclosing Galactic longitudes $200^\circ < l < 260^\circ$ and Galactic latitude $\pm 5^\circ$. It was considered an extension of the very successful PMPS towards the Galactic anti-centre, and with an improved time sampling rate of 125 μ s. Data analysis has resulted in 14 newly-discovered pulsars (Burgay et al., 2013a).

Despite the success of these major surveys at Parkes in the last century, there are always areas for continued improvements. The sampling rate of several hundred of microseconds is only modest, and the analog signal processing equipment had a low intra-channel frequency resolution of 3 MHz. The low time resolution and the dispersion smearing within each channel particularly reduced the detection of MSPs at high DMs (see discussion on survey sensitivity in Section 3.1.2 and in particular Fig. 3.4). In addition, the 1-bit digitisation also meant a roughly 20 per cent loss in sensitivity for weak signals and bright radio bursts (Kouwenhoven & Voûte, 2001).

2.2.2 Contemporary pulsar surveys

Improvements in technology such as the developments in FPGAs and digital filterbanks have led to a new era of radio pulsar surveys. As the analog signal processing equipments are superseded by digital systems, pulsar surveys are conducted with higher time resolution, larger bandwidth and finer frequency resolution. These help to reduce the undesirable effects of interstellar dispersions (as discussed in Sections 1.3.1 and 2.1.2.2) enabling the discoveries of more distant MSPs and allowing these new surveys

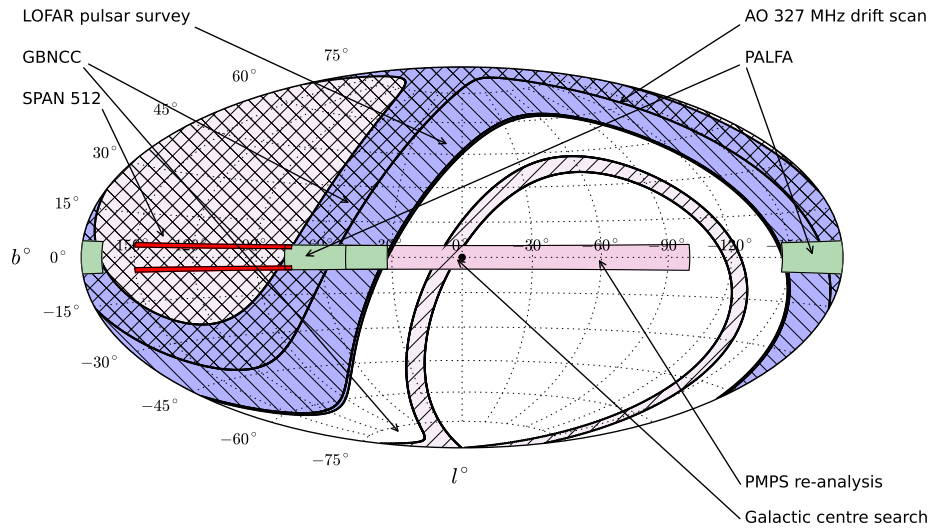


Figure 2.12: Sky coverage of all contemporary pulsar surveys as listed in Table 2.1. The LOFAR pulsar survey is represented by the region filled with back diagonal hatching (\backslash). The GBNCC is represented by the regions filled with diagonal hatching ($/$). The AO 327 MHz drift scan is represented by the purple region, the SPAN 512 survey by the red regions, the PALFA by the green regions, the PMPS re-analysis by the pink region and the Galactic centre search is the black region.

to be sensitive to transient sky on time scales down to several tens of microseconds. Table 2.1 lists the major radio pulsar surveys conducted with contemporary technology and Fig. 2.12 illustrates the sky coverage for each of these surveys.

The Galactic plane is an obvious place to search for pulsars due to the high pulsar population density in this region. The high scattering and dispersion environment in the Galactic plane is the reason why 1.4 GHz is thought to be the optimal observing frequency. At lower frequencies the problem of pulse broadening due to interstellar scattering increases (see Section 1.3.2); whereas going to higher frequencies would lead to a reduction in pulsar flux densities, as pulsars tend to have negative spectral indexes (see e.g., Lorimer et al., 1995). The PALFA pulsar survey (see e.g., Lazarus, 2013) employs the 305-m William E. Gordon radio telescope at Arecibo. The high sensitivity, as offered by the large dish of the Arecibo telescope, means that a short integration length can be used. Hence even tight relativistic binaries would show minimal spectral smearing as a result of its orbital motion during the short observation time, and can potentially be discovered without involving the challenges of an acceleration search (see Section 2.1.3). However, one disadvantage of the Arecibo telescope is its restricted field of view, with observing window limited to declinations between -1° and 38° . The SPAN 512 pulsar survey (Desvignes et al., 2013) with the Nançay telescope is designed to partially fill in the gaps of the Galactic plane visible from the Northern Hemisphere.

Table 2.1: Specifications of pulsar surveys conducted with contemporary technology. f_c is the central observing frequency, $\Delta\nu_{\text{chan}}$ is the frequency channel resolution, B is the observing bandwidth, t_{samp} is the time sampling rate, and t_{obs} is the integration length.

Survey	Telescope	Sky Coverage	f_c (MHz)	$\Delta\nu_{\text{chan}}$ (MHz)	B (MHz)	t_{samp} (μs)	t_{obs} (s)	Survey epoch	Discoveries** Total(MSP)
PALFA	Arecibo	$32^\circ < l < 77^\circ$ (Inner Galaxy)	1420/1400 ^{α}	0.39	322	64	67	2004 – Now	134
		$168^\circ < l < 214^\circ$ (Anti-centre) both for $ b < 5^\circ$							
SPAN512	Nançay	$3.5^\circ < b < 5^\circ$ $74^\circ < l < -150^\circ$	1486	0.5	512	64	1080	January 2012 – Now	2(1)
Galactic centre search AO 327 MHz drift scan	Effelsberg	Single $46''$ around Sgr A*	18950	7.8125	2000	128	8700 ^{β}	January 2012 – Now	1 ^{γ}
GBT 350	GBT	$-7.7^\circ < \delta < -38.4^\circ$ and $-20.7^\circ < l < 38.4^\circ$ for az 229° & 192°	350	0.057	25 ^{$\dagger\dagger$}	125	60 ^{\ddagger}	2003 – Now	44(4)
					0.025	69			
GBNCC	GBT	$\delta > 38^\circ$ (stage1), $\delta > -45^\circ$ (stage2)	350	0.024	100	82	120	2009 – Now	75(10)
LOTAAS	LOFAR HBA	$\delta > 0^\circ$	140	0.012	48	1300	1020	December 2012 – Now	5 ^{\dagger}

** As of 15 June 2014.

^{\dagger} Independent discoveries of the GBT 350 MHz survey.

^{\ddagger} Effective integration time in the drift scan.

^{$\dagger\dagger$} This set of three parameters corresponds to three stages of backend upgrade at the Arecibo telescope, from WAPP to Mock to PUPPI.

^{α} The central frequency was increased to 1420 MHz in 2005 to reduce influence of interference.

^{β} The integration shown is the length of a single scan. Repeated observations are made and incoherently combined afterwards to improve sensitivity.

^{γ} The magnetar discovered from the Galactic centre search was triggered by the initial X-ray detection from the *Swift* telescope.

The Galactic Centre is a special spot in the Galactic plane. At the moment there is a remarkable lack of pulsars detected within the central 100 pc of the centre of our Galaxy, likely due to the extreme scattering caused by inhomogeneities in the ionised component of the ISM around Sgr A*. Although this has been called into question after the recent discovery of radio pulsations from a magnetar at the Galactic centre with much less scattering than expected (Eatough et al., 2013c). Nonetheless, the potential of finding a pulsar orbiting the supermassive black hole in the Galactic centre would provide unprecedented insights to gravitational physics. Dedicated Galactic centre searches such as that with the Effelsberg telescope (Eatough et al., 2013a) go to an even higher frequency of 18.95 GHz and employ an enhanced version of the ‘stack searches’ as described in Section 2.1.3.2 to maximise sensitivity.

For high-latitude pulsar surveys out of the Galactic plane, a lower observing frequency can be used as pulse scattering becomes less problematic. A lower observing frequency is optimal for detecting pulsars that have very steep spectral indices, and has the additional benefit of a larger beam pattern on the sky which improves survey efficiency. The AO 327 MHz drift scan (Deneva et al., 2013) employs the Arecibo telescope observing at declinations of -1° to 28° , while excluding the region $\pm 5^\circ$ of the Galactic plane already covered by the PALFA pulsar survey. The GBT 350 MHz Drift-scan (GBT350; Boyles et al., 2013; Lynch et al., 2013a) made good use of the time when the Robert C. Byrd Green Bank Telescope was immobile during a track reparation in 2007, drift-scanned between mostly declination -21° and $+2^\circ$ which is inaccessible to the Arecibo telescope. The Green Bank North Celestial Cap Survey (GBNCC; Lynch et al., 2013b) is the successor of the GBT350 and in its stage 1 is focusing on surveying declination $> +38^\circ$, which is the other region of sky unobservable from Arecibo. The LOFAR Tied-Array All-Sky Survey (LOTAAS; Coenen, 2013) observes at even lower frequency of 119-151 MHz. Although at such low frequency scattering poses potential problems and may imply limitations to detectable distances (Lorimer, 2013), LOTAAS has the advantages of ‘beam forming’ from multiple stations which greatly increases the instantaneous combined field-of-view. This allows integrations of a much larger area of sky to be taken at any one instant and survey with multiple-pass become feasible, which is necessary for improving the chance of detecting transient, non-repeating sources, scintillating, eclipsing and intermittent pulsars.

2.2.3 Next generations of pulsar surveys

Radio astronomy will be revolutionised in the next 10-15 years by the Square Kilometre Array (SKA)¹, designed to be the largest and most sensitive radio telescope ever built (see e.g., Terzian & Lazio, 2006). The SKA is an international effort currently with eleven member countries, including Australia, Canada, China, Germany, India (associate member), Italy, New Zealand, South Africa, Sweden, the Netherlands and the United Kingdom. The SKA will consist of a large array of thousands of small telescope dishes with 15-m diameters plus aperture arrays. As a whole, they will create a 1 km^2 of collecting area, which makes the SKA 10-100 times more powerful in sensitivity and

¹<https://www.skatelescope.org/>

survey speed as compared to any other current radio telescope facilities. The SKA configuration will be split between South Africa and Australia, each location containing a core and smaller stations. SKA Phase I has been predicted to be producing science as early as in 2020, which will already provide sensitivity equivalent to 20 per cent of the final capability. Full operation has been scheduled by 2025.

The sensitivity of the SKA will enable the discovery of the order of 10,000-20,000 pulsars (Cordes et al., 2004), and will enable unprecedented study of the Galactic neutron star population, as well as provide plenty of opportunities for the tests of gravity theories (Kramer et al., 2004). The SKA will help to find new sources of MSPs suitable to be employed in a PTA, as well as increase the timing precision of all currently timed MSPs. Sesana et al. (2009) argued that, based on the estimated sensitivity of the SKA, it will guarantee detections of Gravitational Wave background from massive black hole binaries. Undoubtedly, the SKA will demand a big leap forward in computational capability as described in Smits et al. (2009), requiring of the order of 10^{15} operations per second and a data rate of the order of 10^{11} bytes per second. The projected costs of the SKA is approximately 1.5 billion Euros.

MeerKAT² is a pathfinder to the SKA in South Africa, which will also be integrated into SKA Phase I. The design of MeerKAT contains 64 antenna each with an effective diameter of 13.5 m, of which 48 antennas will be installed in the core station, together forming a longest baseline approximately 1 km. MeerKAT will operate at a frequency range of 580 MHz to 14.5 GHz (Booth & Jonas, 2012). Until the SKA is completed, MeerKAT will have the world-leading sensitivity in L-Band radio interferometry. The first antenna of MeerKAT has just been installed in March 2014, and the full array is expected to be operational in mid 2017.

²<http://www.ska.ac.za/meerkat/index.php>

The HTRU Pulsar Survey

We have deferred the description of a major contemporary pulsar survey, the HTRU, until this chapter. The HTRU low-latitude Galactic plane sub-survey conducted with the 64-m Parkes radio telescope in Australia forms the main body of this PhD work. In this chapter we introduce the survey and discuss the computational challenges arising from the processing of the petabyte-sized survey data. We present the data processing algorithm with emphasis on newly incorporated elements developed as part of this PhD work, namely that of RFI mitigation (Section 3.3.1) and an innovative ‘partially-coherent segmented acceleration search’ technique (Section 3.3.2), which aims to increase our chances of discovering highly-accelerated relativistic short-orbit binary systems, covering a parameter space including potential pulsar-black hole binaries. A large extent of this chapter is based on a publication in preparation (Ng et al., in prep).

Contents

3.1	Introduction to the HTRU Pulsar Survey	45
3.1.1	Observing system	48
3.1.2	Survey sensitivity	50
3.2	Discovery highlights	53
3.2.1	‘Planet-pulsar’ binaries	53
3.2.2	Magnetar PSR J1622–4950	54
3.2.3	Fast Radio Bursts	55
3.3	The low-latitude Galactic plane survey	57
3.3.1	RFI mitigation	60
3.3.2	Acceleration search	63
3.3.3	Candidate confirmation and gridding strategy	71

3.1 Introduction to the HTRU Pulsar Survey

The HTRU started in 2008 and is a blind pulsar survey of the Southern sky with the 64-m Parkes telescope (Keith et al., 2010) complemented by a twin survey in the North with the 100-m Effelsberg radio telescope (HTRU-North; Barr et al., 2013). The HTRU survey uses multi-beam receivers and backends constructed with recent advancements in technology, providing unprecedented high time and frequency resolution, allowing us to probe deeper into the Galaxy than previous efforts with these two telescopes. Compared to other contemporary pulsar surveys as described in Section 2.2.2, the HTRU

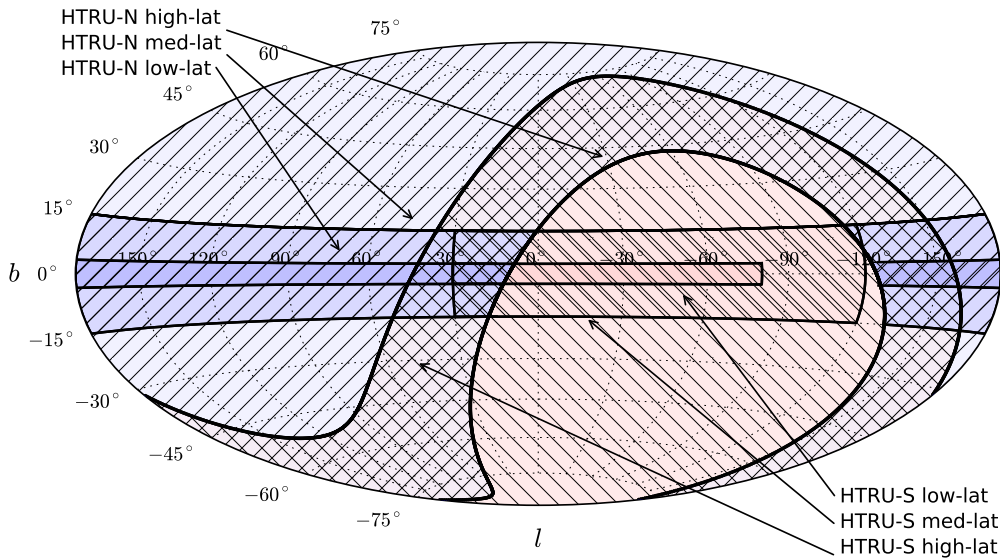


Figure 3.1: The HTRU is split into three regions of the sky, namely the high-latitude all-sky survey, the medium-latitude survey, and the low-latitude Galactic-plane survey. The regions with diagonal hatching (/) are covered by the HTRU-N survey, whereas the regions with back diagonal hatching (\) are covered by the HTRU-S survey. The overlapped regions observed by both surveys are indicated by crossed hatch.

survey has the additional advantage of being the first true all-sky survey, covering the northern and the southern skies with equal sensitivity. This arguably makes HTRU the best pre-SKA survey. The HTRU is an international collaboration with expertise shared among the MPIfR in Germany, ATNF/CASS and Swinburne University of Technology in Australia, University of Manchester in the UK and INAF in Italy.

The HTRU is split into three regions of the sky as illustrated in Fig. 3.1, namely the high-latitude all sky survey, the medium-latitude survey, and the low-latitude Galactic plane survey, tailored for achieving specific scientific goals. The high-latitude survey will provide a snapshot of the whole sky and hence a high chance of detecting transient signals. The medium-latitude survey is tuned to discover a large number of bright MSPs, an extremely useful tool for pulsar timing array. Finally, the low-latitude survey employs the longest observation per pointing, probing the deepest volume along the Galactic plane. The ultimate goal of this part of the survey is the discovery of pulsar-back-hole binaries and to find faint pulsars at the lower end of pulsar luminosity distribution, as further discussed in Section 3.3. Apart from the sky coverage and the integration time, the observational set-up and parameters are identical in these three parts. Table 3.1 is a summary of the survey specifications. More descriptions of the Southern survey with the Parkes telescope are presented in the following.

Table 3.1: Specifications of the HTRU-North and HTRU-South surveys.

	Northern survey			Southern survey		
Start date	Summer 2010			Early 2008		
Telescope	Effelsberg-100m			Parkes-64m		
Receiver	7-beam 1.4-GHz receiver			13-beam 1.35-GHz receiver		
Backend	Pulsar Fast Fourier Transform Spectrometer (PFFTS)			Berkeley-Parkes-Swinburne Recorder (BPSR)		
Bandwidth, B (MHz)	240			340		
Central frequency, f_c (MHz)	1360			1352		
Number of channels, N_{chans}	512			870*		
Frequency resolution, $\Delta \nu_{\text{chan}}$ (MHz)	0.58			0.39		
Time resolution, t_{samp} (μs)	54			64		
Receiver temperature, T_{rec} (K)	21			23		
Gain, G (K Jy ⁻¹)	1.5			0.735		
Number of bits, N_{bits}	8			2		
Number of polarisation summed, n_p	2			2		
Sky region in declination, δ	$\delta > -20^\circ$			$\delta < +10^\circ$		
	High-lat	Med-lat	Low-lat	High-lat	Med-lat	Low-lat
Sky region in Galactic longitude, l	–	–	–	–	$-120^\circ < l < 30^\circ$	$-80^\circ < l < 30^\circ$
Sky region in Galactic latitude, b	$ b > 15^\circ$	$ b < 15^\circ$	$ b < 3.5^\circ$	–	$ b < 15^\circ$	$ b < 3.5^\circ$
Integration length, t_{obs} (s)	90	180	1500	270	540	4300
Mean sky temperature [‡] , T_{sky} (K)	5	8	11	1.0	2.5	7.6
Characteristic minimum sensitivity [†] , S_{min} (mJy)	0.61	0.34	0.13	0.40	0.30	0.13
Total number of beams, N_{beams}	1066135	375067	87395	443287	95056	15990
Number of sample per data set, N_{samp}	1.6×10^6	3.3×10^6	27.4×10^6	$\sim 2^{22}$	$\sim 2^{23}$	$\sim 2^{26}$
Data size per beam (GB)	0.8	1.6	13.4	1.0	2.0	16.6
Total data size (TB)	818	576	1118	435	190	263

* Originally contains 1024 channels but due to RFI filters only 870 channels are usable.

† The S_{min} here denotes a characteristic minimum sensitivity for a pulsar with spin period of a few ms and a duty cycle of 30 per cent. For more detailed discussion on survey sensitivity see Section 3.1.2.

‡ These mean T_{sky} are extrapolated from the [Haslam et al. \(1981\)](#) sky map at 408 MHz.

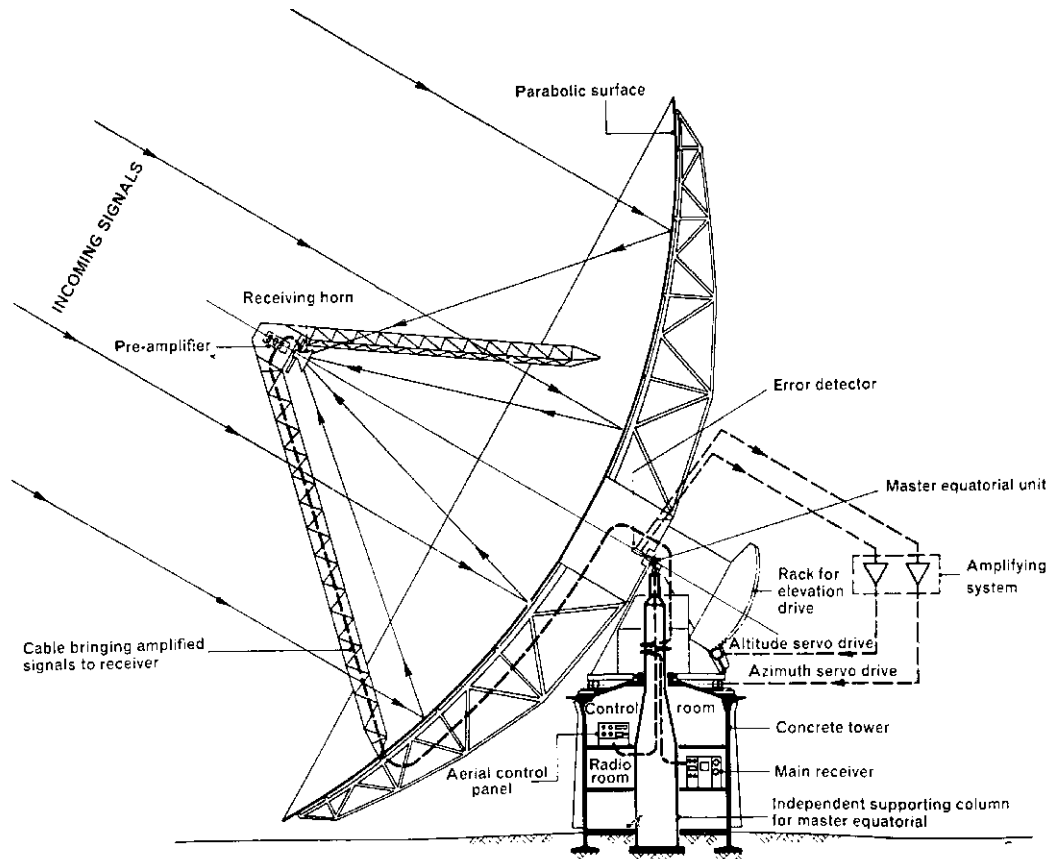


Figure 3.2: A schematic diagram of the Parkes telescope. The locations of the receiver and the backend are shown. (Image credit: CSIRO)

3.1.1 Observing system

The Parkes telescope is a parabolic dish with a diameter of 64 metres, located 20 km north of the little town Parkes in New South Wales of Australia. First commissioned in 1961, it had been employed to receive live, television image from the Apollo 11 moon landing mission in 1969. Apart from that, Parkes has proven to be one of the most successful radio astronomy instruments ever built, with notable achievements including the discovery of the first quasar 3C 273, detailed mapping of the Milky Way spiral arm structure via surveys of the galactic neutral hydrogen distribution, and on many occasions probing the most distant objects known in the Universe. Undoubtedly most relevant to this thesis, the Parkes telescope alone has also been responsible for the discovery of more than half of the currently known pulsars. Fig. 3.2 is a schematic diagram of the hardware set-up of the Parkes telescope, showing the location of the receiver system in the prime focus, which is connected by long cables going via the support leg to the backends located in the Faraday room. Observers were normally working in the control room directly under the dish, which has been the case until the implementation of the remote observing system in 2013.

Table 3.2: Details of the Parkes 20-cm multibeam receiver for the central feed as well as the inner and outer hexagonal ring of feeds (Keith et al., 2010).

Beam	Centre	Inner	Outer
Telescope gain (K Jy^{-1})	0.735	0.690	0.581
Half-power beam width ($'$)	14.0	14.1	14.5
Beam ellipticity	0.0	0.03	0.06
Coma lobe (dB)	none	-17	-14

The observational set-up of the HTRU southern survey with Parkes is described in detail in Keith et al. (2010). To summarise, observations were made using the 20-cm multibeam receiver (Staveley-Smith et al., 1996) at the prime focus on the Parkes radio telescope. This is the same receiver employed in the previous Parkes surveys as described in Section 2.2.1. It is organised as a central feed surrounded by an inner and an outer hexagonal ring. The central feed has a symmetric Gaussian-like beam pattern, whereas the outer feeds have a slightly elliptical pattern as well as some gain degradation (Table 3.2). This receiver is designed for efficient sky surveying, allowing simultaneous observations with its 13 receiver beams each separated by approximately $30'$ (Fig. 3.15). Each receiver beam has a full width at half-maximum (FWHM) of $14'.4$, and thus requires four interleaving pointings to cover an area in mosaic style (see Fig. 3.7). The high-frequency part of the bandwidth between 1525 and 1559 MHz is badly affected by interference from the Thuraya 3 geostationary communications satellite. Low-pass hardware filters were installed to introduce a frequency upper limit at 1522 MHz. Therefore, the receiver has an effective central frequency of 1352 MHz recording data with a bandwidth of 340 MHz.

The Berkeley-Parkes-Swinburne Recorder¹ (BPSR) is a high resolution digital filter-bank backend developed to exploit the wide bandwidth multibeam receiver at Parkes. It is a collaborative work between Swinburne University of Technology and the University of California at Berkeley. The dual-polarisation radio astronomy signals are first converted from analog to digital, before being sent to the digital spectrometers. The BPSR originally consists of 13 pairs of digital spectrometers which are based on the Interconnect Break-Out Board². These incoming signals are subsequently sub-divided into 1024 spectral channels with a channel width of 390 kHz, using a polyphase filter bank programmed into the FPGA logic blocks. Each spectral channel is integrated to return an output time resolution of $64 \mu\text{s}$. This 32-bit output of the spectrometer is then compressed to 8 bits, before being streamed to 13 server-class workstations where the data are formatted.

At these workstations, data are collected into blocks of 10 s (mainly useful for the purpose of statistics monitoring) and are further down sampled to 2 bits. In addition,

¹<http://astronomy.swin.edu.au/pulsar/?topic=bpsr>

²IBOB is developed by the CASPER group at the University of California, Berkeley. See <https://casper.berkeley.edu/wiki/IBOB> (IBOB) platform. In 2012, a hardware platform upgrade was carried out, replacing the IBOB digital frontend by a ROACH digital frontend.

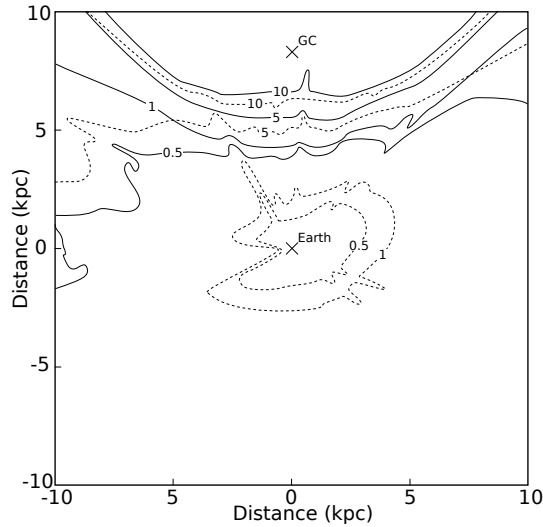


Figure 3.3: Contours of constant pulse broadening time scale in ms, specifically for the line of sight of Galactic latitude $b = 0^\circ$ and for an observing frequency of 1352 MHz. A comparison between the PMPS survey (dotted line) and the HTRU survey (solid line) shows the improvement in HTRU thanks to the high frequency resolution data. (Image taken from [Keith et al. \(2010\)](#))

the two polarisations of each spectral channel are summed and normalised, resulting in a data rate of 4MBs^{-1} from each of the 13 beams. At this rate, the servers in the BPSR cluster has sufficient disk space to buffer ~ 3 days of observations. These data are transferred to two sets of duplicated magnetic tapes for archiving before being removed from the buffer. One copy is written to tape in real-time at Parkes and later sent to be processed in Europe. A second copy is streamed via a dedicated 1Gbs^{-1} fibre link to the supercomputer at Swinburne University of Technology and written to tapes.

3.1.2 Survey sensitivity

The frequency and time resolution of the HTRU offered by the BPSR greatly enhanced the detectability of MSPs compared to the previously successful pulsar surveys at Parkes (see Section 2.2.1). To appreciate how the data resolution is related to MSP detectability, we can first ask the question: what are the challenges associated with MSP detection in comparison to finding a long-period normal pulsar?

Apart from the fact that MSPs are less numerous than normal pulsars in general, their fast spin periods of a few milliseconds mean a reasonably high time resolution is required to have enough time samples across a pulse period to be able to resolve the pulse profile. The previous generation of Parkes pulsar surveys had a time resolution of only $250\ \mu\text{s}$, implying only 4 time samples across the spin period of a 1 ms pulsar, which is far from ideal.

In addition, MSPs tend to have higher duty cycles meaning that their intrinsic

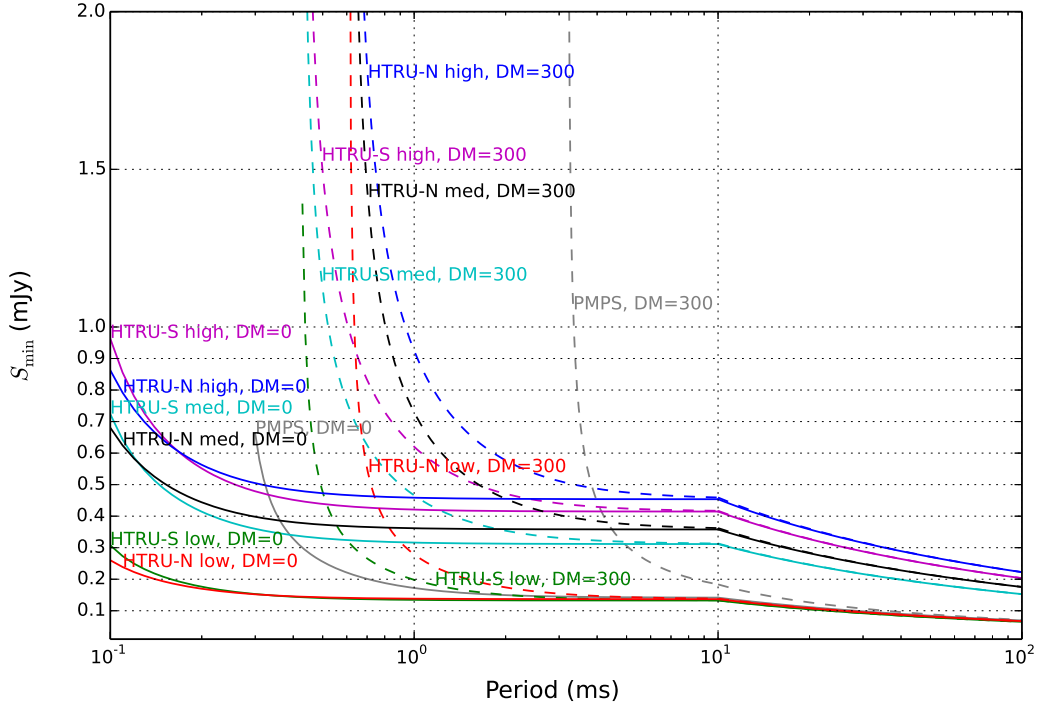


Figure 3.4: The minimum detectable flux density S_{\min} for the PMPS, the HTRU low-, med- and high-latitude survey for the North and South respectively, at $DM=0$ and $300 \text{ cm}^{-3} \text{ pc}$.

pulse widths, W_{int} , is a significant percentage of their respective pulse periods. This already puts MSPs in a less advantageous position, as broad pulse profiles risk being mistaken as RFI and hence overlooked in the candidate selection stage. Any unaccounted binary motion may also broaden the pulse profile as the Doppler shift of spin period results in spectral smearing (see Section 2.1.3). Furthermore, the relatively large duty cycles of MSPs also mean they are more susceptible to dispersion broadening (see Equation (2.3)). The de-dispersion scheme described in Section 2.1.2.2 can only correct for the dispersion smearing up to certain extent; as a result of the finite channel width of the filterbank, intra-channel dispersion smearing is inevitable, which worsen as a function of increasing DM.

Given these harmful influences of dispersion broadening on MSP detectability, it is thus clear that the improvement in frequency resolution from 3 MHz in the PMPS to 0.39 MHz in the HTRU-South survey is a key advancement. Fig. 3.3 plots the contours of constant pulse broadening time scale in milliseconds for these two surveys. For the HTRU survey, dispersion broadening is now negligible compared to ISM scattering in practically all directions, allowing HTRU to detect MSPs out to a much larger distance compared to the PMPS.

The minimum detectable flux density (S_{\min}) of a survey is the indicator of its sensitivity. This is nonetheless non-trivial to quantify, since hardware limitations mean

Table 3.3: Characteristic minimum detectable flux density ($S_{1400,\text{min}}$) for the Galactic plane survey. Considering normal pulsars and MSPs as two separate groups (see Section 1.4), we note the minimum, mean and maximum of the duty cycle δ of these two groups respectively, and we derive the respective $S_{1400,\text{min}}$.

		MSPs		Normal pulsars	
	δ (%)	$S_{1400,\text{min}}$ (mJy)	δ (%)	$S_{1400,\text{min}}$ (mJy)	
min	0.28	0.013	0.014	0.0030	
mean	11.54	0.092	4.21	0.053	
max	65.31	0.35	57.29	0.29	

surveys are never uniformly sensitive at every location (for example decreasing sensitivity from central beam to the outer beams, as well as well degrading sensitivity towards the edges of each beams). In addition, the detectability varies for individual pulsar systems with different pulse period, pulse shape and duty cycle at different DMs. Temporal changes in observing conditions such as scintillation, or the presence of RFI also alter the actual S_{min} . Bearing these factors in mind, the radiometer equation is typically used to estimate a theoretical S_{min} ,

$$S_{\text{min}} = \frac{(S/N_{\text{min}}) \beta T_{\text{sys}}}{G \sqrt{n_p t_{\text{int}} B}} \left(\sqrt{\frac{W_{\text{eff}}}{P - W_{\text{eff}}}} \right). \quad (3.1)$$

The first fraction of Equation (3.1) contains parameters related to the observational set-up. The minimum signal-to-noise ratio, S/N_{min} , is calculated based on the false alarm statistics as introduced in Section 2.1.2.6. The ‘degradation factor’, β , is due to digitisation and is ~ 1.16 for our case. The system temperature, T_{sys} , includes contribution from both sky temperature (T_{sky}) and receiver temperature (T_{rec}) all expressed in units of K, while G is the antenna gain in K Jy^{-1} . The number of polarisations summed, n_p , is always two in our case. The integration time, t_{int} , is in seconds and B is the effective bandwidth of the receiver in MHz. All these parameters for the HTRU can be found in Table 3.1.

The second term of Equation (3.1) contains pulsar dependent parameters, where P is the spin period and W_{eff} is related to W_{int} by Equation (2.3). Gould (1994) has shown that there is some correlation between the spin period of a pulsar and its intrinsic pulse width, where the duty cycle $\delta \propto P^{-1/2}$. Kramer et al. (1998) have shown that this relationship does not apply for an MSP with a spin period less than 10 ms, we have thus introduced a maximum δ of 30 per cent for the purpose of this discussion.

Following the above recipe, Fig. 3.4 shows the theoretical minimum detectable flux density for both the HTRU northern and southern survey. It can be seen that the two surveys indeed have very similar sensitivity at $\text{DM} = 0 \text{ cm}^{-3} \text{ pc}$. At higher DM however, the HTRU-South survey performs better compared to the Northern survey in particular for fast spinning pulsars with period of a few ms or less. This is as expected due to the coarser frequency resolution of 0.58 MHz at Effelsberg compared to 0.39 MHz

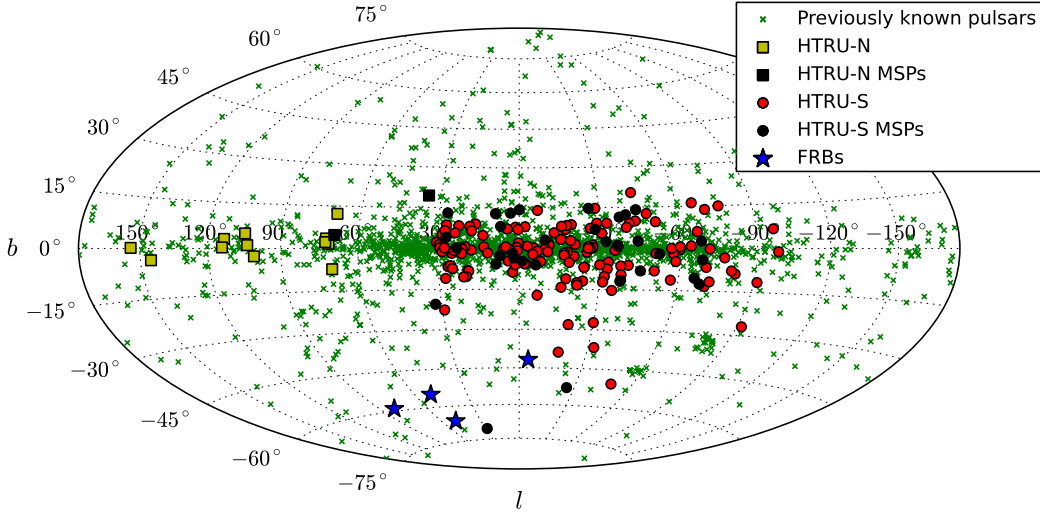


Figure 3.5: All HTRU discoveries as of 15 June 2014.

at Parkes.

A characteristic S_{\min} for any particular survey can also be derived with respect to the minimum, mean and maximum δ of all published pulsar data from PSRCAT. As an example, we list in Table 3.3 the corresponding $S_{1400,\min}$ distinguishing between normal pulsars and separately for MSPs ($P \leq 30$ ms and $\dot{P} \leq 10^{-17}$, see Section 1.4), specifically for the HTRU low-latitude Galactic plane survey at an observing frequency of 1.4 GHz.

3.2 Discovery highlights

As of 15 June 2014, 129 pulsars have been discovered from the HTRU survey of the southern sky with the Parkes telescope, of which 30 are MSPs. These discoveries have led to numerous referred publications. I have been a co-author of the HTRU Paper VI which describes the application of artificial neural network in the HTRU pulsar survey (Bates et al., 2012); Paper VII which includes a discussion on the different luminosity properties of binary and isolated recycled pulsars (Burgay et al., 2013b); Paper VIII which presents an investigation of the Galactic MSP population (Levin et al., 2013), Paper IX which conducts polarimetry study of long-period pulsars (Tiburzi et al., 2013), and Paper XI which describes the discovery of a further five MSPs (Thornton et al., in prep). Furthermore, below are extracts of selected HTRU discovery highlights as presented in Ng & HTRU Collaboration (2013).

3.2.1 ‘Planet-pulsar’ binaries

In 2009 HTRU discovered PSR J1719–1438, a 5.7-ms fast-spinning MSP. A follow-up timing campaign shows that this pulsar is in a binary system with an orbital period of 2.2 hr and has a very low mass function of $7.85(1) \times 10^{-10} M_{\odot}$. Assuming a pulsar mass

Table 3.4: Comparison between the two ‘Planet-pulsar’ binaries.

	PSR J1719–1438	PSR J2322–2652
P (ms)	5.7	3.46
DM-derived distance (kpc)	1.2	0.3
P_{orb} (d)	0.09	0.32
$a \sin i$ (lt-s)	0.0018	0.002
m_c (M_{\odot})	≥ 0.00115 ($\sim 1.2 M_{\text{J}}$)	≥ 0.00076 ($\sim 0.8 M_{\text{J}}$)

of $1.4 M_{\odot}$ and an orbital inclination of $i = 90^{\circ}$, we deduced the minimum companion mass to be $0.00115 M_{\odot}$, which is comparable to that of Jupiter ($\sim 1.2 M_{\text{J}}$). However, according to the so-called mean density-orbital period relation (Frank et al., 1985), we find that the minimum density of this companion is only 23 g cm^{-3} , clearly incompatible with that of Jupiter ($\rho_{\text{J}} < 2 \text{ g cm}^{-3}$). As can be seen in Fig. 5.6, it is unlikely that PSR J1719–1438 is a black widow system (Fruchter et al., 1988), a sub-group of pulsars typically with low companion mass.

Further optical observations with the Keck 10-m Telescope revealed no visible companion at the position of the pulsar and hence ruled out a massive WD companion. This reduced the probability that PSR J1719–1438 is in a face-on orbit, which in turn provided an upper limit on the companion mass. The companion is likely to be an ultra-low mass carbon white dwarf that has lost 99 per cent of its mass, possibly the remains of the degenerate core of the original white dwarf. Ultra-compact low-mass X-ray binaries are potential progenitors of this system, in which the companion has narrowly escaped complete destruction. In fact under such conditions carbon would be crystallised, hence the nickname ‘Diamond planet’ (Bailes et al., 2011). A long-term radio follow-up timing analysis of PSR J1719–1438 is presented in Chapter 5.

A second such ‘planet-pulsar’ system, PSR J2322–2652, has recently been discovered in the HTRU survey. This second system has parameters very similar to those of PSR J1719–1438 (Table 3.4), with a companion mass of the order of magnitude of a planet. Further timing studies are currently underway to improve the phase-coherent timing solution (Thornton et al., in prep). These results may be shedding light on a previously unknown population of pulsars, and perhaps more of such systems will be discovered in the near future.

3.2.2 Magnetar PSR J1622–4950

Magnetars are rare, young and highly magnetised neutron stars, with typical surface magnetic field of the order of $> 10^{14} \text{ G}$ (see Section 1.4.2). They are primarily bright X-ray emitters, and out of the 21 currently known magnetars only four have been also observed at radio-wavelengths.

All of the currently known magnetars were first discovered by their strong X-ray emission, with the exception of PSR J1622–4950. The magnetar PSR J1622–4950 was found from the HTRU medium latitude survey of the southern sky and it was the first magnetar discovered by its radio emission (Levin et al., 2010). PSR J1622–4950

has a spin period of 4.3 s and a surface magnetic field of 3×10^{14} G. Archival X-ray observations from July 2009 with Chandra revealed that this radio source has a bright X-ray counterpart CXOU J162244.8–495054. The discovery epoch of PSR J1622–4950 coincided with a radio bright phase while in X-ray quiescence. At odds with other radio magnetars, PSR J1622–4950 showed that bright radio emission can exist without any associated strong X-ray outburst, or at least can occur years after the outburst (Levin et al., 2010).

Large variations were observed in the radio pulse profiles, where the shape of the integrated pulse changing sometimes within a time scale of hours (Levin et al., 2012). The observed radio flux also fluctuated significantly, at times up to a factor of 6 within a day. These emission characteristics are consistent with other radio magnetars. In fact, the radio emission of PSR J1622–4950 has faded since October 2010, as presented in Section 4.1.

3.2.3 Fast Radio Bursts

The first four Fast Radio Transient Bursts (FRBs) discovered from the high latitude survey of the southern sky were published in Thornton et al. (2013). They are all found at high Galactic latitude of $|b| > 40^\circ$ (see Fig. 3.5) and with high DMs ranging from 553 to $1103 \text{ cm}^{-3} \text{ pc}$. These signals are broadband and show characteristic exponential tails with narrow pulse width of only a few ms. Fitting the pulse shape as a function of frequency results in a dispersion index of -2.003 ± 0.006 and a scattering index of -4 ± 0.4 . These are exactly as expected from dispersive delay due to propagation through the cold-plasma-like ionised ISM, confirming the astrophysical origin of these FRBs.

What makes these FRBs remarkable is the fact that they must have originated from cosmological distances. As illustrated in Fig. 3.6, the Milky Way can only account for at most 6 per cent of the observed dispersive delay, implying the extra-galactic nature of these FRBs. In turn we consider additional contributions from a combination of inter-galactic medium (IGM) and a potential host galaxy. If these FRBs originate from the edge of a spiral galaxy with a nominal inclination of 60° , this host galaxy can account for a DM_{Host} of $\sim 100 \text{ cm}^{-3} \text{ pc}$. To explain the remaining DM observed by IGM contribution would imply FRB distance of redshift $z = 0.8$, corresponding to a FRB distance of 2.8 Gpc. Other scenarios exist which could result in slightly closer FRB distances. For example, the FRBs could have been originated from central BH interaction of the host galaxy, and although highly unlikely, there could be another intervening galaxy, accounting for some of the observed DM. Nonetheless, taking into consideration all the possible cases, we conclude that these FRBs are certainly cosmological and have come from redshift of $z = 0.45 - 0.96$, corresponding to distances of 1.7 to 3.2 Gpc.

The nature of these transient bursts is still not clear. Nonetheless, it is possible to eliminate certain possibilities. They are unlikely to be giant pulses from pulsars because these bursts are too bright. In fact, at such cosmological distances the FRBs are brighter than any currently known radio transient sources. They are not Solar

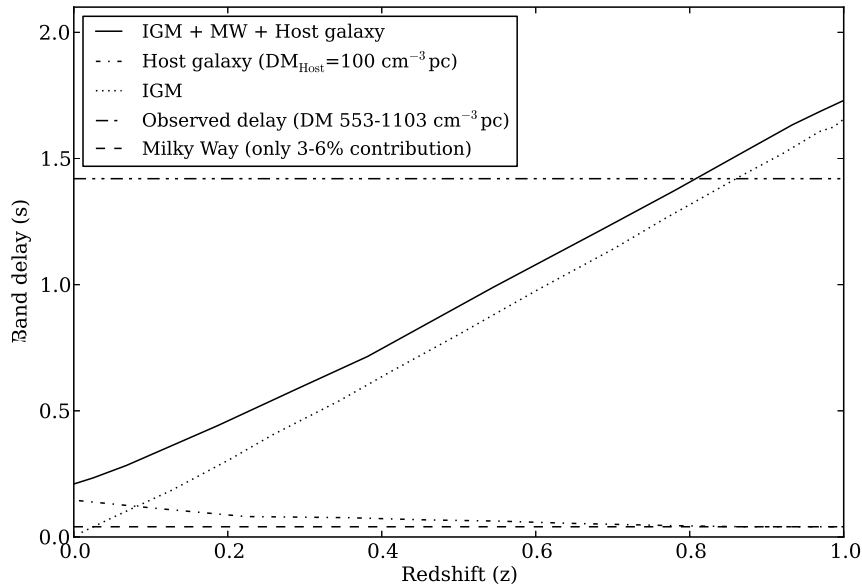


Figure 3.6: Various contributions to the observed band delay of the FRBs. The contribution from ISM in the Milky Way is plotted as a dashed line and can only account for at most 6 per cent of the observed delay. The contribution from IGM is plotted as a dotted line and that of a potential host galaxy with inclination $i = 60^\circ$ is represented by the dot-dashed line. The solid line is the sum of the IGM, host galaxy and Milky Way contribution. The redshift is inferred at the point when the solid line crosses the observed delay.

bursts because some have been detected at night time. They are not from Gamma-ray Bursts (GRBs) because there are no associated *Swift* or *Fermi* detections at X-ray or gamma-ray. In addition, the observed time scales of less than 1 ms for these FRBs are much shorter than the typical duration of even the short GRBs (as a reference, the 2005 giant flare of SGR 1806–20 showed repeated energy injections on a time scale longer than 100 ms; Terasawa et al., 2005).

These FRBs have an event rate of $\sim 1.0_{-0.5}^{+0.6} \times 10^4 \text{ sky}^{-1} \text{ day}^{-1}$, similar to that of core-collapse Supernovae. However, it is not known what would be the associated mechanism that generates such compact and extremely bright bursts. A more recent study by Totani (2013) suggested that the FRB rate is also consistent with the ‘plausible optimistic estimate’ of NS-NS mergers (Abadie et al., 2010), assuming that almost all NS-NS merger produce observable FRBs. If this is the case, FRBs could imply a high rate of detections for GW astronomy study, for example that in the frequency range of Advanced LIGO. Falcke & Rezzolla (2014) proposed that the collapse of supramassive NS (to which they have given the name ‘Blitzers’) could be the cause of these enigmatic bursts, however, the formation scenario of such hypothetical object is unclear.

3.3 The low-latitude Galactic plane survey

The low-latitude Galactic plane region is where the most relativistic binaries are expected to be found (Belczynski et al., 2002). Pulsars in tight binaries orbiting other compact objects, for example neutron stars and, potentially, black holes are of great interest as their strong gravitational fields provide the best tests of GR (Wex, 2014) and other theories of gravity (Freire et al., 2012). The best example of such a binary system so far is the double pulsar system (Burgay et al., 2003; Lyne et al., 2004). The double pulsar has been used to obtain five independent tests of GR and GR has passed the most stringent test, regarding the shape of the Shapiro delay, with a measurement uncertainty of only 0.05 per cent (Kramer et al., 2006). The number and the precision of GR tests increase as the binary systems to be discovered become more relativistic. Hence, one of the main aims of the Galactic plane survey is precisely the discovery and study of ultra-compact relativistic binary systems in short orbits.

The Galactic plane survey covers a strip along the inner Galactic plane, with the central beam of all scheduled pointings between Galactic longitude $-80^\circ < l < 30^\circ$ and latitude $|b| < 3.5^\circ$ (see Fig. 3.7). We employ the longest HTRU integrations of 72 min per pointing to maximise our sensitivity. This means that the HTRU low-latitude Galactic plane data set will be capable of revealing many pulsars that were not luminous enough to be detected by previous surveys. As a collection, these pulsars might increase the sample of sources that glitch, which could lead to improved knowledge of the interior of neutron stars (Espinoza et al., 2011a). They will give us useful insights into the ISM via the study of their dispersion and rotation measures to reveal a picture of the free electron distribution (see e.g., Cordes & Lazio, 2002) and of the magnetic field of the Milky Way (see e.g., Noutsos et al., 2008). They also provide us with an important handle on the lower end of the luminosity distribution function of the Galactic plane pulsar population, valuable knowledge for the planning of survey strategies for the next generation of radio telescopes, such as MeerKAT and the SKA. Furthermore, the archive of the HTRU Galactic plane survey will continue to produce science through future data re-examination. The long observation is also favourable for the detection of transient and nulling sources deep within the Galactic plane (see e.g., related work by Petroff et al., 2014).

However, the sheer volume of the high-resolution Galactic plane data set poses great challenges in data manipulation and analysis. Normally, long integration length (t_{int}) provides an increase in sensitivity. Nonetheless, this is not exactly the case when it comes to searching for tight-orbit relativistic pulsar binaries: a periodicity search in the Fourier domain is the standard method employed in most pulsar surveys, as explained in Section 2.1.2. However, the high orbital acceleration attained by fast relativistic binaries results in a Doppler shift in the spin frequency of the pulsar as a function of the orbital phase. The pulsar signal is thus smeared across neighbouring spectral bins of the Fourier power spectrum (see Section 2.1.3), hence a reduction in the detectability of the periodicity search. Furthermore, the width of the Fourier spectral bin is defined by $1/t_{\text{int}}$ (see Section 2.1.2.3). As a result, the longer the integration time, the larger the portion of the orbit we cover in a particular observation, but

also the narrower the Fourier spectral bin. These two effects combined lead to more severe consequences for Fourier spectral smearing. These complications explain why the data processing of the Galactic plane survey was not included in the previous HTRU publications (see e.g., [Keith et al., 2010](#)) but instead requires adaptations in the search algorithm. Various search techniques targeting binary pulsars have been introduced in Section 2.1.3. Here we present an innovative segmented search technique which aims to increase our chances of discoveries of highly-accelerated relativistic short-orbit binary systems, including potential pulsar-black hole binaries. We stress that the depth of the parameter space to which the survey data can be explored is highly dependent on the available computing resources. Optimisation of pulsar searching algorithms is thus crucial in the era of data intensive astronomy, and the HTRU survey acts as a test bed for the computational challenges of the SKA.

Observations for the Galactic plane survey at Parkes took place between November 2008 and December 2013, which comprise 1230 scheduled pointings each with 72-min long observations with just over 2^{26} samples. Several corrupted pointings (due to severe RFI contamination or hardware issues) were re-observed, hence finally 1246 pointings were recorded. All in all, the Galactic plane survey has resulted in 263 terabytes of observational raw data.

Processing of the Galactic plane survey is currently being carried out using multiple supercomputers. These include facilities of the Australian National Computational Infrastructure (NCI) high performance computing centre at The Australian National University (ANU), which consists of the 57,472-core high-performance distributed-memory cluster ‘Raijin’, the 1492-node Sun Constellation cluster ‘Vayu’ and the 156-node SGI cluster ‘XE’ (the latter two have now been decommissioned). We also employ the 1456-core supercomputer ‘HYDRA’ at the Jodrell Bank Observatory and the 64-core computer ‘Miraculix’ at the Max-Planck-Institut für Radioastronomie.

Two processing pipelines are applied to the data. Our initial, ‘standard search’ pipeline, also known as the HTRUN processing pipeline, is outlined in [Keith et al. \(2010\)](#). This algorithm follows the typical procedures of pulsar searching as described in Section 2.1. Firstly, spurious signals in the data, such as those created by radio frequency interference (RFI), are identified and excised. Next, the observation is dedispersed to compensate for the frequency-dependent delay caused by the free electrons along the line of sight. As the amount of dispersion is dependent on the *a priori* unknown distance of the pulsar to be discovered, we trial a wide range of potential dispersion measures (DMs) between 0 and $3000 \text{ cm}^{-3} \text{ pc}$, which sums to a total of 1069 DM trials per data set. Each of the dedispersed time series is then Fourier transformed. We sum the second, fourth, eighth and the 16th harmonic Fourier spectra respectively and identify significant signals created by any coherently pulsating signals. Based on false-alarm probability (see Section 2.1.2.6), this survey has a signal-to-noise (S/N) threshold of ~ 9 . We have nonetheless inspected by eye every potential pulsar candidate with a S/N above 8. A second pipeline, the ‘partially-coherent segmented acceleration search’, aims to improve the detectability of binary pulsars and is detailed in Section 3.3.2. In addition, advancements regarding RFI mitigation are implemented and are presented in Section 3.3.1. A single-pulse related analysis has not yet been

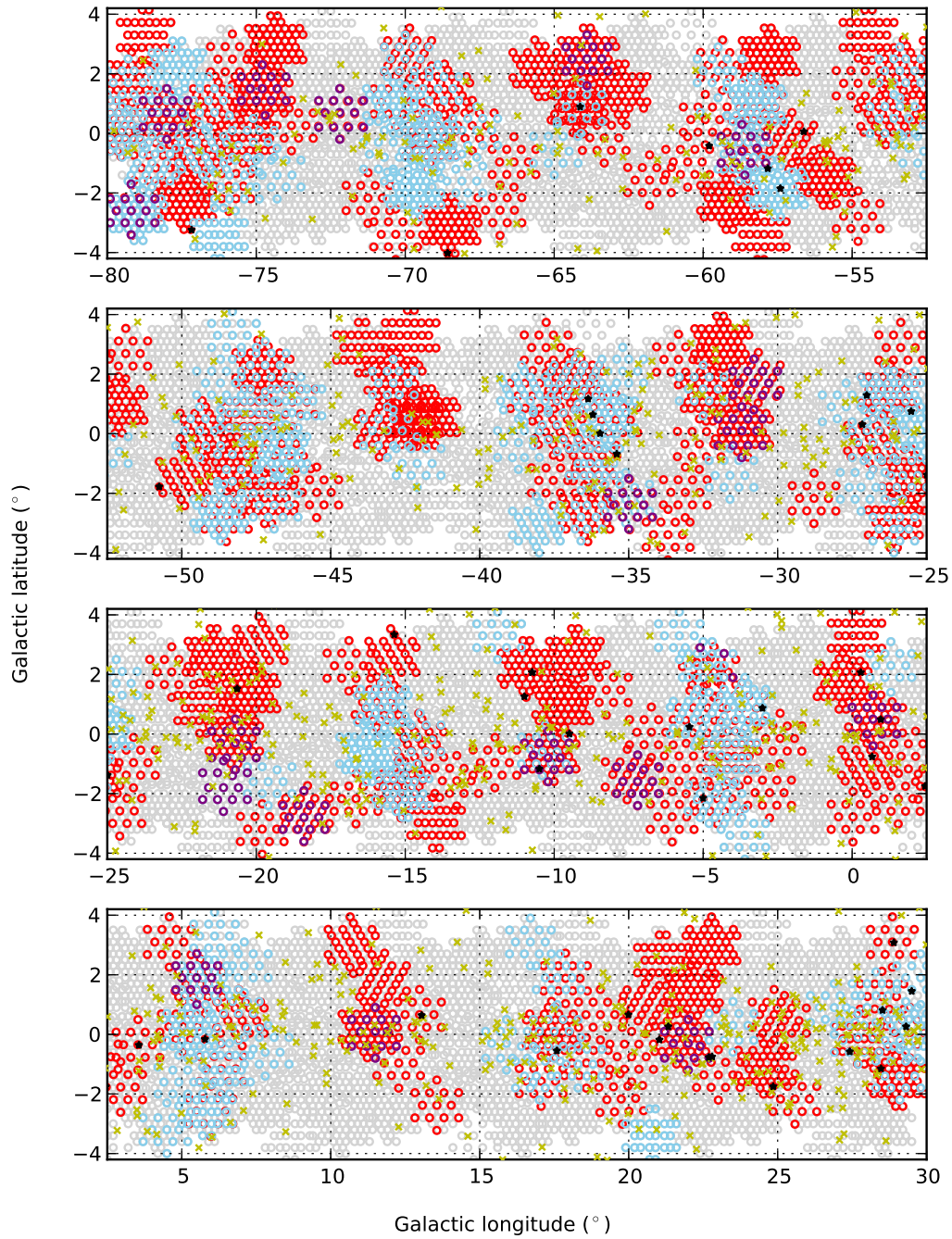


Figure 3.7: The spatial distribution of the processed observations from the HTRU Galactic plane survey. Grey circles denote the 1230 scheduled pointings. Blue circles denote pointings which have been processed with the ‘standard search’ pipeline, red circles with the ‘acceleration search’ pipeline, and purple circles with both pipelines. Yellow crosses are known pulsars and the black stars are the 47 new pulsars discovered thus far.

carried out and will be conducted in future data re-processing.

To date, 456 pointings of the Galactic plane survey have been processed which is 37 per cent of the survey. The spatial distribution of the processed data can be seen in Fig. 3.7. These processed pointings are not contiguous and only depend on availability of data at the location of the computing facilities. In Fig. 3.7, grey circles denote the 1230 pointings for the complete Galactic plane survey. Blue circles denote pointings which have been processed with the ‘standard search’ pipeline (amounting to 14.6 per cent of all pointings), whereas red circles are pointings which have been processed with the ‘partially-coherent segmented acceleration search’ pipeline (amounting to 23.5 per cent of all pointings). A small portion of 156 beams of observations have been processed with both pipelines to check for compatibility between the two algorithms and are represented by purple circles. Yellow crosses are published pulsars and the black stars are the 47 newly-discovered pulsars presented in this thesis.

3.3.1 RFI mitigation

Keith et al. (2010) described two RFI removal procedures employed as part of the HTRUN pipeline; removal of RFI-affected spectral channels in the frequency domain targeting narrow channel interference, and by replacing time samples contaminated by impulsive RFI with noise generated from random sampling of the uncontaminated surrounding data. Two extensions have been incorporated in the Galactic plane survey, both exploiting the fact that RFI is terrestrial hence usually non-dispersed (i.e., most prominent at $DM = 0 \text{ cm}^{-3} \text{ pc}$) and often appears in multiple receiver beams, in contrast to celestial sources which are point-like and tend to show up in only one beam, unless they are very bright.

3.3.1.1 Time domain

Since November 2010 an automated scheme to generate empirical time-domain RFI masks has been incorporated into the BPSR backend. This RFI mitigation algorithm has been developed from the work of Kocz et al. (2012). During each HTRU survey observation, non-dispersed (i.e., at $DM = 0 \text{ cm}^{-3} \text{ pc}$) time series are output every 10s from BPSR. Each of these 10-s time segments are auto- and then cross-correlated to form a covariance matrix and are subsequently decomposed into eigenvalues. We apply a threshold to identify RFI-affected time samples, namely a cut at 6σ for any signal that appears in more than four beams and a lower cut at 4σ if the signal is present in all 13 beams. These potentially contaminated time samples are recorded to a log file, which is stored together with the un-corrected observation. The RFI mask is not beam-specific, and can be applied to each corresponding pointing during subsequent off-line data processing to replace the bad time samples with random noise. Fig. 3.8 shows the statistics of the percentage of masked time samples per observation for the HTRU Galactic plane survey, which also serves as a measure of the quality of the survey data. Typically, for each observation, ~ 0.03 per cent of the time samples are flagged as RFI-affected, and no observation has > 2 per cent of masked time samples.

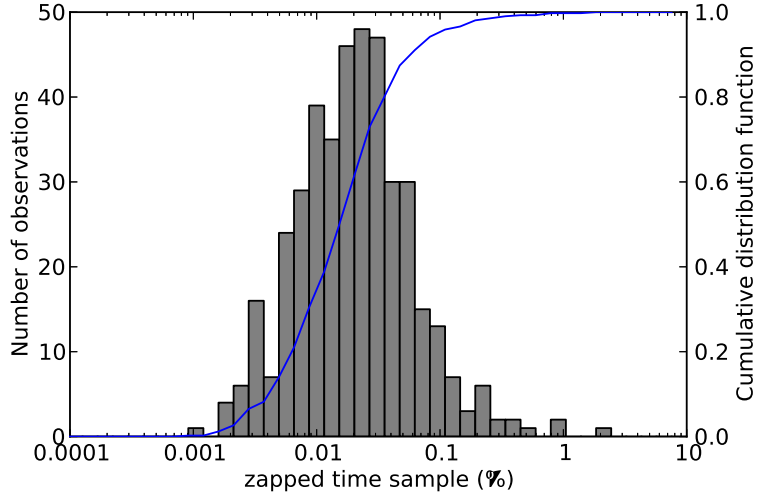


Figure 3.8: Histogram showing the statistics of the percentage of time samples removed per observation, as a result of the automatically generated RFI mask. (Statistics taken from 414 observations, i.e. 34 per cent of the survey)

For the observations taken before this implementation, we apply the time domain RFI mitigation technique as described in Section 4.1.1 of [Keith et al. \(2010\)](#).

3.3.1.2 Fourier domain

The presence of any periodic RFI is most readily identified in the Fourier domain. Nonetheless, great caution must be taken when flagging periodic RFI, to prevent accidentally masking a genuine pulsar signal which is also periodic. As part of the HITRUN pipeline, fixed periodic RFI lists have been applied to mask known RFI periodicities, such as that of the Australian mains power supply at ~ 50 Hz and its harmonics. However, the RFI environment is temporally varying and a fixed list is far from ideal. We have investigated a more robust method of empirically identifying periodicities. For each observation, we create the power spectrum of each of the 13 beams from their time series at $DM = 0 \text{ cm}^{-3} \text{ pc}$. A power threshold of $P_{\text{thres}} \approx 19$ can be calculated based on false-alarm probability as described in Section 2.1.2.6. We then compare the power spectrum Fourier bin by Fourier bin, identifying Fourier frequencies which exceed P_{thres} in more than four beams and flagging them as periodic RFI. Under this scheme, typically < 0.01 per cent of the Fourier spectrum is removed for each data set. This compares very favourably to the fixed periodic RFI list incorporated as part of the HITRUN pipeline, which contains Fourier frequencies associated with known RFI and always results in the removal of 0.57 per cent of the Fourier spectrum. Note that for the acceleration search algorithm as described in Section 3.3.2, as the time re-sampling at every acceleration trial would shift any RFI periodicities in the time series, one periodic RFI list per acceleration trial has to be created.

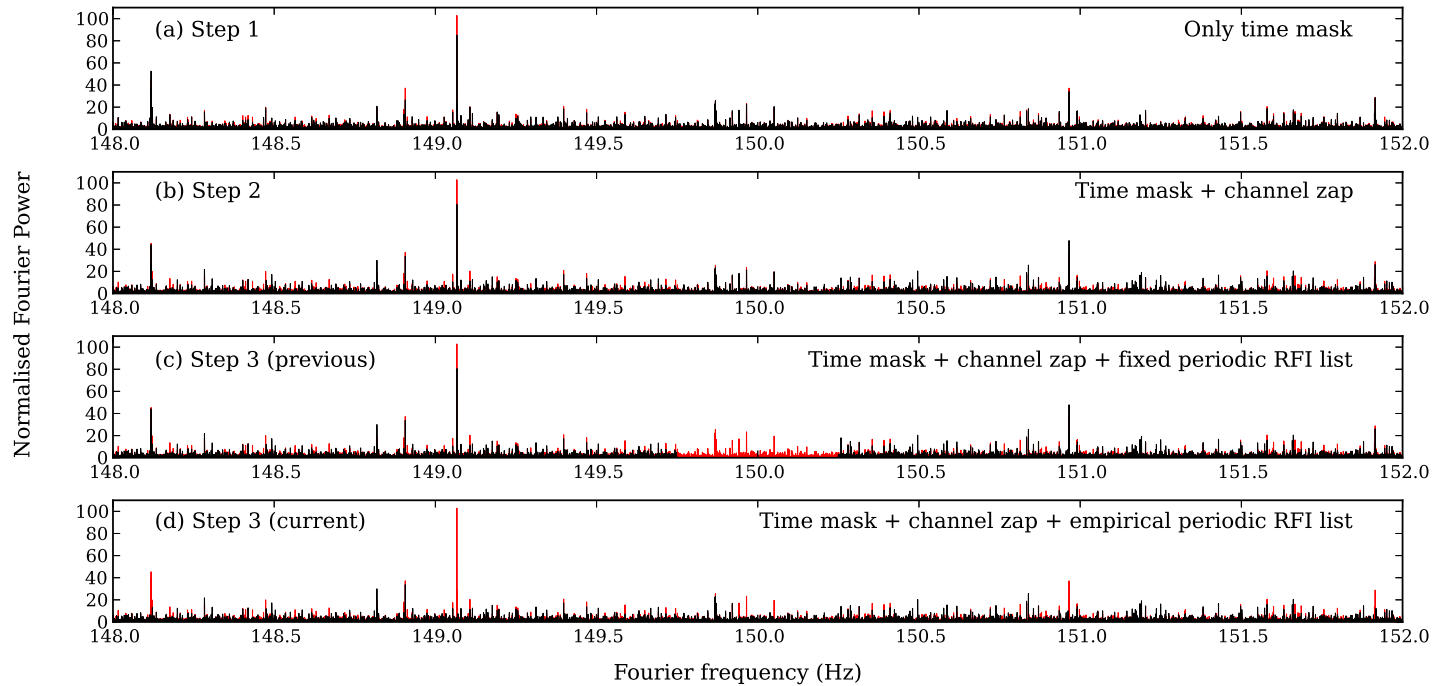


Figure 3.9: Comparison of the effectiveness in mitigating periodic RFI by applying varying extents of RFI cleaning. We show the power spectrum created from the time series at $DM = 0 \text{ cm}^{-3} \text{ pc}$ of an actual survey observation, zooming into the region around 150 Hz where RFI due to harmonics of the Australian mains power supply can be seen clearly. In each panel, the original uncleaned spectrum is plotted in red, whereas the spectrum after each RFI cleaning procedure is plotted in black. In this particular case, the empirically-generated periodic RFI list removed only 0.01 per cent of the Fourier spectral bins (panel (d)), but is still more effective than applying the fixed periodic RFI list which always removed 0.57 per cent of the spectrum (panel (c)). We note that subtle differences in the spectra are a result of the change in weighting due to normalisation.

Fig. 3.9 compares the effectiveness in mitigating periodic RFI by applying varying stages of the above-mentioned techniques on one of the survey observations. In all cases, the original uncleaned spectrum is plotted in red, and the spikes corresponding to harmonics of the Australian mains power supply at ~ 150 Hz can be clearly seen. Plotted in black are the spectra after each RFI cleaning procedure, and in theory no spike should remain, as there is no pulsar in this observation. In panel (a) only the time domain mask as described in Section 3.3.1.1 has been applied, which might have been effective for removing impulsive RFI but remains insensitive in the Fourier space. In panel (b) also the frequency channels with excessive power are removed as described in Section 4.1.1 of Keith et al. (2010), but the result is almost identical to the previous panel. In panel (c) we apply the fixed periodic RFI list incorporated as part of the HTRUN pipeline, which turns out to be masking a part of the spectrum that is relatively RFI-free, but is not able to identify some of the neighbouring narrow spikes. Finally, panel (d) shows the result of applying the empirically-determined multi-beam Fourier domain RFI mitigation method presented in Section 4.2. Occasionally a few RFI-related spikes (for example those at ~ 148.8 and 148.9 Hz), although appearing significant by eye inspection, are still missed out by this RFI mitigation technique, as they are present in less than our chosen conservative threshold of four beams. Nonetheless, most of the prominent spikes have been successfully identified and masked. Indeed, this technique has enabled several of the pulsar discoveries presented here, which from our retrospective checks show that they would not have been found otherwise.

3.3.2 Acceleration search

The challenges related to the searches for binary pulsars have been mentioned in Section 2.1.3. To maximise our detectability towards pulsars in binary systems, we employ the ‘time domain resampling’ technique as described in Section 2.1.3.1, in conjunction with the linear acceleration approximation. In the following we detail the implementation of such an acceleration search for the HTRU Galactic plane survey.

3.3.2.1 The ratio of data length over orbital period, r_{orb}

The linear acceleration approximation is equivalent to the best-fitting tangent to a quadratic $v(t)$ curve, and its effectiveness thus depends on the ratio of the integration length (t_{int}) to the orbital period of the pulsar (P_{orb}). Here we define this ratio to be r_{orb} , where

$$r_{\text{orb}} = \frac{t_{\text{int}}}{P_{\text{orb}}} = \frac{t_{\text{samp}} \times n_{\text{FFT}}}{P_{\text{orb}}}. \quad (3.2)$$

Note that t_{int} is the product of the time sampling rate, t_{samp} , and the number of samples used in the FFT, n_{FFT} . This number should be a power of two for maximum computational efficiency of the FFTs.

To quantify the effectiveness of this linear acceleration approximation versus varying r_{orb} , we employed two observations of the double pulsar system PSR J0737–3039A as test data sets. The double pulsar is the most relativistic pulsar binary system known, with very high maximum orbital acceleration of the order of 250 m s^{-2} and a

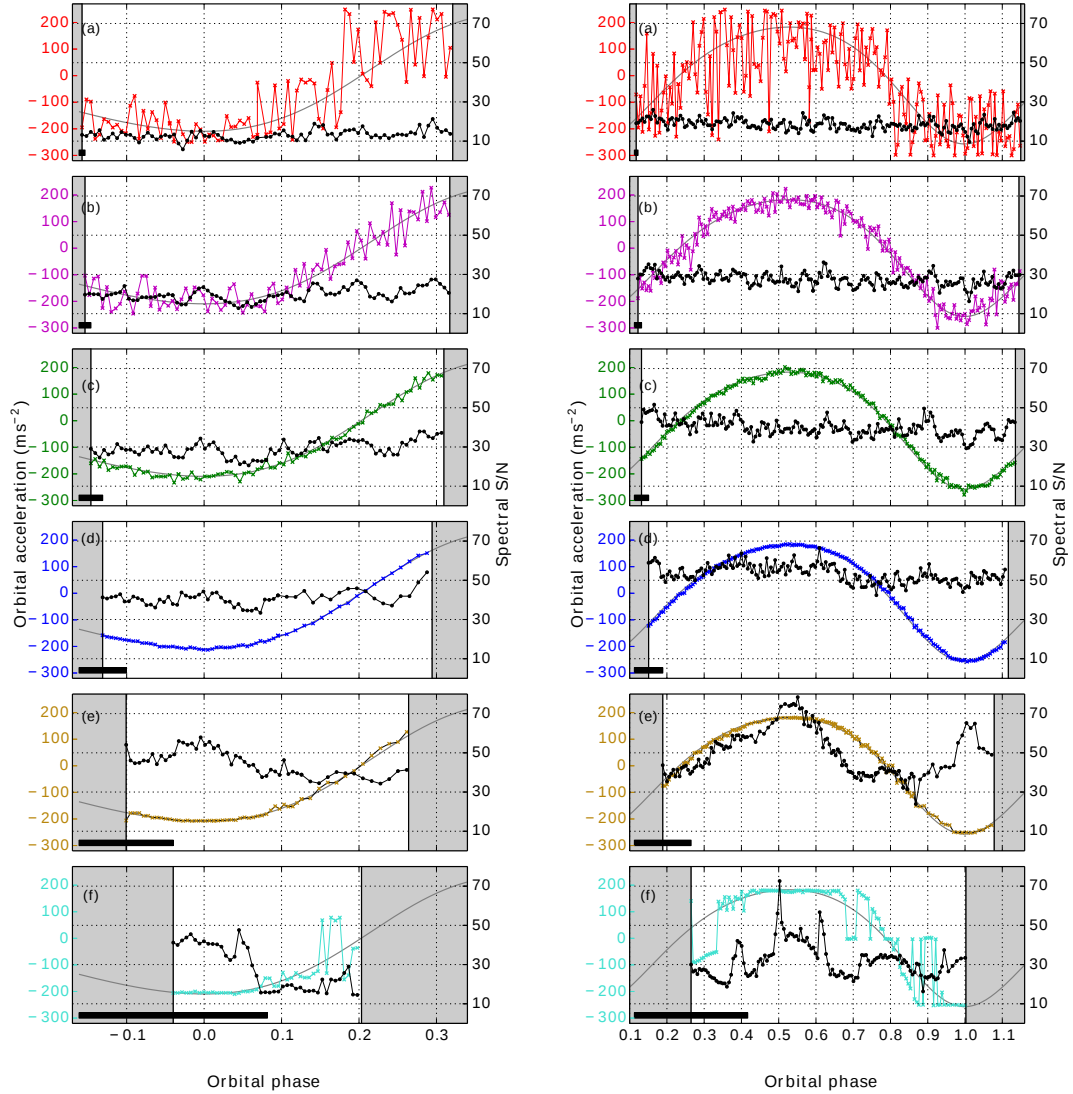


Figure 3.10: Detected orbital acceleration and S/N at various orbital phases of the double pulsar. Each panel corresponds to progressively longer values of r_{orb} . For test data set 1 (left column), we probe values of r_{orb} from (a) 0.0076, (b) 0.015, (c) 0.030, (d) 0.061, (e) 0.12 to (f) 0.24. For test data set 2 (right column), we probe values of r_{orb} from (a) 0.0095, (b) 0.019, (c) 0.038, (d) 0.076, (e) 0.15 and (f) 0.30. The black bar on the bottom left of each panel depicts the length of each segment to be searched coherently. We slide this search window across the test data sets incremented by every 50s, and we plot the acceleration search result at the middle of each segment. The recovered orbital acceleration values are plotted with colours, and the detected S/N is plotted in black. The smooth grey line shows the predicted acceleration curve.

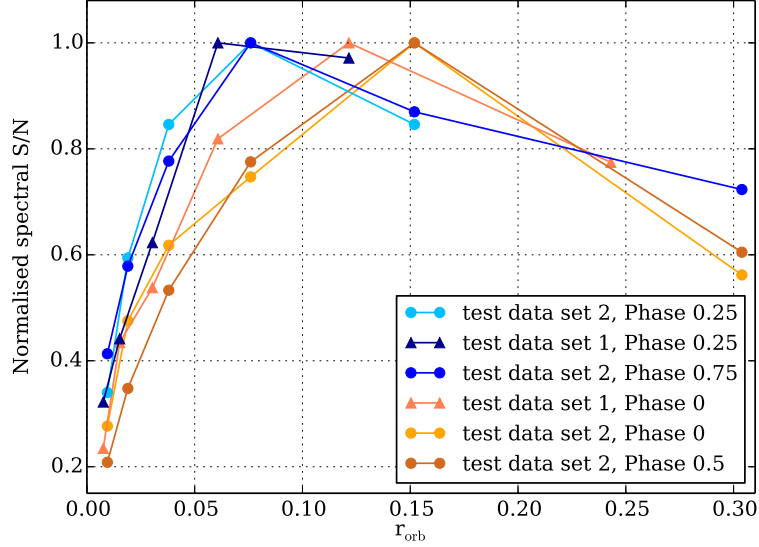


Figure 3.11: Detected S/N versus r_{orb} for the two test data sets (test data set 1: triangle symbol, test data set 2: circle symbol) at selected orbital phases. Phases 0.25 and 0.75 represent orbital phases where \dot{a} is largest. Phases 0 and 0.5 correspond to orbital phases where $\dot{a} \approx 0$.

short P_{orb} of 2.45 hr. The orbital eccentricity is reasonably small ($e = 0.088$), so it closely reproduces the simplest orbital motion; a sinusoidal $v(t)$ of a circular orbit. Two test observations of the double pulsar system were carried out at Parkes. One was collected with the same observational set-up as the HTRU Galactic plane survey, where $t_{\text{samp}} = 64 \mu\text{s}$ (hereafter test data set 1), and the other is identical to the test data set presented in Eatough et al. (2013b), where $t_{\text{samp}} = 80 \mu\text{s}$ (hereafter test data set 2). The two different t_{samp} allow different r_{orb} to be probed, as we segment the test data sets into increasingly shorter t_{int} , each with n_{FFT} of 2^k to allow for maximum computational efficiency of the FFTs, where $k = 25, 24, 23, 22, 21, 20$.

For each r_{orb} , we conduct a series of acceleration searches on a subset of the observation with the relevant length, incrementing at every 50 s across the observed orbital phase. In Fig. 3.10, we plot the detected spectral S/N of the double pulsar in black and the recovered orbital acceleration in other colours. The figures on the left and right correspond to the test data set 1 and 2 respectively. Panels (a) of both figures show the shortest r_{orb} for each respective test data set. From the red data points it can be seen that these short segments with small r_{orb} each contain only a tiny fraction of the orbital motion of the double pulsar. Hence the analyses are not very sensitive to the trial acceleration value, leading to large fluctuations in the recovered orbital acceleration which does not follow the predicted grey curve closely. Nonetheless, the double pulsar has been detected throughout the orbital phase with roughly consistent spectral S/N, an indication that the linear acceleration approximation has been equally effective irrespective of orbital phase. As the coherent segment length gets progressively longer,

as shown from panels (b) to (d), the acceleration searches become more successful in recovering the predicted orbital acceleration and the detected S/N also improves by roughly $\sqrt{2}$ as expected by the radiometer equation. Panels (e) represent yet longer values of r_{orb} which exceed 0.1. At phases 0, 1 and 0.5, where the orbital acceleration is closest to being constant (i.e., the acceleration derivative $\dot{a} \approx 0$), improvements in the detected S/N are still observed compared to the previous r_{orb} . However, the increase is less than $\sqrt{2}$, reflecting that the r_{orb} is now becoming too large resulting in spectral smearing which in turn reduces the detected spectral S/N, making the linear acceleration approximation less effective. At phases 0.25 and 0.75, where the orbital acceleration is increasing the most (i.e., a significant \dot{a}), the detected S/N is worse than the shorter r_{orb} . Finally, panels (f) show the longest r_{orb} where the degradation due to spectral smearing out-weighs the gain in S/N due to longer coherent segments, producing lower S/Ns at all orbital phases. The drastic drop in S/N immediately away from the orbital phases where $\dot{a} \approx 0$ is particularly noticeable.

Fig. 3.11 is a plot of the S/N of these selected orbital phases across varying r_{orb} . We note that the two test data sets employed are taken on different dates with different instrumental set-ups, it is thus not appropriate to compare their detected S/N directly. However, one can attempt a qualitative comparison by normalising the highest S/N of any particular orbital phase to unity. From the plot it can be seen that a r_{orb} of roughly 0.1 can be adopted as a general rule-of-thumb in order to allow for an effective linear acceleration approximation, with a tendency for the orbital phases with a significant \dot{a} to prefer shorter r_{orb} and vice versa for the orbital phases with an $\dot{a} \approx 0$. The introduction of eccentricity in the orbital motion will alter this picture. When the line of sight \dot{a} is significantly non-zero, we expect smaller r_{orb} to perform better (i.e., the peaks of these curves shift towards the left). Otherwise, in the less accelerated part of the eccentric orbit, slightly larger r_{orb} can result in a higher S/N. For a quantification of the detectability of eccentric binary pulsars see e.g. [Bagchi et al. \(2013\)](#).

3.3.2.2 Acceleration ranges

Assuming a circular orbit, we derive the theoretical maximum orbital acceleration (a_{max}) for a given P_{orb} by applying Kepler's third law. We consider the upper limit case by setting the orbital inclination to be edge on (i.e., $i = 90^\circ$):

$$|a_{\text{max}}| = \left(\frac{2\pi}{P_{\text{orb}}} \right)^2 xc = \left(\frac{2\pi}{P_{\text{orb}}} \right)^{4/3} (T_\odot f)^{1/3} c, \quad (3.3)$$

where $T_\odot = GM_\odot/c^3 = 4.925490947 \mu\text{s}$, x is the projected semi-major axis of the pulsar orbit and c is the speed of light. The mass function f is defined by

$$f = \frac{(m_c \sin i)^3}{(m_p + m_c)^2}, \quad (3.4)$$

where $\sin i = 1$ and the pulsar mass, m_p , is taken to be $1.4 M_\odot$. The companion mass, m_c , then remains the only variable. Fig. 3.12 shows the theoretical maximum orbital acceleration as a function of orbital period. We have plotted three scenarios

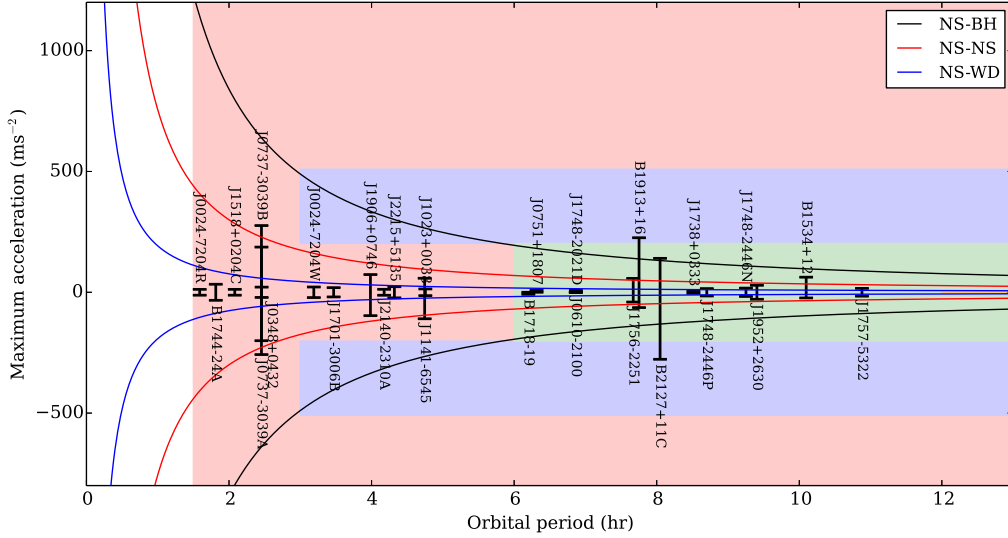


Figure 3.12: Maximum orbital acceleration versus orbital period assuming circular orbits for binary systems of NS-WD (blue line), NS-NS (red line) and NS-BH with a $10 M_{\odot}$ BH (black line). The maximum orbital acceleration for all published relativistic binaries are also shown as a reference. The coloured regions correspond to the parameter spaces probed by different segments as explained in Section 3.3.2.3.

corresponding to binary systems with a $0.2 M_{\odot}$ helium white dwarf companion (NS-WD), with a second $1.4 M_{\odot}$ neutron star companion (NS-NS) and with a hypothetical black hole companion of mass $10 M_{\odot}$ (NS-BH). We overplot all published relativistic pulsar binary systems with P_{orb} less than 12 hr and significant orbital acceleration reaching above $\pm 1 \text{ m s}^{-2}$ as a reference.

Based on Fig. 3.12, sensible acceleration ranges (Δa) can be determined for any particular orbital period. We note that the effect of orbital eccentricity has not been taken into account. Highly-eccentric relativistic binary systems can overshoot these theoretical curves of maximum acceleration significantly, in particular during the orbital phase of periastron. Notable examples in Fig. 3.12 are two NS-NS systems PSRs B1913+16 and B2127+11C with orbital eccentricities of 0.62 and 0.68 respectively. To determine the theoretical maximum acceleration while including eccentric systems would dramatically increase the acceleration search parameter space, making the data processing unfeasible given the current computing resources available. Fortunately, a simple consideration of the Kepler's third law shows that, these eccentric systems spend only a relatively brief moment during the highly-accelerated orbital phase near periastron, whereas the majority of their orbital phases are confined within the less accelerated regime. Therefore, we justify that our acceleration ranges remain a reasonable compromise given the computing resources available.

3.3.2.3 Partially-coherent segmentation

As established in Section 3.3.2.1, the linear acceleration approximation is most effective at $r_{\text{orb}} \approx 0.1$. Hence in order to remain sensitive to a wide range of binary orbits it is strategic to use different integration lengths. Taking this as a rule-of-thumb, the 4300 s full-length observation ($s = 1$) of the HTRU Galactic plane survey would enable us to detect binary systems with $P_{\text{orb}} \gtrsim 12$ hr. Halving the observation into two equal segments ($s = 2$) will correspond to binaries of $P_{\text{orb}} \gtrsim 6$ hr, quartered-length observation ($s = 4$) will correspond to $P_{\text{orb}} \gtrsim 3$ hr and segmenting our observation to one-eighth ($s = 8$) will correspond to $P_{\text{orb}} \gtrsim 1.5$ hr. We set aside binary systems with shorter P_{orb} for future re-processing. This is because given the long coherent integration length of this survey, such tight binaries should be most efficiently detected using the ‘phase modulation’ technique (Ransom et al., 2003) introduced in Section 2.1.3.2.

We search for binary systems using an acceleration range appropriate for the length of each segment, as discussed in Section 3.3.2.2. The maximum acceleration attainable from a $10 M_{\odot}$ NS-BH system is of the order of 1200 m s^{-2} with a P_{orb} of 1.5 hr, hence we have adopted this as the upper bound of our acceleration range for the shortest $s = 8$ segments. The corresponding parameter space probed is shown as the pink region in Fig. 3.12. In order to maximise our detectability towards a NS-BH binary, we additionally search a Δa between $\pm(200 - 500) \text{ m s}^{-2}$ with the $s = 4$ segments (providing sensitivity in the blue region), as well as a Δa between $\pm(1 - 200) \text{ m s}^{-2}$ with the $s = 2$ segments (providing sensitivity in the green region). For the full length $s = 1$ observation we search a Δa of $\pm 1 \text{ m s}^{-2}$, which should allow the detection of all mildly accelerated binary systems with large orbital periods of $P_{\text{orb}} \geq 12$ hr, as well as all isolated pulsar systems.

A schematic of the final pipeline is illustrated in Fig. 3.13. We call it the ‘partially-coherent segmented acceleration search’, as each segment is analysed coherently while across the segments the results are interpreted independently. We search the four configurations ($s = 1, 2, 4, 8$) in parallel, which is essentially equivalent to conducting a multiple pass survey. On one hand, an additional advantage of this partially-coherent scheme is that by independently analysing segments we are less susceptible to some epochs where the detection of the pulsar is more difficult, for instance at an orbital phase where \dot{a} is significantly non-zero in a highly-eccentric orbit, an intermittent pulsar in switching off phase or a scintillation induced reduction in S/N. On the other hand, we note that this scheme relies on the fact that any binary pulsar to be found has to be detectable in at least one of the shortened segments. To be able to coherently combine the acceleration search results across segments would allow us to exploit the full sensitivity achievable with the deep integration of this survey, detecting even the weakest relativistic binary systems. This is the primary goal of our future data re-processing.

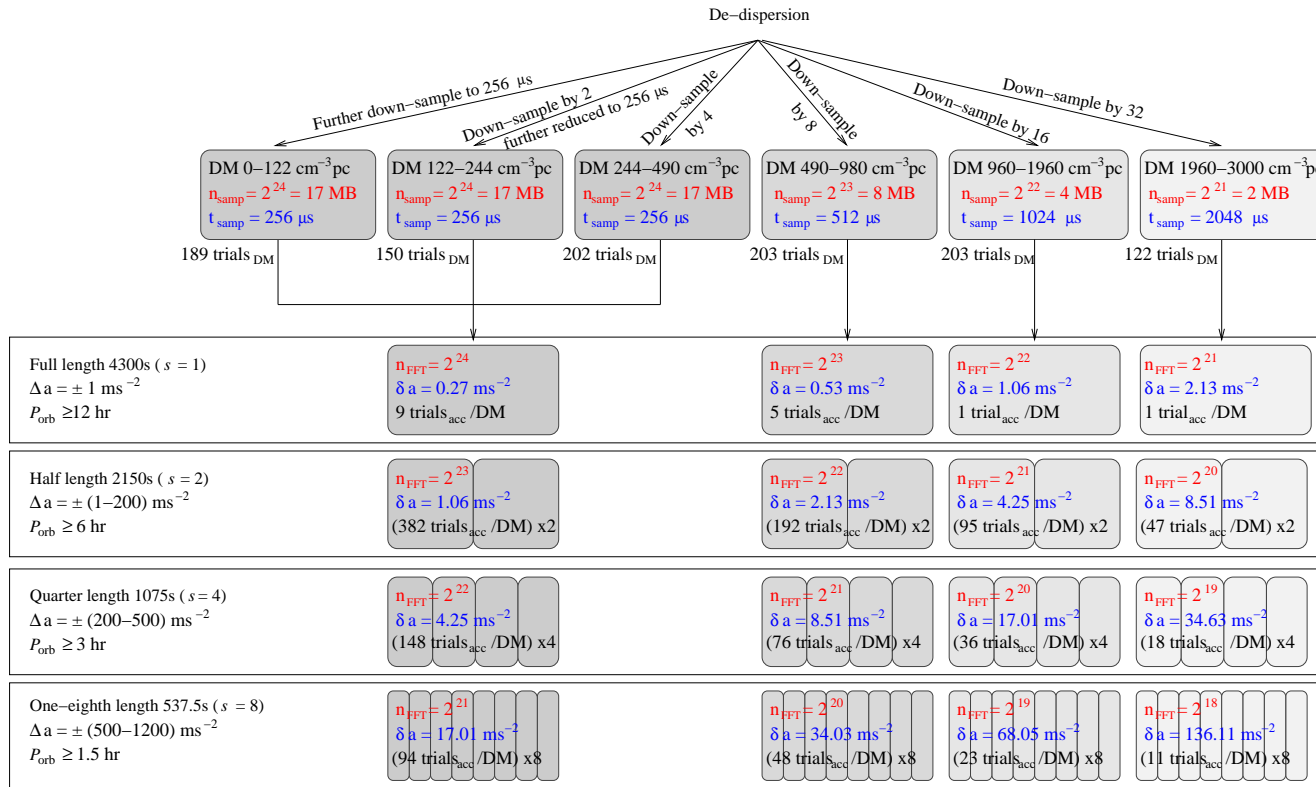


Figure 3.13: A schematic diagram for the ‘partially-coherent segmented’ pipeline adopted for this survey. As we progressively down-sample the observation after $2\times$ the diagonal DM ($\text{DM} = 122 \text{ cm}^{-3} \text{ pc}$; for a definition of the diagonal DM, see Section 2.1.2.2) is reached, we end up with six groups of DM ranges with different t_{samp} (illustrated by the colour density in this schematic) each with different number of DM trials ($\text{trials}_{\text{DM}}$). Each of the subsequent time series is then passed to the four lower panels (corresponding to the four configurations of $s = 1, 2, 4, 8$) to be Fourier transformed, where the number of samples used in each Fourier transform is marked as n_{FFT} . We show also the acceleration range, Δa , the acceleration step size, δa , as well as the resultant number of acceleration trials per DM, $\text{trials}_{\text{acc}}/\text{DM}$.

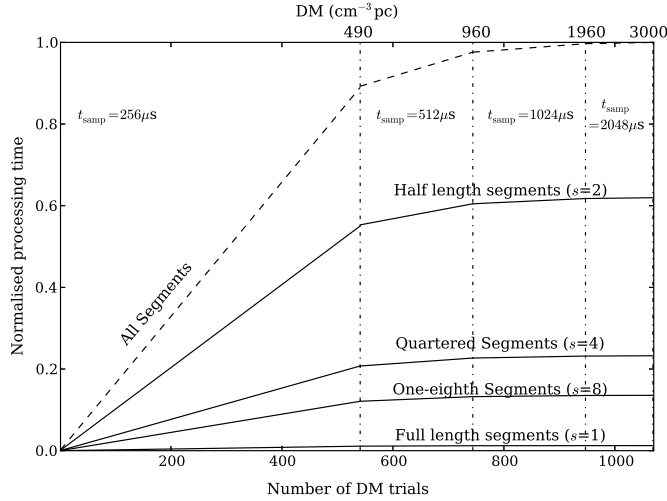


Figure 3.14: The relative processing time required for each of the four configurations ($s = 1, 2, 4, 8$) parallel searches, normalised by the total processing time of all segments together. We plot these curves as a function of the number of increasing DM trials, and we show the corresponding DM values. The relevant t_{samp} is also marked.

We adopt the same acceleration step size as described by Equation (3) of [Eatough et al. \(2013b\)](#). [Eatough et al. \(2013b\)](#) pointed out that pulsars with longer spin periods are less susceptible to a wrong acceleration trial (see Fig. 3 in their publication), and hence this acceleration step size is effectively slightly oversampling for these slow spinning binaries. In turn, the number of computational operations required for Fourier transforming each real time series, C_1 , can be quantified as

$$C_1 \propto \Delta a \times t_{\text{samp}} \times n_{\text{samp}}^3 \times \ln(n_{\text{samp}}). \quad (3.5)$$

Note that because we progressively down-sample in time after $2\times$ the diagonal DM is reached (see Section 2.1.2.2), t_{samp} does not take the same value across different DM values, as indicated in Fig. 3.13. Due to constraints of computational resources, we further down-sample all observations to a $t_{\text{samp}} \geq 256 \mu\text{s}$. This might reduce our detectability towards MSPs with spin periods ≤ 1 ms, but still compares favourable to the $t_{\text{samp}} = 1$ ms used in [Eatough et al. \(2013b\)](#).

The total computational operations required to Fourier transform for each data set, C_{tot} , then becomes

$$C_{\text{tot}} \propto \sum_{s=1,2,4,8}^S C_1 \times \text{trials}_{\text{DM}} \times s, \quad (3.6)$$

where $\text{trials}_{\text{DM}}$ is the number of DM trials and its value is indicated in Fig. 3.13. Summing the four configurations with segments of $s = 1, 2, 4, 8$, we have of the order of $C_{\text{tot}} \sim 1.8 \times 10^{24}$ operations. Such processing typically requires ~ 620 CPU core hour on a single Intel Xeon Sandy Bridge node computer, for the analysis of one beam of an observation. Fig. 3.14 illustrates the relative processing time needed for each of the four configurations as a function of the number of DM trials.

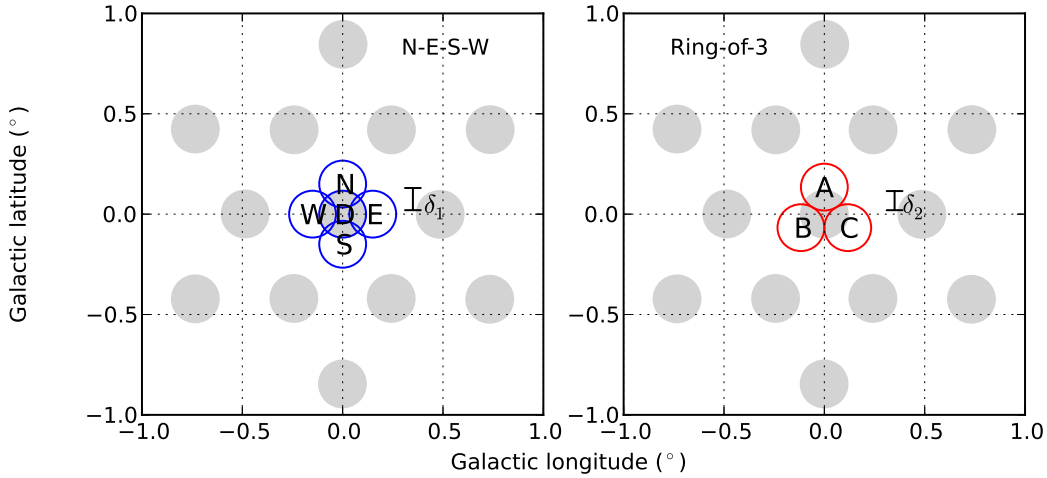


Figure 3.15: Illustration of the gridding configuration. The light grey circles indicate beam pattern of the 13-beam Multibeam receiver with a FWHM of $14'.4$. The left panel shows the gridding strategy as described in [Morris et al. \(2002\)](#) where five positions (‘N-E-S-W’ and the discovery position ‘D’) are required each offsetting the discovery position by $\delta_1 = 9'$. The right panel shows the ‘Ring-of-3’ configuration used in the gridding in this survey, where only three positions (A-B-C) are required each offsetting the discovery position by $\delta_2 = 2/\sqrt{3} \times \text{FWHM} \approx 8'.3$.

3.3.3 Candidate confirmation and gridding strategy

When a promising pulsar candidate is identified, it is necessary to conduct a confirmation observation at the telescope to verify if the candidate is a genuine pulsar. A successful re-detection confirms that the pulsar can be seen within the Gaussian beam of the receiver which has a FWHM of $14'.4$ at Parkes. However, a better localisation of the pulsar position is desirable. Pulsars north of declination -35° are followed-up with a timing campaign at the Lovell Telescope³ (see Section 4.2), which has a smaller FWHM of $12'$. In addition, an accurate position ensures efficient timing observations, as this maximises the S/N and hence reduces the telescope time required.

Major pulsar surveys at the Parkes telescope, such as the PMPS as well as the medium- and high-latitude parts of the HTRU, carried out a ‘N-E-S-W’ gridding strategy as described in [Morris et al. \(2002\)](#) for achieving a better positioning of any newly-discovered pulsar. In addition to one re-observation at the exact position of the discovery (D), a grid surrounding the discovery position is carried out. An offset of $\delta_1 = 9'$ is applied in each direction of North (N), East (E), South (S), West (W) from the discovery position. This offset has been chosen so that these four grids form a tight square pattern through the discovery position (Fig. 3.15 left panel). The Gaussian beam of

³In practice, for the declination between -30° and -35° , only bright pulsars are followed-up at the Lovell Telescope. This is because of the short visible hours, as well as the challenges associated with such low elevation observations, namely the need for low wind conditions and the potential high spillover.

the receiver would overlap enough between each grid position to ensure that the uncertainty of the pulsar position is less than a single beam width. The respective detected S/N from the ‘N-E-S-W’ pointings can then be used to estimate the true position of the pulsar.

The long integration length of the HTRU Galactic plane observations implies that, adopting this ‘N-E-S-W’ gridding scheme, a total of $72 \text{ min} \times 5 = 6 \text{ hr}$ would be needed to confirm each pulsar candidate which is highly inefficient. We hence employed an optimised strategy with a ‘Ring-of-3’ grid (Fig. 3.15 right panel) to minimise telescope time. Furthermore, the integration time for each confirmation observation is scaled down from the nominal discovery S/N to achieve an expected S/N of 10 in the confirmation. Archival data (including overlapping observations from the HTRU medium-latitude survey and the PMPS observations) are checked before any gridding is carried out, in order to improve *a priori* knowledge of the true position of the pulsar.

The low-latitude Galactic plane survey discoveries

This chapter, based on a publication in preparation (Ng et al., in prep), focuses on the discoveries from the HTRU low-latitude Galactic plane survey. From the 37 per cent of data processed thus far, we record 689 independent known pulsar re-detections from 348 pulsars. Furthermore, we discovered 47 pulsars, of which two are fast spinning pulsars with period less than 30 ms. PSR J1101–6424 is an MSP with a heavy WD companion and PSR J1757–27 is likely to be an isolated 17 ms pulsar. One other pulsar PSR J1847–0427 is likely to be an aligned rotator, and another pulsar PSR J1759–24 exhibits transient property that can be resulting from an intermittent pulsar, a long-orbit eclipsing binary or a magnetar. We compare this newly-discovered pulsar population to that previously known, and we suggest that our pulsar detection yield is as expected.

Contents

4.1	Re-detections of known pulsars	73
4.2	New pulsars	78
4.3	Individual pulsars of interest	84
4.3.1	PSR J1101–6424, a Case A Roche lobe overflow cousin of PSR J1614–2230	84
4.3.2	PSR J1759–24, an intermittent pulsar?	85
4.3.3	PSR J1757–27, likely to be a fast-spinning isolated pulsar?	87
4.3.4	PSR J1847–0427, a pulsar with an extremely wide pulse	87
4.4	Comparing with known pulsar population	88
4.4.1	Luminosity	88
4.4.2	Characteristic ages	89
4.4.3	Spin-down power and Fermi association	94
4.5	A comparison with the estimated survey yield	94

4.1 Re-detections of known pulsars

To verify that no previously known pulsar has been missed by the survey, we compute the expected S/N of every pulsar for any particular observation using the radiometer

equation as described in Equation (3.1). From PSRCAT we collect the spin periods, the pulse widths at 50 per cent of the highest peak, as well as the flux densities as observed at 1.4 GHz for all published pulsars. Note that we take into account the reduction in expected flux density, S_{exp} , compared to the catalogue flux density, S_{1400} , if the pulsar is offset from the beam centre, by

$$S_{\text{exp}} = S_{1400} \exp\left(-\frac{\theta^2}{2\sigma^2}\right), \quad (4.1)$$

where θ is the radial distance between the published pulsar position and the centre of the relevant beam. Assuming a Gaussian drop-off of beam sensitivity with a FWHM of $14'.4$, we define σ to be:

$$\sigma = \frac{\text{FWHM}}{2\sqrt{2\ln 2}} \approx 0.1^\circ. \quad (4.2)$$

The minimum detectable S/N is based on the false alarm statistics (see Section 2.1.2.6) and for this survey it is taken to be 9. Within the 37 per cent of processed HTRU Galactic plane observations, we record 689 independent known pulsar re-detections from 348 pulsars (see Appendix A1). Table 4.1 lists all previously-known binary pulsars re-detected thus far. Several known binary systems (namely PSRs J1525–5545 and J1807–2459A) which were undetected in our initial ‘standard search’ pipeline were later found from the ‘partially-coherent segmented acceleration search’ pipeline, and some other binaries have been detected with a much higher S/Ns (for example in the case of PSR J0737–3039A) from the acceleration search. These illustrate the importance of the acceleration search algorithm, allowing us to detect fast binary systems which we would be insensitive to otherwise.

Fig. 4.1 plots the observed S/N_{obs} versus the expected (S/N_{exp}) calculated from Equation (3.1) for the known pulsar re-detections. Out of the 689 re-detections, 204 lie outside the $14'.4$ FWHM of the receiver beam. Note that the sensitivity of the telescope outside the FWHM of the primary beam is complicated by its sidelobe pattern and is not well quantified. Hence these 204 re-detections are disregarded for the purpose of S/N comparison. Another five detections come from known pulsars with no published catalogue flux density. They are therefore not included in Fig. 4.1. The black points in Fig. 4.1 denote the remaining 480 known pulsar re-detections within the FWHM. It can be seen that the correlation between S/N_{exp} and S/N_{obs} is very good. Most of the data points lie close to the line of 1:1, implying the wider Δf and the longer t_{int} of the HTRU survey has provided the increased sensitivity expected.

Keith et al. (2010) have pointed out that, data points below the 1:1 correlation could be influenced by the bias resulting from the tendency to publish the discovery observation which is more likely to have the highest S/N due to scintillation, leading to the higher catalogue flux densities. Despite, a few re-detections are significantly worse than expected and lie below the 99 per cent lower boundary. They are likely to be due to scintillation and/or contamination by RFI. In the case of the very bright pulsars on the top right-hand corner of Fig. 4.1, the loss in survey sensitivity might be a consequence of the 2-bit digitisation. This is however not a problem for our purpose here.

Table 4.1: Previously-known binary pulsars re-detected in the 37 per cent processed data of the HTRU Galactic plane survey, sorted by with their respective catalogue orbital periods ($P_{\text{orb,cat}}$) in descending order. We list the relevant observation where these binaries were detected, as well as the detected spin period (P_{obs}) and the DM of the pulsar. We compare the detected S/N from the ‘standard’ (i.e., no acceleration search) pipeline with those from the full-length, half-length, quartered-length and one-eighth length segments of the ‘partially-coherent segmented acceleration search’ pipeline described in Section 3.3.2.3. The corresponding detected orbital acceleration (a_{orb}) from these acceleration searches are also listed. Note that in some cases, only one of the two pipelines has been employed, hence the non-applicable columns are denoted by ‘-’. If the data were processed but the pulsar was not detected, it is represented by ‘X’.

PSR name	$P_{\text{orb,cat}}$ (hr)	File ID (Pointing/beam)	P_{obs} (ms)	DM_{obs} (cm^{-3}pc)	‘Standard’	Full-length		Half-length		$1/4$ -length		$1/8$ -length	
					S/N	S/N	a_{orb} (m s^{-2})	S/N	a_{orb} (m s^{-2})	S/N	a_{orb} (m s^{-2})	S/N	a_{orb} (m s^{-2})
B1259–63	29681.4	2011-12-05-18:51:30/04	47.763	147.2	63.5	62.7	0.0	58.9	0.03	15.3	202.1	48.0	–6.6
J1711–4322	22139.3	2011-04-24-13:15:17/08	102.618	191.9	18.0	17.6	0.06	11.8	–1.0	X	X	X	X
B1820–11	8586.3	2012-08-07-08:52:51/12	279.837	425.6	–	47.9	0.9	44.7	–2.1	26.2	202.1	34.0	44.5
J1708–3506	3579.2	2011-07-07-09:57:10/03	4.505	146.7	29.6	–	–	–	–	–	–	–	–
J1810–2005	360.3	2011-06-26-12:10:21/09	32.822	238.8	9.1	8.9	0.6	X	X	X	X	X	X
J1753–2240	327.3	2011-05-05-18:50:26/02	95.135	155.3	18.5	–	–	–	–	–	–	–	–
J1454–5846	298.2	2013-01-02-19:24:06/05	45.249	116.8	–	25.5	0.06	19.9	1.0	X	X	X	X
J1543–5149	193.5	2011-07-04-07:23:31/07	2.057	51.1	14.8	12.9	–0.2	9.7	0.03	X	X	X	X
J1232–6501	44.7	2011-04-23-08:08:01/01	88.282	240.0	36.5	39.3	0.9	31.6	1.0	8.9	308.5	17.4	27.4
J1525–5545	23.8	2011-04-19-16:41:28/11	11.360	126.8	X	24.0	–1.0	32.4	–1.0	X	X	17.7	–6.6
B1913+16 [†]	7.8	2010-12-30-03:53:30/01	59.013	169.1	38.7	39.7	–1.0	36.5	–2.1	9.2	–224.2	21.7	–6.6
J0737–3039A [†]	2.5	2010-12-30-17:11:35/01	22.674	47.9	14.1	14.1	0.0	32.0	–198.9	38.2	–207.1	38.0	163.6
J1807–2459A	1.7	2011-05-08-15:24:15/04	3.059	134.3	X	X	X	19.2	–3.2	X	X	14.2	–6.6

[†] PSRs B1913+16 and J0737–3039A are technically not within the HTRU Galactic plane survey region. However, these two binaries are highly relativistic and were observed as test pulsars at the beginning of the survey. The detected parameters are listed in this table, but they are not counted towards the 348 known pulsars re-detection and are not listed in Appendix A1.

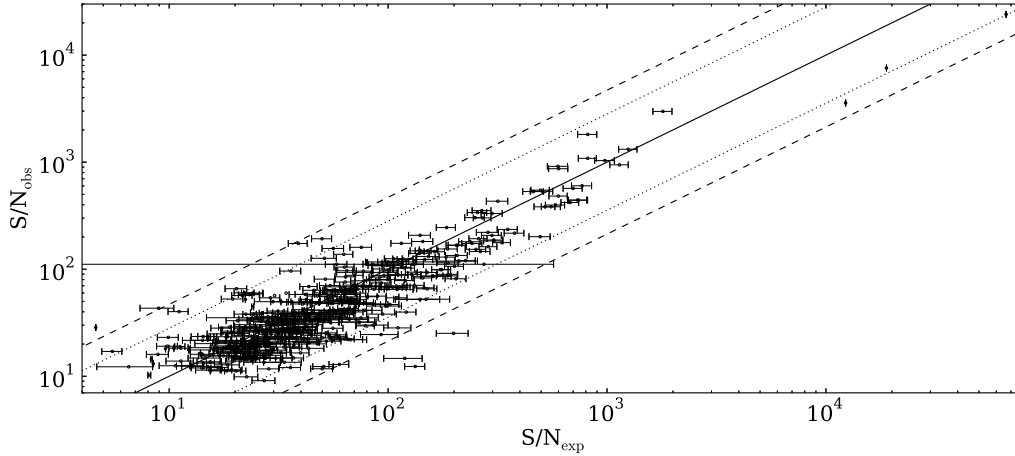


Figure 4.1: A comparison of the observed S/Ns of known pulsar re-detections with their predicted values. The solid line shows the expected 1:1 correlation. The dotted and the dashed lines mark the region containing 95 and 99 per cent of the data points. The errors shown are from the published error in the pulsar flux density from PSRCAT.

Out of all the expected known pulsar re-detections, 10 have been missed in the data processing and are listed in Table 4.2. Folding the observation directly with the catalogue pulsar ephemerides resulted in the recovery of three pulsars with only weak S/Ns (listed as S/N_{eph} in Table 4.2). Among the missed re-detections, one is attributed to the magnetar PSR J1622–4950. This magnetar is being followed up by an on-going HTRU timing programme. However, its radio emission appears to have ceased since October 2010, which is consistent with the non-detection of the HTRU Galactic plane survey observation taken in December 2010. The radio emission of magnetars are known to fade with time, hence we have likely observed the end of the radio emission of PSR J1622–4950. Another three are related to a transient anomalous X-ray pulsar (AXP), probably in a radio quiet state. A further two are associated with pulsars with known intermittency and we might have observed them at a time when they were not emitting. PSR J1746–2849 is known to have a very broad profile and the fact that it is within 1° from Sgr A* explains its significant scattering time scale of $\tau_{\text{sc},1.4\text{GHz}} > 226$ ms, potentially preventing it from being detected in our survey.

The remaining three pulsars with unexpectedly less S/N are PSRs J1644–46, J1644–4657 and J1746–2850. Their relatively high DMs imply that scintillation is unlikely to have an influence on the detectability. It is not clear whether this is a result of an over-estimation in their catalogue flux densities or if some unknown phenomena such as nulling has occurred intrinsic to the pulsar. We note that for PSRs J1644–46, the published declination is not yet well-determined (E. Keane; private communication) and no pulse width is published hence a duty cycle of 50 per cent has been assumed here. This means that the actual S/N_{exp} might be lower if the true offset between the pulsar and the observed position is larger or if the pulse width is larger than 50 per cent. For PSR J1746–2850, other observers have also failed in re-detecting any emission from other telescopes (G. Desvignes, P. Lazarus; private communication).

Table 4.2: Previously known pulsars with an $S/N_{\text{exp}} > 9$ that have been missed in the 37 per cent processed observations of the HTRU Galactic plane survey. We list the file ID of the closest HTRU observation together with the positional offset from the catalogue pulsar position. The catalogue spin period and DM of the missed pulsars are also shown, together with the expected S/N (S/N_{exp}) as well as the recovered S/N when folding observation with catalogue ephemerides (S/N_{eph}).

PSR name	Observation ID (Pointing/Beam)	offset ($^{\circ}$)	P (s)	DM ($\text{cm}^{-3} \text{pc}$)	S/N_{exp}	S/N_{eph}	Comments
J1644–44	2011-07-03-10:59:47/11	0.047	0.173911	535.1	10.0 [†]	13.1	Weak, published declination not well-determined. (Knispel et al., 2013)
B1809–176	2013-01-01-00:04:30/02	0.22	0.538341	518.0	24.1	8.2	Weak, offset relatively large and close to FWHM of receiver beam.
J1622–4950	2010-12-29-03:31:28/08	0.19	4.326100	820.0	20.2 [†]	–	Radio magnetar (Levin et al., 2010)
J1809–1943	2011-05-17-17:28:45/10	0.21	5.540354	178.0	88.4	–	AXP XTE J1810–197 (Camilo et al., 2006)
	2011-06-26-12:10:21/03	0.22			78.1	–	
	2011-07-02-12:25:09/02	0.14			330.1	–	
J1634–5107	2011-05-07-19:53:44/13	0.07	0.507356	372.8	46.4	–	Known intermittency (O’Brien et al., 2006)
J1726–31	2011-05-08-17:04:49/03	0.042	0.123470	264.4	12.2	–	Known intermittency, detection probability 20% (Knispel et al., 2013), published declination not well-determined.
J1746–2849	2011-06-26-10:07:53/08	0.10	1.478480	1456.0	20.5	–	Very broad profile, $\tau_{\text{sc},1.4 \text{ GHz}} > 226 \text{ ms}$ (Deneva et al., 2009)
J1746–2850	2011-06-26-10:07:53/08	0.12	1.077101	962.7	32.2	–	Discovered by Deneva et al. (2009) with $S_{1500} = 0.8 \text{ mJy}$
J1644–46	2011-05-17-13:02:58/02	0.044	0.250941	405.8	24.1 [†]	8.3	Discovered by Knispel et al. (2013) with $S_{1400} = 0.8 \text{ mJy}$, published declination not well-determined.
J1644–4657	2011-05-17-13:02:58/08	0.098	0.125962	718.0	14.7	–	Discovered by Eatough et al. (2013b) with $S_{1400} = 0.6 \text{ mJy}$

[†] For pulsars with no published pulse width, a duty cycle of 50 per cent is assumed when calculating the S/N_{exp} from the expected flux density.

In conclusion, excluding the magnetar, the AXP and the intermittent pulsars, only ~ 1 per cent of the published pulsars expected have been missed and the large number of re-detections indicate that the HTRU Galactic plane survey is performing as expected with little loss of sensitivity.

4.2 New pulsars

A total of 47 pulsars have been discovered in the 37 per cent processed data of the Galactic Plane survey. Listed in Table 4.3 are their folded signal-to-noise ratios (S/N_{HTRU}) at discovery. The PMPS has a complete overlap in the region of sky with the HTRU Galactic plane survey. We have inspected the PMPS archival data to determine if any of the newly-discovered pulsars were detectable in these PMPS observations and listed the folded S/N_{PMPS} in column 3 of Table 4.3. Fourteen pulsars have S/N_{PMPS} greater than the theoretical detection threshold of $S/N_{\text{min,PMPS}} = 8$ which means they could have been discovered in the PMPS. They might have been missed due to the large number of candidates produced in the PMPS processing. Improvements in the RFI mitigation scheme of the current HTRU processing as mentioned in Section 3.3.1 have likely helped avoiding such candidate confusion, enabling the detection of these pulsars. A further 10 pulsars have weak detections from the PMPS data, with S/N_{PMPS} less than 8. In the cases when only tentative detections are suggestive we have listed an upper limit for their S/N_{PMPS} in Table 4.3. These pulsars might have been missed in the PMPS processing as their low S/Ns might have prevented them from being selected for visual inspection. The remaining 23 pulsars are not detectable from the PMPS archival data.

Full flux density calibration is implemented for 20 pulsars with observations taken with the Parkes Digital Filter bank systems (DFB). We calibrate each observation by using an averaged observation of Hydra A, and we account for the differential gain and phase between the feed with an observation of the noise diode coupled to the feeds. Column 4 of Table 4.3 reports the mean flux densities averaging over all available timing observations for each pulsars at 1.4 GHz, S_{1400} . In turn, we infer the luminosity at 1.4 GHz, $L_{1400} = S_{1400} \times d^2$, where d is the distance of the pulsar in kpc. We derive distances in accordance to the NE2001 electron density model (Cordes & Lazio, 2002) and they can be found in column 9 of Table 4.4.

Also listed in column 5 and 6 of Table 4.3 are the pulse widths measured at 50 (W_{50}) and 10 (W_{10}) per cent of the highest peak. The pulse profiles of each pulsar at 1.4 GHz is shown in Fig. 4.2. For the pulsars with coherent timing solutions, we summed all observations to form high S/N mean profiles. Otherwise, we plot the profiles from the single observation at discovery. The peak of the profiles have been normalised to unity and their peaks placed at phase 0.2. Most of the long-period normal pulsars have typical pulse profiles (Lyne & Graham-Smith, 2005), with single-peaked pulses and a duty cycle of $\delta < 10$ per cent. One of the 47 newly-discovered pulsars, PSR J1847–0427, shows a broad pulse profile with a hint of an interpulse and is further discussed in Section 4.3.4. These results are entirely consistent with the

findings of [Weltevrede et al. \(2010\)](#), that ~ 2 per cent of the known pulsar population is observed with an interpulse. A few of the pulsars with high DM display the classical exponential tail of scattering caused by propagation of the radio signal through the ISM, as introduced in Section 1.3.2.

When a pulsar is first discovered, our knowledge of its sky position, rotation period and DM are only approximate. Follow up timing observations of at least 1 yr are necessary to precisely determine its rotational, astrometric and, if any, orbital parameters. A more thorough explanation of the technique of pulsar timing can be found in Section 5.1. In essence, each timing observation is summed over both frequency and time to produce an integrated pulse profile. The PSRCHIVE data analysis package ([Hotan et al., 2004](#)) is used to convolve a noise-free analytic reference template with each individual profile to produce a time of arrival (TOA; [Taylor, 1992](#)). The TEMPO2 software package ([Hobbs et al., 2006](#)) is then employed to fit a timing model to all TOAs of the pulsar.

All observations presented here have been taken at 1.4 GHz at Parkes using backends including the DFBs and the ATNF Parkes Swinburne Recorder¹ (APSR) with coherent dedispersion. Pulsars with declination above -35° ² were timed at the Jodrell Bank Observatory with the Lovell 76-m telescope, using a DFB backend and a ROACH³ backend with coherent dedispersion. Refer to Table 5.1 for the specifications of all observing systems employed. Timing observations at Jodrell Bank were performed approximately once every three weeks, whereas Parkes observations are more irregular with gaps ranging from days to months depending on telescope availability. At both telescopes, integration times of at least 30 min are typically required, with longer observations for weaker pulsars to achieve adequate S/N of at least 10.

Twenty-two of the most recent discoveries have not yet been allocated sufficient follow-up telescope time, but will be monitored in the coming months. For these pulsars we have reported their discovery parameters in Table 4.4. Table 4.5 presents the remaining 25 newly-discovered pulsars from the Galactic plane survey with coherent timing solutions, listing their pulsar names, their J2000 equatorial coordinates in right ascension (RA) and declination (Dec.), as well as the corresponding Galactic coordinates in longitude (l) and latitude (b). Columns 6 and 7 report the spin periods (P) and its first derivative (\dot{P}) when available. Columns 8 and 9 report the DMs and the DM-derived distances based on the NE2001 electron density model ([Cordes & Lazio, 2002](#)). Columns 10 to 14 report fitting related parameters, including the data span of the timing data, the reference epoch used, the number of TOAs (N) employed in the model fitting, the residual (RMS) and the reduced χ^2 of the model fit. Columns 15 to 17 report derived parameters of the pulsar, including the characteristics age (τ_c), the surface magnetic field (B_{surf}) and the spin-down energy (\dot{E}). The equations for these derivations can be found in Chapter 1. Pulsars for which no full timing solution is available have been assigned a temporary name containing only two digits of declination.

¹<http://astronomy.swin.edu.au/pulsar/?topic=apsr>

²See footnote in Section 3.3.3.

³Based on the ROACH FPGA processing board, see <https://casper.berkeley.edu/wiki/ROACH>

Table 4.3: Table listing the S/N, flux density (S_{1400}), derived luminosity (L_{1400}) and pulse widths (W_{50}, W_{10}) of the 47 newly-discovered pulsars.

PSR name	S/N _{HTRU}	S/N _{PMPS}	S_{1400} (mJy)	W_{50} (ms)	W_{10} (ms)	L_{1400} (mJy kpc ²)
J1002–59	18	7.7	0.17	61	69	12.6
J1101–6424	20	–	0.27	0.54	1.39	5.4
J1152–61	10	–	–	5.65	9.89	–
J1227–63	19	–	–	15.0	34.4	–
J1244–64	13	–	–	13.8	15.2	–
J1247–6443	13	< 6.4	0.15	54.3	78.5	3.3
J1255–62	14	–	0.13	34.8	65.0	21.8
J1349–63	17	9.7	–	23.0	49.7	–
J1525–5523	13	10.5	0.21	31.0	40.9	1.2
J1528–5545	14	–	0.07	52.9	110	1.3
J1532–5606	12	9.7	0.10	27.0	54.0	1.8
J1539–56	23	15.7	0.14	34.1	60.6	1.3
J1612–49	13	–	0.16	28.7	73.1	10.4
J1616–50	22	–	–	9.76	20.5	–
J1621–48	12	–	0.15	17.5	42.3	3.2
J1633–49	14	8.5	0.13	43.5	62.5	10.5
J1638–44	16	–	0.15	31.6	50.6	6.8
J1649–39	17	9.6	0.05	56.6	71.9	1.6
J1708–36	13	< 6.5	0.12	29.2	57.2	2.7
J1711–37	13	< 7.7	–	61.4	105	–
J1720–36	15	–	–	8.41	10.8	–
J1722–38	14	10.6	0.08	13.7	35.0	2.8
J1731–33	10	< 6	0.10	33.5	71.4	12.5
J1732–35	11	–	0.13	3.77	10.3	3.3
J1734–3058	21	9.3	0.11	10.7	22.6	1.6
J1738–2736	26	9.5	0.17	13.7	23.7	4.4
J1741–34	12	–	–	19.1	43.4	–
J1746–27	9	–	–	29.9	42.6	–
J1750–28	12	–	–	16.8	35.1	–
J1755–26	16	–	–	16.3	25.7	–
J1757–27	15	–	–	0.492	0.878	–
J1759–24	29	–	–	72.3	159	–
J1811–17	14	< 5.8	–	38.8	59.0	–
J1824–1350	15	–	0.08	19.4	58.2	6.6
J1825–11	18	7.5	–	42.1	68.8	–
J1829–10	20	9.3	–	98.8	125	–
J1830–10	10	< 7.3	–	5.36	12.7	–
J1833–0209	12	< 6.8	–	17.4	30.7	–
J1835–0924b	13	–	–	27.1	45.3	–
J1835–0928	11	–	–	39.5	64.2	–
J1838–0107	27	9.7	–	34.4	45.0	–
J1839–0223	11	8.3	–	45.3	67.9	–
J1839–0332	20	12.7	–	31.9	63.7	–
J1842–0800	10	9.9	–	24.9	52.3	–
J1844–0302	14	–	–	19.0	33.3	–
J1843–0510	12	7.5	–	24.0	36.0	–
J1847–0427	11	–	–	30.9	48.4	–

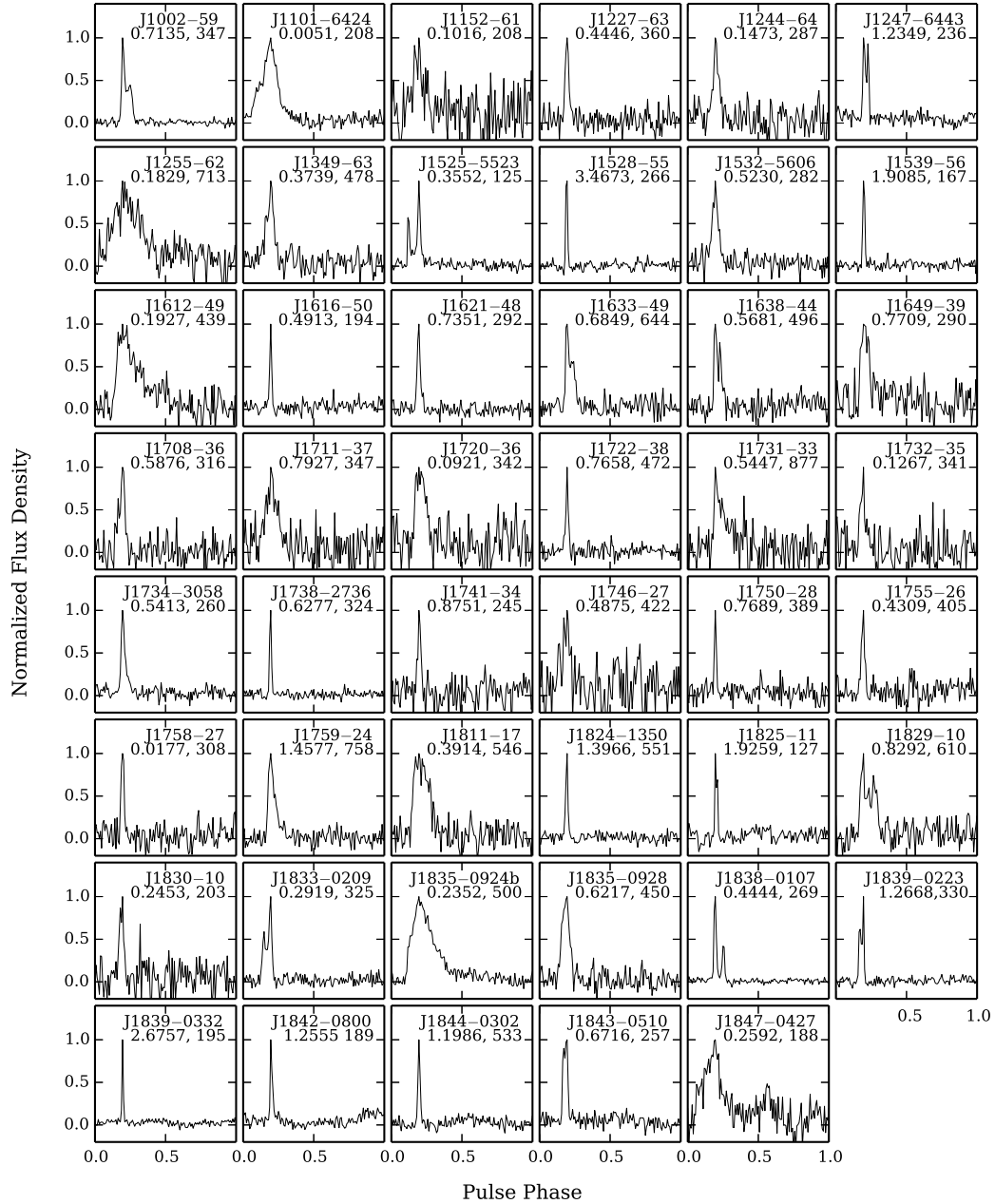


Figure 4.2: Average pulse profile of the 47 newly-discovered pulsars, plotted by placing the peak at phase 0.2. The normalised flux densities are calibrated for the 20 pulsars with Parkes DFB data whereas the rest are not calibrated. Also marked on each profile is the respective pulsar names, the spin period in s and the DM in $\text{cm}^{-3} \text{pc}$.

Table 4.4: Discovery parameters of 22 newly-discovered pulsars from the HTRU Galactic plane survey, which have not yet enough TOAs to produce a coherent timing solution. All of these pulsars have been assigned a temporary name containing only two digits of declination. We list the Galactic latitude (l) and longitude (b), the spin period (P) and the DM of these pulsars. Values in parentheses are the nominal 1σ uncertainties in the last digits. The distances are derived according to Cordes & Lazio (2002).

PSR name	R.A. (J2000) (^h ^m ^s)	Dec. (J2000) ([°] ['] ^{''})	l ([°])	b ([°])	P (ms)	DM (cm^{-3}pc)	Dist (kpc)
J1152–61	11:52.3(5)	–61:10(7)	295.87	0.89	101.63400389(6)	216(1)	4.2
J1227–63	12:27.2(5)	–63:09(7)	300.20	–0.42	444.57796(6)	359(4)	8.4
J1244–64	12:44.4(5)	–64:02(7)	302.17	–1.18	147.274(3)	286(1)	5.6
J1255–62	12:55.3(5)	–62:48(7)	303.38	0.06	182.91151711(13)	713(4)	13.2
J1349–63	13:49.3(5)	–63:56(7)	309.24	–1.78	373.0340(1)	478(3)	9.6
J1539–56	15:39.0(5)	–56:21(7)	324.60	–0.68	1908.4949587(2)	150(18)	3.0
J1612–49	16:12.9(5)	–49:27(7)	332.99	1.29	192.68718815(7)	439(5)	7.9
J1616–50	16:16.5(5)	–50:16(7)	332.84	0.31	491.27729(13)	194(4)	4.7
J1621–48	16:21.7(5)	–48:48(7)	334.48	0.75	735.0916287(9)	292(7)	4.6
J1633–49	16:33.5(5)	–49:53(7)	335.01	–1.38	684.936422(4)	649(12)	8.8
J1638–44	16:38.1(5)	–44:43(7)	339.36	1.52	568.0566300(6)	494(5)	6.7
J1649–39	16:49.3(5)	–39:33(7)	344.63	3.34	770.85653(7)	290(7)	5.4
J1711–37	17:11.4(5)	–37:23(7)	349.00	1.26	792.6603(11)	346(15)	4.7
J1720–36	17:20.9(5)	–36:53(7)	350.51	0.01	92.13212(3)	341(1)	4.2
J1732–35	17:32.4(5)	–35:09(7)	349.26	2.07	126.6900039(2)	340(2)	5.1
J1741–34	17:41.9(5)	–34:19(7)	355.00	–2.15	875.137(2)	241(8)	4.1
J1746–27	17:46.0(5)	–27:51(7)	0.96	0.49	487.527(3)	422(9)	5.2
J1750–28	17:50.1(5)	–28:45(7)	0.67	–0.76	1300.517(6)	388(12)	5.1
J1755–26	17:55.2(5)	–26:03(7)	3.56	–0.36	430.8719(3)	405(4)	5.2
J1759–24	17:59.4(5)	–24:02(7)	5.78	–0.16	1457.739(11)	772(14)	10.9
J1825–11	18:25.1(5)	–11:11(7)	19.99	0.66	1925.882(13)	121(19)	2.7
J1830–10	18:30.1(5)	–10:39(7)	21.03	–0.18	245.260(3)	203(2)	3.6

Table 4.5: TEMPO2 best-fitting parameters of the 25 newly-discovered pulsars from the HTRU Galactic plane survey. We list the equatorial (R.A. and Dec.) and Galactic (l and b) position, the spin period and the DM of these pulsars. Values in parentheses are the nominal 1σ uncertainties in the last digits. Pulsars for which no full timing solution is available have been assigned a temporary name containing only two digits of declination. Pulsar distances are derived according to Cordes & Lazio (2002). We include fitting related parameters such as the data span, the reference epoch, the number of TOAs employed (N_{TOA}), the RMS of the TEMPO2 fit and the reduced χ^2 (χ_{red}^2). The characteristic age (τ_c), the surface magnetic field (B_{surf}) and the spin-down energy (\dot{E}) are derived using equations introduced in Chapter 1.

PSR name	R.A. (J2000) (hms)	Dec. (J2000) ($^{\circ}$ ' ")	l ($^{\circ}$)	b ($^{\circ}$)	P (ms)	\dot{P} (10^{-18})	DM (cm^{-3}pc)	Dist (kpc)	Data span (MJD)	Epoch (MJD)	N N_{TOA}	RMS (μs)	χ_{red}^2	τ_c (Myr)	B_{surf} (10^{10}G)	\dot{E} (10^{30}erg s^{-1})
J1002–59	10:02:20.9(8)	–59:19(7)	282.83	–3.24	713.48925966(17)	–	347(2)	8.7	56498–56794	56646	24	2082	2.9	–	–	–
J1101–6424	11:01:37.1906(8)	–64:24:39.335(3)	291.42	–4.02	5.109272904277(3)	–	207	4.5	56401–56793	56597	30	25	0.9	–	–	–
J1247–64	12:47:20.6(17)	–64:43(7)	302.59	–1.85	1234.893545(4)	–	236.4(11)	4.8	56498–56657	56577	11	1103	1.8	–	–	–
J1525–5523	15:25:36.075(10)	–55:23:27.4(3)	323.64	1.17	355.156037466(4)	9.3(4)	124.7(3)	2.3	55984–56571	56277	18	403	0.7	600	5.8	8.2
J1528–5547	15:28:39.17(15)	–55:47:25(7)	323.80	0.64	3467.3019330(7)	7730(80)	269	4.3	56127–56793	56460	17	8342	11	7.1	520	7.3
J1532–5606	15:32:22.66(10)	–56:06:47(4)	324.04	0.01	522.97708638(6)	55(7)	282	4.3	55984–56584	56284	11	2970	1.4	149	17.3	15
J1708–36	17:08:34.2(2)	–36:42(7)	349.26	2.07	587.5668045(3)	–	316(3)	4.8	56500–56678	56588	14	2673	1.7	–	–	–
J1722–38	17:22.9(5)	–38:23(7)	349.50	–1.17	765.7958224(16)	–	472(2)	5.8	56500–56508	56504	10	1750	1.3	–	–	–
J1731–33	17:31:01(6)	–33:25(7)	354.54	0.24	544.663512(7)	–	877.4	11.0	56500–56660	56579	12	55504	161	–	–	–
J1734–3058	17:34:50.832(13)	–30:58:39(2)	356.99	0.87	541.28568905(4)	16.2(19)	260.0(14)	3.8	56098–56654	56376	67	1618	2.8	528	9.5	4.0
J1738–2736	17:38:14.58(2)	–27:36:33(4)	0.29	2.07	627.71560415(2)	4643(11)	323.6(7)	5.1	56341–56669	56505	27	553	3.2	2.14	172	740
J1757–27	17:57:54.7829(10)	–27:45(7)	2.45	–1.75	17.6872150455(4)	–	334	5.3	56680–56790	56735	36	0.7	14	–	–	–
J1811–17	18:11.6(5)	–17:18(7)	13.05	0.64	391.3850721(5)	–	545.5	6.7	56640–56677	56658	11	3564	2.9	–	–	–
J1824–1350	18:24:50.23(6)	–13:50:17(8)	17.59	–0.55	1396.5985624(2)	620(100)	551(7)	6.5	56341–56669	56505	33	2490	1.8	35.7	94.2	9.0
J1829–10	18:29.1(5)	–10:09(7)	21.33	0.26	829.1660039(12)	–	610	6.7	56627–56679	56653	10	6303	3.7	–	–	–
J1833–0209	18:33:05.69(17)	–02:09:09(4)	28.90	3.08	291.9306111(3)	2751(14)	325.4	7.2	56341–56668	56504	55	1807	2.8	1.68	90.7	4400
J1835–0924b	18:35:21.81(2)	–09:24:18.1(17)	22.80	–0.75	235.248928536(17)	10.5(8)	500	6.3	55905–56658	56281	78	4452	2.9	352	5.05	32
J1835–0928	18:35:21.6(2)	–09:28:04(7)	22.69	–0.77	621.7339795(8)	990(20)	450	5.8	55905–56353	56129	26	4796	3.6	9.93	79.5	160
J1838–0107	18:38:39.423(2)	–01:07:48.64(9)	30.54	2.28	444.425731453(2)	5.3(3)	268.9	6.1	56095–56655	56375	61	380	1.0	1311	4.95	2.4
J1839–0223	18:39:57.97(5)	–02:23:11(2)	29.50	1.45	1266.79010024(10)	4742(15)	330	6.4	56095–56670	56382	70	8956	6.5	4.23	248	92
J1839–0332	18:39:56.60(2)	–03:32:59.8(16)	28.52	0.81	2675.6822615(3)	4766(18)	195.1	4.8	56112–56670	56382	59	2507	1.6	8.9	361	9.8
J1842–0800	18:42:54.98(7)	–08:00:54(6)	24.85	–1.75	1255.4685920(2)	150(110)	188.6	4.1	56341–56660	56500	25	2418	1.7	125	45.2	3.0
J1844–0302	18:44:06.93(7)	–03:02:09(4)	29.31	0.26	1198.63022072(19)	7810(100)	533	7.3	56341–56658	56505	36	3365	2.1	2.43	310	180
J1843–0510	18:43:09.747(16)	–05:10:03.4(5)	27.42	–0.58	671.613801222(17)	389(3)	257	5.2	56145–56658	56401	61	1932	1.3	2.74	164	51
J1847–0427	18:47:18.4(2)	–04:27:34(14)	28.47	–1.15	259.24664638(14)	190(70)	188.3	4.7	56341–56668	56504	31	7991	2.5	21.0	22.8	430

Table 4.6: Binary parameters for PSR J1101–6424 compared to that of PSR J1614–2230 (data taken from Demorest et al. (2010)).

	J1101–6424	J1614–2230
Orbital period, P_{orb} (d)	9.6117082(3)	8.6866194196(2)
Projected semi-major axis, x (lt-s)	14.02466(3)	11.2911975(2)
Epoch of ascending node, T_{asc} (MJD)	55689.00791(3)	52331.1701098(3)
$e \sin \omega$, ε_1 (10^{-6})	25(3)	0.11(3)
$e \cos \omega$, ε_2 (10^{-6})	6(3)	–1.29(3)
Longitude of periastron, ω ($^\circ$)	75(7)	–
Minimum companion mass [†] , $m_{\text{c,min}}$ (M_\odot)	0.47	–
Median companion mass [†] , $m_{\text{c,med}}$ (M_\odot)	0.57	0.500(6)*
Binary model	ELL1	–

[†] These companion masses are calculated for an orbital inclination of $i = 90^\circ$ and an assumed pulsar mass of $1.35 M_\odot$.

* This companion mass is measured from the detected Shapiro delay.

Despite the improved acceleration search algorithm used in this analysis, no previously unknown relativistic binary pulsar has yet been found. However, as mentioned earlier all known relativistic binary pulsars in the survey region of the 37 per cent processed observations have been re-detected with a higher significance than obtained in previous analyses (see Table 4.1).

4.3 Individual pulsars of interest

4.3.1 PSR J1101–6424, a Case A Roche lobe overflow cousin of PSR J1614–2230

PSR J1101–6424 is a binary MSP with an orbital period of ~ 10 d and a spin period of 5 ms (Table 4.6). Assuming an orbital inclination of $i = 90^\circ$ and a pulsar mass of $1.35 M_\odot$, we find the minimum companion mass of PSR J1101–6424 to be $0.47 M_\odot$. A heavy companion mass as such tends to point to an evolutionary track from an intermediate-mass X-ray binary (IMXB; Tauris, 2011), with the companion being a carbon-oxygen white dwarf (CO-WD). However, the fast spin period of 5 ms indicates contradictory full-recycling from a long mass-transfer phase. This can only be achieved via Case A Roche lobe overflow (RLO) as discussed in Tauris et al. (2011), making PSR J1101–6424 the second known IMXB descending from this evolutionary track. The only other IMXB formed from Case A RLO is the 3-ms binary PSR J1614–2230. Fig. 4.3 shows the spin periods versus the minimum companion masses of all known pulsars as listed in PSRCAT. It can be seen that PSR J1101–6424 is indeed located at the edge of the CO-WD population, together with PSR J1614–2230.

We recall that PSR J1614–2230 is one of the heaviest neutron star known,

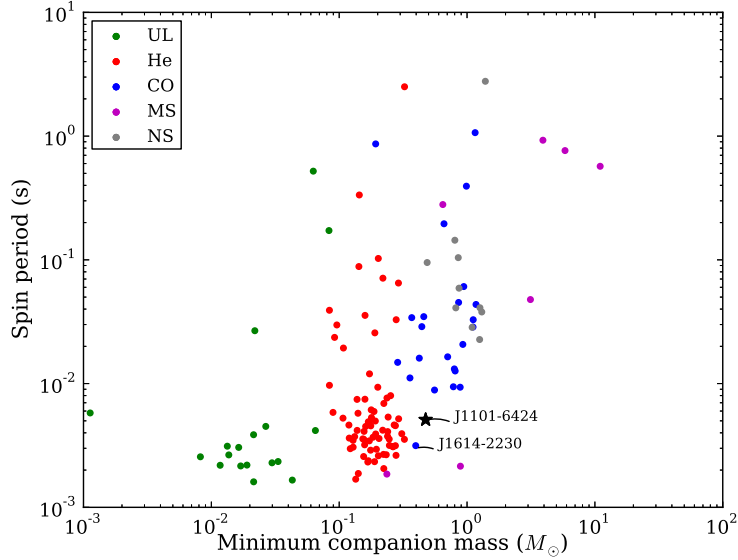


Figure 4.3: Spin period versus minimum companion mass for all published pulsars in binary systems. We have classified their companions according to the description in [Tauris et al. \(2012\)](#). Green points indicate ultra-light (UL) binaries, red points indicate helium white dwarf (He-WD) companions, blue points indicate CO-WD, purple points indicate main-sequence star (MS) companion and gray points indicate NS-NS systems.

with a mass of $2.0 M_{\odot}$ ([Demorest et al., 2010](#)). This does not yet necessarily imply PSR J1101–6424 should also have a heavy pulsar mass. The reason being that the initial orbital separation is the only deciding factor as to whether an IMXB should follow Case A, B or C RLO, and has no link with the pulsar mass. However, given the similarities between the two systems (see Table 4.6), we can deduce that PSR J1101–6424 is likely to have a similar initial donor mass of $\sim 4.5 \pm 0.5 M_{\odot}$ just like that of PSR J1614–2230. According to Fig. 9 of [Tauris et al. \(2011\)](#), this would suggest a neutron star mass $> 1.7 M_{\odot}$ for PSR J1101–6424. Any potential detection or constraint of Shapiro delay in PSR J1101–6424 thus implies good prospects for measuring a pulsar with high mass, and continued monitoring of this binary system is of great interest.

PSR J1101–6424 also has a relatively high DM of $207.5 \text{ cm}^{-3} \text{ pc}$ for an MSP. In fact it has the tenth highest value of DM/P of $40.6 \text{ cm}^{-3} \text{ pc ms}^{-1}$. This high DM/P ratio is an indication that our survey is probing a more distant MSP population in the Galactic disk, as expected from the improvement in the survey specification in terms of time and frequency resolution.

4.3.2 PSR J1759–24, an intermittent pulsar?

PSR J1759–24 was first discovered from a survey observation taken at MJD 55675.9 with strong, self-confirming pulsar characteristics (Fig. 4.4). Ten subsequent confirmation observations at Parkes were conducted at the discovery position between

BC P(ms)= 1457.739621085 TC P(ms)= 1457.620827099 DM= 772.500 RAJ= 17:59:24.72 DecJ= -24:02:34.8
 BC MJD = 55675.905916 Centre freq(MHz) = 1382.000 Bandwidth(MHz) = -400 l = 5.782 b = -0.164
 NBin = 128 NChan = 32 NSub = 433 TBin(ms) = 11.388 TSub(s) = 8.000 TSpan(s) = 4324.637
 P(us): offset = -30.00000, step = 3.83822, range = 2074.86179 DM: offset = 0.000, step = 4.457, range = 280.00

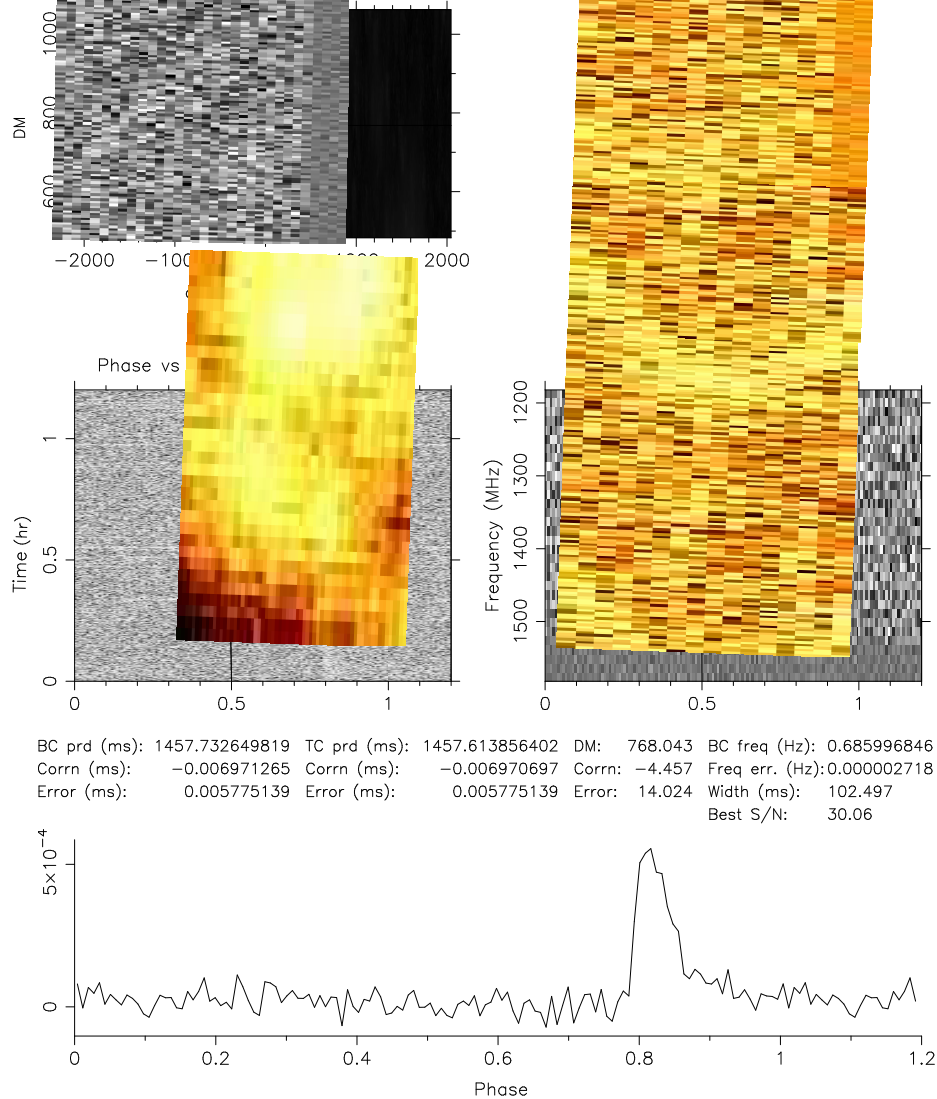


Figure 4.4: Discovery plot of PSR J1759–24 as generated by the search pipeline used in this survey. The top left panel shows the period-DM plot, where the colour scale illustrates the drop off of S/N versus increasing offsets from the nominal period and DM. The middle left panel shows 128 time sub-integrations of the observation, and it can be seen that PSR J1759–24 is clearly visible during the complete 4300 s survey integration. The middle right panel shows 16 frequency sub-bands, again PSR J1759–24 is observed with stable flux density over the observing frequency bandwidth. The solid lines in these panels indicate the optimal parameters which provide the highest S/N. Finally, the bottom panel shows the integrated pulse profile by folding the filterbank data with the optimal parameters found.

MJD 56408 and 56675 each with 20 min integration time. The pulsar was not detected except a marginal re-detection at the 10th attempt with a S/N of 8. Another 12 attempts with the Lovell telescope have been made between MJD 56655 and 56671, spending a total of 10 hr at the same position, of which none has re-detected the pulsar. PSR J1759–24 was detected again for 14 attempts between MJD 56728 and 56793 with both the Lovell and the Parkes telescopes.

Given the high DM of $758 \text{ cm}^{-3} \text{ pc}$ of PSR J1759–24, it is highly unlikely that scintillation could be responsible for the intermittent detections. PSR J1759–24 could potentially be a nulling pulsar with long nulls lasting at least as long as the 20 min observation time, in which the pulsar is completely switched off. Otherwise, PSR J1759–24 could be in an eclipsing binary system with a long orbital period of the order of years. Similar examples include PSR J1638–4725 which has a P_{orb} of 5.3 yr and a $\sim 20 M_{\odot}$ MS companion, where the pulsar is undetectable in the radio wavelength for ~ 1 yr around periastron (Lyne et al., in prep); or PSR B1259–63 which has a P_{orb} of 3.4 yr and a $\sim 10 M_{\odot}$ MS companion, where the pulsar is undetectable during a 40-d eclipse behind the MS star (Johnston et al., 1992a). The transient nature of PSR J1759–24 could also be explained if it is a time varying radio source such as a magnetar (see Section 1.4.2). Further observations are crucial to determine the nature of this pulsar and the cause for the intermittency.

4.3.3 PSR J1757–27, likely to be a fast-spinning isolated pulsar?

PSR J1757–27 has a fast spinning period of 17 ms. We have a coherent timing solution across a time span of more than 100 d with observations taken using the Lovell telescope. The timing analysis is consistent with PSR J1757–27 being an isolated pulsar, or in a very wide binary orbit with P_{orb} of the order of years. Further timing observations is crucial for revealing the nature of this pulsar. If it is indeed proved to be isolated, it will add to the currently small population of Galactic (i.e., not associated with a GC) millisecond-period isolated pulsars of 30. If the above hypothesis is true, this system would have important implications to the evolution scenarios of millisecond-period isolated pulsars. Currently, the most adopted formation scenario of isolated MSP is that, a pulsar system with a very-low mass companion could continue ablating its companion until it cease to exist (see e.g., Ruderman et al., 1989). This however would imply fully recycling and hence the pulsar should have very fast spin period of the order of a few ms, at odds with PSR J1757–27. In addition, MSP J1757–27 has a small duty cycle of 2.8 per cent. If timing residuals with an RMS of the order of a few μs can be achieved with future timing observations, MSP J1757–27 can potentially be a good candidate to be employed in a pulsar timing array.

4.3.4 PSR J1847–0427, a pulsar with an extremely wide pulse

PSR J1847–0427 has a very wide profile with emission over almost the entire 360° of pulse phase. Given that most radio pulsars have narrow emission patterns, PSR J1847–0427 is likely an aligned rotator with an angle between the magnetic and

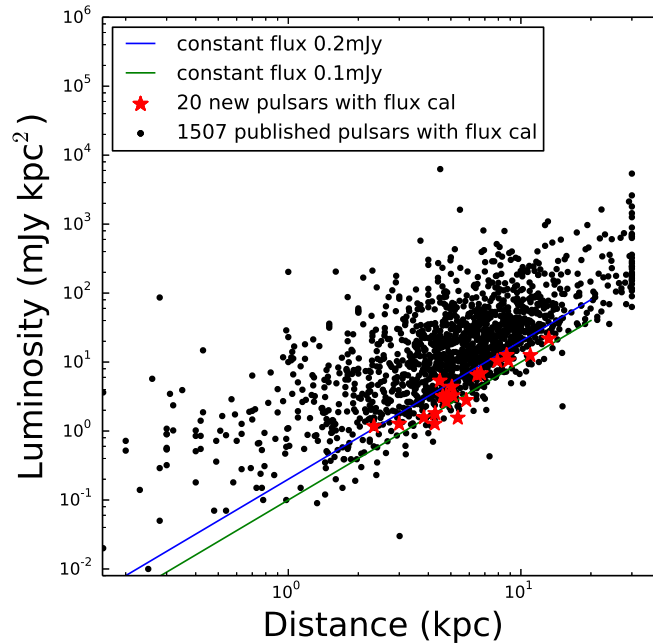


Figure 4.5: Luminosity versus distance of the 20 newly-discovered pulsars with flux density measurements (red stars) and the published pulsars taken from PSRCAT (black dots).

rotational axis, $\alpha \sim 0^\circ$. This would imply that we are sampling the emission pattern along a ring around the magnetic axis that is entirely within the beam of emission. On top of this, the profile of PSR J1847–0427 exhibits a second component located at a rotation phase $\sim 180^\circ$ from the main pulse (see relevant panel in Fig. 4.2), similar to that observed in PSR B0826–34 (Biggs et al., 1988). This second component is most likely an interpulse, and could be due to oblateness in the emission beam. If future observations show evidences of drifting subpulses like the case of PSR B0826–34, this could provide insight into the conical beam of emission. Further measurements of the polarisation properties and observations of any frequency evolution are crucial to solve for the emission geometry, and would also allow us to constrain the angle α . These can potentially lead to studies of pulsar magnetosphere and testing of emission mechanism models.

4.4 Comparing with known pulsar population

4.4.1 Luminosity

Twenty out of the 47 new pulsars have calibrated flux density measurements and we have inferred their luminosities as reported in column 8 of Table 4.3. We caution that the derived luminosities are dependent on our knowledge of the pulsar distances. In this work we have calculated pulsar distances based on the NE2001 electron density model

(Cordes & Lazio, 2002), which is typically thought to have an associated uncertainty of 25 per cent for each DM-derived distance. Assuming that this uncertainty is of comparable magnitude irrespective of the line of sight, we compare our new luminosity derivations to the luminosity distribution of the known pulsars as listed on PSRCAT. It is interesting to see from Fig. 4.5 that the HTRU Galactic plane survey is indeed probing the low luminosity region particularly for distant pulsars, as expected from the improved data resolution and the longer integration time of 72 min.

No nearby pulsars have been discovered thus far out to a distance of at least 2 kpc (see Tables 4.4 and 4.5). This null result might seem surprising at first, as a quick examination of Fig. 4.5 would suggest new discoveries to populate the region between the blue and green lines of constant flux densities. However, consider that the sky volume increases with radius to the third power. If we assume that pulsars are uniformly distributed in the Galaxy, there are thus more pulsars at larger distances. Furthermore, a uniform pulsar distribution is certainly not a good assumption. In fact towards the inner Galactic plane, the pulsar density should increase as our line-of-sight crosses more spiral arms and approaches the Galactic centre. This uneven Galactic distribution of pulsars further contributes to a higher number pulsars at larger distances for the HTRU Galactic plane survey region. Indeed, for the 713 known pulsars with a published luminosity within the HTRU Galactic plane survey region, only 27 (i.e., 3.8 per cent) lies within a distance of 2 kpc. Extrapolating this to the 47 newly discovered pulsars thus far, we therefore expect to have less than two pulsars within a distance of 2 kpc, consistent with the current statistics.

However, if the complete HTRU Galactic plane survey produces a significantly smaller percentage of nearby discoveries than 3.8 per cent, it could indicate that we have completed the nearby pulsar population, or at least reached a point where the yield of pulsar surveys are reducing as we are no longer flux limited. This has important implications to future pulsar surveys such as those to be conducted with MeerKAT and the SKA. Any pulsar surveys targeting the Galactic plane will have to go to higher observing frequency which could help discovering pulsars that would be otherwise undetected due to scattering. A yet longer dwell time or a telescope with larger collecting area would thus be needed to compensate for the typically negative spectral index of pulsars as they get weaker at a higher observing frequency.

4.4.2 Characteristic ages

Young pulsars (conventionally defined as having characteristic ages less than 100 kyr) are expected to be located not far from their birth places hence mostly populating the Galactic plane region. Indeed the previous Galactic plane survey, the PMPS, discovered a sample of pulsars with an average characteristic age lower than the previously-known population (Morris et al., 2002), and these PMPS discoveries account for about half of the young pulsars currently known (Kramer et al., 2003). No young pulsars have been discovered in the HTRU medium-latitude survey (Bates et al., 2012). This null result was attributed to the fact that the HTRU medium-latitude survey has a higher minimum detectable flux density of 0.2 mJy compared to the PMPS of 0.15 mJy along

the Galactic plane. [Bates et al. \(2012\)](#) predicted that young pulsar discoveries are instead expected from the HTRU Galactic plane survey, given the higher sensitivity of this project part.

Of the 47 newly-discovered pulsars presented here, 16 now have coherent timing solutions obtained over a time span of about half a year, allowing us to infer the preliminary characteristic ages and to locate them on a $P-\dot{P}$ diagram as in Fig. 4.6. All of these 16 pulsars lie within the region containing known normal pulsars, with \dot{P} between 10^{-14} and 10^{-17} . Note that we have not corrected for any potential contribution in the observed \dot{P} from the Galactic potential and from the transverse proper motion of the pulsar ([Shklovskii, 1970](#)). These effects are expected to be significant only for recycled pulsars ([Camilo et al., 1994](#)).

We point out that there is a noticeable lack of young pulsars within this 16 pulsars as they all have τ_c at least of the order of Myr (also see Table 4.4). This is at odds with the expectation mentioned above. The identity of this older population is intriguing, and may account for the missing population of disrupted mildly recycled pulsars as predicted by [Lorimer et al. \(2004\)](#) and further investigated by [Belczynski et al. \(2010\)](#), a population that has as yet largely eluded pulsar surveys due to their small average flux density.

In addition, there is a long standing debate regarding the relationship of radio luminosity of pulsars and their ages. As discussed in Section 1.2, the radio emission only contributes to a small portion of the energy budget of a pulsar. However, [Narayan & Ostriker \(1990\)](#) suggested that radio luminosity is proportional to the cube root of the spin-down luminosity of a pulsar (i.e., $L \propto \dot{P}^{1/3}/P$). In other words, older pulsars would have a lower radio luminosity. [Lorimer et al. \(1993\)](#) showed that there is a large scatter in this relationship. Nonetheless, [Arzoumanian et al. \(2002\)](#) argued that the spread is simply caused by viewing geometry and intrinsically there is a strong luminosity-age relationship that scales with the voltage drop above the polar cap. If this is true, it would provide an explanation for the discovery of these older pulsars, as the HTRU Galactic plane survey probes deeper in the low luminosity end of the Galactic pulsar population.

Disregarding the two MSPs discovered from this survey as inferred characteristic ages are known to be unreliable estimates for MSPs (see Section 1.2), the remaining 27 newly discovered pulsars have not yet long enough timing solutions to determine their characteristic ages. However, their spin periods have been determined upon discovery. As apparent from Equation (1.3), the characteristic age of a pulsar is related to its spin period. Reviewing any $P-\dot{P}$ diagram such as Fig. 4.6 shows that young pulsars tend to have smaller spin periods. This is more obvious if we split the $P-\dot{P}$ diagram into different spin period bins and create normalised age distribution for each period group as shown in Fig. 4.7. These histograms thus represent the probability of a pulsar with a given spin period to be of a certain age.

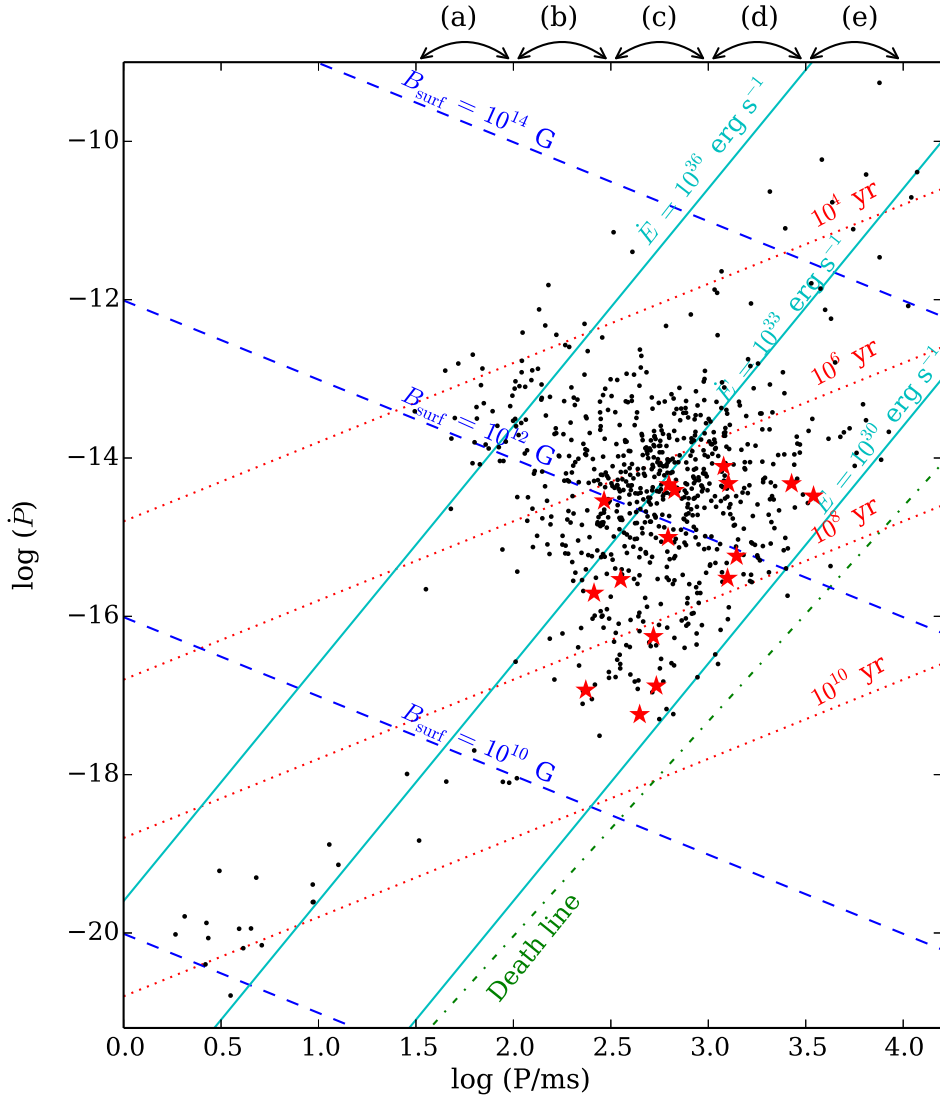


Figure 4.6: P - \dot{P} diagram of the known pulsar population within the HTRU Galactic plane survey region (black) and the 16 new discoveries (red) that have now preliminary timing solutions. Lines of constant characteristic ages are shown as red dotted lines, spin-down energies as cyan solid lines and surface magnetic field strength as blue dashed lines. The death line as described in [Chen & Ruderman \(1993\)](#) is shown as green dot-dashed line. The period bins used in Fig. 4.7 are indicated on the top.

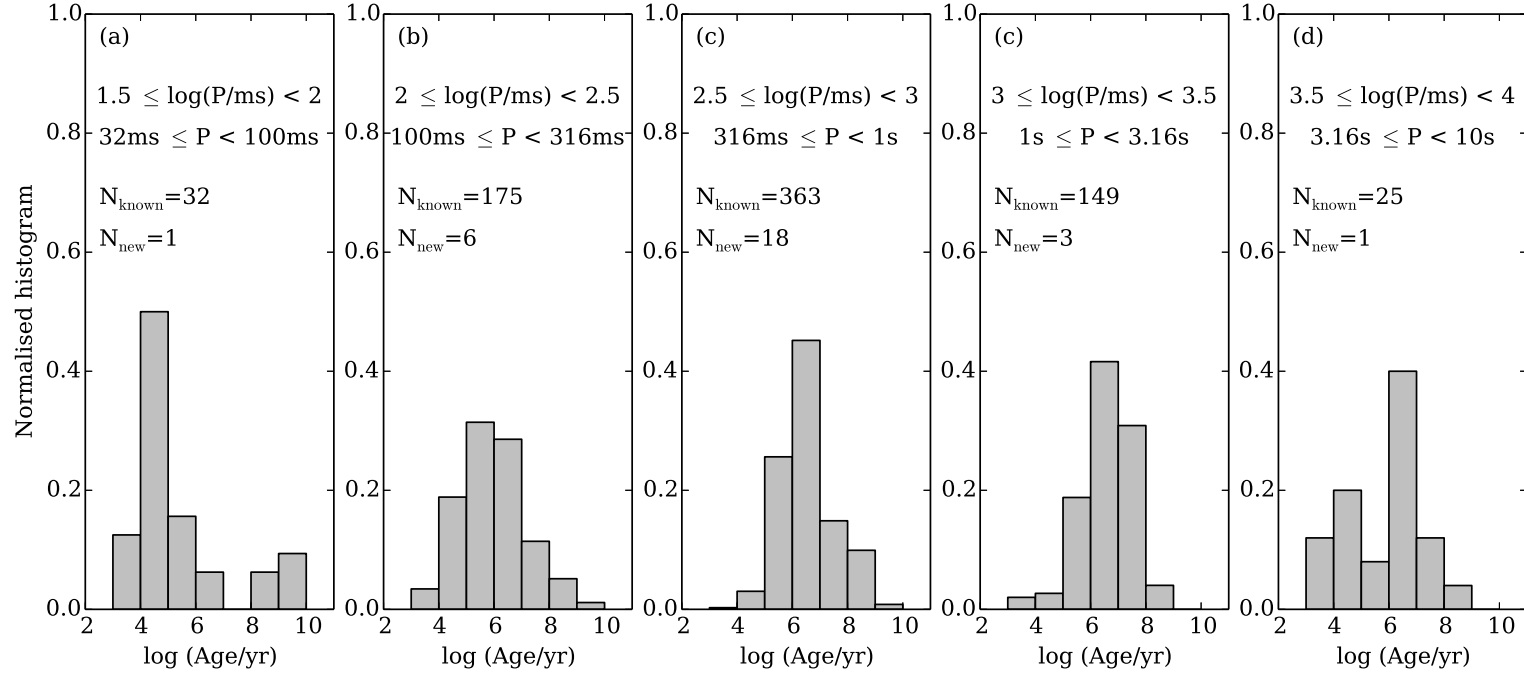


Figure 4.7: Normalised histograms of characteristic age of known pulsars within the inner Galactic plane region surveyed by the HTRU, with $-80^\circ < l < 30^\circ$ and $|b| < 3.5^\circ$. MSPs are disregarded and therefore there is a total of 748 known ‘normal’ pulsars in our sample. We differentiate between various spin period bins, with panel (a) $1.5 \leq \log(P/\text{ms}) < 2$, (b) $2 \leq \log(P/\text{ms}) < 2.5$, (c) $2.5 \leq \log(P/\text{ms}) < 3$ and (d) $3.5 \leq \log(P/\text{ms}) < 4$. The number of known pulsars that falls into each period bin is indicated by N_{known} . The number of newly discovered pulsars from the HTRU Galactic plane is indicated by N_{new} .

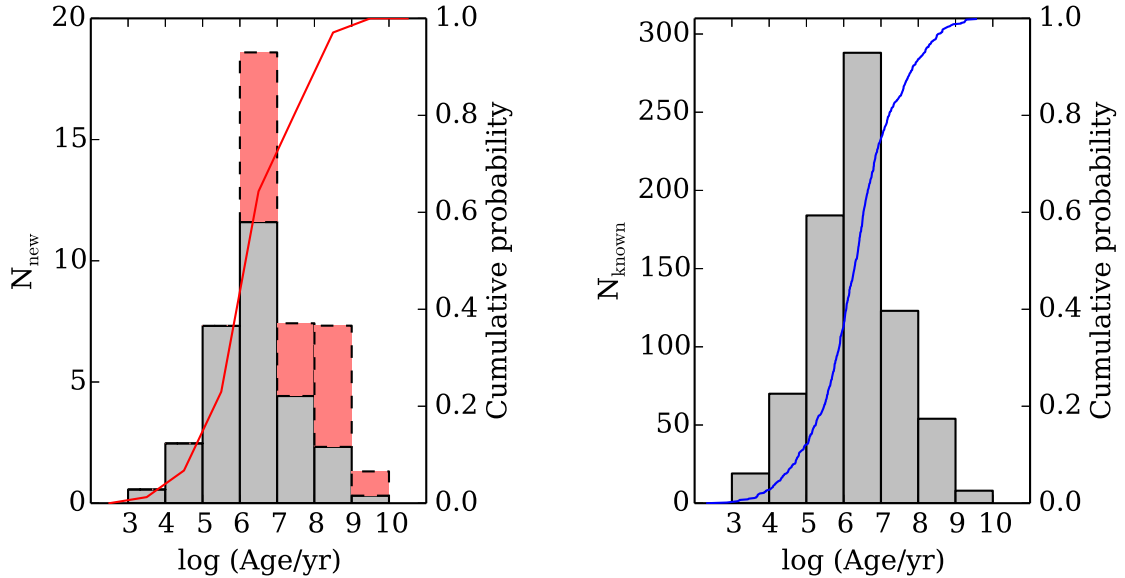


Figure 4.8: Histograms and CDFs of characteristic ages of (left) newly discovered and (right) previously known pulsars. For the newly discovered pulsars, the grey histogram with solid outline represents the probability distribution of the characteristic ages of the 27 pulsars yet without \dot{P} measurements. The red histogram with dashed outline represents the ages as inferred from the timing solutions of the 16 pulsars.

If we assume that the pulsar age distribution is independent of the luminosity distribution (i.e., as the HTRU Galactic plane survey probes the lower end of the luminosity distribution function, this observed population of less-luminous pulsars is similar to and can be extrapolated from the known population), we can therefore construct a probability distribution of the characteristic age for the remaining 27 newly-discovered pulsars yet without a \dot{P} measurement, by summing these histograms weighted by the number of newly discovered pulsars that fall within each period groups (N_{new}). This result is represented by the grey histogram in the left panel of Fig. 4.8. On top of this we plot the actual inferred ages of the 16 newly discovered pulsars in red. The cumulative distribution curve overplotted shows the combination of ages from both contributions. Comparing this to the age distribution of all the 748 ‘normal’ pulsars within the inner Galactic plane region covered by the HTRU Galactic plane survey (the right panel of Fig. 4.8), it is suggestive that the newly-discovered pulsars have a similar age distribution as the known pulsars. A Kolmogorov-Smirnov (KS) test indicates that the two samples are consistent with being drawn from the same populations, with a p-value of 0.012.

This analysis implies that the current lack of young pulsars is purely due to small number statistics and at least a few young pulsars can be expected from the remaining 27 pulsars currently without a \dot{P} measurement. Timing solutions for these remaining pulsars and any future discoveries from the HTRU Galactic plane survey will be crucial to study the age distribution of this less-luminous pulsar population and might help to

resolve some of the degeneracy of the arguments introduced above.

4.4.3 Spin-down power and Fermi association

Theoretical expectations and results from gamma-ray telescopes (e.g., [Thompson, 2008](#); [Abdo et al., 2013](#)) indicate that pulsars with large spin-down power ($\dot{E} > 1 \times 10^{34} \text{ erg s}^{-1}$) are the most likely gamma-ray pulsar candidates. Successful identification of multiwavelength counterparts provide key insights into the relative geometry of the different emission regions, and allow us to study the population of gamma-ray emitting pulsars as a whole. Phase-folding the gamma-ray photons with a radio ephemeris is a very effective way to recover gamma-ray pulsations from high energy data, for example from the Large Area Telescope (LAT) on the *Fermi Gamma-Ray Space Telescope*. Currently, the short time span of the radio ephemerides of the newly-discovered pulsars presented in this paper are inadequate to phase-fold the now more than five years of LAT data. Continuous follow-up timing of these pulsars and any future discoveries from the HTRU Galactic plane survey would provide up-to-date radio ephemerides critical for recovering any associated gamma-ray pulsations. We note that for the 16 pulsars currently with P and \dot{P} measurements, none of them has high $\log \sqrt{\dot{E}}/d^2$ values (see [Abdo et al., 2013](#), for details), hence unlikely to be detected by *Fermi* in the future.

4.5 A comparison with the estimated survey yield

Using the PSRPOP⁴ software based on the pulsar population model by [Lorimer et al. \(2006\)](#), [Keith et al. \(2010\)](#) simulated that the number of normal pulsar detections expected from the HTRU Galactic plane survey to be 957. We have conducted a similar simulation using the more up-to-date PSRPOPpy⁵ software as presented in [Bates et al. \(2014\)](#). By assuming the same power-law luminosity model as employed in [Keith et al. \(2010\)](#), we find that the expected number of normal pulsar detections is 1020, statistically consistent with the result in [Keith et al. \(2010\)](#).

Scaling these estimated numbers down to reflect the current HTRU Galactic plane survey data processing progress of 37 per cent, it can be seen that of the order of 350 to 380 normal pulsar detections are predicted. We note that strictly speaking such intrapolation is inaccurate, as it assumes pulsars to be uniformly distributed in the survey region. This is not true and for example a higher density of pulsars should be observed along the line of sights that cut through any spiral arms. However, as shown in [Fig. 3.7](#), this 37 per cent of processed observations are drawn from random selection, hence this intrapolated estimation should hold.

Among the 348 known pulsar re-detections, 344 are normal pulsars. Adding this to the 45 normal pulsars discovered thus far, we have a current normal pulsar detection rate of 389. The close match between the estimated and observed yield is satisfying, and would imply that our survey is performing as expected. In addition, the ability

⁴<http://psrpop.sourceforge.net>

⁵<https://github.com/samb8s/PsrPopPy>

of these simulation tools to closely reproduce the observed yield could be used as an indication of a sound understanding of the underlying pulsar population parameters. Nonetheless, we note that a more mature judgment can be formed when the complete HTRU Galactic plane survey is analysed in the near future.

For MSPs, PSRPOP and PSRPOPpy have predicted 51 and 43 detections respectively for the complete HTRU Galactic plane survey. A dedicated study of MSP luminosity by [Levin et al. \(2013\)](#) suggested even a higher MSP yield of 68. Hence within the current 37 per cent of processed observations, these simulations predict a MSP detection rate between 16 and 25. Among the 348 re-detected known pulsars, four are attributed to previously known MSPs (see [Table 4.1](#) or [Appendix A1](#)), and two additional MSP detections come from the new discoveries of MSPs J1101–6424 ([Section 4.3.1](#)) and J1757–27 ([Section 4.3.3](#)). These sum to a current total MSP yield of six. It thus appears that we are roughly a factor of three short of MSP detections.

A major caveat in the estimation of MSP detection is that, our understanding of the underlying MSP distribution is still inadequate and hampered by the small number statistics of known Galactic MSPs. For this reason, MSP population simulation was not considered in [Lorimer et al. \(2006\)](#). In addition, [Lorimer \(2013\)](#) pointed out potential issues involved in the MSP period model devised by [Cordes & Chernoff \(1997\)](#) which is used as an input parameter in PSRPOPpy. [Levin et al. \(2013\)](#) found a steeper luminosity distribution and suggested a larger z -height for MSPs than what was used in the simulation by [Keith et al. \(2010\)](#). These disagreements in the input parameters mean that we should treat any predictions from MSP population simulations with care.

Despite these uncertainties in the MSP population model, several other reasons could come into play reducing our MSP yield. [Eatough et al. \(2013b\)](#) have provided a detailed discussion on the possible causes of MSP non-detection. For instance, they suggested that the influence of unfavourable orbital phases where the acceleration was not constant, the emission beam having precessed out of our line of sight, intermittency, as well as human inspection error during pulsar candidate selection could have accounted for some of the missed MSPs.

Furthermore, scattering broadening caused by the ISM is particularly harmful for MSP detection. Any broadening of a time scale of ms already represents a significant portion of the spin period of an MSP, and the fact that MSPs tend to have larger duty cycles (see [Table 3.3](#)) makes them more susceptible to profile broadening. Scattering is not well quantified and if this effect is underestimated in the population model, could partially explain the apparent low yield of MSPs. We expect that the large sample of pulsars (both normal and MSPs) to be detected by the HTRU Galactic plane survey will provide further information for a better quantification of the extent of scattering.

Apart from these, and perhaps the most relevant explanation here, is that we have only processed the HTRU Galactic plane data in a partially coherent manner. The segmentation scheme means that we have not made use of the full sensitivity achievable by the complete 4300s observations. In fact, running the MSP simulation again with PSRPOPpy for each of the parallel searches of halved, quartered, and one-eighth segment length, the corresponding predicted MSP detections would be reduced to 27, 22, and 16 respectively. And the current number of six MSP detections in 37 per cent

of processed data then become at least consistent. As discussed in Section 3.3.2.3, coherently analysing the full 4300 s observation with acceleration search is our priority in future data reprocessing.

The presence of RFI could also have reduced our sensitivity which would have particularly affected the detection of low luminosity pulsars. However, as demonstrated by the close match of yield in normal pulsar detections, the HTRU Galactic plane survey does not seem to have any obvious general loss of sensitivity, hence RFI should not be a significant factor for the explanation of our lack of MSP detections.

Discovery of four millisecond pulsars and updated timing solutions of a further 12

This chapter is an enhanced version of [Ng et al. \(2014\)](#). We report on the discovery of four MSPs in the HTRU medium latitude survey. All four MSPs are in binary systems and are likely to have white dwarf companions. In addition, we present updated timing solutions for 12 previously published HTRU MSPs, revealing new observational parameters such as significant temporal DM variations in PSR J1017–7156. We discuss the case of PSR J1801–3210, which shows a \dot{P} of the order of 10^{-23} , an extremely small number compared to that of a typical MSP. Furthermore, we highlight the potential to employ PSR J1801–3210 in the strong equivalence principle test due to its wide and circular orbit. In a broader comparison with the known MSP population, we suggest a correlation between higher mass functions and the presence of eclipses in ‘very low-mass binary pulsars’, implying that eclipses are observed in systems with high orbital inclinations. We also suggest that the distribution of the total mass of binary systems is inversely-related to the Galactic height distribution. Finally, we report on the first detection of PSRs J1543–5149 and J1811–2404 as gamma-ray pulsars.

Contents

5.1	Observations and analysis	98
5.2	Discovery of four millisecond pulsars	100
5.2.1	On the nature of the binary companions	100
5.2.2	Polarisation Profiles	101
5.3	Updated timing of 12 HTRU millisecond pulsars	107
5.3.1	Dispersion measure variations	107
5.3.2	Proper motion and transverse velocities	108
5.3.3	Observed and inferred intrinsic period derivatives	109
5.3.4	Binary companions and mass functions	116
5.3.5	Galactic height distribution	118
5.3.6	Orbital eccentricity	121
5.3.7	Change in projected semi-major axis, \dot{x}	123
5.3.8	Orbital period variation, \dot{P}_{orb}	124
5.3.9	Variation in the longitude of periastron, $\dot{\omega}$	125
5.3.10	Gamma-ray pulsation searches	125

5.1 Observations and analysis

All 16 MSPs presented in this paper were discovered in 540-s-long integrations as part of the medium-latitude section ($-120^\circ < l < 30^\circ$, $|b| < 15^\circ$) of the HTRU survey. Follow-up timing observations were made at Parkes initially with a set-up similar to that of the survey, employing the central beam of the same 13-beam Multibeam receiver at a centre frequency near 1.4 GHz and the BPSR with 1024 frequency channels incoherently dedispersed at a time resolution of 64 μ s. Later when the pulsar parameters were identified with sufficient accuracy, observations were carried out using the DFBs which are based on the implementation of a polyphase filter in FPGA processors with incoherent dedispersion. Coherently dedispersed data are collected by the APSR and the CASPER Parkes Swinburne Recorder¹ (CASPSR). Pulsars with declination above -35° are also being timed at the Jodrell Bank Observatory with the Lovell 76-m telescope, using a DFB backend and a ROACH backend. The latter is based on the ROACH FPGA processing board² and coherently dedisperses the data. Refer to Table 5.1 for the specifications of all observing systems employed.

Observations have also been taken at different frequencies at Parkes using the 10/50 cm receiver (Granet et al., 2005), to allow for precise DM measurements and to study any variations of pulsar profiles across frequencies. The various combinations of receivers and backends had central frequencies as listed in column 3 of Table 5.1. Note that predetermined offsets were applied to the observational data from Parkes to account for instrumental delay across observations with different backends in accordance with Manchester et al. (2013).

Timing observations of these 16 pulsars have first been made with an intense timing campaign within roughly their first year of discovery, and gradually decreased to weekly observation for the case of Jodrell Bank observations, whereas Parkes observations are more irregular with gaps ranging from days to months depending on telescope availability. Integration times vary from a few minutes to more than 2 hr, with longer observations for weaker pulsars to achieve adequate S/N of at least 10.

We have used the PSRCHIVE data analysis package (Hotan et al., 2004) for data reduction. Each observation is corrected for dispersion and folded at the predicted topocentric pulse period, before finally summing over both frequency and time to produce an integrated profile. We align these profiles from each observation using an ephemeris created from the initial timing solution. This forms the basis of a noise-free analytic reference template, and we convolve the template with each individual profile to produce a Time of Arrival (TOA) (Taylor, 1992). The DE421 Solar System ephemeris of the Jet Propulsion Laboratory (Folkner et al., 2009) was used to transform the TOAs to the Solar System barycentre. The TEMPO2 software package presented in

¹<http://astronomy.swin.edu.au/pulsar/?topic=caspsr>

²<https://casper.berkeley.edu/wiki/ROACH>

Table 5.1: Specifications of the observing system employed for the timing observations in this work. G represents the antenna gain and T_{sys} is the receiver system temperature. f_c represents the central frequency in MHz and B is the bandwidth in MHz.

Receiver	G (K Jy ⁻¹)	T_{sys} (K)	Backend	f_c (MHz)	B (MHz)
10/50CM	0.74	40	Parkes DFBs	732	64
			Parkes APSR	732	64
			Parkes CASPSR	728	64
Multibeam	0.74	23	Parkes DFBs	1369	256
			Parkes BPSR	1352	340
			Parkes APSR	1369	256
			Parkes CASPSR	1382	320 [†]
Single-pixel	1.00	28	Jodrell DFB	1532	384
			Jodrell ROACH	1532	400
10/50CM	0.74	30	Parkes DFBs	3094	256

[†] CASPSR has a bandwidth of 400 MHz. But only 320 MHz can be used due to the Thuraya-3 filters.

Hobbs et al. (2006) was then used to fit a timing model to all TOAs, taking into account the astrometry, spin, and orbital motion of the pulsar. This process of cross-correlating a template with individual profiles can then be iterated to improve the quality of the model fit. We generate multiple TOAs per observation when possible, especially for the pulsars with small orbital periods. This is to make sure each TOA does not cover more than one tenth of an orbit, to avoid masking orbital information within a seemingly high S/N TOA. If simultaneous observations with different backends were taken, we include only one of the observations to avoid otherwise over-weighting duplicated TOAs.

All 16 MSPs in this work are in binary systems. The Damour-Deruelle (DD) timing model (Damour & Deruelle, 1986) in TEMPO2 is a theory-independent description for eccentric binary orbits. However, for binaries with small eccentricities the location of periastron is not well-defined and using the DD timing model results in a high covariance between the longitude of periastron (ω) and the epoch of periastron (T_0). A useful quantity to help choosing the best timing model is xe^2 , where e is the eccentricity and x is the projected semi-major axis of the pulsar orbit as defined by:

$$x \equiv \frac{a_p \sin i}{c}, \quad (5.1)$$

with a_p being the semi-major axis, i the orbital inclination and c the speed of light. For pulsars with xe^2 smaller than the timing precision as represented by the RMS, we use the ELL1 timing model (Lange et al., 2001) alternatively. The ELL1 timing model avoids the covariance by using the Laplace-Lagrange parameters ($\epsilon_1 = e \sin \omega$ and $\epsilon_2 = e \cos \omega$) and the time of ascending node passage (T_{asc}) instead of T_0 as in the

DD timing model.

Towards the end of the timing analysis procedure when the respective reduced χ^2 comes close to one, we can then assume a reliable fit is achieved which is only influenced by the presence of radiometer noise in the template. As a last step, we compensate for these systematic effects by calculating dataset-specific calibration coefficients (also known as ‘EFAC’ in TEMPO2). These coefficients are applied to scale the TOA uncertainties such that each final respective reduced χ^2 is unity.

In addition, full flux density and polarisation calibration are implemented for the four newly-discovered MSPs, in order to study their polarisation profiles. This analysis is not repeated for the rest of the 12 MSPs in this paper since their polarisation properties are already presented in Keith et al. (2012). With the only exception of PSR J1017–7156, a high-precision timing pulsar which is noticeably polarised in both linear and circular sense, we have fully calibrated the data to correctly assess the uncertainties on the TOAs.

To carry out the calibration we make use of Parkes DFB observations which record the four Stokes parameters in each frequency channel. We calibrate each observation for the differential gain and phase between the feed with an observation of the noise diode coupled to the receptors in the feeds. This calibration observation triggers a square-wave signal which is used to retrieve the true Stokes parameters, and it is important that this calibration is taken adjacent to the targeted pulsar observations. In addition, we correct for the non-orthogonality of the receptors in the Multibeam receiver by computing a model of the Jones matrix for the receiver using an averaged observation of the bright pulsar PSR J0437–4715, in accordance with the ‘measurement equation modelling’ technique described in van Straten (2004), and we calibrate the flux density by using an averaged observation of Hydra A.

5.2 Discovery of four millisecond pulsars

We present the discoveries of four MSPs in the HTRU survey, namely PSRs J1056–7117, J1525–5545, J1529–3828 and J1755–3716. They all have observations spanning more than one year, and their coherent timing solutions are shown in Table 5.2. All four are in binary systems.

5.2.1 On the nature of the binary companions

PSR J1529–3828 and PSR J1056–7117 are likely to be formed from wide-orbit low mass X-ray binaries (LMXBs), leading to the formation of classic MSPs with helium white dwarf (He-WD) companions. According to Tauris (2011), wide-orbit LMXBs with $P_{\text{orb}} \geq 1$ d lead to He-WDs with masses between about 0.15 to 0.46 M_{\odot} .

PSR J1755–3716 has a relatively high median companion mass of 0.35 M_{\odot} . Although this would fit in the above classification, the fact that PSR J1755–3716 has a spin period of 12.8 ms implies that the system is only mildly recycled. This, combined with its P_{orb} of just 11.5 d (which is too short for LMXB evolution to produce a 0.35 M_{\odot} WD, Tauris & Savonije (1999)), indicates that its evolutionary track is more

likely to have started from an intermediate mass X-ray binary pulsar (IMXB) accreting via early Case B Roche-lobe overflow (RLO) (Tauris, 2011). The companion of PSR J1755–3716 is probably a CO-WD.

PSR J1525–5545 has a solar mass companion with a median mass of $0.99 M_{\odot}$ and an P_{orb} of 0.99 d. These fit the typical characteristics of binary evolution from a wide-orbit IMXB via Case C RLO and common envelope evolution (Tauris, 2011). The companion is likely to be a massive CO-WD, or an ONeMg-WD if the orbital inclination is low.

5.2.2 Polarisation Profiles

Fig. 5.1 shows the integrated polarisation profiles of the four MSPs in total intensity, linear and circular polarisation. We measure the Faraday rotation observed towards each pulsar by fitting the position angle (P.A.) variations across the 256 MHz band centred at 1369 MHz, and the plots shown here have their rotation measure (RM) corrected with the respective RMs as listed in Table 5.2. Multi-frequency data are included only if the S/N ratio is high enough, and are plotted here with an arbitrary alignment. None of the four MSPs are detectable at 3100 MHz with at least 1 hr of observation, except a tentative detection of PSR J1755–3716. At 732 MHz only PSRs J1056–7117 and J1525–5545 are detectable, both with limited S/N. Although pulsars typically have steep spectral indexes and thus higher flux at lower observing frequencies, our receiver system at 50 cm has a reduced sensitivity due to its higher system temperature and narrow bandwidth (Table 5.1). Hence we cannot comment if there is any profile evolution across frequency.

PSR J1056–7117 has a profile comprising three components. The emission of the middle component changes handedness in circular polarisation, whereas the S/N of the other two components are not sufficient for identifying the polarisation fraction. Linear polarisation is present in the middle component, although noisy. PSR J1525–5545 has a simple, single peak profile. It is almost completely unpolarised, and such low polarisation profile is typically associated with aligned gamma-ray and radio profiles (Espinoza et al., 2013). Although no *Fermi Gamma-ray Space Telescope (Fermi)* association has been reported for PSR J1525–5545 yet, it is worth following-up as the radio ephemeris improves with longer timing baseline. PSR J1529–3828 has a broad single peak profile with a hint of interpulse, and the P.A. is relatively flat over the profile. PSR J1755–3716 also has a profile formed of three components with some degree of linear polarisation in the middle component which is narrower compared to the total intensity, and the P.A. seems to show an ‘S-shaped’ swing.

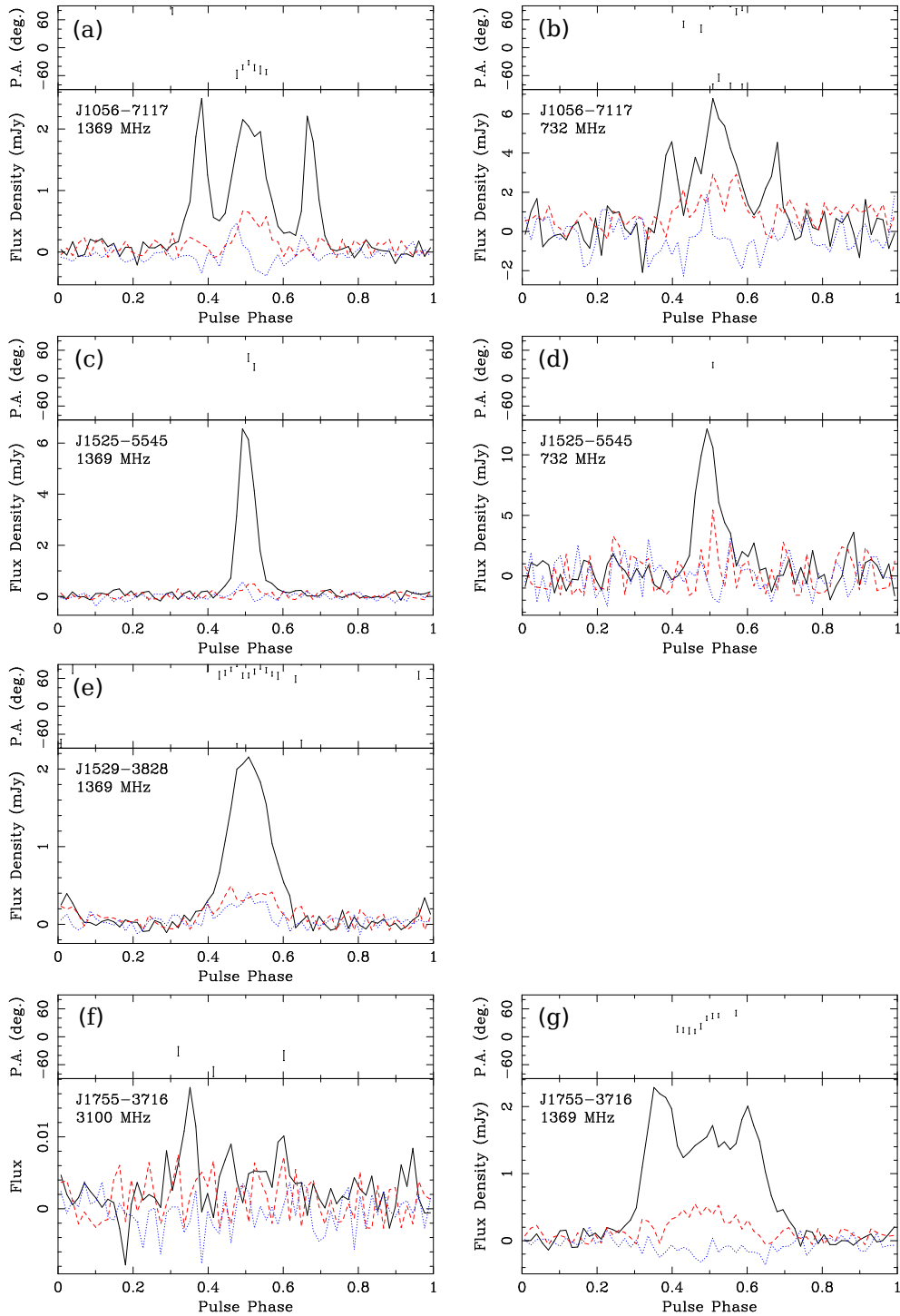


Figure 5.1: Polarisation profiles of PSRs J1056-7117 at (a) 1369 and (b) 732 MHz, J1525-5545 at (c) 1369 and (d) 732 MHz, J1529-3828 at (d) 1369 MHz, and J1755-3716 at (e) 3100 and (f) 1369 MHz. The upper panel shows the RM-corrected P.A. variation in longitude with respect to the celestial north. The lower panel shows the integrated profile where the black solid line, red dashed line and blue dotted line represent total intensity, linear and circular polarisation respectively.

Table 5.2: TEMPO2 best-fit parameters for the four newly-discovered MSPs. Values in parentheses are the nominal 1σ uncertainties in the last digits. The last panel shows derived parameters, the respective equations for which can be found in Lorimer & Kramer (2005), except for the DM distance which is derived according to Cordes & Lazio (2002).

Parameter	J1056–7117	J1525–5545	J1529–3828	J1755–3716
Right ascension, α (J2000)	10:56:45.980(4)	15:25:28.1340(2)	15:29:15.1066(10)	17:55:35.4462(4)
Declination, δ (J2000)	–71:17:53.394(14)	–55:45:49.842(5)	–38:28:45.85(3)	–37:16:10.78(4)
Galactic longitude, l ($^\circ$)	293.933	323.439	333.886	353.882
Galactic latitude, b ($^\circ$)	–10.458	0.851	14.728	–6.041
Spin frequency, ν (Hz)	38.0088284880(10)	88.02908501431(14)	117.8372326493(7)	78.2101189443(6)
Spin period, P (ms)	26.3096769823(7)	11.359881791766(18)	8.48628211573(5)	12.78606928998(9)
Frequency derivative, $\dot{\nu}$ (s^{-2})	$-9.1(9)\times 10^{-17}$	$-1.018(4)\times 10^{-15}$	$-3.75(18)\times 10^{-16}$	$-1.9(2)\times 10^{-16}$
Period derivative, \dot{P}	$6.3(6)\times 10^{-20}$	$1.313(5)\times 10^{-19}$	$2.70(13)\times 10^{-20}$	$3.1(3)\times 10^{-20}$
Dispersion measure, DM (cm^{-3} pc)	93.04(4)	126.934(7)	73.62(2)	167.603(19)
Orbital period, P_{orb} (days)	9.1387994(5)	0.9903149542(7)	119.674809(16)	11.5156057(3)
Projected semi-major axis, x (lt-s)	4.14855(2)	4.710520(6)	29.34054(2)	10.645131(12)
Epoch of ascending node, T_{asc} (MJD)	57436.53532(7)	55891.5285616(2)	55941.60(16) [†]	55958.790341(9)
$e \sin \omega$, ε_1 (10^{-6})	6(8)	–4.4(17)	– [†]	–7(2)
$e \cos \omega$, ε_2 (10^{-6})	–12(10)	–1.8(16)	– [†]	12(3)
Inferred eccentricity, e (10^{-6})	14(10)	4.8(17)	168.6(14) [†]	14(3)
Longitude of periastron, ω ($^\circ$)	150(30)	247(19)	282.2(4)	329(9)
Minimum companion mass*, $m_{\text{c,min}}$ (M_\odot)	0.13	0.81	0.16	0.30
Median companion mass**, $m_{\text{c,med}}$ (M_\odot)	0.15	0.99	0.19	0.35
Binary model	ELL1	ELL1	DD	ELL1
First TOA (MJD)	55954.5	55987.6	55905.0	56053.9
Last TOA (MJD)	56491.1	56510.5	56510.5	56510.6
Timing epoch (MJD)	57436.5	55891.5	55847.0	55958.8
Points in fit	24	25	31	27
Weighted RMS residuals (μs)	41	8.3	51	19
Reduced χ^2 [‡]	0.9	0.9	2.0	0.7
Mean flux density at 1.4-GHz, S_{1400} (mJy)	0.34	0.33	0.16	0.53
Pulse width at 50 per cent of peak, W_{50} ($^\circ$)	69	17	52	110
Rotation measure, RM (rad m^{-2})	–22(8)	–19(9)	–29(9)	54(3)
DM distance (kpc)	2.6	2.4	2.2	3.9
Characteristic age, τ_c (Myr)	6.6×10^3	1.4×10^3	5.0×10^3	6.4×10^3
Spin down energy loss rate, \dot{E} (10^{33} erg s^{-1})	0.14	3.5	1.7	0.57
\dot{E}/d^2 (10^{33} erg kpc^{-2} s^{-1})	0.021	0.62	0.36	0.037
Characteristic dipole surface mag- netic field strength at equator, B_{eq} (10^8 G)	13	12	4.9	6.5

* $m_{\text{c,min}}$ is calculated for an orbital inclination of $i = 90^\circ$ and an assumed pulsar mass of $1.35 M_\odot$.

** $m_{\text{c,med}}$ is calculated for an orbital inclination of $i = 60^\circ$ and an assumed pulsar mass of $1.35 M_\odot$.

† For PSR J1529–3228 the DD model is used. We quote T_0 instead of T_{asc} . e is directly fitted for and not inferred from the ε parameters.

‡ The reduced χ^2 stated here represents the value before the application of EFAC. Note that the rest of the timing solutions have EFACs incorporated, bringing the reduced χ^2 to unity.

Table 5.3: TEMPO2 best-fit parameters using the ELL1 timing model. Values in parentheses are the nominal 1σ uncertainties in the last digits. If only an upper limit is constrained, we quote it at the 2σ level. For repeated footnotes refer to Table 5.2.

Parameter	J1337–6423	J1446–4701	J1502–6752	J1543–5149
Right ascension, α (J2000)	13:37:31.883(2)	14:46:35.71391(2)	15:02:18.615(2)	15:43:44.1498(2)
Declination, δ (J2000)	–64:23:04.915(9)	–47:01:26.7675(4)	–67:52:16.759(18)	–51:49:54.685(2)
Galactic longitude, l ($^\circ$)	307.889	322.500	314.798	327.920
Galactic latitude, b ($^\circ$)	–1.958	+11.425	–8.067	+2.479
Spin frequency, ν (Hz)	106.11873496995(19)	455.644016442381(13)	37.39097199147(8)	486.15423208300(13)
Spin period, P (ms)	9.423406717796(17)	2.19469577985000(6)	26.74442376699(6)	2.0569603924156(5)
Frequency derivative, $\dot{\nu}$ (s^{-2})	$-2.78(2)\times 10^{-16}$	$-2.0367(4)\times 10^{-15}$	$-4.397(19)\times 10^{-16}$	$-3.819(3)\times 10^{-15}$
Period derivative, \dot{P}	$2.47(2)\times 10^{-20}$	$9.810(2)\times 10^{-21}$	$3.145(13)\times 10^{-19}$	$1.6161(14)\times 10^{-20}$
Dispersion measure, DM (cm^{-3} pc)	259.2(13)	55.83202(14)	151.2(18)	50.93(14)
Proper motion in α , μ_α (mas yr^{-1})	–6(6)	–4.0(2)	–6(9)	–4.3(14)
Proper motion in δ , μ_δ (mas yr^{-1})	–7(5)	–2.0(3)	–14(16)	–4(2)
Orbital period, P_{orb} (days)	4.785333912(5)	0.27766607732(13)	2.48445723(18)	8.060773125(9)
Projected semi-major axis, x (lt-s)	13.086505(5)	0.0640118(3)	0.31754(2)	6.480288(2)
Epoch of ascending node, T_{asc} (MJD)	55234.7703674(6)	55647.8044392(2)	55421.21199(3)	54929.0678261(11)
$e \sin \omega$, ε_1 (10^{-6})	18.3(8)	18(8)	21(140)	20.8(5)
$e \cos \omega$, ε_2 (10^{-6})	7.7(9)	–11(9)	–23(150)	5.3(6)
Inferred eccentricity, e (10^{-6})	19.8(8)	21(8)	<330	21.5(5)
Longitude of periastron, ω ($^\circ$)	67(2)	120(20)	130(260)	75.6(16)
Minimum companion mass*, $m_{\text{c,min}}$ (M_\odot)	0.78	0.019	0.022	0.22
Median companion mass**, $m_{\text{c,med}}$ (M_\odot)	0.95	0.022	0.025	0.26
Binary model	ELL1	ELL1	ELL1	ELL1
First TOA (MJD)	55540.0	55460.0	55360.4	55540.8
Last TOA (MJD)	56510.2	56497.2	56510.3	56510.3
Timing epoch (MJD)	55234.7	55647.8	55421.2	55522
Points in fit	76	154	57	52
Weighted RMS residuals (μs)	26	2.1	87	6.9
Reduced χ^2 ‡	0.9	1.0	1.0	1.2
Mean flux density at 1.4-GHz, S_{1400} (mJy)	0.29	0.40	0.69	0.55
Pulse width at 50 per cent of peak, W_{50} ($^\circ$)	28	18	40	49
DM Distance, d (kpc)	5.1	1.5	4.2	2.4
Transverse velocity, V_T (km s^{-1})	230(140)	32(8)	< 960	70(30)
Intrinsic period derivative, \dot{P}_{int} (10^{-20})	1.0(13)	0.972(2)	15(14)	1.54(3)
Characteristic age††, τ_c (Myr)	1.4×10^4	3.6×10^3	2.7×10^3	2.1×10^3
Spin down energy loss rate††, \dot{E} (10^{33} erg s^{-1})	0.51	36	0.32	70
\dot{E}/d^2 †† (10^{33} erg kpc^{-2} s^{-1})	0.020	16	0.018	12
Characteristic dipole surface magnetic field strength at equator††, B_{eq} (10^8 G)	3.2	1.5	21	1.8

†† These parameters are derived from the intrinsic period derivatives \dot{P}_{int} . For the derivation of \dot{P}_{int} refer to Section 5.3.3.

Table 5.4: TEMPO2 best-fit parameters using the ELL1 timing model. Values in parentheses are the nominal 1σ uncertainties in the last digits. For repeated footnotes refer to Tables 5.2 and 5.3.

Parameter	J1622–6617	J1719–1438	J1801–3210	J1811–2405
Right ascension, α (J2000)	16:22:03.6681(4)	17:19:10.07293(5)	18:01:25.8896(2)	18:11:19.85315(2)
Declination, δ (J2000)	–66:17:16.978(6)	–14:38:00.942(4)	–32:10:53.714(17)	–24:05:18.365(11)
Galactic longitude, l ($^\circ$)	321.977	8.858	358.922	7.073
Galactic latitude, b ($^\circ$)	–11.56	+12.838	–4.577	–2.559
Spin frequency, ν (Hz)	42.33082901464(2)	172.707044602370(13)	134.16363857901(4)	375.856014397575(9)
Spin period, P (ms)	23.623444739389(12)	5.7901517700238(4)	7.453584373467(2)	2.66059331683918(7)
Frequency derivative, $\dot{\nu}$ (s^{-2})	$-1.054(4) \times 10^{-16}$	$-2.399(2) \times 10^{-16}$	$8(7) \times 10^{-19}$	$-1.8898(2) \times 10^{-15}$
Period derivative, \dot{P}	$5.88(2) \times 10^{-20}$	$8.044(8) \times 10^{-21}$	$-4(4) \times 10^{-23}$	$1.33780(16) \times 10^{-20}$
Dispersion measure, DM ($\text{cm}^{-3} \text{pc}$)	88.024(9)	36.862(4)	177.713(4)	60.6005(17)
Proper motion in α , μ_α (mas yr^{-1})	–3(2)	1.9(4)	–8(2)	0.53(13)
Proper motion in δ , μ_δ (mas yr^{-1})	–6(4)	–11(2)	–11(10)	–¶
Orbital period, P_{orb} (days)	1.640635150(8)	0.0907062900(12)	20.77169942(8)	6.2723020692(12)
Projected semi-major axis, x (lt-s)	0.979386(5)	0.0018212(7)	7.809317(4)	5.7056616(3)
Epoch of ascending node, T_{asc} (MJD)	55253.087283(2)	55235.516505(8)	55001.934484(2)	55136.16862345(7)
$e \sin \omega$, ε_1 (10^{-6})	–4(12)	–700(700)	1.7(11)	1.46(10)
$e \cos \omega$, ε_2 (10^{-6})	14(11)	400(700)	1.0(10)	0.75(10)
Inferred eccentricity, e (10^{-6})	14(11)	800(700)	2.0(11)	1.64(10)
Longitude of periastron, ω ($^\circ$)	340(40)	300(50)	50(30)	62(3)
Minimum companion mass*, $m_{\text{c,min}}$ (M_\odot)	0.092	0.0011	0.14	0.23
Median companion mass**, $m_{\text{c,med}}$ (M_\odot)	0.11	0.0013	0.16	0.27
Binary model	ELL1	ELL1	ELL1	ELL1
First TOA (MJD)	55256.9	55237.0	54996.4	55136.1
Last TOA (MJD)	56510.3	56491.6	56485.7	56411.2
Timing epoch (MJD)	55253.1	55235.5	55001.9	55208.5
Points in fit	86	236	135	97
Weighted RMS residuals (μs)	31	10	37	2.8
Reduced χ^2 ‡	1.3	2.1	1.6	2.6
Mean flux density at 1.4-GHz, S_{1400} (mJy)	0.60	0.42	0.32	0.37
Pulse width at 50 per cent of peak, W_{50} ($^\circ$)	12	19	30	16
DM Distance, d (kpc)	2.2	1.2	4.0	1.8
Transverse velocity, V_{T} (km s^{-1})	40(20)	60(20)	270(170)	–¶
Intrinsic period derivative, \dot{P}_{int} (10^{-20})	5.0(8)	0.54(11)	$-2.7(17)^\dagger$	$1.284(15)^\P$
Characteristic age ^{††} , τ_{c} (Myr)	7.5×10^3	1.7×10^4	$>1.5 \times 10^4^\dagger$	3.3×10^3
Spin down energy loss rate ^{††} , \dot{E} ($10^{33} \text{erg s}^{-1}$)	0.15	1.1	$< 0.78^\dagger$	27
\dot{E}/d^2 ^{††} ($10^{33} \text{erg kpc}^{-2} \text{s}^{-1}$)	0.031	0.76	$< 0.048^\dagger$	8.3
Characteristic dipole surface magnetic field strength at equator ^{††} , B_{eq} (10^8G)	11	1.8	$< 2.5^\dagger$	1.9

[†] For PSR J1801–3210 the potential causes of this apparent negative \dot{P}_{int} is discussed in Section 5.3.3.2. The period derivative related parameters are derived with the 2σ upper limit of $\dot{P}_{\text{int}} < 8.1 \times 10^{-21}$.

[¶] For PSR J1811–2405 we have fixed the unconstrained μ_δ at zero because this pulsar is very close to the ecliptic plane. Its V_{T} is therefore also not measurable. The derived \dot{P}_{int} only symbolises a lower limit without correcting for any Shklovskii contribution in μ_δ .

Table 5.5: TEMPO2 best-fit parameters using the DD timing model, except in the case of PSR J1731–1847, for which we have instead used BTX model to accommodate the higher order orbital period changes. Values in parentheses are the nominal 1σ uncertainties in the last digits. For repeated footnotes refer to Tables 5.2 and 5.3.

Parameter	J1017–7156	J1125–5825	J1708–3506	J1731–1847
Right ascension, α (J2000)	10:17:51.32828(2)	11:25:44.36564(5)	17:08:17.62215(10)	17:31:17.609823(17)
Declination, δ (J2000)	–71:56:41.64586(11)	–58:25:16.8798(4)	–35:06:22.640(4)	–18:47:32.666(3)
Galactic longitude, l ($^\circ$)	291.558	291.893	350.469	6.880
Galactic latitude, b ($^\circ$)	–12.55	+2.602	+3.124	+8.151
Spin frequency, ν (Hz)	427.621905105409(6)	322.350432991279(16)	221.96775106948(3)	426.51934403983(2)
Spin period, P (ms)	2.33851444011854(3)	3.10221391893416(16)	4.5051589484588(6)	2.34455954688563(11)
Frequency derivative, $\dot{\nu}$ (s^{-2})	$-4.0584(12) \times 10^{-16}$	$-6.3280(2) \times 10^{-15}$	$-5.627(5) \times 10^{-16}$	$-4.6220(8) \times 10^{-15}$
Period derivative, \dot{P}	$2.2193(6) \times 10^{-21}$	$6.0899(2) \times 10^{-20}$	$1.1421(11) \times 10^{-20}$	$2.5407(4) \times 10^{-20}$
Dispersion measure, DM ($\text{cm}^{-3} \text{pc}$)	94.22407(3) [♣]	124.7946(8)	146.732(2)	106.4711(6)
Proper motion in α , μ_α (mas yr^{-1})	–7.31(6)	–10.0(3)	–5.3(8)	–1.7(3)
Proper motion in δ , μ_δ (mas yr^{-1})	6.76(5)	2.4(3)	–2(3)	–6(3)
Parallax, π (mas)	3.9(12) [◇]	–	–	–
Orbital period, P_{orb} (days)	6.511905(2)	76.40321683(5)	149.1332226(4)	0.3111341185(10)
First derivative of orbital frequency, \dot{n}_b (Hz s^{-1})	–	–	–	$1.50(9) \times 10^{-19}$
Second derivative of orbital frequency, \ddot{n}_b (Hz s^{-2})	–	–	–	$-5.0(2) \times 10^{-27}$
Projected semi-major axis, x (lt-s)	4.83004509(11)	33.6383599(8)	33.584236(2)	0.1201611(6)
Epoch of periastron, T_0 (MJD)	55335.0641(3)	55181.5562(15)	55206.801(10)	55132.4363(10)
Eccentricity, e	0.00014204(2)	0.00025724(3)	0.00024449(10)	$2.9(6) \times 10^{-5}$
Longitude of periastron, ω ($^\circ$)	329.682(18)	260.128(7)	180.00(2)	144(12)
Minimum companion mass*, $m_{c,\text{min}}$ (M_\odot)	0.19	0.26	0.16	0.033
Median companion mass**, $m_{c,\text{med}}$ (M_\odot)	0.22	0.31	0.19	0.039
Change in x , \dot{x}	$9.1(17) \times 10^{-15}$	–	–	–
Variation in ω , $\dot{\omega}$ ($^\circ \text{yr}^{-1}$)	0.022(9)	–	–	–
Binary model	DD	DD	DD	BTX
First TOA (MJD)	55343.2	55131.8	55129.1	55138.1
Last TOA (MJD)	56480.0	56510.0	56491.5	56302.1
Timing epoch (MJD)	55329.1	55126.3	55132.9	55215.1
Points in fit	332	181	99	196
Weighted RMS residuals (μs)	0.8	5.5	7.4	3.7
Reduced χ^2 ‡	2.0	1.5	0.7	1.9
Mean flux density at 1.4-GHz, S_{1400} (mJy)	1.00	0.86	1.31	0.37
Pulse width at 50 per cent of peak, W_{50} ($^\circ$)	10	36	44	20
DM Distance, d (kpc)	3.0 [◇]	2.6	2.8	2.5
Transverse velocity, V_T (km s^{-1})	140(30)	120(30)	70(20)	80(40)
Intrinsic period derivative, \dot{P}_{int} (10^{-20})	0.12(2)	5.94(3)	0.85(9)	2.40(7)
Characteristic age ^{††} , τ_c (Myr)	3.1×10^4	8.3×10^2	8.4×10^3	1.5×10^3
Spin down energy loss rate ^{††} , \dot{E} ($10^{33} \text{erg s}^{-1}$)	3.7	79	3.7	74
\dot{E}/d^2 ^{††} ($10^{33} \text{erg kpc}^{-2} \text{s}^{-1}$)	0.41	12	0.47	12
Characteristic dipole surface magnetic field strength at equator ^{††} , B_{eq} (10^8G)	0.53	4.3	2.0	2.4

♣ Temporal DM variations have also been taken into account in the model fit, see explanation in Section 5.3.1.

◇ We disregard the 3σ π measurement when deriving the distance of PSR J1017–7156, as it is likely to be influenced by the Lutz-Kelker bias for example discussed in Verbiest et al. (2010).

5.3 Updated timing of 12 HTRU millisecond pulsars

We have achieved considerable improvement in the timing accuracy for 12 HTRU MSPs compared with results published in their respective discovery papers (Bates et al., 2011; Keith et al., 2012; Bailes et al., 2011). This is thanks to the now longer timing baseline of more than three years in all cases, and only slightly less for PSR J1337–6423 which has 2.7 yr of timing data. The timing parameters resulting from the best fits to the expanded set of TOAs are presented in Tables 5.3 and 5.4 for pulsars fitted with the ELL1 timing model and in Table 5.5 for pulsars fitted with the DD timing model.

In the following we discuss the physical implications arising from our timing measurements, including DM variations (Section 5.3.1), proper motion and transverse velocities (Section 5.3.2), intrinsic period derivatives (Section 5.3.3), binary companions and mass functions (Section 5.3.4), Galactic height distributions (Section 5.3.5), orbital eccentricities (Section 5.3.6), change in projected semi-major axis (Section 5.3.7), orbital period variation (Section 5.3.8), variation in the longitude of periastron (Section 5.3.9), and gamma-ray associations (Section 5.3.10).

5.3.1 Dispersion measure variations

Temporal variations in DM, due to turbulence in the ionised ISM and the changing line of sight to the pulsar, are in theory present in the TOAs of every pulsar (see e.g., Petroff et al., 2013). However this is typically not observable in slow pulsars since they have limited timing precision. In contrast, for MSPs such variations in DM can become significant and thus require special data treatment (You et al., 2007).

Indeed for the high-precision timing of PSR J1017–7156 we identified significant temporal variations in its DM measurement, implying changes in the electron density in the ISM along the line of sight over a time scale of a few months. We have attempted to model this variation via three correction methods, firstly by fitting DM variations across short ranges of TOAs while holding fixed all other parameters, secondly by including higher order DM derivatives and thirdly by the DM model described in Keith et al. (2013). In Fig. 5.2 we plot the manually identified values of DM across every few TOAs in black. We plot the best-fit curve from the timing solution of TEMPO2, employing up to eight DM-derivatives as the green dashed line. We plot the DM model derived using the method outlined in Keith et al. (2013) as red crosses, and the red solid line joining them shows the resulting DM model. It can be seen that the DM derivatives provide a smooth fit to the DM variations, however there are still small scale variations that are not properly accounted for. On the other hand, the DM model essentially creates a linear interpolation between DM offsets identified at specific epochs (note that here we have adopted a gap of 50 days between successive DM offsets), and hence can be tailor-made to follow more closely variations on all scales. We conclude that the DM model of Keith et al. (2013) gives a more successful fit and hence have adopted this for the timing solution of PSR J1017–7156.

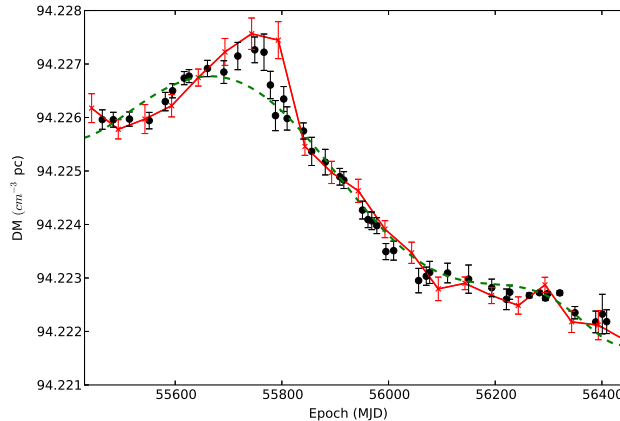


Figure 5.2: DM variations for PSR J1017–7156 with time. The manually identified DM variations across every few TOAs are plotted as black filled circles. The green dashed line shows the best-fit curve from timing solution generated in TEMPO2, employing DM-derivative terms up to the eighth order. The red crosses are the DM offsets identified by applying the method in accordance with the description in Keith et al. (2013) and the red solid line joining them shows the resulting DM model.

5.3.2 Proper motion and transverse velocities

The proper motion (μ) of a pulsar introduces a positional offset over time and is measurable from pulsar timing data. Within our sample of 12 MSPs with extended timing solutions, we have measured five new proper motions with significances greater than 3σ , for PSRs J1017–7156, J1125–5825, J1446–4701, J1708–3506 and J1719–1438. PSR J1811–2405 is very close to the ecliptic plane with $(\lambda, \beta) = (272.586^\circ, -0.675^\circ)$ which means its proper motion in ecliptic latitude (μ_β) cannot be well-constrained. With a λ so close to 270° , the translation from ecliptic frame to equatorial frame would have almost no rotation. This implies that the large uncertainty associated with β is only inherited in the declination, δ , without also contaminating the right ascension, α . Hence for PSR J1811–2405 we can choose to continue using the equatorial coordinates and we fixed μ_δ at zero for the rest of the analysis. For the four newly-discovered MSPs in this paper, their time spans are not yet long enough for proper motion to be detected with significance.

From μ and their respective pulsar distances, d , we can derive their corresponding transverse velocities, V_T , with the following equation,

$$V_T = 4.74 \text{ km s}^{-1} \times \left(\frac{\mu}{\text{mas yr}^{-1}} \right) \times \left(\frac{d}{\text{kpc}} \right). \quad (5.2)$$

In this work we have calculated pulsar distances based on the NE2001 electron density model (Cordes & Lazio, 2002) and we assume an associated uncertainty of 25 per cent for each DM-derived distance. MSP proper motion measurements are relatively rare and hence there are not many derived velocities (only about 40 currently published values in the literature), making it difficult to place constraints on MSP velocity dis-

Table 5.6: Table listing the derived \dot{P}_{shk} and \dot{P}_{gal} for the 12 MSPs with updated timing solutions. The final column shows the inferred \dot{P}_{int} . Values in parentheses are the nominal 1σ uncertainties in the last digits.

PSR	\dot{P}_{obs} (10^{-20})	\dot{P}_{shk} (10^{-20})	\dot{P}_{gal} (10^{-20})	\dot{P}_{int} (10^{-20})
J1017–7156	0.22193(6)	0.16(4)	−0.067(15)	0.12(2)
J1125–5825	6.0899(2)	0.20(5)	−0.066(19)	5.94(3)
J1337–6423	2.47(2)	1.8(13)	−0.40(15)	1.0(13)
J1446–4701	0.9810(2)	0.016(4)	−0.007(2)	0.972(2)
J1502–6752	31.45(13)	16(14)	−0.8(3)	15(14)
J1543–5149	1.6161(14)	0.06(3)	0.0124(13)	1.54(3)
J1622–6617	5.88(2)	1.0(8)	−0.17(7)	5.0(8)
J1708–3506	1.1421(11)	0.14(7)	0.14(4)	0.85(9)
J1719–1438	0.8044(8)	0.23(10)	0.028(9)	0.54(11)
J1731–1847	2.5407(4)	0.08(6)	0.048(14)	2.40(7)
J1801–3210	−0.004(4)	2.3(16)	0.41(15)	−2.7(17)*
J1811–2405	1.33780(16)	0.00035(18) [†]	0.052(15)	1.284(15)

* The potential causes of this apparent negative period derivative are discussed in the main text of Section 5.3.3.2.

[†] This is a lower limit of \dot{P}_{shk} since PSR J1811–2405 is very close to the ecliptic plane (refer to Section 5.3.2). Its μ_δ cannot be constrained and is fixed to zero.

tribution models. The latest MSP velocity discussions can be found in [Toscano et al. \(1999\)](#) and [Hobbs et al. \(2005\)](#), proposing an average velocity for recycled MSPs of $85 \pm 13 \text{ km s}^{-1}$ and $87 \pm 13 \text{ km s}^{-1}$ respectively. [Hobbs et al. \(2005\)](#) also quoted a median velocity for recycled MSPs of 73 km s^{-1} . Our new V_T measurements largely agree with these previous results (refer to Table 5.3 to 5.5). Note that we believe the high V_T of 670 and 350 km s^{-1} reported for PSRs J1708–3506 and J1731–1847 in [Bates et al. \(2011\)](#) should in fact be corrected to more modest values of 70 ± 20 and $80 \pm 40 \text{ km s}^{-1}$ respectively.

5.3.3 Observed and inferred intrinsic period derivatives

The vast majority of pulsars are rotation-powered objects and hence their respective period derivatives (\dot{P}) are fundamental to their identities. The observed period derivatives (\dot{P}_{obs}) however contain a contribution from kinematic effects ([Shklovskii, 1970](#)) and acceleration due to the Galactic potential ([Damour & Taylor, 1991](#)). Determination of the intrinsic period derivative is important for properly placing pulsars in the P - \dot{P} diagram from which physical conclusions (such as magnetic field strength, characteristic ages) may be drawn. To obtain the intrinsic period derivative (\dot{P}_{int}) we

employed the following equation,

$$\dot{P}_{\text{int}} = \dot{P}_{\text{obs}} - \dot{P}_{\text{shk}} - \dot{P}_{\text{gal}}. \quad (5.3)$$

The term \dot{P}_{shk} accounts for the apparent acceleration that arises from the transverse motion of the pulsar. It is related to the pulsar spin period, P , the proper motion, μ , and the pulsar distance, d , by the following equation from Shklovskii (1970),

$$\dot{P}_{\text{shk}} = \left(\frac{P}{c}\right) d \mu^2. \quad (5.4)$$

The term \dot{P}_{gal} accounts for difference in the line-of-sight components of the acceleration of the pulsar and the Solar System under the influence of the Galactic gravitational potential. There exist several Galactic potential models in the literature, and we have chosen the one described in Paczynski (1990). This model reproduces a flat rotation curve and uses a Solar Galactocentric distance R_0 of 8 kpc and a Solar Galactic rotation velocity of 220 km s^{-1} .

Table 5.6 lists the \dot{P} contributions as calculated for the 12 MSPs with updated timing solutions in our sample. Monte Carlo simulations with 1,000,000 runs per pulsar have been used to estimate the associated error. Note that the errors in \dot{P}_{shk} and \dot{P}_{gal} do not reflect the effect of errors in the distance estimates. The results are illustrated in Fig. 5.3, which is a P - \dot{P} diagram around the region where MSPs are located. The \dot{P}_{obs} and the corrected \dot{P}_{int} of the 12 MSPs studied in this paper are plotted, together with other known pulsars in this region.

Some of the results (noticeably those of PSRs J1337–6423 and J1502–6752) have large associated errors and should be considered with caution. One reason is that \dot{P}_{shk} relies on the square of V_T , which is in turn dependent on proper motion as seen from Equation (5.2). Hence \dot{P}_{shk} is only meaningful for MSPs with well-constrained proper motion measurements. Additionally, \dot{P}_{gal} is dependent on the distance of the pulsar, d . As mentioned in Section 5.3.2, the DM-derived distance is thought to have ~ 25 per cent error, and can be much larger for individual pulsars.

5.3.3.1 PSR J1017–7156

Disregarding these two unconstrained measurements, PSR J1017–7156 stands out with one of the smallest inferred intrinsic \dot{P} at a value of 1.2×10^{-21} . We are aware that if red noise is present in the data this could potentially also contaminate our \dot{P} measurement. However if we include the frequency second derivative in the model fit in an attempt to whiten the data with a quadratic component, the \dot{P} measurement remains statistically consistent. PSR J1017–7156 is thus located at the bottom left of the P - \dot{P} diagram, which yields a characteristic age, $\tau_c \equiv P/(2\dot{P})$, of 31 Gyr, i.e. larger than the Hubble age. Note that τ_c is by no means a reliable age indicator for MSPs, since it is only applicable for pulsars which have a braking index $n = 3$ and an initial spin period (P_0) much less than the current spin period, which is not thought to be the case for MSPs. However for MSPs with such small \dot{P}_{obs} like that of PSR J1017–7156, we can deduce that the MSP was probably born with small initial period derivative and must

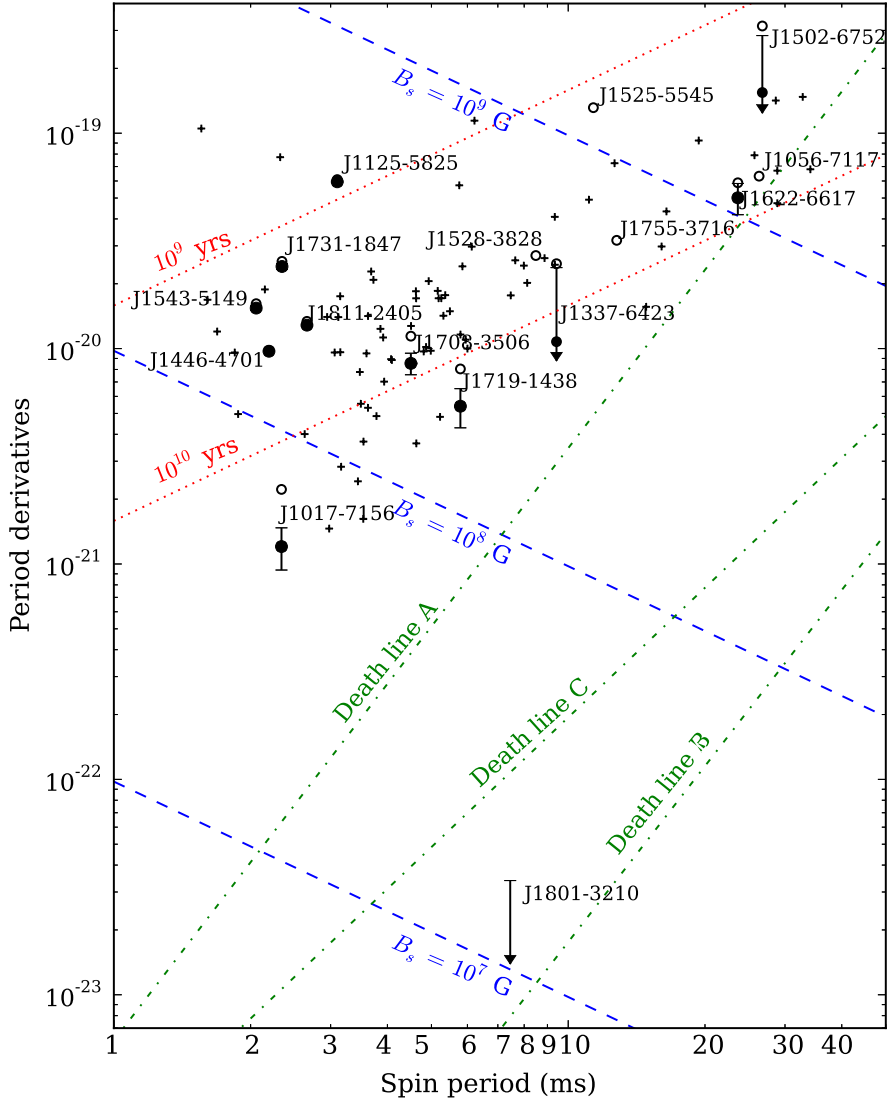


Figure 5.3: The P - \dot{P} diagram plotted for the region of MSPs. Black open circles show the \dot{P}_{obs} for all 16 MSPs in this work, except PSR J1801–3210 for which a 2σ upper limit is shown because we have a measured \dot{P}_{obs} value consistent with zero within 1σ even with four years of timing data. For the 12 MSPs in this work with updated timing solutions, we are able to plot also their corrected locations of \dot{P}_{int} in the P - \dot{P} diagram represented by black filled circles with associated error bars. Two of the MSPs (PSRs J1337–6423 and J1502–6752) have unconstrained \dot{P}_{int} , hence we plot the 95 per cent confidence upper limit. Note that PSR J1801–3210 has an apparent negative \dot{P}_{int} even at the 95 per cent confidence upper limit therefore we show only its \dot{P}_{obs} . The red dotted lines correspond to characteristic ages of 10^9 and 10^{10} yr respectively, whereas the blue dashed lines show derived surface magnetic field strength at the equator (B_{eq}) of 10^7 , 10^8 and 10^9 G. Both of these sets of lines are derived according to equations in Lorimer & Kramer (2005). The green dot-dashed lines plot the three pulsar death lines as described in Chen & Ruderman (1993), derived from the theoretical relationship between surface magnetic field strength at the polar region (B_p) and pulsar spin period (P).

not have moved very far from its current location on the $P-\dot{P}$ diagram since its birth (Tauris et al., 2012). The derived surface magnetic field strength at the equator³ of PSR J1017–7156 is also at one of the lowest known at 5.3×10^7 G.

5.3.3.2 PSR J1801–3210

There is one peculiar case, PSR J1801–3210, for which no significant period derivative has been measured, even with more than four years of timing data. The best-fit solution in TEMPO2 shows a \dot{P}_{obs} of $-4 \pm 4 \times 10^{-23}$, an extremely small number compared to that of typical MSPs (\dot{P}_{obs} of the order of 10^{-19} to 10^{-20}). A 2.7σ \dot{P} value of $0.265(97) \times 10^{-20}$ was presented in the initial discovery paper by Bates et al. (2011) which at that time had just over one year of timing data, however this value is inconsistent with our current longer time baseline TOAs. Shortening our data span to the same epoch as that in Bates et al. (2011) results in an unconstrained \dot{P}_{obs} measurement of $0.2(20) \times 10^{-20}$, eliminating the possibility of an actual change in period derivative over time.

Referring again to Equation (5.3), proper-motion-induced \dot{P}_{shk} has an always positive contribution to \dot{P}_{obs} , so that \dot{P}_{int} will be even smaller. \dot{P}_{gal} however could have a positive or negative contribution depending on the relative location of the pulsar in the Galaxy with respect to the Earth.

PSR J1801–3210 has a proper motion measurement of $15(7) \text{ mas yr}^{-1}$, corresponding to a positive \dot{P}_{shk} of the order of 10^{-20} . The Paczynski (1990) Galactic potential model shows that at the NE2001 DM-derived distance of 4 kpc PSR J1801–3210 would be accelerated away from the Sun, giving a positive \dot{P}_{gal} of the order of 10^{-21} (Table 5.6) to further decrease the already negative \dot{P}_{obs} . Even if we assume the proper motion to be zero to get the smallest possible contribution from \dot{P}_{shk} , we still cannot overcome this apparent negative \dot{P}_{int} at the given DM distance of 4 kpc, since the \dot{P}_{gal} is positive and dominates the tiny \dot{P}_{obs} of 10^{-23} . We acknowledge that the Paczynski (1990) model consists basically of only three elements: a bulge, a disk and the surrounding halo. However this is considered a valid approximation, and for example the effect of spiral arm structure should not significantly skew the model.

In the following we consider other potential explanations to this apparent negative \dot{P}_{int} , i.e. effects that would have contributed to the \dot{P}_{obs} but are not yet accounted for in Equation (5.3). We discuss the cases of (a) acceleration due to local stars; (b) acceleration due to giant molecular clouds (GMCs); and (c) acceleration due to a third orbiting object if PSR J1801–3210 is in a triple system.

If there exists a third body (with mass M_3) located near the pulsar, in a direction towards the Earth and close to the line of sight, it will potentially cause a radial acceleration of PSR J1801–3210 towards the Earth. We can express the mass of the third body required to produce a \dot{P} contribution of \dot{P}_{M_3} as,

$$M_3 = \left(\frac{\dot{P}_{M_3}}{P_{\text{spin}}} \right) \left(\frac{c r^2}{G} \right) (\cos \theta)^{-1}, \quad (5.5)$$

³Note throughout the paper we differentiate between the derived surface magnetic field at the polar region (B_p), and that of the equatorial region (B_{eq}) which is only half the strength comparing to the polar region.

where r is the distance between the third body and the pulsar, G is Newton's gravitational constant and θ is the angle between the direction from the pulsar to the third body and the direction from the pulsar to the Sun. We imagine the scenario of $\theta \approx 0^\circ$ where the line-of-sight acceleration induced on the pulsar is the largest, and we first examine the potential contribution from stars located near the pulsar. The probability distribution of fluctuation in Galactic acceleration due to local clustering centres has been studied in the literature (see e.g., [Holtsmark, 1919](#)), and based on Equation (3.1) and (3.5b) in [Damour & Taylor \(1991\)](#) one finds for PSR J1801–3210 at 1σ confidence level,

$$|\dot{P}|_{1\sigma} = 3.3 \times 10^{-24} \left(\frac{\hat{M}}{M_\odot} \right)^{1/3} \left(\frac{\rho}{\rho_\odot} \right)^{2/3}, \quad (5.6)$$

where \dot{P}_* is the potential period derivative contribution from nearby stars, \hat{M} is the average of mass taken over the mass spectrum of the attracting centres and we use the same value of $1 M_\odot$ as in [Damour & Taylor \(1991\)](#). The local stellar-mass density, ρ_\odot , has a value of $0.06 M_\odot \text{pc}^{-3}$ according to [Mihalas & Binney \(1981\)](#) and the stellar-mass density, ρ , can be extrapolated by,

$$\rho = \rho_\odot \times \exp\left(\frac{R_0 - R}{L_{\text{disk}}}\right) \exp\left(-\frac{z}{z_h}\right), \quad (5.7)$$

where R_0 is the aforementioned Solar Galactocentric distance at 8 kpc. L_{disk} is the stellar disk scale length and z_h is the scale height of the stellar disk component, which from the most recent literature by [Bovy & Rix \(2013\)](#) $L_{\text{disk}} = 2.15 \text{ kpc}$ and $z_h = 0.4 \text{ kpc}$. R is the distance of the pulsar from the Galactic Centre, and for the case of PSR J1801–3210 it is approximately 4 kpc as derived from the NE2001 model. This corresponds to a Galactic height, z , of 0.32 kpc. Substituting these into Equations (5.7) and (5.6) gives $\rho = 0.17 M_\odot \text{pc}^{-3}$ and a tiny \dot{P}_* of the order of 10^{-24} which is unlikely to have led to the negative \dot{P}_{int} . To appreciate the improbability of this scenario we can also hypothesise a nominal \dot{P}_* of the order of -10^{-21} . From Equation (5.6) this would require ρ to be more than $300 M_\odot \text{pc}^{-3}$ and no position along the line-of-sight direction of PSR J1801–3210 has such high stellar-mass density.

Alternatively let us consider the contribution from GMCs, and again we assume that there exists such an acceleration acting upon the pulsar towards the Earth which induces a nominal \dot{P}_{GMC} of the order of -10^{-21} . GMCs typically have masses between 10^3 to $10^7 M_\odot$; substituting this into Equation (5.5) corresponds to a distance, r , of about 2 to 190 pc from the pulsar. No GMCs are known to exist near PSR J1801–3210, but not all GMCs have necessarily been detected, so this possibility cannot be ruled out. It may also be that multiple smaller molecular clouds (also known as Bok globules) act together to accelerate PSR J1801–3210 in our direction.

Another possible candidate of this third body could be a tertiary star or an exoplanet orbiting PSR J1801–3210 in a weakly-bounded hierarchical triple orbit. This third component would accelerate the pulsar system towards it, and hence if the third component happened to provide a net acceleration on PSR J1801–3210 towards the Earth it would lead to the negative \dot{P}_{int} like in the case of a GMC as mentioned above.

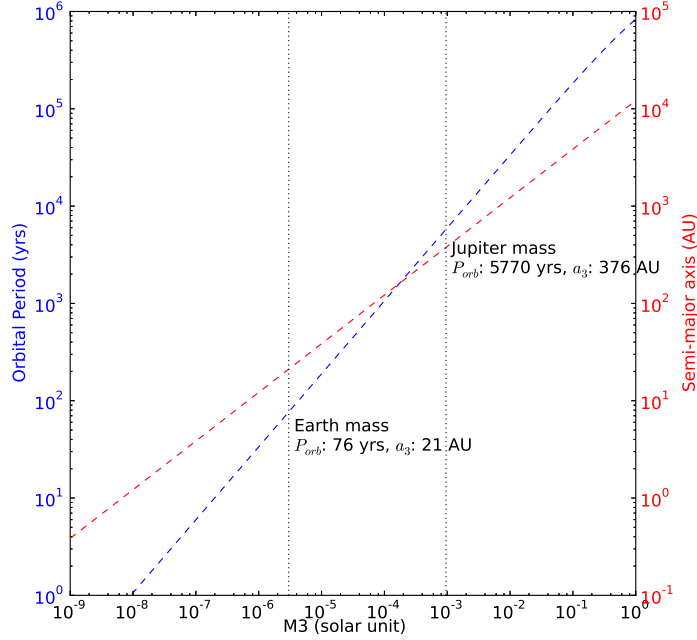


Figure 5.4: Plot showing different M_3 and the respective orbital period and semi-major axis.

We can achieve the same \dot{P}_{exo} of the order of -10^{-21} , for example with an Earth-sized exoplanet at distance of ~ 20 AU in an orbit of ~ 70 yr around PSR J1801–3210, or a Jupiter-sized exoplanet at a distance of ~ 400 AU in a large orbit of ~ 6000 yr, assuming circular orbit (Fig. 5.4).

The relative motion between the pulsar system and the exoplanet would have induced variations in the acceleration, as well as variations in the second derivative of spin frequency, $\ddot{\nu}$ (Backer et al., 1993). We do not have a significant measurement of $\ddot{\nu}$ except a 2σ upper limit of $8 \times 10^{-26} \text{ s}^{-3}$. This thus excludes the existence of a nearby exoplanet and favours the case of a further-out heavier object. However at the same time, for a third orbiting object to stay bound with the pulsar system, a very strict limit on the post-supernova (SN) recoil velocity of the inner binary is required (Hills, 1983). Precisely, the recoil velocity has to be no more than 30 km s^{-1} and 7 km s^{-1} for the case of an Earth-mass and a Jupiter-mass exoplanet respectively. According to simulations by Tauris & Bailes (1996), the recoil velocity of any surviving binary is expected to be larger than 20 km s^{-1} , even for a symmetric SN explosion, unless the pulsar formed via an accretion-induced collapse of a white dwarf (Nomoto et al., 1979). Hence, we are inclined to exclude a very distant third body with a Jupiter mass, and notice that a closer Earth-mass object would require quite some fine-tuning in the SN event to remain bound. To summarise, we conclude that this scenario of an exoplanet is possible but unlikely.

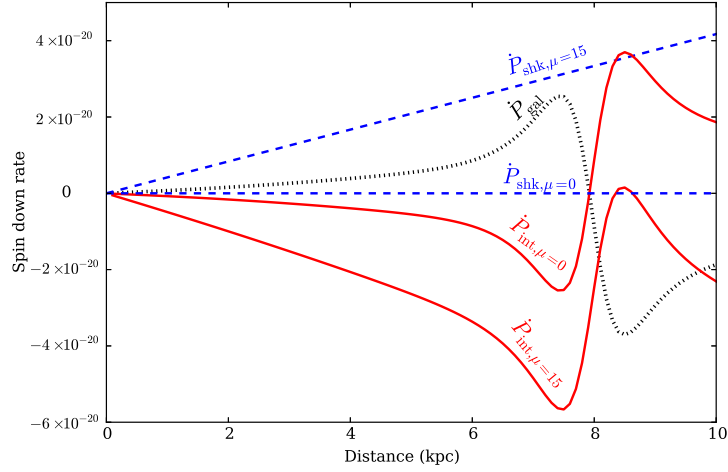


Figure 5.5: Plot showing various \dot{P} contributions for PSR J1801–3210. The black dotted line is the \dot{P}_{gal} as a function of distance and is independent of proper motion. The two blue dashed lines show the \dot{P}_{shk} caused by a proper motion (μ) of 0 and 15 mas yr^{-1} respectively. The two red solid lines show the resulting \dot{P}_{int} . In the case of $\mu = 15 \text{ mas yr}^{-1}$ the corresponding $\dot{P}_{\text{int}, \mu=15}$ is always negative. In the case of no proper motion ($\mu = 0 \text{ mas yr}^{-1}$) the corresponding $\dot{P}_{\text{int}, \mu=0}$ can become positive only after a distance of at least 8 kpc.

Finally, we consider the possibility that the NE2001 DM-derived distance of 4 kpc is significantly wrong, hence locating PSR J1801–3210 in a different quadrant of the Galaxy which would reverse the direction of the Galactic potential and the sign of \dot{P}_{gal} . In Fig. 5.5 we plot the various \dot{P} contribution as a function of distance along the line of sight of PSR J1801–3210. It can be seen that in the limiting case of \dot{P}_{shk} being zero, we can achieve a positive period derivative beyond a distance of 8 kpc, and can reach an upper limit of \dot{P}_{int} of 3×10^{-20} at a distance of 8.5 kpc. At a distance of 8 kpc, the NE2001 model requires a corresponding DM of $326.1 \text{ cm}^{-3} \text{ pc}$ which is inconsistent with the well-constrained DM measurement of PSR J1801–3210 of only $177.713(4) \text{ cm}^{-3} \text{ pc}$. However other electron density models give very different results. For example the TC93 model (Taylor & Cordes, 1993) requires a corresponding DM of only $227.0 \text{ cm}^{-3} \text{ pc}$, whereas including a thick disk component to the TC93 model (Schnitzeler, 2012) predicts an even smaller corresponding DM of $185.5 \text{ cm}^{-3} \text{ pc}$, which is only a factor of 1.07 from our measured value. These large discrepancies between various models reflect uncertainties in the electron density distribution along this line of sight, and thus it seems plausible that the DM-derived distances of PSR J1801–3210 have been underestimated. PSR J1801–3210 is located at $(l, b) = (358^\circ.922, -4^\circ.577)$, a distance of at least 8 kpc in this direction would put PSR J1801–3210 just beyond the Galactic Centre, hence reversing the direction of \dot{P}_{gal} . In any case, we suggest that PSR J1801–3210 would serve as an important test pulsar for improving future electron density models.

Otherwise, if PSR J1801–3210 has indeed an extremely small \dot{P}_{int} it would imply

an exceptionally small surface magnetic field. Popular theories on the pulsar emission mechanism require electron-positron pair production, and the longer the spin period of the pulsar, the larger the potential needed to power the particle acceleration (see for example Beskin et al., 1988). The following implication is known as the ‘pulsar death line’, which predicts for a particular pulsar spin period, there exists a lower limit of period derivative and surface magnetic field for which radio emission can be produced. Therefore, we can derive a lower limit of \dot{P}_{int} for PSR J1801–3210 to stay above the pulsar death line. We adopt the theoretical study from Chen & Ruderman (1993) which described three possible death lines also plotted in Fig. 5.3. If we take the lowest limiting case imposed by death line B, we derive a lower limit of $\dot{P}_{\text{int}} = 7.9 \times 10^{-24}$ and a corresponding surface magnetic field at the equator (B_{eq}) of 7.8×10^6 G. We note that this derivation assumes a contribution only from a model of a vacuum magnetic dipole. However as discussed by Tauris et al. (2012), if the spin-down torque caused by the plasma current in the magnetosphere (Spitkovsky, 2006) is also taken into account, the realistic surface magnetic field would even be lower, by at least a factor of $\sqrt{3}$.

5.3.4 Binary companions and mass functions

A plot of mass function versus orbital period is a standard way of distinguishing different types of binary systems and can be used to gain insight into the nature of the binary companion, as shown in Fig. 5.6. Indeed it can be seen immediately that PSR J1719–1438 occupies an otherwise empty region in the bottom left corner of this figure, as a result of its uniquely light, planet-mass companion. This has been extensively discussed in the literature (e.g., Bailes et al., 2011; van Haften et al., 2012b) and briefly introduced in Section 3.2.1, so will not be further elaborated here.

A cluster of pulsars can be seen in the left side of Fig. 5.6, with $P_{\text{orb}} \leq 1$ d and mass functions between 10^{-7} to $10^{-4} M_{\odot}$. They are considered descendants of close LMXB systems, resulting in the formation of a binary with an ultra-light companion (Tauris, 2011), also known as the ‘very low-mass binary pulsars’ (VLMBPs). In our sample we have three MSPs that fit into this category, namely PSRs J1446–4701, J1502–6752 and J1731–1847.

Some of the VLMBPs exhibit eclipses and are typically referred to as black widow pulsars (BW; Roberts, 2013). Eclipses have already been reported for PSR J1731–1847 by Bates et al. (2011), but not for PSRs J1446–4701 nor J1502–6752. Freire (2005) proposed a correlation between the possibility of observing eclipses and orbital inclination for these VLMBPs in GC. The essence of the idea is that the companions of these VLMBPs have a narrow intrinsic mass distribution, and subsequently whether a VLMBP shows eclipses or not, becomes exclusively dependent on its orbital inclination. In other words, a VLMBP viewed relatively face-on (low inclination) is less likely to be observed as an eclipsing system and will also have a smaller mass function, and vice versa.

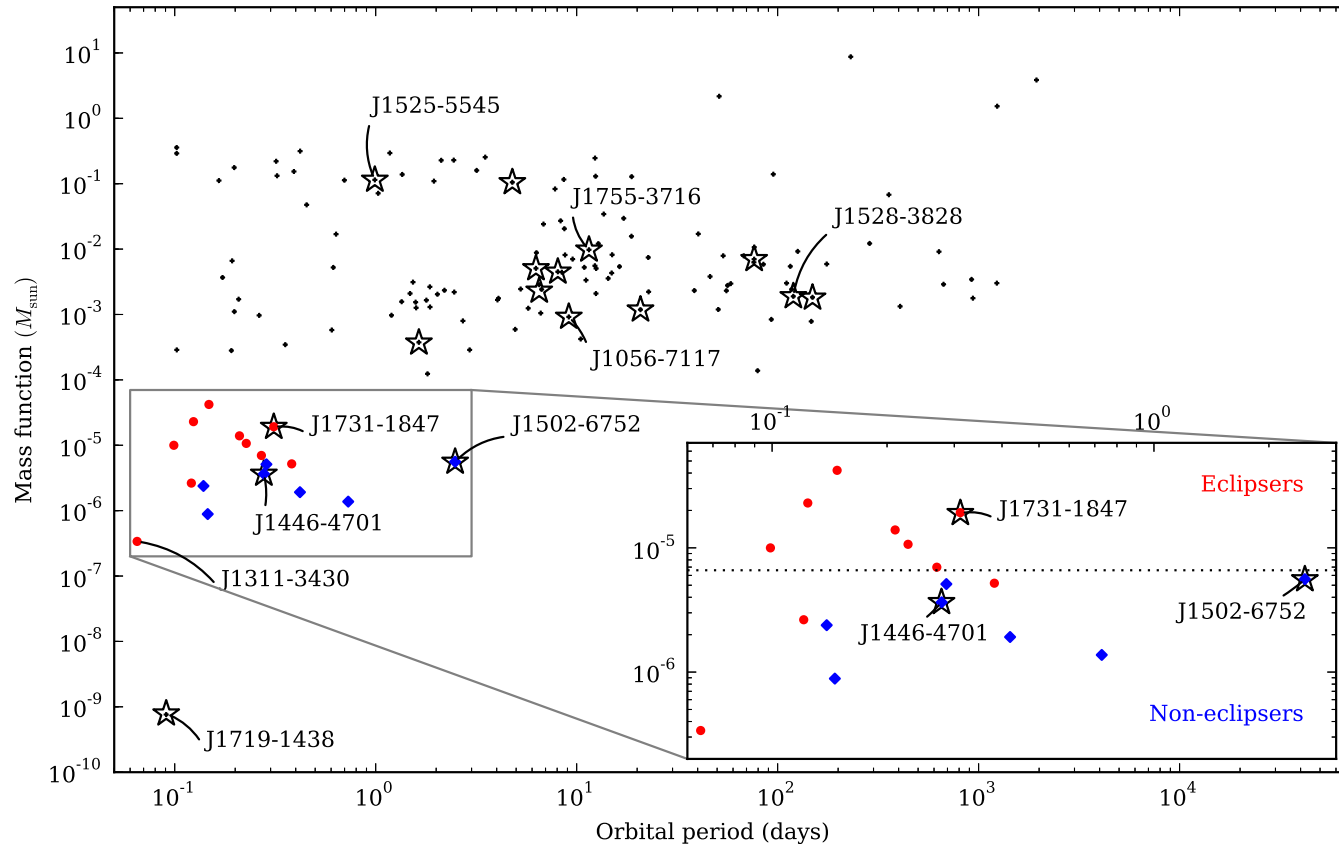


Figure 5.6: Plot showing mass function vs orbital period for all binary pulsars. Known ‘eclipsers’ are represented by red circles and ‘non-eclipsers’ by blue diamonds. The 16 MSPs studied in this paper are represented by star symbols. The zoomed-in panel focuses on the region of the VLMBPs, and the dotted line plotted within represents the dividing mass function value of $6.7 \times 10^{-6} M_{\odot}$, which corresponds to $m_c = 0.029 M_{\odot}$ and $M_p = 1.7 M_{\odot}$ assuming an orbital inclination of 70° .

While this hypothesis seems to work well in GCs, there has not yet been a similar study on the non-GC associated VLMBP population. We have compiled all related literature, and colour-coded in Fig. 5.6 the known ‘eclipsers’ as red circles and the ‘non-eclipsers’ as blue diamonds. Two distinct groups composed of ‘eclipsers’ and ‘non-eclipsers’ do seem to exist, with only one outlier, PSR J1311–3430, which is the tightest binary pulsar known with a P_{orb} of just 93 min (Romani et al., 2012; Pletsch et al., 2012; Ray et al., 2013). But this pulsar may have evolved from an ultra-compact X-ray binary (UCXB), hence belonging to a different population (van Haften et al., 2012a) and might not be applicable to the hypothesis as mentioned above. Disregarding this system, it is striking to see a bimodal distribution. Particularly interesting is that there is no non-eclipsing system found within the red cluster of ‘eclipsers’, although from a pulsar searching point-of-view these kinds of systems should in fact be easier to detect due to their non-eclipsing nature.

Plotted as a dotted line in the zoomed-in panel of Fig. 5.6 is our nominal split between the ‘eclipsers’ and the ‘non-eclipsers’, representing a dividing mass function of $6.7 \times 10^{-6} M_{\odot}$. We assume a pulsar mass of $1.7 M_{\odot}$, and an orbital inclination of 70° to postulate a lower limit on inclination which eclipses can be observed. This dividing mass function would then correspond to $m_c = 0.029 M_{\odot}$, which is also within the range of typical companion masses of BWs as shown in Chen et al. (2013). Indeed orbital eclipses are observed for PSR J1731–1847 which has a median m_c of $0.0385 M_{\odot}$ and lies above the dotted line, whereas no eclipse is observed for PSRs J1446–4701 and J1502–6752 with lower companion masses (median m_c of $0.022 M_{\odot}$ and $0.025 M_{\odot}$ respectively) located below this line. These measurements are in agreement with Freire (2005).

5.3.5 Galactic height distribution

Based on theoretical grounds we expect an anti-correlation between the absolute Galactic height and the inferred mass function of binary pulsars. The reason is the following: assuming that the momentum kick imparted to a newborn neutron star during the SN explosion is independent of exterior parameters, such as the mass of the companion star, the resulting systemic recoil velocity is larger for systems with smaller companion star masses (and thus smaller mass functions) as a simple consequence of conservation of momentum. Since the acquired amplitude of the Galactic motion of the system only depends on the systemic recoil velocity, we therefore expect the above mentioned anti-correlation between the distribution of observed Galactic heights and the measured mass functions of pulsar binaries. Some theoretical studies (e.g., Tauris & Bailes, 1996) have suggested the possibility of a weak relation between orbital period and systemic recoil velocity of pulsar binaries. However, Gonzalez et al. (2011) found no observational evidence for such a relation based on the 2D velocities of binary MSPs. Thus we disregard orbital periods in the following discussion.

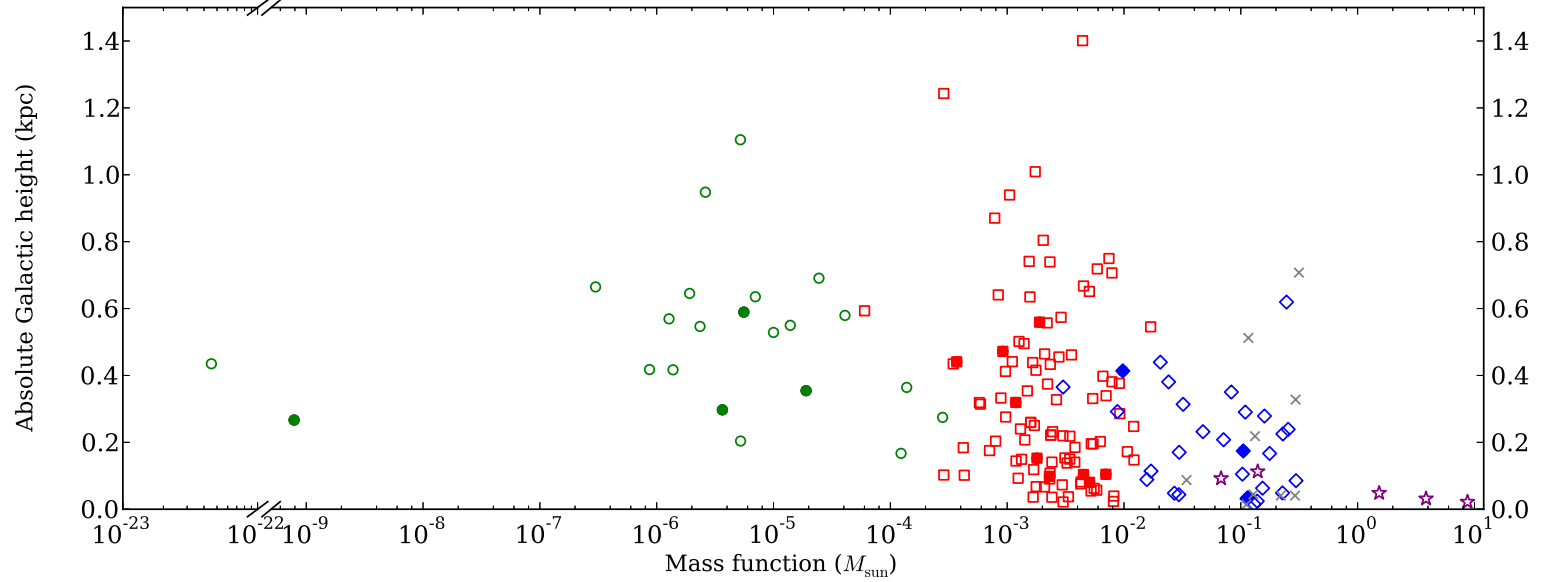


Figure 5.7: Mass function vs absolute Galactic height from the plane, $|d \sin b|$. We derived the distances, d , according to the Cordes & Lazio (2002) NE2001 model of the Galactic electron density, except for 19 binary systems for which independent distance measurements existed. In those cases we used the independently-measured distances instead of the DM-derived distances. Ultra-light systems are plotted as green circles, binaries with He-WD companions as red squares, massive CO or ONeMg-WD companions as blue diamonds, and main-sequence star companions as purple stars. The 16 MSPs in this work are also plotted with the same scheme, but emphasised by filling the symbols with the relevant colours. NS-NS systems are plotted as grey crosses but since they have received two kicks from SN explosions they are not considered further in this discussion.

Table 5.7: A summary of the statistical distribution of Galactic height for each binary group, classified in accordance with the description in Tauris et al. (2012). N is the number of pulsar systems in each group. The average ($|z_{\text{mean}}|$) and the median ($|z_{\text{med}}|$) Galactic heights in kpc are listed, as well as the corresponding standard deviation (σ).

Binary group	N	z_{mean} (kpc)	z_{med} (kpc)	σ
UL	22	0.52	0.55	0.22
He-WD	99	0.32	0.23	0.26
Massive WD	29	0.21	0.20	0.15
NS-NS	9	0.23	0.09	0.24
MS	5	0.06	0.04	0.04

Our sample of 16 MSPs has a wide distribution of mass functions, from PSR J1719–1438 with an ultra-low mass companion and a mass function of $7.8 \times 10^{-10} M_{\odot}$ to PSR J1525–5545 with a massive WD companion and a mass function of $0.11 M_{\odot}$. With the addition of these systems, we investigate whether there exists a correlation between mass function and vertical distance from the Galactic plane ($|d \sin b|$). We have taken our sample of MSPs from PSRCAT and an online MSP catalogue maintained by Lorimer⁴. We have included the 16 MSPs in this work and also six additional newly-discovered HTRU MSPs (Ng et al., in prep; Thornton et al., in prep). All recycled MSPs in binary systems are considered, provided that they are not associated with a GC or extragalactic, which amounts to 164 MSPs in total. We continue to use the Cordes & Lazio (2002) model of Galactic electron density to derive the distances of all known pulsars in order to calculate their respective Galactic heights. Independent distance measurements are available for 19 binary systems and we use these, instead of the DM distances, when calculating their Galactic heights. In Fig. 5.7 we plot the absolute Galactic heights against mass functions, and we classify the nature of each of the binary companions in accordance with the description in Tauris et al. (2012). This results in five binary groups, namely those with ultra-light (UL) companions, with He-WD companions, with massive CO or ONeMg-WD companions, neutron-star–neutron-star (NS-NS) systems and those with main-sequence star (MS) companions. For the rest of the discussion we set aside the nine NS-NS systems, since they were born with two SN explosions (hence received two kicks) and would complicate our discussion.

Table 5.7 summarises the statistical distribution of Galactic height for each of the binary groups mentioned above, from which we draw two main interpretations. Firstly, the heavier systems tend to stay closer to the plane, as seen for example from the MS systems with a mean Galactic height of only 0.06 kpc, whereas the lightest UL systems tend to be found at a higher Galactic height with a mean of 0.52 kpc. Secondly there is a larger scatter in the height distribution of the lighter systems, whereas the heaviest MS

⁴<http://astro.phys.wvu.edu/GalacticMSPs/GalacticMSPs.txt>

system are found almost exclusively within the Galactic plane. We note that a potential caveat here is that the ages of the MSPs might also have an influence on the Galactic height scattering. For example the fully-recycled He-WD binaries are generally older and hence might have more time to scatter away from the Galactic plane, whereas the less-recycled binaries with heavier companions tend to be younger. In addition, there is also a longer time interval between the SN explosion and the formation of the MSP for systems with UL and with He-WD companions, because their low-mass progenitors have much longer nuclear evolution timescales. Nonetheless, this does not change the outcome of the overall picture in Fig. 5.7, explicitly that the distribution of the total mass of binary systems is inversely-related to the Galactic height distribution.

We are aware that the MSP distribution depicted in Fig. 5.7 is skewed by another observational bias. That is from a pulsar searching point-of-view, pulsars with shorter spin periods, meaning the more recycled UL and He-WD systems, are more difficult to be discovered at higher DM regions, for example deep in the Galactic plane. This is because short spin period pulsars are more vulnerable to dispersion smearing and interstellar scattering. However, the less recycled massive WD and MS systems have longer spin periods, and we should have a relatively more uniform ability to detect them whether they are in the Galactic plane where DM is high or out of the plane.

This leads to two further implications. The first is that the smaller Galactic heights of the heavier systems are genuine, since if massive WD or MS systems exist at high Galactic heights we would have been more likely to have discovered them, given that we have detected the in-theory more difficult He-WD at those Galactic heights. The second is that this gives an explanation to the lack of light systems at small Galactic heights in the Galactic plane, resulting in the sparsely populated region in Fig. 5.7 below 0.2 kpc and for mass function less than $10^{-3} M_{\odot}$. Indeed a large number of the UL systems at high Galactic heights are only discovered thanks to the *Fermi* Large Area Telescope (LAT; Atwood et al., 2009), which has much less ability to detect pulsars in the Galactic plane due to confusion with background emission.

These results show that the observed MSP distribution is not as isotropic as previously thought (see e.g., Johnston & Bailes, 1991) prior to the latest generation of pulsar surveys with improved backends, which have allowed us to probe a much bigger volume within the Galaxy. Conventional MSP population synthesis using the scale factor method typically takes into consideration only the pulsar luminosities (see for example Levin et al., 2013), and we suggest that including the mass function as an extra parameter could be a potential improvement for future population studies.

5.3.6 Orbital eccentricity

We have measured initial eccentricities for the four newly-discovered binary MSPs and improved precision for the eccentricities of the 12 previously published MSPs, except for PSR J1502–6752 where only upper limits can be achieved. Fig. 5.8 shows a plot of orbital period versus orbital eccentricity and the 16 MSPs in this work are marked together with 1 and 2σ uncertainties of their eccentricities. The dotted lines denote the eccentricity predicted by the convective fluctuation-dissipation theory of Phinney

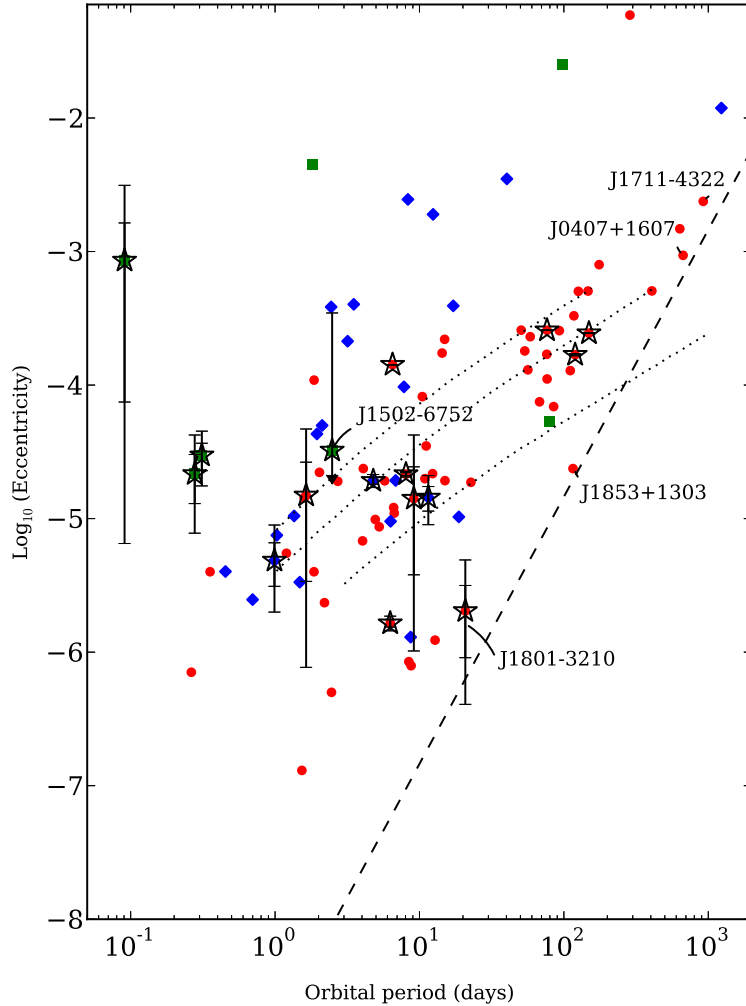


Figure 5.8: Plot of eccentricity vs. orbital period (P_{orb}). Known pulsars with He-WD companions are plotted as red circles, CO-WD companions in blue diamonds, and ultra-light companions in green squares. The 16 MSPs studied in this work are plotted with star symbols filled with the respective colour according to their companion types, together with the 1 and 2σ uncertainties of the eccentricity measurements. We plot a 2σ upper limit for PSR J1502–6752 where the eccentricity is not constrained. The solid line illustrates the median eccentricity predicted by [Phinney \(1992\)](#). The dot-dashed line and the dotted line are predicted to contain 68 and 95 per cent of the final eccentricities respectively. The dashed line indicates $e \propto P_{\text{orb}}^2$.

(1992), applicable to binary systems formed by stable mass transfer from a Roche-lobe filling red giant. It can be seen that our MSPs with He-WD companions (plotted as red stars in Fig. 5.8) largely agree with the predictions of Phinney (1992). Within the 2σ eccentricity measurement uncertainties, only PSRs J1017–7156, J1811–2405 and J1801–3210 lie outside the 95 per cent confidence-level range (the first one above and the latter two below). However as seen in Fig. 5.8 they have the same scatter as the rest of the MSP population. In addition, these three pulsars have typical He-WD companions and their spin periods indicate highly recycled systems. Therefore, we find little evidence for unusual evolutionary scenarios for these three pulsars.

The low eccentricity of $e = 2.1 \pm 1.1 \times 10^{-6}$ of PSR J1801–3210 combined with its large orbital period of $P_{\text{orb}} = 21$ d makes it a ‘wide-orbit binary millisecond pulsar’ (WBMSP), and an interesting object to be employed for tests of the strong equivalence principle (SEP) as described in Damour & Schäfer (1991); Stairs et al. (2005); Freire et al. (2012). The basic idea being that in the case of SEP violation, the extreme difference between the gravitational binding energy of the heavy neutron star and its much less compact companion star implies that they would experience different accelerations in the presence of an external gravitational field (Nordvedt effect). This translates to an observable effect, most prominent in systems with small eccentricity and wide orbits, that the eccentricity would oscillate between the minimum and maximum value. The dashed line overplotted on Fig. 5.8 indicates $e \propto P_{\text{orb}}^2$, a figure-of-merit for a SEP test. With a P_{orb}^2/e ratio of $2.1 \times 10^8 \text{ day}^2$, PSR J1801–3210 thus provides the best test for SEP together with PSRs J1835+1303 and J0407+1607 as detailed in Gonzalez et al. (2011). Note that although PSR J1711–4322 appears to lie close to the figure-of-merit in Fig. 5.8, it is in fact not usable for this SEP test (Kehl & Krieger, 2012).

5.3.7 Change in projected semi-major axis, \dot{x}

For PSR J1017–7156 we determine a change in projected semi-major axis (\dot{x}) of $9.1 \pm 1.7 \times 10^{-15}$. The projected semi-major axis, x , is related to the semi-major axis, a_p , and the inclination, i , by Equation (5.1). Hence a measurement of \dot{x} could be due either to a physical change of the intrinsic orbit size as measured by a_p , or to a change in i , or both.

In the case of an actual change in a_p due to gravitational wave emission, we would expect this to also be reflected in a detection of \dot{P}_{orb} (Peters, 1964). From this we can predict the corresponding observable change in $a_p \sin i/c$ to be of the order of 10^{-21} for PSR J1017–7156, which is many orders of magnitude too small to be observed. So we conclude that the observed \dot{x} is most likely due to an apparent change in the orbital inclination as a result of proper motion affecting the viewing geometry. This effect has been first proposed by Arzoumanian et al. (1996) and Kopeikin (1996) using,

$$\dot{x} = 1.54 \times 10^{-16} x \left(\frac{\mu}{\text{mas yr}^{-1}} \right) \cot i \sin(\Theta - \Omega). \quad (5.8)$$

In this equation proper motion has a total magnitude of μ and a position angle of Θ , whereas Ω is the position angle of the line of nodes.

To assess if any physical constraints of the orientation of the line of nodes in relation to the direction of the proper motion (i.e. $\Theta - \Omega$) can be subsequently drawn, one must compare the uncertainty of the measured \dot{x} with the product of μ and x . For PSR J1017–7156 we have $\mu x = 7.6 \times 10^{-15}$, which is indeed in the same order of magnitude as compared to our \dot{x} measurement, and can already provide constraints to the possible ranges of Ω . Future improved timing precision and additional information, such as constraints on or detection of a Shapiro delay, will allow us to extract more information on the binary systems, including mass measurements. None of the other MSPs reported in this chapter have a detectable \dot{x} yet and are unlikely to be measurable in the near future. With the possible exceptions of PSRs J1125–5825 and J1708–3506, which both have μx of the order of 10^{-14} , we can quote a marginal \dot{x} limit of $1.6 \pm 2.0 \times 10^{-14}$ and $-9 \pm 6 \times 10^{-14}$ respectively. Hence they might achieve reliable \dot{x} measurements with additional timing data.

5.3.8 Orbital period variation, \dot{P}_{orb}

We measure an orbital period variation (\dot{P}_{orb}) in PSR J1731–1847. However rather than due to gravitational-wave damping, the \dot{P}_{orb} observed in this case is more likely due to the eclipsing nature of PSR J1731–1847, a BW system, inducing orbital interaction. We refer to Lazaridis et al. (2011) for a detailed discussion of such orbital period variations caused by changes in the gravitational quadrupole moment of a tidally interacting BW system. For the case of PSR J1731–1847, a straight-forward fit of \dot{P}_{orb} is not adequate, since the orbital period exhibits quadratic changes over the last three years. We have achieved the best fit using the BTX model (Nice, D., unpublished) implemented in TEMPO2, taking into account the orbital frequency changes up to the second order term (i.e. $n_{\text{b}}, \dot{n}_{\text{b}}, \ddot{n}_{\text{b}}$). The phase (ϕ) of the orbit is thus a function of the binomial expansion of the $n_{\text{b}}^{(k)}$ terms, where k denotes the k^{th} derivative with respect to time. At any particular time, t , the phase ϕ can be represented by,

$$\phi(t) = \sum_{k=1}^K \left(\frac{n_{\text{b}}^{(k)}}{k+1!} \right) \left(\frac{t - T_0}{s} \right)^{k+1} / n_{\text{b}}. \quad (5.9)$$

To get a better visualisation of the change of the orbit over time, we express this phase shift as the shift of the epoch of periastron (T_0). One can consider that a positive phase shift corresponds to an earlier arrival of the observed periastron, $T_{0,\text{obs}}$, as compared to the predicted arrival of the periastron, $T_{0,\text{pre}}$. The result is a negative ΔT_0 , which also symbolises a decrease in \dot{P}_{orb} ,

$$\Delta T_0 = T_{0,\text{pre}} - T_{0,\text{obs}} = \Delta\phi \times P_{\text{orb}}. \quad (5.10)$$

Fig. 5.9 shows this ΔT_0 as derived from the $n_{\text{b}}^{(k)}$ terms of the BTX model fit in TEMPO2. It can be seen that the orbit of PSR J1731–1847 shrinks until approximately MJD 55800 but gets wider after. We identified manually a value of T_0 across every few TOAs, while holding fixed all other parameters (shown by black points in Fig. 5.9). The BTX model results in a close agreement. We remark, however, that this model

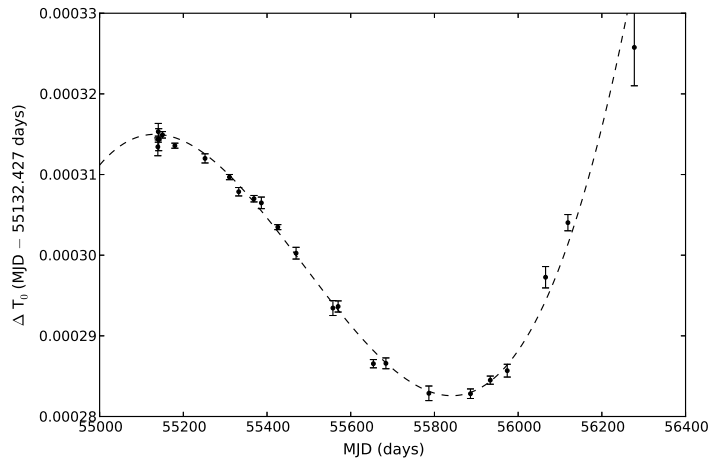


Figure 5.9: A plot of ΔT_0 as a function of time for PSR J1731–1847. The dashed line shows the best-fit curve from the timing solution generated with the BTX model in TEMPO2, employing up to the second orbital frequency derivative terms.

has no predictive power for the orbital period variations outside of the current TOA timeline.

5.3.9 Variation in the longitude of periastron, $\dot{\omega}$

We measured a marginally significant variation in the longitude of periastron ($\dot{\omega}$) for PSR J1017–7156 with a value of $0.022 \pm 0.009^\circ \text{ yr}^{-1}$. If we assume a typical pulsar mass of $1.4 M_\odot$ and an orbital inclination of 60° , using Equation (2) of [Weisberg & Taylor \(1981\)](#) we obtain a predicted $\dot{\omega}$ in general relativity of $0.012^\circ \text{ yr}^{-1}$, which agrees with our measured value within 1.1σ . In general $\dot{\omega}$ is a useful Post-Keplerian (PK) parameter as it can be used to calculate the total mass of the binary system, from which a measurement of the pulsar mass may be extracted. The variation in $\dot{\omega}$ is the easiest to measure for orbits with significant eccentricities. In the case of PSR J1017–7156 with $e = 1.4 \times 10^{-4}$ and an already good timing residual RMS of $1.3 \mu\text{s}$, we expect its $\dot{\omega}$ measurement to be much improved with another 5 yr of timing data.

5.3.10 Gamma-ray pulsation searches

Among the pulsars in our sample, PSRs J1125–5825 and J1446–4701 have been observed to emit $> 0.1 \text{ GeV}$ pulsations by [Keith et al. \(2012\)](#), through the analysis of data taken by the *Fermi* Large Area Telescope (LAT; [Atwood et al., 2009](#)), with post-trial significances just under 5σ . High confidence detections of these two MSPs in gamma rays were later presented in [Abdo et al. \(2013\)](#).

To determine whether other MSPs in our sample also emit gamma-ray pulsations, we analysed LAT photons recorded between 2008 August 4 and 2013 May 1, with energies from 0.1 to 100 GeV, and belonging to the ‘Source’ class of the reprocessed

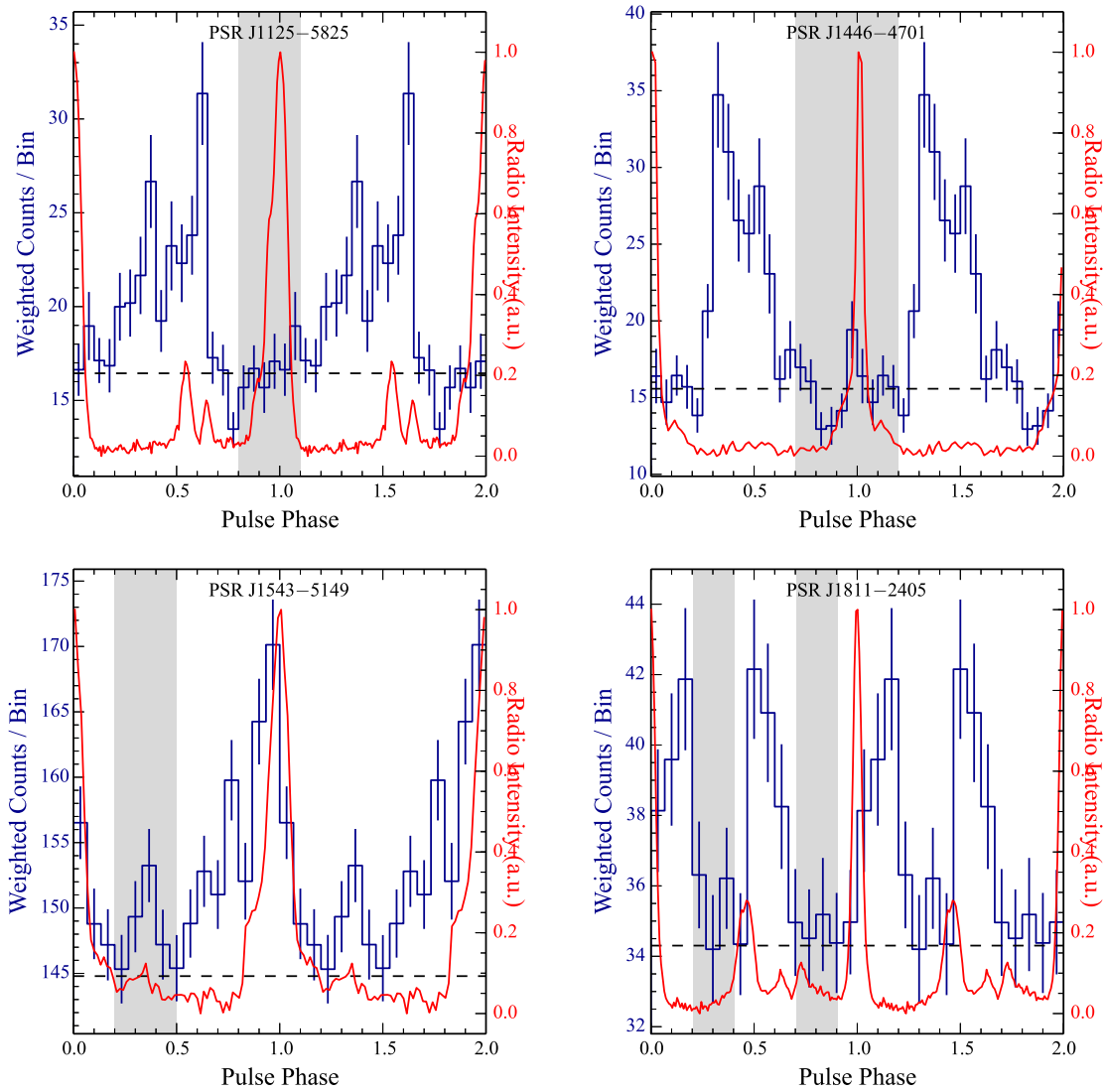


Figure 5.10: Radio and gamma-ray light curves for the four MSPs in our sample with *Fermi* LAT detections. Two pulsar cycles are shown for clarity. The radio profiles are based on 1.4 GHz observations conducted at Parkes, while the gamma-ray profiles were obtained by selecting *Fermi* LAT photons with reconstructed directions found within 5° of the MSPs, and with energies larger than 0.1 GeV. The photons were weighted by the probability that they originate from the pulsars as described in e.g. [Kerr \(2011\)](#). Photons with weights smaller than 0.01 were rejected. Horizontal dashed lines show the estimated background levels, obtained by following the method described in [Guillemot et al. \(2012\)](#). The grey shaded regions indicate the OFF-pulse intervals used for the spectral analyses presented in Section 5.3.10, the ON-pulse regions being defined as the complementary intervals.

Table 5.8: Gamma-Ray emission properties of PSRs J1125–5825, J1446–4701, J1543–5149, and J1811–2405. The weighted H -test parameters were calculated by selecting photons found within 5° of the pulsars, with energies larger than 0.1 GeV and weights larger than 0.01. See Fig. 5.10 for the corresponding gamma-ray light curves under the same selection cuts. Details on the measurement of the spectral parameters can be found in Section 5.3.10.

Parameter	J1125–5825	J1446–4701	J1543–5149	J1811–2405
Weighted H -test	100.7	165.4	65.1	37.9
Spectral index, Γ	1.6 ± 0.5	1.3 ± 0.4	2.3 ± 0.3	1.6 ± 0.4
Cutoff energy, E_c (GeV)	8 ± 7	4 ± 2	6 ± 3	3 ± 2
Photon flux above 100 MeV, F_{100} (10^{-8} cm $^{-2}$ s $^{-1}$)	0.8 ± 0.7	0.6 ± 0.2	5.4 ± 0.4	2 ± 2
Energy flux above 100 MeV, G_{100} (10^{11} erg cm $^{-2}$ s $^{-1}$)	0.9 ± 0.3	0.7 ± 0.1	2.4 ± 0.2	1.4 ± 0.8
Luminosity, $L_\gamma = 4\pi G_{100} d^2$ (10^{33} erg, s $^{-1}$)	7.1 ± 2.4	1.9 ± 0.3	17 ± 1	5.5 ± 3.1
Efficiency, $\eta = L_\gamma / \dot{E}$	0.09 ± 0.03	0.05 ± 0.01	0.23 ± 0.02	0.2 ± 0.1

P7REP data, a version of Pass7 data⁵ reprocessed with improved calibrations. Events with zenith angles larger than 100° were excluded, to reject atmospheric gamma rays from the Earth’s limb. In addition, events recorded when the instrument was not operating in nominal science operations mode, when the limb of the Earth infringed upon the regions of interest (see below for the definition of these regions), or when the data were not flagged as good were excluded. These cuts were made using the *Fermi* Science Tools⁶ (STs) v9r32p5, and the selected photons were assigned pulse phases using the ephemerides listed in Tables 5.3 and 5.5 and the *Fermi* plug-in for TEMPO2 (Ray et al., 2011; Hobbs et al., 2006).

Weighting each event by the probability that it originates from a pulsar has been shown to make pulsation searches more sensitive (e.g., Kerr, 2011). We calculated these weights by performing binned maximum likelihood analyses for each pulsar, using the *pyLikelihood* python module distributed with the STs. For each MSP we selected photons found in a region of radius 15° centred on the pulsar, and built a spectral model for this region by including sources within 20° , from a preliminary list based on four years of LAT data. The Galactic diffuse emission was modelled using the *gll_iem_v05.fit* map, and the isotropic diffuse emission and residual instrumental background were modelled using the *iso_source_v05.txt* template. We used the P7REP_SOURCE_V15 instrument response functions, and followed the analysis prescriptions described in Abdo et al. (2013). However, in a first iteration of the analysis the MSPs were modelled with simple power laws of the form $N_0 (E/\text{GeV})^{-\Gamma}$, where N_0 is a normalisation factor, E denotes the photon energy and Γ the photon index. A test statistic (see Nolan et al., 2012, for a definition) larger than 40 was found for PSRs J1125–5825, J1446–4701, J1543–5149 and J1811–2405, indicating the presence of significant gamma-ray emission. Apart from these, no evidence for gamma-ray emission from any of the other pulsars was found. For these pulsars, we have conducted an unweighted search for pulsations, testing a range of angular and energy cuts to the

⁵See Bregeon et al. (2013) and http://fermi.gsfc.nasa.gov/ssc/data/analysis/documentation/Pass7REP_usage.html for more information.

⁶<http://fermi.gsfc.nasa.gov/ssc/data/analysis/scitools/overview.html>

LAT data to optimise the H -test statistic (de Jager & Büsching, 2010). We did not find evidence for gamma-ray pulsations with significance greater than 3σ in any of the data selection cuts used, for these pulsars without significant continuous emission.

For the four MSPs with gamma-ray detections, we computed the weights using the ST `gtsrcprob` and the best-fit spectral models as obtained from the preliminary likelihood analyses. For PSRs J1125–5825, J1446–4701, and J1543–5149, we found spectrally-weighted H -test significances (Kerr, 2011) above 5σ , while for J1811–2405 we obtained a 4.4σ detection, suggesting that J1543–5149 and J1811–2405 are indeed gamma-ray pulsars. In order to improve the quality of the spectral results and thereby increase the weighted pulsation significances we inspected the preliminary light curves for the four MSPs visually to determine ON-pulse regions, that we refit with `gtlike`, this time modelling the MSPs with exponentially cutoff power laws of the form $N_0 (E/\text{GeV})^{-\Gamma} \exp(-E/E_c)$, where E_c is the cutoff energy. The best-fit spectral parameters obtained from this second iteration are listed in Table 5.8, and the spectrally-weighted light curves are shown in Fig. 5.10 along with the ON-pulse intervals chosen for this analysis. For all four pulsars, the H -test parameters using a minimum weight cut of 0.01 all indicate $> 5\sigma$ detections, even after accounting for the trial factor due to the two analysis steps.

The spectral parameters listed in Table 5.8 for PSRs J1125–5825 and J1446–4701 are consistent with those reported in Abdo et al. (2013) to within uncertainties. The parameters for PSRs J1543–5149 and J1811–2405 are only weakly constrained at present, but are reminiscent of those of known gamma-ray MSPs (Abdo et al., 2013). Also listed in Table 5.8 are the gamma-ray luminosities L_γ deduced from the energy flux measurements, and the efficiencies of conversion of spin-down power into gamma-ray emission, $\eta = L_\gamma/\dot{E}$, calculated using the Shklovskii-corrected \dot{E} values and the DM distances given in Tables 5.3 and 5.5. The uncertainties reported in Table 5.8 are statistical. Studies of systematic uncertainties in the effective area suggest a 10 per cent uncertainty at 100 MeV, decreasing linearly in $\text{Log}(E)$ to 5 per cent in the range between 316 MeV and 10 GeV and increasing linearly in $\text{Log}(E)$ up to 10 per cent at 1 TeV⁷.

The two newly-identified gamma-ray pulsars, PSRs J1543–5149 and J1811–2405, bring the total number of MSPs with detected gamma-ray pulsations to 53 objects. It is unlikely that the *Fermi* LAT will detect many of the remaining MSPs presented in this paper. Assuming an average gamma-ray efficiency for MSPs of 0.245 following the prescription of Johnson et al. (2013), we derive expected energy fluxes for these pulsars much smaller than the lowest value reported in Abdo et al. (2013) for an MSP, because of the generally large distance values; with the notable exception of PSR J1731–1438. The latter MSP may be inefficient at converting its spin-down power into gamma-ray emission, or its gamma-ray beams may not cross the Earth’s line of sight. The high \dot{E} but distant MSPs in this sample could contribute to the diffuse emission seen by the *Fermi* LAT around the Galactic plane.

⁷see http://fermi.gsfc.nasa.gov/ssc/data/analysis/LAT_caveats.html

Conclusion and future work

Contents

6.1 Conclusion	129
6.1.1 The HTRU Galactic plane survey	129
6.1.2 Timing 16 MSPs from the medium latitude survey	132
6.2 Future work	133
6.2.1 Continued processing	133
6.2.2 Follow-up on discoveries from the Galactic plane survey	134
6.2.3 Further improvements in the search algorithms	134
6.3 Closing remarks	135

6.1 Conclusion

In this thesis, we have exploited the capability of the Parkes telescope as a searching and timing instrument for pulsars. We have presented the HTRU survey, which has benefited from recent advancements in technology and provided unprecedented time and frequency resolution, making the HTRU the first true all-sky survey and the best pre-SKA survey. Thus far, 129 newly-discovered pulsars have been reported from the HTRU survey with Parkes (Keith et al., 2010; Bates et al., 2011; Keith et al., 2012; Bates et al., 2012; Burgay et al., 2013b; Ng et al., 2014, Thornton et al., in prep).

6.1.1 The HTRU Galactic plane survey

The HTRU low-latitude Galactic plane survey promises to provide the deepest large-scale search conducted thus far for the Galactic plane region, where the most relativistic binaries are expected to be found (Belczynski et al., 2002). In addition, this survey will represent a unique record of the Galactic plane with high yet uniform sensitivity, enabling an unbiased Galactic census to explore the true boundaries of pulsar phase space. The discoveries from the HTRU will also provide valuable knowledge of the Galactic pulsar population for the planning of survey strategies with the SKA.

Searching for new pulsars in high resolution observations with long integration lengths is computationally intensive, and the depth to which the data can be explored is limited by the available computing resources. In order to improve the searching algorithm, we introduce two RFI mitigation techniques in the time and Fourier domain.

The Fourier domain method (Ng et al., in prep) has been shown to be very effective and for some cases new pulsars have been discovered only when this technique is applied. Furthermore, we present the implementation of a novel partially-coherent segmented acceleration search algorithm, based on the time-domain re-sampling method. This segmented search technique aims to increase our chances of discoveries of highly-accelerated relativistic short-orbit binary systems. In Section 3.3.2.1 we show that a $r_{\text{orb}} \approx 0.1$ results in the highest effectiveness of the linear acceleration approximation, hence we split the long data sets of the HTRU Galactic plane survey into segments of various lengths and search for the binary systems using an acceleration range appropriate for the length of the segment. We push the maximum achievable acceleration value to 1200 m s^{-2} . Within this range we can find a double-pulsar-like system deeper in the Galaxy with orbital periods as short as 1.5 hr, and explore the parameter space occupied by expected pulsar-black hole systems. Of the order of 1.8×10^{24} computational operations per data set are required by the search configuration adopted in this survey. The high computational requirements of such data-intensive astronomy also act as a test bed for SKA technologies.

Analysis of 37 per cent of the HTRU Galactic plane observations with the partially-coherent segmented acceleration search outlined above has resulted in 689 re-detections of 348 previously-known pulsars, demonstrating that the survey is performing as expected. In addition, we present the discovery of 47 pulsars, of which two are fast spinning pulsars with periods less than 30 ms. One of the two pulsars, PSR J1101–6424 is likely a descendant from an IMXB. Its fast spin period of 5 ms indicates contradictory full-recycling from a long mass-transfer phase, making it only the second known IMXB which has evolved from a Case A Roche lobe overflow. The second one, PSR J1757–27, is likely to be an isolated pulsar. The most adopted formation scenario of an isolated MSP requires the pulsar to have a very fast spin period of the order of a few ms, at odds with the unexpectedly long spin period of 17 ms in the case of PSR J1757–27. Furthermore, we report on the discovery of PSR J1759–24 which shows transient emission property. This pulsar could be an intermittent pulsar, a magnetar or it can be in an eclipsing binary system with a long orbital period of the order of years. We also report on the discovery of an aligned rotator PSR J1847–0427 whose pulse profile contains a main pulse and an interpulse, together forming a wide profile with emission over almost the entire 360° of longitude. From the current discovery rate, extrapolation shows that the Galactic plane survey will result in at least a further 120 discoveries.

We note that the sky region of the HTRU Galactic plane survey has a complete overlap with that of the PMPS, as well as the HTRU medium-latitude survey. Despite the common sky coverage and the high success rates of these previous pulsar surveys, pulsar discoveries are still continuously being made from this survey. The improved dynamic range of the BPSR digital backend over the previous analogue filterbank system employed by the PMPS, as well as the long integration length of 72 min of this survey, both account for the high survey sensitivity crucial for the discoveries of many less luminous pulsars. Nonetheless, some of the newly-discovered pulsars presented in this paper are later found to be detectable in the archival data. The discoveries of these relatively bright pulsars which have eluded previous survey efforts could be attributed to

advancements in the data processing techniques. Particularly, the improvement in RFI mitigation techniques have reduced the number of false-positive candidates. Moreover, the ‘multiple-pass’ nature of the partially-coherent segmented acceleration search has increased the chance of discovering pulsars by avoiding parts of the observation which they might be less detectable. In principle, the acceleration search would also provide sensitivity to highly-accelerated relativistic pulsar binaries. However, none of the newly-discovered pulsars reported here were found at an orbital phase with noticeable orbital acceleration.

Twenty out of the 47 newly-discovered pulsars have calibrated flux density measurements for which luminosities can be inferred. Comparing them to the luminosity distribution of the published pulsars, we conclude that the HTRU Galactic plane survey is indeed probing the low luminosity region of the pulsar phase space especially for the distant population. No nearby low luminosity pulsars have yet been found. If the complete HTRU Galactic plane survey produces a significantly smaller percentage of nearby discoveries, this could indicate that we have reached a point where the yield of pulsar surveys are reducing as we are no longer flux limited. This has important implications for the planning of the future generations of pulsar surveys along the Galactic plane, for example those with MeerKAT and the SKA. Any pulsar surveys targeting the Galactic plane will have to go to higher observing frequency to increase the effective search volume by reducing interstellar scattering. In addition, multiple-shallow surveys are likely to be less successful, compared to a single deep survey designed with a low minimum detectable flux density.

Of the newly-discovered pulsars presented here, 16 now have coherent timing solutions allowing us to infer their preliminary characteristic ages. There is a noticeable lack of young pulsars within this 16 pulsars as they all have τ_c at least of the order of Myr. The old age and low \dot{E}/d^2 of these pulsars make Fermi associations unlikely. Nonetheless, we suggest that the current lack of young pulsars is purely due to small number statistics and at least a few young pulsars can be expected from the remaining pulsars currently without an inferred age. Timing solutions for these pulsars and any future discoveries from the HTRU Galactic plane survey will be crucial to study the characteristic age distribution of this less-luminous pulsar population and might help to resolve some of the long standing arguments regarding the relationship of radio luminosity of pulsars and their ages.

A comparison with the estimated survey yield shows that we currently have a close match between the estimated and observed yield of ‘normal’ pulsars. This is satisfying and would imply that our survey is performing as expected. We appear to be roughly a factor three short of MSP detections, and in Section 4.5 we explore the potential causes of the missing MSPs. We point out that the most relevant explanation is the fact that we have only processed the HTRU Galactic plane data in a partially coherent manner. The segmentation scheme means that we have not make use of the full sensitivity of the survey.

6.1.2 Timing 16 MSPs from the medium latitude survey

The HTRU survey for pulsars and fast transients has discovered 30 MSPs to date, of which four from the medium latitude sub-survey are announced in this work. All four MSPs have phase-coherent timing solution with RMS already of the order of tens of μs . We have presented their pulse profiles and polarimetric properties at different frequencies. PSRs J1529–3828 and J1056–7117 are likely to be formed from wide-orbit LMXBs, leading to the formation of classic MSPs with He-WD companions. PSR J1755–3716 is likely to have evolved from an IMXB and possesses a CO-WD companion. PSR J1525–5545 is likely to have a massive CO-WD companion, or an ONeMg-WD companion if the orbital inclination angle is low.

In addition, we present updated timing solutions for 12 previously published HTRU MSPs, as compared with results in their respective discovery papers (Bates et al., 2011; Keith et al., 2012; Bailes et al., 2011), thanks to the now longer timing baseline of over three years in all cases, except one with 2.7 years of timing data.

We measure five new proper motions with significance greater than 3σ , from PSRs J1017–7156, J1125–5825, J1446–4701, J1708–3506 and J1719–1438. Their derived transverse velocities are all consistent with previous MSP velocity distribution studies. In turn, with the proper motion measurements, we are able to constrain the period derivative contribution from the Shklovskii effect. In addition, we take into account the acceleration due to the Galactic potentials and correct for the intrinsic period derivatives for the 12 MSPs in this work. PSR J1017–7156 has one of the smallest inferred intrinsic period derivatives at 1.2×10^{-21} , hence also one of the lowest derived surface magnetic field strengths within the known MSP population at a value of 5.4×10^7 G.

We further discuss the case of PSR J1801–3210 for which no significant period derivative can be measured, even with more than four years of timing data. The best-fit solution in TEMPO2 shows a \dot{P}_{obs} of $-4 \pm 4 \times 10^{-23}$, an extremely small number comparing to that of a typical MSP. The both positive \dot{P}_{shk} and \dot{P}_{gal} of the order of 10^{-20} and 10^{-21} , respectively, act to further decrease the already negative period derivative. It seems unlikely that the DM-derived distance is significantly wrong and hence reversing the direction of Galactic potential. Alternatively we consider the presence of a third body near PSR J1801–3210 which might be accelerating the pulsar towards Earth. Giant molecular clouds seem to be a plausible scenario, whereas an exoplanet orbiting in a large hierarchical orbit seems unlikely due to the small probability of surviving the SN, as well as the fact that we do not measure any significant second derivatives of spin frequency. Based on radio emission theory, we derive a theoretical lower limit of period derivative of 7.9×10^{-24} and a corresponding surface magnetic field strength at the equator of 7.8×10^6 G for PSR J1801–3210, in order for it to stay above the pulsar death line. We also highlight the potential of PSR J1801–3210 to be employed in the SEP test due to its wide and circular orbit.

We have undertaken a comparison study between MSPs in our sample and the complete known pulsar population. We point to a strong dependence on inclination for eclipses to be observed in VLMBPs, as indicated by an apparent bimodal distribution of

eclipsing and non-eclipsing systems separated by a companion mass of about $0.027 M_{\odot}$. We also suggest that the distribution of the total mass of binary systems is inversely-related to the Galactic height distribution. In other words, MSPs with the heaviest companions have larger tendencies to stay close to the Galactic plane, whereas lighter systems with smaller mass functions show larger mean value and larger scatter in the Galactic height distribution.

A change in the projected semi-major axis (\dot{x}) is observed in PSR J1017–7156 at $9.1 \pm 1.7 \times 10^{-15}$. Rather than due to gravitational wave emission, this \dot{x} is likely due to an apparent change in the orbital inclination as a result of proper motion affecting the viewing geometry. We also report an $\dot{\omega}$ of $0.022(9)^\circ \text{ yr}^{-1}$, and we highlight the potential of measuring more relativistic orbital parameters with PSR J1017–7156. Together with its small period derivative and the corresponding low derived magnetic field as mentioned above, this makes PSR J1017–7156 a very interesting pulsar to be closely followed-up with further timing campaign, and indeed it is already being monitored by the Parkes Pulsar Timing Array Project (Manchester et al., 2013). Although we stress the importance of a careful dispersion measure variation treatment as discussed in Section 5.3.1 and a proper polarisation calibration to correctly assess the uncertainties on the TOAs for the high-precision timing required for PSR J1017–7156. Furthermore, orbital period variations are observed in the BW system PSR J1731–1847. We present the timing solution with the BTX timing model which demonstrate the quadratic changes in orbital period over the last three years.

We detected highly significant gamma-ray pulsations from PSRs J1125–5825 and J1446–4701, confirming the results of Keith et al. (2012) and Abdo et al. (2013). PSRs J1543–5149 and J1811–2405 were identified for the first time as gamma-ray pulsars: after folding the *Fermi* LAT photons with radio timing ephemerides, we obtained $> 5\sigma$ detections of these two MSPs, bringing the total number of MSPs with detected gamma-ray pulsations to 53 objects.

6.2 Future work

6.2.1 Continued processing

Only 37 per cent of the HTRU low-latitude Galactic plane survey has been assessed, and hence a lot more discoveries are still to be made. Advanced survey hardware and a carefully-designed search algorithm are the most important criteria leading to a successful pulsar survey as demonstrated in this work. Nonetheless, pulsar searching is also a race against time. To further increase our data processing speed, we are actively exploring other additional collaborators with world-class computing resources such as the Albert Einstein Institute, the Forschungszentrum Jülich, and the Swinburne supercluster. In addition, a dedicated single pulse search for transient signals will soon begin and will surely be returning exciting discoveries.

6.2.2 Follow-up on discoveries from the Galactic plane survey

Given the large number of discoveries expected from the HTRU Galactic plane survey, a dedicated follow-up timing campaign is now underway at the Parkes and the Lovell telescopes. Follow-up timing study is necessary for identifying any individual interesting pulsar systems discovered in the HTRU Galactic plane: one year of initial timing is the minimum time span required to fully-characterise any newly-discovered pulsars, essential for deriving pulsar parameters such as the characteristic age, magnetic field strength, spin-down rate, as well as to detect any unexpected behaviour of the pulsar which might result from emission instabilities. The four pulsars of individual interests mentioned in Section 4.3 are obvious examples. For instance, if PSR J1759–24 is indeed in an eclipsing binary system with a large orbital period of the order of years, it would require great patience before we can achieve a reliable timing solution. In addition, this follow-up timing project will enable a large-scale examination of the Galactic plane pulsar population, exploring the true boundaries of pulsar phase space. An unbiased census as such can potentially shed light to the characteristic age and radio luminosity distribution of pulsars in the Galactic plane. An analysis of the scattering time scale of the newly discovered pulsar is in progress. Discoveries made at high DMs are particularly useful for providing constraints on the higher end of the scattering relation which is currently not well quantified (see Section 1.3.2).

6.2.3 Further improvements in the search algorithms

The search algorithm employed in this PhD thesis has still much room for development, which will help improve future reprocessing of the HTRU Galactic plane data. In particular, the capability of the ‘partially-coherent segmented acceleration search’ as described in Section 3.3.2.3 can be maximised if the analysis of the individual segments can be combined coherently. This would allow us to exploit the full sensitivity achievable with the deep integration of this survey, essential for detecting the missing MSPs as described in Section 4.5. The effect of an eccentric orbit can be better quantified, and the acceleration step size can be further optimised. As discussed in Section 3.3.2.3, the current scheme effectively oversamples for the slow spinning binaries and vice versa. The Fourier domain RFI mitigation technique as described in Section 3.3.1.2 can also be taken one step further. As can be seen in Fig. 3.9, significant peaks due to RFI still occasionally remain in the ‘cleaned’ spectrum. We will investigate to adapt a flexible power threshold for the flagging of RFI affected Fourier frequencies based on the number of affected receiver beams, and we will apply the concept of spatial filtering that takes into account any directional spread of RFI as observed by the multibeam receiver.

Other search algorithms not considered in this thesis, such as the Fast Folding Algorithm (FFA) in time domain, can provide extra sensitivity towards long period pulsars. In addition, as mentioned in Section 3.3.2.3, the application of a phase modulation search will increase the chance of detecting pulsars in tight binary orbits. We shall certainly include these techniques when data reprocessing of the Galactic plane survey

will be conducted in the future.

6.3 Closing remarks

It has been a privilege to work as part of the HTRU Pulsar Survey consortium, and to have the chance to discover pulsars never known to mankind before. Looking backward, it has been almost 50 years since the discovery of the first radio pulsar. Yet pulsar astronomy is still a research field that continues to surprise us and generates exciting results. Looking forward, pulsar research is heading towards an era of data intensive astronomy that calls for international collaboration. Computing is going to be, if not already, a crucial component in the high throughput data analysis as required by the next generations of telescope facilities such as MeerKAT and the SKA. I am eager to get involved in and contribute to the new discoveries these future projects will bring about. I would also stay hopeful and keep watching out for the potential pulsar-black hole binaries that await to be discovered...

Bibliography

- Abadie J. et al., 2010, *Classical and Quantum Gravity*, 27, 173001 (Cited on page 56.)
- Abbott B. et al., 2008, *Phys. Rev. D*, 77, 062002 (Cited on page 20.)
- Abdo A. A. et al., 2009, *Science*, 325, 848 (Cited on page 20.)
- Abdo A. A. et al., 2013, *ApJS*, 208, 17 (Cited on pages 20, 94, 125, 127, 128 and 133.)
- Ables J. G., Manchester R. N., 1976, *A&A*, 50, 177 (Cited on page 10.)
- Alpar M. A., Cheng A. F., Ruderman M. A., Shaham J., 1982, *Nature*, 300, 728 (Cited on page 13.)
- Anderson P. W., Itoh N., 1975, *Nature*, 256, 25 (Cited on page 21.)
- Antoniadis J. et al., 2013, *Science*, 340, 448 (Cited on page 21.)
- Arzoumanian Z., Joshi K., Rasio F. A., Thorsett S. E., 1996, in Johnston S., Walker M. A., Bailes M., eds, *IAU Colloq. 160: Pulsars: Problems and Progress Vol. 105 of Astronomical Society of the Pacific Conference Series, Orbital Parameters of the PSR B1620-26 Triple System*. pp 525–530 (Cited on page 123.)
- Arzoumanian Z., Chernoff D. F., Cordes J. M., 2002, *ApJ*, 568, 289 (Cited on page 90.)
- Atwood W. B. et al., 2009, *ApJ*, 697, 1071 (Cited on pages 121 and 125.)
- Baade W., Zwicky F., 1934, *Proceedings of the National Academy of Science*, 20, 254 (Cited on page 5.)
- Backer D. C., Hellings R. W., 1986, *ARA&A*, 24, 537 (Cited on page 19.)
- Backer D. C., Foster R. S., Sallmen S., 1993, *Nature*, 365, 817 (Cited on page 114.)
- Bagchi M., Lorimer D. R., Wolfe S., 2013, *MNRAS*, 432, 1303 (Cited on page 66.)
- Bailes M. et al., 2011, *Science*, 333, 1717 (Cited on pages 20, 54, 107, 116 and 132.)
- Barr E. D. et al., 2013, *MNRAS*, 435, 2234 (Cited on page 45.)
- Baym G., Pethick C., Pines D., 1969, *Nature*, 224, 872 (Cited on page 21.)
- Bhat N. D. R., Cordes J. M., Camilo F., Nice D. J., Lorimer D. R., 2004, *ApJ*, 605, 759 (Cited on page 11.)
- Bhattacharya D., van den Heuvel E. P. J., 1991, *Phys. Rep.*, 203, 1 (Cited on page 13.)
- Bhattacharya D., 2002, *Journal of Astrophysics and Astronomy*, 23, 67 (Cited on page 13.)

- Bates S. D. et al., 2011, MNRAS, 416, 2455 (Cited on pages 107, 109, 112, 116, 129 and 132.)
- Bates S. D. et al., 2012, MNRAS, 427, 1052 (Cited on pages 53, 89, 90 and 129.)
- Bates S. D., Lorimer D. R., Rane A., Swiggum J., 2014, MNRAS, 439, 2893 (Cited on page 94.)
- Belczynski K., Kalogera V., Bulik T., 2002, ApJ, 572, 407 (Cited on pages 20, 57 and 129.)
- Belczynski K., Lorimer D. R., Ridley J. P., Curran S. J., 2010, MNRAS, 407, 1245 (Cited on page 90.)
- Beskin V. S., Gurevich A. V., Istomin I. N., 1988, Ap&SS, 146, 205 (Cited on page 116.)
- Biggs J. D., Lyne A. G., Hamilton P. A., McCulloch P. M., Manchester R. N., 1988, MNRAS, 235, 255 (Cited on page 88.)
- Booth R. S., Jonas J. L., 2012, African Skies, 16, 101 (Cited on page 43.)
- Boyles J. et al., 2013, ApJ, 763, 80 (Cited on page 42.)
- Bovy J., Rix H.-W., 2013, ApJ, 779, 115 (Cited on page 113.)
- Bregeon J., Charles E., M. Wood for the Fermi-LAT collaboration 2013, Proceedings of the 4th *Fermi* symposium, eConf C121028 (arXiv:1304.5456) (Cited on page 127.)
- Burgay M. et al., 2003, Nature, 426, 531 (Cited on pages 15, 21, 39 and 57.)
- Burgay M. et al., 2006, MNRAS, 368, 283 (Cited on page 38.)
- Burgay M. et al., 2013a, MNRAS, 429, 579 (Cited on pages 38 and 39.)
- Burgay M. et al., 2013b, MNRAS, 433, 259 (Cited on pages 53 and 129.)
- Camilo F., Thorsett S. E., Kulkarni S. R., 1994, ApJ, 421, L15 (Cited on page 90.)
- Camilo F., Lorimer D. R., Freire P., Lyne A. G., Manchester R. N., 2000, ApJ, 535, 975 (Cited on pages 33 and 34.)
- Camilo F., Manchester R. N., Gaensler B. M., Lorimer D. R., Sarkissian J., 2002a, ApJ, 567, L71 (Cited on page 13.)
- Camilo F. et al., 2002b, ApJ, 574, L71 (Cited on page 13.)
- Camilo F. et al., 2006, Nature, 442, 892 (Cited on pages 15 and 77.)
- Camilo F. et al., 2009, ApJ, 703, L55 (Cited on page 13.)
- Champion D. J. et al., 2008, Science, 320, 1309 (Cited on page 20.)

- Chen K., Ruderman M., 1993, *ApJ*, 402, 264 (Cited on pages 12, 13, 91, 111 and 116.)
- Chen H.-L., Chen X., Tauris T. M., Han Z., 2013, *ApJ*, 775, 27 (Cited on page 118.)
- Cheng K. S., Ho C., Ruderman M., 1986, *ApJ*, 300, 500 (Cited on page 9.)
- Clifton T. R., Lyne A. G., Jones A. W., McKenna J., Ashworth M., 1992, *MNRAS*, 254, 177 (Cited on page 37.)
- Crawford F., Kaspi V. M., Manchester R. N., Lyne A. G., Camilo F., D'Amico N., 2001, *ApJ*, 553, 367 (Cited on page 13.)
- Coenen T., 2013, in *IAU Symposium Vol. 291 of IAU Symposium, Pilot pulsar surveys with LOFAR*. pp 229–232 (Cited on page 42.)
- Cooley J. W., Tukey J. W., 1965, *Math. Comput.*, 19, 297 (Cited on pages 25 and 29.)
- Cordes J. M., Chernoff D. F., 1997, *ApJ*, 482, 971 (Cited on page 95.)
- Cordes J. M., Lazio T. J. W., 2002, *ArXiv Astrophysics e-prints* (Cited on pages 11, 57, 78, 79, 82, 83, 89, 103, 108, 119 and 120.)
- Cordes J. M., Kramer M., Lazio T. J. W., Stappers B. W., Backer D. C., Johnston S., 2004, *New A Rev.*, 48, 1413 (Cited on page 43.)
- Damour T., Deruelle N., 1986, *Ann. Inst. Henri Poincaré Phys. Théor.*, Vol. 44, No. 3, p. 263 - 292, 44, 263 (Cited on page 99.)
- Damour T., Schäfer G., 1991, *Physical Review Letters*, 66, 2549 (Cited on pages 22 and 123.)
- Damour T., Taylor J. H., 1991, *ApJ*, 366, 501 (Cited on pages 109 and 113.)
- Daugherty J. K., Harding A. K., 1986, *ApJ*, 309, 362 (Cited on page 9.)
- de Jager O. C., Büsching I., 2010, *A&A*, 517, L9 (Cited on page 128.)
- Demorest P. B., Pennucci T., Ransom S. M., Roberts M. S. E., Hessels J. W. T., 2010, *Nature*, 467, 1081 (Cited on pages 21, 84 and 85.)
- Deneva J. S., Cordes J. M., Lazio T. J. W., 2009, *ApJ*, 702, L177 (Cited on page 77.)
- Deneva J. S. et al., 2013, *ApJ*, 775, 51 (Cited on page 42.)
- Desvignes G. et al., 2013, in *IAU Symposium Vol. 291 of IAU Symposium, SPAN512: A new mid-latitude pulsar survey with the Nançay Radio Telescope*. pp 375–377 (Cited on page 40.)
- Deutsch A. J., 1955, *Annales d'Astrophysique*, 18, 1 (Cited on page 9.)
- Duncan R. C., Thompson C., 1992, *ApJ*, 392, L9 (Cited on page 15.)

- Eatough R. P. et al., 2013a, in IAU Symposium Vol. 291 of IAU Symposium, Can we see pulsars around Sgr A \star ? The latest searches with the Effelsberg telescope.. pp 382–384 (Cited on page 42.)
- Eatough R. P., Kramer M., Lyne A. G., Keith M. J., 2013b, MNRAS, 431, 292 (Cited on pages 34, 39, 65, 70, 77 and 95.)
- Eatough R. P. et al., 2013c, Nature, 501, 391 (Cited on pages 15 and 42.)
- Edwards R. T., Bailes M., van Straten W., Britton M. C., 2001, MNRAS, 326, 358 (Cited on page 37.)
- Erber T., 1966, Rev. Mod. Phys., 38, 626 (Cited on page 9.)
- Espinoza C. M., Lyne A. G., Stappers B. W., Kramer M., 2011a, MNRAS, 414, 1679 (Cited on page 57.)
- Espinoza C. M., Lyne A. G., Kramer M., Manchester R. N., Kaspi V. M., 2011b, ApJ, 741, L13 (Cited on page 8.)
- Espinoza C. M. et al., 2013, MNRAS, 430, 571 (Cited on pages 20 and 101.)
- Falcke H., Rezzolla L., 2014, A&A, 562, A137 (Cited on page 56.)
- Faulkner A. J. et al., 2004, MNRAS, 355, 147 (Cited on page 34.)
- Faulkner A. J. et al., 2005, ApJ, 618, L119 (Cited on page 38.)
- Folkner W. M., Williams J. G., Boggs D. H., 2009, Interplanetary Network Progress Report, 178, C1 (Cited on pages 16 and 98.)
- Foster R. S., Fairhead L., Backer D. C., 1991, ApJ, 378, 687 (Cited on page 16.)
- Frank J., King A. R., Raine D. J., 1985, Accretion power in astrophysics (Cited on page 54.)
- Freire P. C. C., 2005, in Rasio F. A., Stairs I. H., eds, Binary Radio Pulsars Vol. 328 of Astronomical Society of the Pacific Conference Series, Eclipsing Binary Pulsars. p. 405 (Cited on pages 116 and 118.)
- Freire P. C. C. et al., 2012, MNRAS, 423, 3328 (Cited on pages 22, 57 and 123.)
- Freire P. C. C., 2013, in IAU Symposium Vol. 291 of IAU Symposium, The pulsar population in Globular Clusters and in the Galaxy. pp 243–250 (Cited on page 13.)
- Fruchter A. S., Stinebring D. R., Taylor J. H., 1988, Nature, 333, 237 (Cited on page 54.)
- Gavriil F. P., Gonzalez M. E., Gotthelf E. V., Kaspi V. M., Livingstone M. A., Woods P. M., 2008, Science, 319, 1802 (Cited on page 15.)

- Gold T., 1968, *Nature*, 218, 731 (Cited on pages 5 and 7.)
- Goldreich P., Julian W. H., 1969, *ApJ*, 157, 869 (Cited on page 9.)
- Gonzalez M. E. et al., 2011, *ApJ*, 743, 102 (Cited on pages 118 and 123.)
- Gould D. M., 1994, PhD thesis, , Univ. of Manchester, (1994) (Cited on page 52.)
- Granet C. et al., 2005, *IEEE Antennas Propagation Magazine*, 47, 13 (Cited on page 98.)
- Guillemot L. et al., 2012, *ApJ*, 744, 33 (Cited on page 126.)
- Haslam C. G. T. et al., 1981, *A&A*, 100, 209 (Cited on page 47.)
- Hewish A., Bell S. J., Pilkington J. D. H., Scott P. F., Collins R. A., 1968, *Nature*, 217, 709 (Cited on page 5.)
- Hills J. G., 1983, *ApJ*, 267, 322 (Cited on page 114.)
- Hobbs G. et al., 2004, *MNRAS*, 352, 1439 (Cited on page 38.)
- Hobbs G., Lorimer D. R., Lyne A. G., Kramer M., 2005, *MNRAS*, 360, 974 (Cited on page 109.)
- Hobbs G. B., Edwards R. T., Manchester R. N., 2006, *MNRAS*, 369, 655 (Cited on pages 79, 99 and 127.)
- Holtzmark J., 1919, *Annalen der Physik*, 363, 577 (Cited on page 113.)
- Hotan A. W., van Straten W., Manchester R. N., 2004, *PASA*, 21, 302 (Cited on pages 79 and 98.)
- Jackson J. D., 1962, *Classical Electrodynamics* (Cited on page 8.)
- Jacoby B. A. et al., 2003, *ApJ*, 599, L99 (Cited on page 39.)
- Jacoby B. A., 2004, in Camilo F., Gaensler B. M., eds, *Young Neutron Stars and Their Environments Vol. 218 of IAU Symposium, A Search for Radio Pulsars at High Galactic Latitude*. p. 129 (Cited on page 37.)
- Jenet F. A., Hobbs G. B., Lee K. J., Manchester R. N., 2005, *ApJ*, 625, L123 (Cited on page 22.)
- Johnson T. J. et al., 2013, *ApJ*, submitted (Broadband Pulsations from PSR B1821–24) (Cited on page 128.)
- Johnston S., Bailes M., 1991, *MNRAS*, 252, 277 (Cited on page 121.)
- Johnston S., Manchester R. N., Lyne A. G., Bailes M., Kaspi V. M., Qiao G., D'Amico N., 1992a, *ApJ*, 387, L37 (Cited on page 87.)

- Johnston S. et al., 1992b, MNRAS, 255, 401 (Cited on page 37.)
- Jouteux S., Ramachandran R., Stappers B. W., Jonker P. G., van der Klis M., 2002, A&A, 384, 532 (Cited on page 35.)
- Kaspi V. M., Helfand D. J., 2002, in Slane P. O., Gaensler B. M., eds, Neutron Stars in Supernova Remnants Vol. 271 of Astronomical Society of the Pacific Conference Series, Constraining the Birth Events of Neutron Stars.p. 3 (Cited on page 8.)
- Kehl M., Krieger A., 2012, Auswirkungen der Verletzung des Starken Äquivalenzprinzips auf die Dynamik von Binärpulsaren im Gravitationsfeld der Milchstraße und in Kugelsternhaufen. Bachelor thesis, University of Bonn, Germany, 2012. (Cited on page 123.)
- Keith M. J. et al., 2009, MNRAS, 393, 623 (Cited on page 38.)
- Keith M. J. et al., 2010, MNRAS, 409, 619 (Cited on pages 45, 49, 50, 58, 60, 61, 63, 74, 94, 95 and 129.)
- Keith M. J. et al., 2012, MNRAS, 419, 1752 (Cited on pages 100, 107, 125, 129, 132 and 133.)
- Keith M. J. et al., 2013, MNRAS, 429, 2161 (Cited on pages 107 and 108.)
- Kerr M., 2011, ApJ, 732, 38 (Cited on pages 126, 127 and 128.)
- Knispel B. et al., 2013, ApJ, 774, 93 (Cited on pages 39 and 77.)
- Kopeikin S. M., 1996, ApJ, 467, L93 (Cited on page 123.)
- Kocz J., Bailes M., Barnes D., Burke-Spolaor S., Levin L., 2012, MNRAS, 420, 271 (Cited on page 60.)
- Kouwenhoven M. L. A., Voûte J. L. L., 2001, A&A, 378, 700 (Cited on page 39.)
- Kramer M., Wielebinski R., Jessner A., Gil J. A., Seiradakis J. H., 1994, A&AS, 107, 515 (Cited on page 16.)
- Kramer M. et al., 1998, ApJ, 501, 270 (Cited on page 52.)
- Kramer M. et al., 2003, MNRAS, 342, 1299 (Cited on pages 38 and 89.)
- Kramer M., Backer D. C., Cordes J. M., Lazio T. J. W., Stappers B. W., Johnston S., 2004, New A Rev., 48, 993 (Cited on pages 20 and 43.)
- Kramer M. et al., 2006, Science, 314, 97 (Cited on pages 22, 39 and 57.)
- Kumar H. S., Safi-Harb S., 2008, ApJ, 678, L43 (Cited on page 15.)
- Lange C. et al., 2001, MNRAS, 326, 274 (Cited on page 99.)
- Large M. I., Vaughan A. E., Mills B. Y., 1968, Nature, 220, 340 (Cited on page 5.)

- Lattimer J. M., Prakash M., 2001, *ApJ*, 550, 426 (Cited on page 6.)
- Lazaridis K. et al., 2011, *MNRAS*, 414, 3134 (Cited on page 124.)
- Lazarus P., 2013, in *IAU Symposium Vol. 291 of IAU Symposium, The PALFA Survey: Going to great depths to find radio pulsars.* pp 35–40 (Cited on page 40.)
- Lazarus P. et al., 2014, *MNRAS*, 437, 1485 (Cited on page 15.)
- Lee K. J., Guillemot L., Yue Y. L., Kramer M., Champion D. J., 2012, *MNRAS*, 424, 2832 (Cited on page 11.)
- Levin L. et al., 2010, *ApJ*, 721, L33 (Cited on pages 15, 54, 55 and 77.)
- Levin L. et al., 2012, *MNRAS*, 422, 2489 (Cited on page 55.)
- Levin L. et al., 2013, *MNRAS*, 434, 1387 (Cited on pages 53, 95 and 121.)
- Lorimer D. R., Bailes M., Dewey R. J., Harrison P. A., 1993, *MNRAS*, 263, 403 (Cited on page 90.)
- Lorimer D. R., Yates J. A., Lyne A. G., Gould D. M., 1995, *MNRAS*, 273, 411 (Cited on page 40.)
- Lorimer D. R. et al., 2004, *MNRAS*, 347, L21 (Cited on page 90.)
- Lorimer D. R., Kramer M., 2005, *Handbook of Pulsar Astronomy* (Cited on pages 7, 8, 27, 31, 103 and 111.)
- Lorimer D. R. et al., 2006, *MNRAS*, 372, 777 (Cited on pages 38, 94 and 95.)
- Lorimer D. R., 2008, *Living Reviews in Relativity*, 11 (Cited on page 14.)
- Lorimer D. R., Karastergiou A., McLaughlin M. A., Johnston S., 2013, *MNRAS*, 436, L5 (Cited on pages 42 and 95.)
- Lorimer D. R., 2013, in van Leeuwen J., ed., *IAU Symposium Vol. 291 of IAU Symposium, The Galactic Millisecond Pulsar Population.* pp 237–242 (Cited on pages 42 and 95.)
- Lynch R. S. et al., 2013a, *ApJ*, 763, 81 (Cited on page 42.)
- Lynch R. S. et al., 2013b, in *IAU Symposium Vol. 291 of IAU Symposium, The hunt for new pulsars with the Green Bank Telescope.* pp 41–46 (Cited on page 42.)
- Lyne A. G., 1992, *Royal Society of London Philosophical Transactions Series A*, 341, 29 (Cited on page 21.)
- Lyne A. G. et al., 2000, *MNRAS*, 312, 698 (Cited on page 38.)
- Lyne A. G. et al., 2004, *Science*, 303, 1153 (Cited on pages 15, 21, 39 and 57.)

- Lyne A. G., Graham-Smith F., 2005, *Pulsar Astronomy* (Cited on page 78.)
- Lyne A. G., 2008, in Bassa C., Wang Z., Cumming A., Kaspi V. M., eds, *40 Years of Pulsars: Millisecond Pulsars, Magnetars and More* Vol. 983 of *American Institute of Physics Conference Series*, Parkes 20-cm Multibeam Pulsar Surveys. pp 561–566 (Cited on page 37.)
- Lyne A., Hobbs G., Kramer M., Stairs I., Stappers B., 2010, *Science*, 329, 408 (Cited on page 21.)
- Manchester R. N., Taylor J. H., 1972, *Astrophys. Lett.*, 10, 67 (Cited on page 10.)
- Manchester R. N. et al., 2001, *MNRAS*, 328, 17 (Cited on pages 34 and 38.)
- Manchester R. N., Hobbs G. B., Teoh A., Hobbs M., 2005, *VizieR Online Data Catalog*, 7245, 0 (Cited on pages 12, 23 and 38.)
- Manchester R. N. et al., 2013, *PASA*, 30, 17 (Cited on pages 98 and 133.)
- McLaughlin M. A. et al., 2006, *Nature*, 439, 817 (Cited on page 38.)
- Middleditch J., Kristian J., 1984, *ApJ*, 279, 157 (Cited on page 33.)
- Mihalas D., Binney J., 1981, *Galactic astronomy: Structure and kinematics* /2nd edition/ (Cited on page 113.)
- Morris D. J. et al., 2002, *MNRAS*, 335, 275 (Cited on pages 38, 71 and 89.)
- Narayan R., Ostriker J. P., 1990, *ApJ*, 352, 222 (Cited on page 90.)
- Ng C., HTRU Collaboration 2013, in van Leeuwen J., ed., *IAU Symposium Vol. 291 of IAU Symposium, Conducting the deepest all-sky pulsar survey ever: the all-sky High Time Resolution Universe survey*. pp 53–56 (Cited on page 53.)
- Ng C. et al., 2014, *MNRAS*, 439, 1865 (Cited on pages 97 and 129.)
- Nolan P. L. et al., 2012, *ApJS*, 199, 31 (Cited on page 127.)
- Nomoto K., Nariai K., Sugimoto D., 1979, *PASJ*, 31, 287 (Cited on page 114.)
- Noutsos A., Johnston S., Kramer M., Karastergiou A., 2008, *MNRAS*, 386, 1881 (Cited on pages 21 and 57.)
- O’Brien J. T., Kramer M., Lyne A. G., Lorimer D. R., Jordan C. A., 2006, *Chinese Journal of Astronomy and Astrophysics Supplement*, 6, 020000 (Cited on page 77.)
- Oppenheimer J. R., Volkoff G. M., 1939, *Phys. Rev.*, 55, 374 (Cited on page 6.)
- Pacini F., 1967, *Nature*, 216, 567 (Cited on pages 5 and 7.)
- Paczynski B., 1990, *ApJ*, 348, 485 (Cited on pages 110 and 112.)

- Papitto A. et al., 2013, *Nature*, 501, 517 (Cited on page 13.)
- Peters P. C., 1964, *Phys. Rev.*, 136, B1224 (Cited on page 123.)
- Petroff E., Keith M. J., Johnston S., van Straten W., Shannon R. M., 2013, *MNRAS* (Cited on page 107.)
- Petroff E., et al., 2014, *ApJ*, in press (Cited on page 57.)
- Phinney E. S., 1992, *Royal Society of London Philosophical Transactions Series A*, 341, 39 (Cited on pages 121, 122 and 123.)
- Pletsch H. J. et al., 2012, *Science*, 338, 1314 (Cited on page 118.)
- Ransom S. M. et al., 2001, *ApJ*, 546, L25 (Cited on page 35.)
- Ransom S. M., Eikenberry S. S., Middleditch J., 2002, *AJ*, 124, 1788 (Cited on pages 31 and 34.)
- Ransom S. M., Cordes J. M., Eikenberry S. S., 2003, *ApJ*, 589, 911 (Cited on pages 35 and 68.)
- Ransom S. M. et al., 2014, *Nature*, 505, 520 (Cited on page 20.)
- Ray P. S. et al., 2011, *ApJS*, 194, 17 (Cited on page 127.)
- Ray P. S. et al., 2013, *ApJ*, 763, L13 (Cited on page 118.)
- Rea N. et al., 2010, *Science*, 330, 944 (Cited on page 16.)
- Richards D. W., Comella J. M., 1969, *Nature*, 222, 551 (Cited on page 5.)
- Roberts M. S. E., 2013, in *IAU Symposium Vol. 291 of IAU Symposium, Surrounded by spiders! New black widows and redbacks in the Galactic field.* pp 127–132 (Cited on page 116.)
- Romani R. W., 1996, *ApJ*, 470, 469 (Cited on page 9.)
- Romani R. W. et al., 2012, *ApJ*, 760, L36 (Cited on page 118.)
- Ruderman M. A., Sutherland P. G., 1975, *ApJ*, 196, 51 (Cited on page 9.)
- Ruderman M., Shaham J., Tavani M., 1989, *ApJ*, 336, 507 (Cited on page 87.)
- Scheuer P. A. G., 1968, *Nature*, 218, 920 (Cited on page 11.)
- Schnitzeler D. H. F. M., 2012, *MNRAS*, 427, 664 (Cited on page 115.)
- Sesana A., Vecchio A., Volonteri M., 2009, *MNRAS*, 394, 2255 (Cited on page 43.)
- Shklovskii I. S., 1970, *Soviet Ast.*, 13, 562 (Cited on pages 90, 109 and 110.)

- Smits R., Kramer M., Stappers B., Lorimer D. R., Cordes J., Faulkner A., 2009, *A&A*, 493, 1161 (Cited on page 43.)
- Staelin D. H., Reifenstein III E. C., 1968, *Science*, 162, 1481 (Cited on page 5.)
- Staveley-Smith L. et al., 1996, *PASA*, 13, 243 (Cited on pages 37 and 49.)
- Steiner A. W., Lattimer J. M., Brown E. F., 2013, *ApJ*, 765, L5 (Cited on page 6.)
- Sturrock P. A., 1971, *ApJ*, 164, 529 (Cited on page 9.)
- Spitkovsky A., 2006, *ApJ*, 648, L51 (Cited on page 116.)
- Stairs I. H. et al., 2001, *MNRAS*, 325, 979 (Cited on page 38.)
- Stairs I. H. et al., 2005, *ApJ*, 632, 1060 (Cited on pages 22 and 123.)
- Staveley-Smith L. et al., 1996, *PASA*, 13, 243 (Cited on pages 37 and 49.)
- Tauris T. M., Bailes M., 1996, *A&A*, 315, 432 (Cited on pages 114 and 118.)
- Tauris T. M., Savonije G. J., 1999, *A&A*, 350, 928 (Cited on pages 15 and 100.)
- Tauris T. M., van den Heuvel E. P. J., 2006, *Formation and evolution of compact stellar X-ray sources*. pp 623–665 (Cited on page 13.)
- Tauris T. M., 2011, in Schmidtobreick L., Schreiber M. R., Tappert C., eds, *Evolution of Compact Binaries Vol. 447 of Astronomical Society of the Pacific Conference Series, Five and a Half Roads to Form a Millisecond Pulsar*. p. 285 (Cited on pages 84, 100, 101 and 116.)
- Tauris T. M., Langer N., Kramer M., 2011, *MNRAS*, 416, 2130 (Cited on pages 21, 84 and 85.)
- Tauris T. M., Langer N., Kramer M., 2012, *MNRAS*, 425, 1601 (Cited on pages 8, 85, 112, 116 and 120.)
- Taylor J. H., Huguenin G. R., 1969, *Nature*, 221, 816 (Cited on page 31.)
- Taylor J. H., Weisberg J. M., 1989, *ApJ*, 345, 434 (Cited on page 21.)
- Taylor J. H., 1992, *Royal Society of London Philosophical Transactions Series A*, 341, 117 (Cited on pages 79 and 98.)
- Taylor J. H., Cordes J. M., 1993, *ApJ*, 411, 674 (Cited on page 115.)
- Terasawa T. et al., 2005, *Nature*, 434, 1110 (Cited on page 56.)
- Terzian Y., Lazio J., 2006, in *Society of Photo-Optical Instrumentation Engineers (SPIE) Conference Series Vol. 6267 of Society of Photo-Optical Instrumentation Engineers (SPIE) Conference Series, The Square Kilometre Array* (Cited on page 42.)

- Thompson D. J., 2008, *Reports on Progress in Physics*, 71, 116901 (Cited on pages 20 and 94.)
- Thornton D. et al., 2013, *Science*, 341, 53 (Cited on page 55.)
- Tiburzi C. et al., 2013, *MNRAS*, 436, 3557 (Cited on page 53.)
- Toscano M. et al., 1999, *MNRAS*, 307, 925 (Cited on page 109.)
- Totani T., 2013, *PASJ*, 65, L12 (Cited on page 56.)
- van Haften L. M., Nelemans G., Voss R., Wood M. A., Kuijpers J., 2012a, *A&A*, 537, A104 (Cited on page 118.)
- van Haften L. M., Nelemans G., Voss R., Jonker P. G., 2012b, *A&A*, 541, A22 (Cited on page 116.)
- van Haasteren R. et al., 2011, *MNRAS*, 414, 3117 (Cited on page 22.)
- van Straten W., 2004, *ApJS*, 152, 129 (Cited on page 100.)
- Verbiest J. P. W., Lorimer D. R., McLaughlin M. A., 2010, *MNRAS*, 405, 564 (Cited on page 106.)
- Weisberg J. M., Taylor J. H., 1981, *General Relativity and Gravitation*, 13, 1 (Cited on page 125.)
- Weltevrede P. et al., 2010, *PASA*, 27, 64 (Cited on page 79.)
- Wex N., 2014, *ArXiv e-prints* (Cited on page 57.)
- Wood K. S. et al., 1991, *ApJ*, 379, 295 (Cited on page 34.)
- Yardley D. R. B. et al., 2011, *MNRAS*, 414, 1777 (Cited on page 22.)
- You X. P. et al., 2007, *MNRAS*, 378, 493 (Cited on page 107.)

HTRU Galactic plane survey

known pulsar re-detections

Table A1: The 348 previously known pulsars re-detected in the HTRU Galactic plane survey thus far from the 37 per cent of processed observations. The Galactic longitude (l) and latitude (b) of the pulsar is listed, as well as the file ID of the observation for which the pulsar was re-detected. We list also the offset of the central position of the receiver beam from the true position of the pulsar. Note that in the case when a pulsar was re-detected multiple times in different observations, we have listed only the re-detection which was closest to the pulsar, i.e. that with the smallest offset. We list the observed spin period (P) and the DM, as well as the expected flux density at 1.4 GHz (S_{exp}) and the expected S/N (S/N_{exp}) calculated according to the description in Section 4.1. For the pulsars where no flux density is published on PSRCAT, we indicate with an asterisk (*). Finally, we list the observed S/N (S/N_{obs}).

PSR name	l ($^{\circ}$)	b ($^{\circ}$)	file Pointing/beam	offset ($^{\circ}$)	P_{obs} (ms)	DM_{obs} (cm^{-3}pc)	S_{exp} (mJy)	S/N_{exp}	S/N_{obs}
B0959–54	280.226	0.085	2010-12-29-17:18:50/01	0.21	1436.622	137.4	0.6	208.0	167.6
B1011–58	283.706	-2.144	2011-01-29-15:34:44/08	0.13	819.922	374.8	0.7	184.0	129.7
B1014–53	281.201	2.451	2010-12-08-17:01:17/08	0.031	769.583	65.5	0.8	204.0	81.4
B1015–56	282.732	0.341	2011-04-25-06:10:43/13	0.11	503.462	434.5	1.6	378.0	217.0
B1030–58	285.907	-0.98	2011-05-19-06:55:11/05	0.069	464.209	420.1	0.7	187.0	154.5
B1036–58	286.284	-0.023	2011-07-03-04:49:38/06	0.19	661.993	73.5	0.1	24.3	20.2
B1039–55	285.192	2.999	2011-07-07-02:30:49/03	0.11	1170.865	299.4	0.3	75.4	160.1
B1044–57	287.065	0.733	2011-07-03-04:49:38/11	0.16	369.427	238.8	0.3	51.6	80.7
B1046–58	287.425	0.577	2012-08-07-00:41:51/03	0.12	123.713	128.8	3.0	462.0	531.1
B1054–62	290.292	-2.966	2011-07-18-00:07:15/12	0.12	422.449	322.2	9.9	1250.0	1319.6
B1105–59	290.249	0.515	2011-05-06-05:57:46/13	0.15	1516.530	82.2	0.1	22.4	38.0
B1112–60	291.443	-0.322	2011-04-25-07:24:17/09	0.18	880.850	680.0	0.4	62.6	137.8
B1124–60	292.834	0.292	2011-04-25-07:24:17/06	0.1	202.736	280.1	0.6	119.0	102.4
B1131–62	294.213	-1.296	2011-07-29-00:04:30/13	0.19	1022.872	579.2	0.5	22.1	60.2
B1143–60	294.977	1.343	2011-06-26-02:43:44/10	0.093	273.374	112.6	2.3	317.0	431.8
B1154–62	296.705	-0.199	2011-07-02-03:46:37/01	0.055	400.524	323.4	5.1	978.0	1034.2
B1221–63	299.984	-1.415	2011-07-18-01:20:47/13	0.23	216.479	99.7	0.3	41.9	58.2
B1222–63	300.131	-1.414	2011-07-18-01:20:47/13	0.088	419.619	411.2	0.3	51.3	126.3
B1240–64	302.051	-1.532	2011-05-04-08:15:17/04	0.11	388.484	297.3	7.1	1800.0	2978.7
B1259–63	304.184	-0.992	2011-12-05-18:51:30/04	0.056	47.763	147.2	1.4	50.0	192.4
B1302–64	304.411	-2.092	2008-11-20-19:16:48/07	0.14	571.650	494.9	0.6	100.0	116.6
B1316–60	306.314	1.742	2011-05-18-08:45:16/07	0.093	284.352	402.0	0.8	163.0	145.6
B1323–62	307.074	0.204	2011-05-17-08:51:29/12	0.17	529.925	316.2	3.6	700.0	568.8
B1323–62*	306.966	-0.429	2011-05-19-09:21:59/02	0.12	196.479	293.8	1.5	258.0	192.7
B1334–61	308.373	0.305	2011-07-03-07:18:09/12	0.19	1238.986	642.1	0.6	58.7	62.4

150 Appendix A. HTRU Galactic plane survey known pulsar re-detections

B1353-62	310.474	-0.565	2011-04-27-10:25:20/13	0.2	455.777	419.3	1.0	133.0	12.3
B1356-60	311.239	1.126	2010-12-12-18:12:48/10	0.12	127.507	292.9	3.8	597.0	914.2
B1358-63	310.568	-2.14	2011-05-07-09:46:47/09	0.081	842.802	96.4	4.5	1140.0	943.7
B1409-62	312.053	-1.718	2011-04-24-09:35:05/10	0.028	394.950	117.1	0.9	237.0	180.5
B1518-58	321.63	-1.215	2011-04-23-18:50:11/13	0.13	395.354	198.9	1.9	270.0	301.2
B1523-55	323.639	0.59	2010-12-31-19:49:57/02	0.12	1048.716	378.4	0.4	105.0	113.9
B1530-53	325.716	1.944	2011-12-05-02:25:17/12	0.25	1368.878	31.1	0.3	65.6	95.6
B1530-539	325.463	1.483	2011-05-09-11:33:02/12	0.18	289.689	193.5	0.2	39.7	27.1
B1535-56	324.621	-0.806	2011-04-24-18:34:39/09	0.069	243.394	175.2	3.6	520.0	382.8
B1541-52	327.271	1.32	2011-06-27-06:35:48/02	0.088	178.553	34.7	2.4	495.0	201.2
B1550-54	327.186	-0.901	2011-06-27-12:21:33/05	0.14	1081.343	220.3	0.3	62.7	61.4
B1555-55	327.238	-2.024	2012-08-07-03:38:29/05	0.16	957.263	206.4	0.2	71.0	59.8
B1556-57	325.971	-3.697	2012-08-07-11:27:02/05	0.15	194.456	175.8	0.4	57.1	64.6
B1601-52	329.732	-0.484	2011-06-26-06:24:21/12	0.12	658.013	33.3	6.2	556.0	383.2
B1609-47	334.573	2.835	2011-04-22-19:48:13/02	0.069	382.375	158.1	1.2	243.0	173.9
B1610-50	332.206	0.172	2011-05-05-12:06:36/13	0.16	231.898	581.8	0.6	80.9	68.7
B1629-50	334.699	-1.569	2011-04-23-20:03:59/01	0.099	352.144	399.9	3.5	770.0	601.4
B1630-44	338.725	1.982	2011-06-30-14:20:50/03	0.12	436.508	474.2	0.9	205.0	167.3
B1634-45	338.478	0.761	2011-07-12-08:31:53/05	0.15	118.773	194.4	0.3	62.7	37.8
B1635-45	338.5	0.459	2011-06-26-16:09:12/03	0.073	529.120	260.5	0.6	153.0	131.3
B1641-45	339.193	-0.195	2011-06-27-13:35:15/01	0.062	455.075	477.1	254	66400	24044
B1657-45	341.36	-2.177	2013-01-01-19:34:19/03	0.12	322.908	528.4	1.2	151.0	148.2
B1703-40	345.718	-0.198	2010-12-09-21:35:04/01	0.22	581.017	353.4	0.6	89.5	56.0
B1706-44	343.098	-2.686	2013-01-05-19:45:58/07	0.097	102.508	75.5	4.5	600.0	482.3
B1714-34	352.12	2.025	2011-10-13-03:03:17/04	0.18	656.305	587.3	0.7	147.0	123.2
B1715-40	347.653	-1.533	2013-01-05-04:06:07/04	0.19	189.095	386.8	0.2	29.7	35.5
B1718-32	354.561	2.525	2011-04-19-20:04:52/12	0.07	477.158	125.1	2.6	505.0	534.5
B1718-35	351.687	0.67	2011-10-13-03:03:17/13	0.072	280.432	494.9	8.5	741.0	441.5
B1719-37	350.49	-0.507	2011-06-27-14:48:40/02	0.13	236.180	99.1	1.3	332.0	177.0
B1727-33	354.133	0.09	2010-12-09-22:48:23/08	0.062	139.498	261.2	2.6	287.0	162.2
B1734-35	353.175	-2.268	2013-01-31-18:55:37/09	0.1	397.589	89.4	0.4	91.8	84.3
B1735-32	356.466	-0.491	2010-12-12-03:46:51/07	0.23	768.500	46.9	0.2	50.7	12.3
B1736-29	359.206	1.064	2011-07-03-13:48:57/04	0.23	161.443 [†]	138.3	0.1	34.0	37.6
B1736-31	357.096	-0.22	2010-12-12-03:46:51/08	0.32	529.451	602.1	0.0	3.36	14.4
B1740-31	357.299	-1.148	2011-10-13-10:01:19/13	0.071	2414.623	206.1	1.5	299.0	206.9
B1746-30	359.459	-1.244	2011-07-02-11:08:49/08	0.23	609.874	494.9	0.2	22.6	16.8
B1747-31	357.982	-2.516	2011-10-13-10:01:19/09	0.12	910.362	204.4	0.6	146.0	66.9
B1749-28	1.54	-0.961	2012-12-29-04:38:59/05	0.24	562.565	51.0	1.0	270.0	352.7
B1749-28	1.54	-0.961	2013-02-01-19:56:34/10	0.36	562.564	52.9	0.0	4.69	191.8
B1750-24	4.274	0.512	2011-01-03-22:32:45/09	0.16	528.343	674.2	0.7	53.0	39.1
B1753-24	5.027	0.044	2011-01-03-03:23:59/05	0.11	670.480	366.5	1.0	176.0	98.9
B1754-24	5.281	0.054	2011-01-03-03:23:59/01	0.12	234.106	178.0	1.9	256.0	338.2
B1756-22	7.472	0.81	2010-12-31-00:45:15/06	0.17	460.979	175.8	0.3	110.0	54.0
B1757-24	5.254	-0.882	2011-01-03-22:32:45/13	0.14	124.957	291.2	0.3	32.5	49.6
B1758-23	6.837	-0.066	2010-12-10-01:47:49/02	0.12	415.839	1070.3	1.1	70.6	87.7
B1758-29	1.436	-3.249	2013-02-01-19:56:34/13	0.26	1081.909	115.7	0.1	7.41	35.9
B1804-27	3.843	-3.257	2011-01-23-02:52:31/05	0.15	827.782	310.6	0.3	75.8	69.2
B1809-173	13.109	0.538	2013-01-01-00:04:30/01	0.18	1205.377	253.3	0.2	56.0	28.0
B1815-14	16.405	0.61	2009-04-16-16:38:15/10	0.21	291.490	619.2	0.8	85.2	111.4
B1817-13	17.161	0.483	2009-04-16-16:38:15/04	0.1	921.456	766.1	1.2	200.0	106.4
B1820-11	19.767	0.946	2012-08-07-08:52:51/12	0.14	279.837	425.6	1.2	106.0	125.3
B1820-14	17.252	-0.176	2010-12-10-03:01:21/03	0.086	214.771	649.7	0.5	86.3	65.0
B1821-11	19.809	0.741	2013-01-01-01:17:40/09	0.17	435.759	605.9	0.3	36.3	49.3
B1822-09	21.449	1.324	2013-01-01-03:46:01/13	0.16	769.015	18.1	3.3	734.0	441.9

B1822-14	16.805	-1.001	2011-04-23-21:19:27/05	0.15	279.198	353.3	0.8	130.0	110.9
B1823-11	19.8	0.293	2012-08-07-08:52:51/13	0.058	2093.120	315.4	0.6	58.2	111.1
B1823-13	18.001	-0.691	2011-01-03-23:46:27/04	0.19	101.495	231.3	0.4	48.6	34.1
B1824-10	21.286	0.798	2011-06-26-13:23:59/09	0.19	245.758	428.8	0.3	26.7	34.4
B1828-11	20.812	-0.478	2011-07-02-13:38:31/10	0.11	405.074	158.4	0.7	226.0	120.0
B1829-10	21.587	-0.597	2011-07-06-12:52:40/02	0.034	330.356	474.2	1.2	251.0	153.3
B1831-04	27.042	1.749	2011-01-04-00:59:52/11	0.18	290.108	79.1	0.9	38.8	173.9
B1832-06	25.093	0.552	2012-08-07-10:05:54/01	0.17	305.852	466.7	0.3	33.6	31.7
B1834-04	27.167	1.13	2011-01-04-00:59:52/05	0.17	354.237	229.9	0.4	80.4	55.3
B1834-06	25.191	0.002	2012-08-07-10:05:54/02	0.21	1905.782	310.3	0.3	38.1	21.0
B1834-10	22.263	-1.415	2013-01-02-00:27:11/03	0.27	562.717	312.2	0.1	25.2	41.7
B1838-04	27.818	0.279	2010-12-30-02:35:36/06	0.1	186.149	326.0	1.5	285.0	221.0
B1839-04	28.347	0.174	2010-12-30-02:35:36/13	0.12	1839.943	183.1	2.1	140.0	207.5
B1841-04	28.096	-0.548	2009-04-16-17:52:00/07	0.06	991.028	125.9	0.9	264.0	146.1
B1842-02	29.727	0.235	2011-01-03-00:48:46/06	0.072	507.730	421.5	0.7	109.0	69.6
B1842-04	28.193	-0.785	2011-07-02-14:51:49/11	0.17	486.755	227.0	0.4	54.3	70.3
B1844-04	28.876	-0.939	2011-05-09-20:12:05/05	0.038	597.800	138.2	4.0	678.0	420.0
J1001-5559	280.691	-0.648	2011-01-03-12:44:55/11	0.093	1661.172	151.7	0.4	113.0	68.1
J1012-5830	283.459	-1.762	2011-04-23-10:49:40/11	0.049	2133.583	290.3	0.1	16.3	17.6
J1013-5934	284.13	-2.596	2011-06-27-00:28:13/09	0.054	442.903	376.4	1.6	352.0	235.3
J1015-5719	283.088	-0.578	2011-05-04-05:48:18/01	0.068	139.902	278.5	0.7	36.0	96.1
J1016-5819	283.708	-1.363	2011-01-29-15:34:44/09	0.12	87.834	252.3	0.1	18.1	20.6
J1016-5857	284.079	-1.88	2011-06-27-00:28:13/01	0.11	107.407	394.6	0.2	31.4	40.6
J1019-5749	283.837	-0.679	2011-05-07-05:20:00/06	0.11	162.506	1043.2	0.4	24.1	59.9
J1022-5813	284.347	-0.834	2011-01-29-15:34:44/10	0.094	1643.773	733.5	0.1	23.8	21.3
J1028-5819	285.065	-0.496	2011-06-27-07:53:06/05	0.084	45.702 [†]	96.4	0.3	199.0	25.1
J1043-6116	288.221	-2.106	2012-08-06-23:25:15/03	0.078	288.605	449.5	0.7	141.0	148.3
J1055-6028	289.133	-0.745	2011-05-05-05:55:13/01	0.2	99.664	640.0	0.1	15.1	22.5
J1055-6236	290.081	-2.66	2011-05-07-06:33:29/08	0.082	448.635	151.4	0.1	18.6	19.2
J1103-6025	289.994	-0.294	2011-05-05-05:55:13/12	0.076	396.587	277.4	0.1	29.7	49.7
J1104-6103	290.331	-0.828	2011-05-08-06:31:44/11	0.11	280.906	77.4	0.1	27.9	21.9
J1105-6107	290.49	-0.846	2010-12-30-15:48:12/02	0.076	63.199	270.8	0.6	64.7	96.7
J1107-5907	289.944	1.106	2011-05-06-05:57:46/06	0.037	252.773	40.4	0.2	28.6	22.2
J1107-6143	290.921	-1.316	2011-05-07-06:33:29/12	0.049	1799.454	415.4	0.3	77.7	77.9
J1112-6103	291.221	-0.462	2010-12-30-15:48:12/06	0.11	64.973	598.3	0.7	54.8	58.0
J1115-6052	291.564	-0.126	2011-04-25-07:24:17/09	0.059	259.779	229.0	0.3	61.1	50.7
J1117-6154	292.102	-1.028	2011-05-16-08:05:44/04	0.13	505.101	489.1	0.3	72.7	65.1
J1119-6127	292.151	-0.537	2011-04-25-07:24:17/08	0.11	409.199	705.9	0.4	48.0	48.4
J1123-6102	292.509	0.049	2011-05-09-06:24:56/01	0.14	640.236	436.0	0.2	55.4	62.8
J1123-6259	293.183	-1.783	2011-07-27-23:42:48/11	0.049	271.436	222.1	0.5	87.8	69.1
J1138-6207	294.506	-0.463	2011-05-19-08:08:26/02	0.1	117.568	519.0	0.3	27.7	32.0
J1142-6230	295.11	-0.675	2011-05-19-08:08:26/01	0.14	558.382	351.0	0.1	14.5	16.7
J1144-6217	295.186	-0.438	2011-05-19-08:08:26/01	0.18	850.677	279.6	0.0	13.3	11.3
J1152-6012	295.716	1.843	2011-06-28-07:51:16/09	0.081	376.573	66.5	0.1	21.1	26.4
J1224-6208	299.818	0.565	2011-04-22-11:13:59/02	0.1	585.770	452.1	0.1	33.0	26.5
J1227-6208	300.153	0.576	2011-05-05-07:08:53/01	0.22	34.522	362.6	0.1	12.2	11.8
J1231-6303	300.644	-0.273	2010-12-29-19:46:16/08	0.11	1351.241	275.7	0.8	58.2	99.8
J1232-6501	300.911	-2.221	2011-04-23-08:08:01/01	0.06	88.282	240.0	0.3	26.7	39.1
J1233-6344	300.968	-0.945	2010-12-12-15:48:39/02	0.14	756.894	502.4	0.0	6.52	12.2
J1235-6354	301.231	-1.088	2010-12-29-19:46:16/06	0.082	256.777	439.0	0.1	18.7	16.3
J1244-6531	302.227	-2.658	2011-05-07-07:47:10/08	0.066	1546.811	386.1	0.1	32.4	14.2
J1245-6238	302.233	0.215	2008-12-10-18:22:48/09	0.06	2283.112	337.7	0.1	19.6	17.7
J1249-6507	302.771	-2.251	2011-05-08-07:45:39/07	0.062	434.444	214.3	0.1	17.0	15.5
J1252-6314	303.075	-0.371	2011-04-27-09:12:06/01	0.033	823.342	272.2	0.6	140.0	118.7

152 Appendix A. HTRU Galactic plane survey known pulsar re-detections

J1302-63	304.107	-0.901	2011-12-05-18:51:30/04	0.068	325.728	876.0	0.1	17.7	15.5
J1314-6101	305.71	1.727	2011-06-30-10:40:03/03	0.053	2948.382	279.8	0.4	82.6	69.5
J1316-6232	305.848	0.191	2011-07-01-03:25:09/02	0.085	342.825	963.1	0.5	23.2	57.8
J1317-6302	305.908	-0.328	2011-07-01-03:25:09/08	0.18	261.270	678.3	0.2	24.1	44.4
J1319-6105	306.311	1.597	2011-05-18-08:45:16/07	0.078	421.118	441.2	0.6	115.0	104.0
J1322-6241	306.489	-0.041	2011-06-26-03:57:20/07	0.14	505.188	620.2	0.1	33.2	31.9
J1324-6146	306.859	0.851	2011-06-26-03:57:20/12	0.031	844.102	819.2	0.7	63.7	75.9
J1329-6158	307.334	0.567	2011-07-12-12:17:58/12	0.14	1565.240	515.7	0.1	16.7	15.8
J1348-6307	309.353	-0.962	2011-06-28-12:51:42/13	0.11	927.765	580.6	0.3	25.8	33.4
J1349-6130	309.813	0.587	2011-05-16-10:33:17/09	0.11	259.364	285.2	0.3	58.5	51.7
J1354-6249	310.07	-0.832	2008-11-20-20:28:21/10	0.11	2951.940	218.5	0.1	25.1	19.7
J1355-6206	310.332	-0.156	2011-04-27-10:25:20/07	0.1	276.602	542.1	0.3	37.7	39.7
J1403-6310	310.928	-1.423	2011-04-24-17:20:57/12	0.059	399.170	304.6	0.5	69.9	70.9
J1406-5806	312.673	3.345	2011-05-09-09:12:21/10	0.24	288.351	233.4	0.0	3.05	13.7
J1406-6121	311.841	0.203	2010-12-12-18:12:48/02	0.037	213.095	539.1	0.3	39.1	25.6
J1407-6048	312.13	0.681	2010-12-12-18:12:48/01	0.054	492.344	578.7	0.2	28.9	27.6
J1407-6153	311.81	-0.354	2011-04-23-17:36:38/08	0.088	701.636	665.3	0.2	22.7	14.2
J1410-6132	312.196	-0.09	2010-12-12-18:12:48/08	0.15	50.055	964.2	1.9	52.1	21.2
J1413-6141	312.462	-0.337	2011-01-02-18:40:00/09	0.18	285.740	666.4	0.1	8.85	16.0
J1413-6222	312.241	-0.988	2011-04-22-16:43:56/03	0.098	292.408	811.2	0.6	67.0	62.8
J1416-6037	313.179	0.535	2010-12-31-17:25:45/10	0.25	295.581	286.4	0.0	3.77	13.9
J1420-6048	313.541	0.227	2011-01-01-16:35:45/11	0.091	68.208	359.4	0.6	41.3	41.8
J1425-6210	313.63	-1.258	2011-01-02-18:40:00/06	0.089	501.730	433.6	0.1	28.2	22.9
J1444-5941	316.791	0.098	2011-06-26-05:10:45/01	0.17	2759.908	141.6	0.1	28.0	17.3
J1449-5846	317.72	0.664	2011-06-27-11:08:03/07	0.055	463.329	213.3	0.2	43.6	38.2
J1452-5851	318.087	0.398	2013-01-04-22:34:47/04	0.076	386.646	258.2	0.2	34.6	28.2
J1452-6036	317.296	-1.169	2011-05-19-10:40:04/02	0.25	154.991	348.9	0.1	10.7	11.6
J1454-5846	318.272	0.391	2013-01-02-19:24:06/05	0.067	45.243	116.8	0.2	24.3	21.2
J1457-5900	318.561	-0.027	2013-01-02-19:24:06/12	0.074	1498.624	168.8	0.2	24.5	21.1
J1457-5902	318.538	-0.037	2013-01-04-20:09:48/12	0.074	390.745	472.6	0.2	37.2	38.7
J1504-5621	320.671	1.849	2011-05-06-11:18:02/09	0.059	412.987	149.6	0.2	34.2	33.5
J1511-5414	322.598	3.177	2011-04-22-18:34:35/02	0.18	200.383	84.9	0.1	26.1	29.3
J1518-5415	323.383	2.675	2010-12-12-19:26:19/10	0.11	214.924	168.4	0.0	8.45	13.0
J1519-5734	321.8	-0.238	2010-12-29-22:13:36/13	0.089	518.757	662.7	0.3	28.2	32.9
J1522-5525	323.231	1.397	2011-04-20-18:21:53/04	0.088	1389.615	78.9	0.2	66.0	22.0
J1524-5625	323.0	0.351	2010-12-29-22:13:36/04	0.11	78.231	152.1	0.4	33.9	34.3
J1525-5417	324.258	2.078	2011-05-09-11:33:02/02	0.057	1011.699	236.7	0.2	41.2	48.9
J1525-5545	323.497	0.848	2011-04-19-16:41:28/11	0.1	11.363	126.8	*	*	30.1
J1525-5605	323.286	0.565	2010-12-29-22:13:36/10	0.12	280.348	326.6	0.1	10.7	12.5
J1529-5611	323.678	0.173	2011-01-03-17:39:31/08	0.076	822.253	132.5	0.1	12.5	12.4
J1531-5610	323.897	0.033	2011-04-22-13:41:43/08	0.06	84.206	110.7	0.5	51.3	60.0
J1535-5848	322.797	-2.406	2011-04-24-10:48:37/09	0.11	307.178	108.5	0.2	37.1	38.4
J1536-5433	325.374	0.98	2011-04-22-13:41:43/11	0.12	881.438	148.8	0.6	84.1	93.3
J1536-5907	322.722	-2.734	2011-05-08-10:33:52/11	0.037	557.840	320.2	0.2	37.1	19.4
J1537-5645	324.283	-0.943	2010-12-11-23:55:11/04	0.051	430.464	704.6	0.9	67.8	53.4
J1538-5519	325.219	0.134	2011-01-03-17:39:31/12	0.11	395.733	595.2	0.2	12.3	17.6
J1538-5638	324.378	-0.871	2011-01-02-19:53:24/05	0.12	843.955	585.2	0.1	17.4	24.8
J1539-5521	325.256	0.077	2011-04-22-13:41:43/12	0.062	1004.950	377.8	0.1	21.0	13.8
J1540-5736	324.109	-1.891	2011-01-02-19:53:24/13	0.16	612.889	308.1	0.1	12.7	13.0
J1542-5034	328.568	3.577	2011-07-07-07:30:06/11	0.13	599.247	87.4	0.2	58.5	39.9
J1542-5133	327.913	2.827	2011-06-30-13:07:22/06	0.12	1783.864	185.4	0.1	31.7	25.8
J1542-5303	327.073	1.578	2011-06-27-06:35:48/09	0.12	1207.591	261.1	0.2	21.9	23.9
J1543-5149	327.921	2.479	2011-07-04-07:23:31/07	0.1	2.056	51.1	0.4	38.5	15.7
J1546-5302	327.47	1.301	2011-06-27-06:35:48/02	0.13	580.842	286.5	0.1	37.0	36.7

J1547-5750	324.663	-2.601	2011-05-16-11:48:21/07	0.018	647.196	143.3	0.2	29.7	38.8
J1547-5839	324.167	-3.243	2011-05-04-11:55:27/12	0.052	242.190	223.7	0.4	42.1	29.0
J1550-5242	328.144	1.198	2011-07-01-06:28:52/05	0.092	749.667	334.7	0.2	56.4	38.2
J1550-5317	327.78	0.737	2011-07-01-06:28:52/06	0.13	710.563 [†]	528.2	0.2	22.5	9.8
J1551-5310	328.034	0.669	2011-07-06-06:46:53/09	0.12	453.456	484.7	0.3	19.3	25.6
J1554-5209	329.006	1.194	2011-07-03-09:45:32/06	0.07	125.229	123.9	*	*	23.3
J1556-5358	328.117	-0.436	2011-05-17-11:18:22/08	0.11	994.679	429.5	0.3	46.0	63.5
J1558-5419	328.1	-0.87	2011-06-27-12:21:33/10	0.094	594.575	641.7	0.3	36.4	26.0
J1601-5244	329.448	0.065	2011-06-26-06:24:21/05	0.037	853.124 [‡]	273.2	0.1	25.5	16.8
J1601-5335	328.935	-0.628	2011-07-06-06:46:53/13	0.07	288.481	193.0	0.2	29.5	20.2
J1603-5657	326.884	-3.309	2012-08-07-11:27:02/03	0.11	496.077	261.2	0.3	93.1	74.4
J1610-5006	332.278	1.05	2011-05-05-12:06:36/01	0.18	481.124	413.4	0.3	34.9	30.3
J1611-4949	332.59	1.14	2011-05-05-12:06:36/04	0.17	666.436	554.0	0.1	27.5	18.8
J1618-4723	335.037	2.184	2011-05-06-13:02:25/03	0.087	203.553	136.0	0.7	94.8	100.5
J1621-5243	331.718	-2.045	2012-08-06-10:57:27/03	0.13	371.922	355.5	0.1	18.1	18.1
J1622-4802	335.139	1.17	2011-05-06-13:02:25/07	0.12	265.072	365.6	0.4	53.8	33.6
J1622-4944	333.911	-0.013	2010-12-29-03:31:28/08	0.087	1072.978	751.6	0.4	54.6	36.2
J1622-4950	333.849	-0.102	2010-12-31-21:03:27/08	0.15	4326.239	955.0	1.5	42.3	52.2
J1623-4949	334.003	-0.214	2010-12-31-21:03:27/08	0.054	725.746	180.0	0.3	69.9	51.8
J1625-4904	334.69	0.145	2010-12-31-21:03:27/01	0.12	460.345	688.3	0.1	20.2	14.4
J1625-4913	334.578	0.041	2011-01-02-21:07:04/02	0.021	355.856	720.2	*	*	24.9
J1626-4537	337.346	2.367	2011-12-05-03:39:15/07	0.14	370.144	240.0	0.4	69.5	48.7
J1627-4845	335.137	0.15	2011-01-02-21:07:04/01	0.11	612.332	555.4	0.3	35.8	23.5
J1628-4804	335.766	0.461	2011-01-02-21:07:04/11	0.043	865.971	950.0	0.9	111.0	88.0
J1632-4509	338.343	2.002	2011-06-30-14:20:50/04	0.073	523.410 [†]	409.1	0.1	30.7	14.7
J1632-4621	337.527	1.1	2011-06-26-16:09:12/12	0.21	1709.167	559.4	0.1	29.8	17.8
J1635-4944	335.391	-1.57	2011-10-13-06:08:35/08	0.17	671.973	466.1	0.1	10.8	13.1
J1636-4440	339.18	1.799	2011-07-03-10:59:47/08	0.12	206.654	449.0	0.2	22.0	15.0
J1636-4803	336.7	-0.515	2012-08-07-04:51:33/11	0.09	1204.655	501.9	0.7	105.0	68.0
J1637-4450	339.248	1.475	2011-07-03-10:59:47/07	0.12	252.869	471.6	0.2	27.2	22.4
J1637-4642	337.788	0.312	2011-07-12-08:31:53/07	0.15	154.048	418.7	0.2	21.5	21.5
J1638-4344	340.191	2.081	2011-10-13-01:23:53/13	0.038	1121.942	230.7	0.2	25.0	25.8
J1638-4417	339.768	1.73	2011-07-13-07:33:40/03	0.064	117.802	436.6	0.2	25.3	26.8
J1638-4608	338.343	0.544	2011-07-12-08:31:53/06	0.094	278.156	422.7	0.2	41.4	32.7
J1638-5226	333.702	-3.739	2011-04-24-12:01:57/13	0.12	340.503	168.0	0.3	42.7	26.5
J1639-4359	340.023	1.875	2011-07-03-10:59:47/03	0.075	587.557	255.3	0.7	111.0	88.7
J1643-4505	339.728	0.547	2011-07-06-08:00:14/13	0.12	237.390	480.7	0.1	18.2	23.2
J1643-4550	339.115	0.105	2011-05-17-13:02:58/03	0.1	717.516	452.1	0.2	45.5	33.7
J1648-4611	339.438	-0.794	2011-05-17-13:02:58/06	0.067	164.958	391.4	0.5	54.7	31.7
J1649-4653	339.019	-1.38	2011-05-19-14:18:15/03	0.15	557.038	327.6	0.1	18.6	12.7
J1649-4729	338.538	-1.759	2011-05-19-14:18:15/07	0.1	297.686	540.1	0.2	22.0	19.0
J1650-4126	343.291	1.997	2012-12-29-19:20:46/06	0.14	308.916	250.6	0.1	22.0	19.4
J1651-4519	340.506	-0.719	2011-01-22-00:58:23/13	0.074	517.446	555.5	0.4	34.2	27.5
J1653-4030	344.422	2.107	2011-04-20-20:48:56/04	0.051	1019.368	407.7	0.3	31.1	33.9
J1654-4140	343.609	1.247	2011-01-02-22:20:50/09	0.075	1273.909	313.6	0.5	121.0	39.7
J1658-4306	342.933	-0.214	2011-01-03-20:05:59/09	0.12	1166.459	857.6	0.4	37.3	28.5
J1659-4316	343.0	-0.547	2011-05-05-13:20:12/02	0.095	474.381	643.8	0.1	28.5	22.4
J1702-4128	344.744	0.123	2010-12-09-21:35:04/09	0.098	182.154	367.5	0.7	62.9	41.6
J1702-4217	344.078	-0.329	2011-01-01-20:16:16/04	0.095	227.564	622.3	0.3	22.3	27.8
J1702-4306	343.405	-0.813	2011-01-01-20:16:16/02	0.075	215.508	536.1	0.2	34.4	31.4
J1702-4310	343.352	-0.852	2011-05-05-13:20:12/07	0.12	240.601	374.8	0.4	44.1	49.8
J1705-4108	345.291	-0.042	2010-12-09-21:35:04/03	0.12	861.081	1092.2	0.7	94.4	38.0
J1706-4310	343.758	-1.375	2010-12-31-22:16:59/13	0.054	616.980	654.5	0.2	41.3	22.7
J1707-4341	343.521	-1.915	2013-01-05-19:45:58/04	0.18	890.599	394.5	0.1	25.0	19.6

154 Appendix A. HTRU Galactic plane survey known pulsar re-detections

J1707-4729	340.424	-4.135	2009-01-12-02:39:17/10	0.25	266.473	268.2	0.1	15.3	15.0
J1708-3506	350.47	3.124	2011-07-07-09:57:10/03	0.099	4.505	146.7	0.2	14.9	44.0
J1709-3626	349.578	2.095	2011-07-12-09:46:00/05	0.037	447.858	391.9	0.5	90.7	79.5
J1709-4342	343.706	-2.193	2013-01-05-19:45:58/05	0.13	1735.907	269.1	0.1	11.3	13.8
J1711-4322	344.145	-2.244	2011-04-24-13:15:17/08	0.11	102.618	191.9	0.1	14.0	16.4
J1713-3949	347.279	-0.491	2013-01-05-04:06:07/12	0.044	392.453	346.7	0.3	50.0	11.7
J1715-3700	349.757	0.886	2011-07-06-09:13:30/02	0.019	779.619	414.4	0.4	29.8	26.7
J1715-4034	346.912	-1.277	2011-10-13-07:22:02/07	0.14	2072.164	257.3	0.6	95.8	87.4
J1716-3720	349.596	0.519	2011-07-06-09:13:30/08	0.12	630.326	680.6	0.2	35.7	24.8
J1716-4005	347.418	-1.155	2011-10-13-07:22:02/08	0.045	311.813	433.8	1.2	79.8	115.2
J1718-3714	349.928	0.237	2011-06-27-14:48:40/13	0.075	1289.388	878.9	0.2	17.1	13.2
J1718-3825	348.951	-0.432	2011-05-17-14:17:08/09	0.13	74.675	246.8	0.5	64.6	41.2
J1719-4302	345.341	-3.325	2012-08-07-13:53:21/11	0.1	235.493	296.9	0.2	37.3	36.1
J1720-3659	350.332	0.1	2011-07-01-08:58:10/13	0.12	351.124	380.4	0.3	63.1	49.9
J1723-3659	350.682	-0.409	2011-07-02-09:55:20/11	0.096	202.725	253.5	0.9	132.0	117.0
J1724-3149	355.142	2.228	2011-05-09-17:42:14/01	0.12	948.241	412.2	0.2	30.9	25.7
J1724-3505	352.437	0.38	2013-01-29-00:48:10/12	0.14	1221.728	887.0	0.1	17.7	14.7
J1730-3353	354.135	-0.004	2010-12-09-22:48:23/08	0.053	3270.234	254.6	0.3	71.3	34.0
J1731-3123	356.233	1.354	2011-01-03-21:19:26/03	0.084	753.049	352.1	0.2	41.7	28.6
J1733-3030	357.32	1.301	2011-01-03-21:19:26/11	0.058	362.052	637.0	0.2	22.0	15.2
J1733-3322	354.917	-0.238	2011-01-01-21:29:36/13	0.15	1245.871	522.0	0.3	43.9	32.7
J1734-3333	354.819	-0.433	2010-12-09-22:48:23/13	0.092	1169.829	592.2	0.3	10.5	18.3
J1736-2843	359.142	1.764	2011-07-03-13:48:57/05	0.11	6444.420	305.7	0.2	52.4	25.4
J1736-3511	353.614	-1.598	2013-01-30-18:19:00/08	0.084	502.805	98.4	0.1	20.1	16.7
J1737-3102	357.298	0.373	2011-01-03-21:19:26/12	0.081	768.686	273.6	0.4	85.5	46.8
J1738-2647	0.94	2.544	2011-05-18-17:07:42/06	0.21	349.591	179.7	0.0	8.36	12.7
J1740-3327	355.564	-1.436	2011-05-04-15:20:06/10	0.1	515.002	270.3	0.2	32.4	23.3
J1741-2733	0.636	1.582	2011-07-01-10:11:21/10	0.081	892.953	142.7	0.8	98.9	108.4
J1743-3153	357.221	-1.109	2011-10-13-10:01:19/13	0.019	193.109	506.9	0.5	55.1	47.7
J1744-2335	4.463	2.937	2013-02-01-23:19:04/01	0.2	1683.509	103.5	0.0	7.27	16.0
J1747-2802	0.971	0.121	2011-05-17-15:33:25/07	0.081	2780.071	823.2	0.4	119.0	14.6
J1751-3323	356.829	-3.382	2011-01-28-21:43:39/05	0.068	548.227	295.5	1.0	274.0	111.2
J1752-2410	4.93	1.039	2011-04-24-21:02:42/13	0.14	191.037	506.9	0.2	25.2	20.1
J1753-2240	6.297	1.661	2011-05-05-18:50:26/02	0.052	95.135	155.3	0.1	24.1	14.9
J1754-2422	4.947	0.618	2011-01-01-22:43:00/03	0.11	2090.215	741.5	*	*	18.5
J1755-2521	4.255	-0.15	2011-04-24-21:02:42/11	0.063	1175.999	252.6	0.6	149.0	52.4
J1755-2725	2.432	-1.135	2012-12-29-04:38:59/03	0.07	261.954	113.1	0.4	41.1	22.1
J1758-2206	7.378	0.933	2010-12-10-01:47:49/05	0.12	143.426 [†]	681.0	0.2	33.5	13.5
J1758-2540	4.263	-0.807	2013-01-22-01:43:12/09	0.033	2107.278	201.5	0.6	70.0	62.1
J1758-2630	3.555	-1.225	2013-01-22-01:43:12/10	0.038	1202.900	341.1	0.4	92.8	24.5
J1758-2846	1.556	-2.294	2013-02-01-19:56:34/01	0.12	766.705	60.6	0.1	42.5	32.6
J1759-2302	6.702	0.257	2010-12-31-00:45:15/02	0.038	810.720	865.1	1.2	140.0	52.2
J1759-2549	4.261	-1.082	2011-05-16-16:24:16/11	0.09	956.585	422.0	0.4	85.9	30.0
J1802-1745	11.573	2.377	2011-07-06-11:40:16/04	0.077	514.671	261.2	0.2	39.1	27.2
J1807-2459A	5.837	-2.203	2011-05-08-15:24:15/04	0.11	3.059	134.3	0.6	58.0	24.3
J1809-1917	11.094	0.08	2011-05-17-17:28:45/04	0.12	82.756	197.0	1.2	75.0	35.1
J1809-2004	10.363	-0.202	2011-07-02-12:25:09/09	0.042	434.813	852.2	0.8	66.6	34.1
J1810-2005	10.545	-0.563	2011-06-26-12:10:21/09	0.21	32.820	238.8	0.2	8.13	10.2
J1811-1835	11.909	0.049	2011-05-17-17:28:45/07	0.037	557.473	771.2	0.4	74.0	31.9
J1811-2439	6.632	-2.954	2011-05-08-15:24:15/13	0.095	415.813	168.3	0.2	22.4	52.1
J1812-1910	11.522	-0.456	2011-06-26-12:10:21/07	0.11	431.008	916.9	0.1	15.3	11.4
J1812-2526	6.013	-3.448	2011-05-08-15:24:15/08	0.041	315.835	361.8	0.2	4.62	28.5
J1814-1649	13.82	0.245	2013-01-01-00:04:30/13	0.11	957.475	768.7	0.6	97.4	45.2
J1814-1744	13.021	-0.215	2013-01-01-00:04:30/08	0.051	3976.312	794.5	0.6	111.0	28.3

J1815-1910	11.81	-0.963	2013-01-01-23:13:45/03	0.015	1249.942	535.1	0.3	72.9	32.1
J1818-1519	15.55	0.192	2011-01-01-02:19:28/05	0.16	939.691	824.3	0.5	44.9	39.4
J1818-1541	15.27	-0.063	2011-01-01-02:19:28/11	0.17	551.137	704.5	0.2	27.4	14.8
J1819-0925	20.935	2.633	2012-04-14-18:35:20/01	0.17	852.050	378.0	0.2	36.5	27.2
J1819-1408	16.797	0.394	2010-12-30-00:55:56/10	0.089	1788.497	1139.2	0.3	35.4	20.0
J1821-1432	16.628	-0.168	2010-12-10-03:01:21/10	0.049	1915.116	554.4	0.2	38.7	26.1
J1822-0907	21.53	2.161	2011-12-05-06:18:35/02	0.095	974.708	463.1	0.1	14.7	14.7
J1822-1252	18.218	0.394	2010-12-30-00:55:56/12	0.099	2071.082	813.4	0.2	18.3	11.2
J1823-1526	16.033	-0.948	2011-01-03-04:37:22/11	0.18	1625.402	618.8	0.1	14.4	13.3
J1824-1159	19.253	0.324	2012-08-07-08:52:51/07	0.093	362.493	465.1	0.5	85.4	47.4
J1824-1423	17.146	-0.796	2011-04-23-21:19:27/12	0.11	359.394	429.8	0.4	70.0	47.6
J1826-1526	16.358	-1.553	2011-05-07-15:44:36/03	0.021	382.073	528.1	0.4	78.3	41.3
J1827-0750	23.176	1.803	2011-07-03-16:30:26/13	0.17	270.502	375.4	0.3	48.7	57.7
J1827-0934	21.724	0.841	2011-07-02-13:38:31/12	0.18	512.547	263.2	0.1	7.25	12.3
J1828-1007	21.324	0.424	2013-01-01-03:46:01/08	0.038	153.197	299.3	0.2	22.2	20.2
J1828-1057	20.587	0.025	2013-01-01-03:46:01/09	0.027	246.334	243.7	0.2	24.4	16.3
J1828-1101	20.495	0.042	2013-01-01-03:46:01/09	0.068	72.057	604.0	2.3	161.0	85.7
J1830-1135	20.193	-0.59	2009-01-13-03:32:35/01	0.18	3110.768 [†]	283.4	0.2	67.7	21.9
J1831-0952	21.897	-0.128	2011-07-06-12:52:40/01	0.052	67.269	246.3	0.3	27.7	24.6
J1831-1223	19.618	-1.217	2011-12-06-05:56:02/12	0.14	2857.955	329.8	0.4	61.5	63.8
J1832-0644	24.806	1.07	2012-12-30-01:26:15/04	0.17	744.311	568.4	0.2	28.1	20.9
J1834-0602	25.64	0.965	2012-12-30-01:26:15/12	0.12	487.916	441.5	0.4	56.8	41.4
J1834-0731	24.288	0.366	2012-12-30-01:26:15/09	0.19	512.996	306.5	0.2	17.4	11.4
J1834-0742	24.151	0.223	2012-12-30-01:26:15/09	0.015	788.369	520.4	0.3	63.4	38.6
J1834-1202	20.287	-1.743	2011-12-06-05:56:02/13	0.18	610.254	349.5	0.1	11.2	18.3
J1835-0924	22.767	-0.804	2011-05-17-18:42:22/08	0.081	859.199	433.5	0.4	44.3	25.0
J1835-1020	21.98	-1.302	2011-05-17-18:42:22/09	0.11	302.450	114.9	1.1	212.0	119.0
J1837-0559	26.001	0.379	2011-01-04-00:59:52/09	0.14	201.063	314.8	0.2	20.5	17.7
J1837-1243	19.983	-2.662	2011-12-06-05:56:02/02	0.087	1876.041	288.8	0.1	33.3	18.7
J1839-0402	28.016	0.73	2009-04-16-17:52:00/11	0.11	520.941	233.7	0.1	27.1	13.5
J1839-0459	27.147	0.321	2009-04-16-17:52:00/10	0.056	585.321	237.0	0.3	50.2	22.8
J1840-04	27.592	0.241	2010-12-30-02:35:36/05	0.16	422.315	365.7	*	*	22.5
J1840-0753	24.698	-1.242	2013-01-01-02:30:42/01	0.1	437.867	670.0	0.2	11.3	18.9
J1840-0809	24.441	-1.308	2013-01-02-01:39:47/01	0.17	955.671	349.7	0.5	173.0	99.0
J1840-0815	24.314	-1.283	2013-01-01-02:30:42/04	0.13	1096.440	228.8	0.6	139.0	140.5
J1840-0840	24.01	-1.616	2013-01-01-02:30:42/10	0.037	5309.379	270.3	0.9	139.0	151.2
J1840-1207	20.94	-3.197	2011-01-26-00:34:08/01	0.2	754.470	283.0	0.0	7.81	15.5
J1841-0310	28.968	0.776	2011-01-01-03:33:05/08	0.075	1657.650	218.3	0.1	16.5	20.1
J1841-0345	28.424	0.437	2011-07-06-14:46:36/09	0.076	204.088	195.6	1.0	132.0	70.6
J1841-0500	27.323	-0.034	2009-04-16-17:52:00/03	0.15	912.918	484.2	*	*	23.0
J1842-0309	29.078	0.584	2011-01-03-00:48:46/04	0.097	404.921	962.4	0.2	14.9	12.3
J1842-0415	28.086	0.111	2009-04-16-17:52:00/05	0.17	526.692	184.7	0.1	17.4	14.9
J1843-0211	30.084	0.768	2011-01-03-00:48:46/12	0.094	2027.528	438.0	0.6	151.0	65.5
J1843-0408	28.374	-0.172	2009-04-16-17:52:00/06	0.03	781.936	248.6	0.2	43.4	18.2
J1843-0459	27.581	-0.505	2009-04-16-17:52:00/02	0.11	754.962	442.1	0.9	110.0	64.7
J1843-0744	25.092	-1.68	2013-01-01-02:30:42/02	0.14	475.395	320.0	0.1	16.0	17.6
J1843-0806	24.806	-1.934	2013-01-01-02:30:42/09	0.085	536.423	217.9	0.2	34.4	32.8
J1844-0310	29.343	0.036	2011-04-27-18:46:59/01	0.09	525.052	831.5	0.3	61.6	39.8
J1845-0316	29.39	-0.255	2011-01-03-02:08:40/03	0.11	207.638	498.1	0.2	26.0	18.9
J1845-0743	25.429	-2.304	2012-10-03-07:38:33/01	0.2	104.694	280.3	0.3	55.2	54.8
J1846-0749	25.386	-2.431	2012-10-03-07:38:33/03	0.17	350.109	389.4	0.1	19.3	22.9
J1847-0438	28.371	-1.268	2011-07-02-14:51:49/04	0.091	957.990	238.6	0.3	99.5	79.9
J1847-0443	28.318	-1.361	2011-07-02-14:51:49/04	0.047	340.833	455.5	0.1	28.9	16.4

156 Appendix A. HTRU Galactic plane survey known pulsar re-detections

J1849-0317	29.834	-1.173	2011-04-21-21:21:41/13	0.1	668.410	41.0	0.4	60.5	68.5
------------	--------	--------	------------------------	-----	---------	------	-----	------	------

[†] Spin period detected at the second harmonics, i.e. at half of the fundamental spin period.

[‡] Spin period detected at the third harmonics, i.e. at one third of the fundamental spin period.

Erklärung

Ich versichere, dass ich die von mir vorgelegte Dissertation selbständig angefertigt, die benutzten Quellen und Hilfsmittel vollständig angegeben und die Stellen der Arbeit – einschließlich Tabellen, Karten und Abbildungen –, die anderen Werken im Wortlaut oder dem Sinn nach entnommen sind, in jedem Einzelfall als Entlehnung kenntlich gemacht habe; dass diese Dissertation noch keiner anderen Fakultät oder Universität zur Prüfung vorgelegen hat; dass sie noch nicht veröffentlicht worden ist sowie, da ich eine solche Veröffentlichung vor Abschluss des Promotionsverfahrens nicht vornehmen werde. Die Bestimmungen dieser Promotionsordnung sind mir bekannt. Die von mir vorgelegte Dissertation ist von Prof. Dr. Michael Kramer betreut worden.

Unterschrift: Cherry W. Y. Ng

Datum: 16 - 06 - 2014

Publications that account for major parts of the thesis

Referred:

- **Ng, C.**; Bailes, M.; Bates, S. D.; Bhat, N. D. R.; Burgay, M.; Burke-Spolaor, S.; Champion, D. J.; Coster, P.; Johnston, S.; Keith, M. J.; Kramer, M.; Levin, L.; Petroff, E.; Possenti, A.; Stappers, B. W.; van Straten, W.; Thornton, D.; Tiburzi, C.; Bassa, C. G.; Freire, P. C. C.; Guillemot, L.; Lyne, A. G.; Tauris, T. M.; Shannon, R. M.; Wex, N.
'The High Time Resolution Universe pulsar survey - X. Discovery of four millisecond pulsars and updated timing solutions of a further 12'
Monthly Notices of the Royal Astronomical Society, 2014, Volume 439, Issue 2, p.1865-1883

Non-referred:

- **Ng, C.**; HTRU Collaboration
'Conducting the deepest all-sky pulsar survey ever: the all-sky High Time Resolution Universe survey'
Proceedings of the International Astronomical Union, 2013, Volume 291, pp. 53-56

In preparation:

- **Ng, C.**; Champion, D. J.; Bailes, M.; Barr, E. B.; Bates, S. D.; Bhat, N. D. R.; Burgay, M.; Burke-Spolaor, S.; Johnston, S.; Keith, M. J.; Kramer, M.; Levin, L.; Petroff, E.; Possenti, A.; Stappers, B. W.; van Straten, W.; Tiburzi, C.; Eatough, R. P., Lyne, A. G.
'The High Time Resolution Universe Pulsar Survey XII : Galactic plane acceleration search and its implications for the SKA'
To be submitted to Monthly Notices of the Royal Astronomical Society, 2014